

INSIGHTS INTO POLYMERISATION OF FtsZ AND OTHER CYTOMOTIVE FILAMENTS



James Mark Wagstaff

St Catharine's College, University of Cambridge

and

MRC Laboratory of Molecular Biology

This dissertation is submitted for the degree of

Doctor of Philosophy

June 2019

Declaration

This dissertation is the result of my own work and includes nothing that is the outcome of work done in collaboration except where specifically indicated in the text.

It is not substantially the same as any that I have submitted, or, is being concurrently submitted for a degree or diploma or other qualification at the University of Cambridge or any other University or similar institution except as declared in the Preface and specified in the text. I further state that no substantial part of my dissertation has already been submitted, or, is being concurrently submitted for any such degree, diploma or other qualification at the University of Cambridge or any other University or similar institution except as declared in the Preface and specified in the text.

This dissertation does not exceed the regulation length of 60,000 words, including tables and footnotes.

INSIGHTS INTO POLYMERISATION OF FTSZ AND OTHER CYTOMOTIVE FILAMENTS

James Mark Wagstaff

Abstract

Protein filaments are used in different ways to organise other molecules in space and time within cells. Some proteins form filaments that couple hydrolysis of nucleotides to their polymerisation cycle in order to power the directed movement of other molecules, these filaments are termed cytomotive. Only members of the actin and tubulin superfamilies are known to form cytomotive filaments. The protein FtsZ, a homologue of eukaryotic tubulins, forms cytomotive filaments that are used in almost all bacteria and many archaea to organise cell division.

Here I show using X-ray crystallography and electron cryomicroscopy (cryoEM) that FtsZ switches conformation when it polymerises into filaments. I then show using cryoEM that this conformational switch is likely needed for recognition of filaments by the widely conserved filament cross-linking protein ZapA. I also present the development of a high-throughput assay for detection of better FtsZ inhibitors, which uses principles derived from the structural studies. Finally, I demonstrate that the conformational switch upon polymerisation seen in FtsZ is conserved within the tubulin superfamily, that actin superfamily members also exhibit a conserved conformational switch upon polymerisation, and that having such a switch explains the coupling of kinetic and structural polarities required for cytomotivity of the filaments formed by these protein families.

Acknowledgements

There are many people to whom I am grateful for their support during my PhD.

Firstly, a thank you to my scientific collaborators. Within Jan Löwe's group this includes my "FtsZ bro", Tim Nierhaus, and Danguole Kuresaite-Ciziene, who helped me a lot at the start of my time here. In the wider LMB, I am very grateful to the huge team of scientific and non-scientific staff who make this such a remarkable place to work. In particular, I am grateful to: David Barford for acting as my second supervisor, Wolfgang Schmied for his help with robotics; the entire EM facility, but especially Christos Savva and Giuseppe Cannone; Stephen McLaughlin for getting me going with FP; Mark Skehel for help with mass spectrometry; Minmin Yu for help with X-ray data collection logistics; and Fabrice Gorrec for help with setting up crystallography trials. I am very grateful to Christina Rada and Julian Sale, as Directors of Studies at the LMB, for their support and guidance, especially in helping me complete a Policy Fellowship at the Ministry of Justice.

Beyond the LMB, I have been lucky to work, and subsequently correspond, with Jose Manuel Andreu and colleagues at CSIC, in Madrid. At some point I stopped being surprised when I had an idea and subsequently realised that Jose Manuel (or, equally likely, Linda Amos) had published it several decades ago. I am grateful to Tony Hope at the Dundee Drug Discovery Unit for supplying the pilot screening library. I am also grateful to Martin Welch at the Department of Biochemistry for acting as my University supervisor, and for being a kind mentor.

I have been very fortunate to be supported by the Boehringer Ingelheim Fonds during my PhD. The BIF have supported me financially, but I am most grateful to them for the opportunity to get to know the other Fellows at Hirschegg.

In retrospect, I was remarkably naïve about the world of academia when I applied to work in Jan Löwe's group. I can see now how easy it would have been for me to end up with a supervisor who I did not like or respect, and working on a project I ultimately found uninteresting. I feel incredibly lucky, therefore, to have spent the last four years working with Jan: learning from someone who I have the utmost respect for and who has provided me with the guidance and freedom to work on projects that I care about deeply.

Acknowledgements

I am also grateful to the other members of our group who I have had the great pleasure of working alongside. I will miss the lunchtime discussions ranging from science to literally everything else.

All PhD students face their fair share of challenges, and I was certainly no exception. I am certain that I could not have completed my work here without the support of my amazing friends. In particular: The Super Duper Fun House et al., the Gents of SCCBC, Ben and The Rat, Aaron and Ben, El Commodore, and Uncle Dave – thank you.

Finally, there are the people to whom I will never be able to adequately express the gratitude I feel for their love and belief in me. To my parents, Anne and Mark, thank you for giving me wings to carry me away and roots to come back to. To Emma, thank you for making me so proud to be your brother. And to Clare, thank you for making everything better.

James Wagstaff

Cambridge, 2019

For Tom.

Table of Contents

ABSTRACT	5
DECLARATION	3
ACKNOWLEDGEMENTS	7
TABLE OF CONTENTS	10
TABLE OF FIGURES	11
ABBREVIATIONS.....	12
1 INTRODUCTION.....	14
1.1 Cytoskeletons.....	14
1.2 The tubulins	17
1.3 The actins	22
1.4 Coiled coil filaments.....	29
1.5 Other prokaryotic cytoskeletons.....	33
1.6 Perspective on prokaryotic cytoskeletons.....	37
1.7 Motivation and outline.....	39
2 RESULTS AND DISCUSSION	41
2.1 FtsZ does polymerisation-coupled conformational switching	41
2.2 ZapA cross-links FtsZ filaments.....	69
2.3 An assay to find better FtsZ inhibitors.....	81
2.4 Polymerisation-coupled conformational switching across the actin and tubulin superfamilies	94
3 MATERIALS AND METHODS.....	119
3.1 General methods.....	119
3.2 Strains.....	122
3.3 Growth Media and Standard Solutions.....	122
3.4 Expression and purification of proteins	124
3.5 X-ray crystallography.....	130
3.6 Electron cryo-microscopy (cryoEM).....	131
3.7 Fluorescence polarisation assay for GTP-competitive inhibitors of FtsZ.....	134
3.8 Superfamily analysis	136
4 APPENDICES.....	137
4.1 Principles of X-ray Crystallography	137
4.2 Principles of Electron Cryo-Microscopy (CryoEM).....	147
4.3 Principles of Fluorescence Polarisation.....	152
4.4 Additional figures.....	157
5 TABLES.....	161
6 REFERENCES	176

Table of Figures

Figures are numbered with the one digit section number followed by a dash and a number that resets for each section (x-n). They are usually placed at the end of the subsection (x.y.z) in which they are first mentioned.

Figure 1-1 – Prokaryotic cytoskeletons discussed here.....	16
Figure 1-2 – Tubulin superfamily filaments.....	18
Figure 1-3 – Actin superfamily filaments	24
Figure 1-4 – Towards structural understanding of diverse prokaryotic cytoskeletal filaments.....	36
Figure 2-1 – SaFtsZ mutants T66W and F138A have compromised polymerisation and GTPase activities.....	46
Figure 2-2 – Nucleotide-bound SaFtsZ crystal structures group into two conformations: open and closed....	49
Figure 2-3 – All FtsZ structures can be placed in one of two groups: open and closed.	51
Figure 2-4 – Atomic details of the SaFtsZ regions allowing the conformational switch.....	54
Figure 2-5 – Crystallised pairs of FtsZ molecules show the differences in longitudinal interactions between open and closed structures	58
Figure 2-6 – CryoEM of <i>S. aureus</i> FtsZ filaments.....	61
Figure 2-7 – CryoEM of <i>E. coli</i> FtsZ filaments.....	62
Figure 2-8 – A polymerisation-associated conformational switch allows treadmilling of single-stranded filaments.....	66
Figure 2-9 – A polymerisation-associated conformational switch generates asymmetry between filament end interfaces.....	67
Figure 2-10 – Proposed role of ZapA	72
Figure 2-11 – Distribution of ZapA across Bacteria	74
Figure 2-12 – “Ladders” of FtsZ and ZapA are seen in cryoEM	77
Figure 2-13 – Attempted 3D reconstruction of FtsZ:ZapA copolymer.....	79
Figure 2-14 – Rationale for a GTP-competitive FtsZ inhibitor.....	85
Figure 2-15 – An FP assay for GTP-competitive FtsZ binding molecules.....	88
Figure 2-16 – Interaction of SaFtsZ with GTP analogues.....	90
Figure 2-17 – Validation of FP assay for High Throughput Screening	92
Figure 2-18 – Investigating the conserved basis of cytomotivity	98
Figure 2-19 – Approach for analysing conservation of conformational dynamics	102
Figure 2-20 – PCA of tubulin superfamily structures.....	105
Figure 2-21 – The conformational switches within tubulin subfamilies are similar	109
Figure 2-22 – PCA of actin superfamily structures.....	112
Figure 2-23 – The conformational switches within cytomotive actin subfamilies are similar	113
Figure 4-1- Diffraction by an arbitrary object.....	141
Figure 4-2 - Diffraction by a lattice	145
Figure 4-3 – Typical electron microscope optics	148
Figure 4-4 - Iterative projection matching and the central slice theorem.....	151
Figure 4-5 – Calculated projections of SaFtsZ crystal filaments.....	157
Figure 4-6 – Invariant regions plotted on conserved structural cores.....	158
Figure 4-7 – PCA of tubulin subfamilies, coloured by nucleotide state	159
Figure 4-8 – PCA of actin subfamilies, coloured by nucleotide state	160

Abbreviations

Alp	Actin-like protein
AMB	<i>Magnetospirillum magneticum</i> AMB-1
ASU	Asymmetric Unit
ATP/ADP	adenosine tri/diphosphate
BSA	Bovine serum albumin
CCRP	Coiled coil rich protein
cryoEM	Electron cryo-microscopy
CTP	cytosine tri-phosphate
C α	Alpha-carbon of an amino acid
DMSO	dimethyl sulfoxide
DNA	deoxyribonucleic acid
DTT	dithiothreitol
EDTA	ethylenediaminetetraacetic acid
ESCRT	Endosomal sorting complexes required for transport
FA	Fluorescence anisotropy
FI	Fluorescence intensity
FP	Fluorescent polarisation
FtsZ	Filamentous temperature sensitive Z
GMPCPP	guanosine-5'-[(α,β)-methylene]triphosphate
GTDB	Genome Taxonomy Database
GTP/GDP	guanosine tri/diphosphate
GTP γ S	guanosine 5'-O-[gamma-thio]triphosphate
HDX-MS	Hydrogen-deuterium exchange mass spectrometry
HIV/AIDS	Human immunodeficiency virus/ acquired immune deficiency syndrome
IC ₅₀	50% inhibition concentration
IF	Intermediate filament
LDA	Linear discriminant analysis
LMB	Laboratory of Molecular Biology
MeOH	Methanol
MPD	2-methyl-2,4-pentanediol
MRC	Medical Research Council
MRSA	Methicillin-resistant <i>Staphylococcus aureus</i>
MSR	<i>Magnetospirillum gryphiswaldense</i> MSR-1
MT	Microtubule
NCS	Non-crystallographic symmetry

NTD/CTD	N/C-terminal domain
NTP/NDP	nucleoside di/triphosphate
OD ₆₀₀	Optical density at 600 nm
OECD	Organisation for Economic Cooperation and Development
PCA	Principal component analysis
PCR	Polymerase chain reaction
PDB	Protein Data Bank
QC	Quality control
RMSD	Root mean squared deviation
SCOP	Structural Classification Of Proteins
SDS	sodium dodecyl sulphate
SDS-PAGE	sodium dodecyl sulfate polyacrylamide gel electrophoresis
TACK	Thaumarchaeota, Crenarchaeota and Korarchaeota
TB	Tuberculosis
TBE	Tris/borate/EDTA
TWEEN-20	polysorbate 20

I INTRODUCTION

Much of this introduction derives from initial drafts of (Wagstaff and Löwe, 2018), and roughly follows its structure. Some sections are quoted verbatim.

Cellular life is complex and to make it work a great number of systems are in place to enforce more or less strict choreography on the molecules within the cell. The role of “cytoskeletons” in organising the cytoplasm of eukaryotic cells has been recognised since the earliest visualisations of chromosome segregation; and was once considered a feature distinguishing eukaryotic cells from their anucleate prokaryotic cousins. We now know that most, if not all, prokaryotic cells also contain at least one protein filament system responsible for organising other molecules in space and time. While these filament systems in some cases form structures comparable to eukaryotic cytoskeletons, the term prokaryotic cytoskeletons is used to loosely and non-exhaustively refer to many different kinds of protein filaments. These systems are united by the functional properties which stem from polymerisation, and the resulting ability to access length scales bigger than the size of the monomer. Prokaryotic cytoskeletons are involved in many fundamental aspects of cell biology, and are most prevalent in processes of cell shape determination, cell division, and non-chromosomal DNA segregation. Some, but by no means all, of the filament-forming proteins fall into a small number of conserved groups, in particular the almost ubiquitous tubulin and actin families. Understanding what makes these molecular architectures special and, above all, useful in the cellular context demands the study of diverse examples of each, and 25 years of investigation have yielded structural and functional data on cytoskeletal molecules from many bacteria and archaea. This progress is summarised here.

I.1 Cytoskeletons







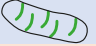
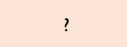




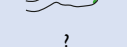


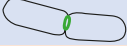
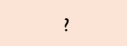
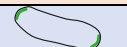


Eukaryotic cytoskeletons are canonically defined by their constitutive protein components: actin, tubulin and intermediate filaments (IFs). These three families of filament-forming proteins are involved in a diverse set of processes that require long-range organisation of subcellular components, across broad time and length scales. In particular, protein filaments are used in eukaryotes for control of cell and endomembrane morphology (dynamically and for long term maintenance of shape), as a scaffold for long-range organisation of cytoplasmic processes (including as a support matrix for cytoskeleton-associated motor proteins, which apparently do not exist in prokaryotes), and for directly

pushing and pulling other molecules in the cytoplasm (especially for the segregation of DNA during division).

The existence of prokaryotic cytoskeletons was first postulated more than 25 years ago in analogy to eukaryotic counterparts when a protein related to tubulin, FtsZ, was discovered in bacteria and archaea and found to have a role in cytokinesis (Bi and Lutkenhaus, 1991; de Boer et al., 1992; Löwe and Amos, 1998; Mukherjee et al., 1993; RayChaudhuri and Park, 1992; Wang and Lutkenhaus, 1996). Prokaryotic actin followed about 5 years later when MreB's role in cell shape maintenance was linked to its polymerisation (Bork et al., 1992; van den Ent et al., 2001; Jones et al., 2001). Many other discoveries have followed since then, including more relatives of eukaryotic cytoskeletal filaments (Ausmees et al., 2003; Derman et al., 2009; Duggin et al., 2015; Ettema et al., 2011; Obita et al., 2007; Szwedziak et al., 2012), but also entirely new classes of filaments such as those formed by bactofilin, SepF, and DivIVA proteins (Bartlett et al., 2017; Kühn et al., 2010; Ramamurthi and Losick, 2008), leading to an expanded concept of what a cytoskeleton can be. We now know that, even at their comparatively small typical cell sizes, prokaryotes often require the function of protein filaments and their ability to act as large, and often dynamic, assemblies of monomers (cytoskeletons) in order to accomplish cellular processes on large length scales (reviewed (Amos and Löwe, 2017)). This is because prokaryotic cells are still extremely big when compared to individual proteins or even large protein complexes such as ribosomes. Protein filaments may have been an important innovation in the evolution of early cells. Figure 1-1 summarises the diversity of prokaryotic cytoskeletons reviewed here. Like eukaryotic cytoskeletons, prokaryotic cytoskeletons rely on interactions between filament forming proteins and a vast number of other proteins to modulate or provide function. These accessory factors are mostly not discussed here.

Below, the rapidly advancing state of our knowledge regarding the molecular biology of known filament-forming proteins in prokaryotes is summarised, with the filaments placed where possible into evolutionarily or structurally related classes. This classification reveals that diverse biological functions are carried out by strikingly similar filaments, and the converse: that a given biological function is carried out in different organisms by unrelated filaments. Mechanistic understanding at a molecular level, incomplete in almost all cases, is the key to making sense of whether and how the diversity observed in filament systems relates to the awe inspiring diversity of natural history seen across the prokaryotic universe.

INTRODUCTION

Protein	Cartoon	Distribution	Function
Tubulin superfamily			
FtsZ		Almost all bacteria.	Organisation of cell division processes.
		Almost all Euryarchaeota. Some other archaea.	Organisation of cell division processes.
FtsZm		Some magnetotactic bacteria.	Unclear role in magnetosome function.
CetZ		Some Euryarchaeota.	Control of cell shape.
TubZ		Diverse bacterial plasmids, bacteriophage genomes, some chromosomal copies.	Segregation of plasmids and phage DNA, others unknown.
BtubAB		Prostheco bacter spp.(Verrucomicrobia).	Unknown.
Artubulin	?	Some Thaumarchaeota.	Unknown.
FtsZl	?	Diverse bacteria.	Unknown, possibly membrane remodelling.
	?	Diverse Euryarchaeota, possibly Crenarchaea.	Unknown, possibly membrane remodelling.
Actin superfamily			
MreB		Almost all non-coccoid bacteria.	Organisation of cell wall synthesis.
	?	Archaeal actins whose closest homologues are MreB remain unstudied.	Unknown.
FtsA		Many bacteria. Not identified in archaea.	Cooperates with FtsZ during cell division.
MamK		Magnetotactic bacteria.	Alignment of magnetosomes.
ParM-like		Diverse bacterial plasmids, bacteriophage genomes, some chromosomal copies.	Segregation of plasmids and phage DNA, others unknown.
	?	A group of archaeal actins, including Ta0583, is related to bacterial ParMs.	Unknown.
Crenactin	?	Some Crenarchaea.	Putative role in cell division.
Coiled coil filaments			
Crescentin		Caulobacter spp.	Required for cell curvature, modulates cell wall synthesis.
Scy, FilP		Actinobacteria	Role in organisation of polar growth.
CCRPs	?	Diverse bacteria.	Diverse cytoskeletal roles, mostly unknown.
DivIVA		Most Gram positive bacteria and some others.	Varied roles in organisation of growth at poles and division.
ESCRT		Diverse archaea. Ubiquitous in some classes of Crenarchaea.	Division in some cases. Others unknown.
CrvA		Vibrio spp.	Promotes cell curvature.
Other filament systems			
Bactofilins	?	Diverse bacteria.	Control of cell shape. Mostly unknown.
SepF		Most Gram positives, all Cyanobacteria.	Cooperates with FtsZ during cell division.
	?	FtsZ containing archaea (Euryarchaeota and others).	Putative FtsZ membrane anchor.
PopZ		Some Gram negatives.	Cell pole marker, signalling hub.
SpoIVA		Sporulating Firmicutes.	Forms a protein coat around forespores.
Periplasmic flagella		Spirochetes.	Forms helical cytoskeleton and produce motility.
Fibril		Spiroplasma spp.	Forms cytoskeletal ribbon.

Rows shaded in blue are bacterial proteins, those in red are archaeal

Figure 1-1 – Prokaryotic cytoskeletons discussed here

Rows shaded blue refer to bacterial systems, those in red are archaeal.

1.2 The tubulins

Homologues of eukaryotic tubulin are widely distributed and are involved in many different cellular processes, in many different ways, often using the dynamic properties of tubulin filaments for “cytomotive” functions (Figure 1-1). The concept of cytomotivity is an important one, to which I will return many times. In short, cytomotive filaments are a subset of cytoskeletal ones which catalyse the hydrolysis of nucleotides in a way that is coupled to the (de)polymerisation cycle of the filament subunits, allowing the filament to directly push or pull other molecules around in the cytoplasm. I discuss this concept in detail in the context of FtsZ in Section 2.1.8, and more broadly in Section 2.4.

Tubulin superfamily members share a distinctive globular domain formed of two independently folded but closely associated subdomains, the N-terminal GTPase domain (Structural Classification of Proteins (SCOP) ID: 52490) and the C-terminal activation domain (SCOP: 55307) (Figure 1-2). The subdomains are separated by the ‘core helix’ (Helix 7 in the consensus topology scheme (Nogales et al., 1998)). Polymerisation occurs via association of one monomer’s GTP-bound GTPase domain with another’s activation domain, altogether forming a catalytically active GTPase site around a GTP molecule at the centre of the intersubunit interface. The intrinsic nucleotide hydrolysis activity of the tubulin polymer, and the reduced stability of a GDP-containing intersubunit interface, make the protofilament dynamic.

We have a good structural understanding of the conserved tubulin protofilament architecture (Figure 1-2A). This basic protofilament has been repurposed several times by cellular genomes and by mobile genetic elements including plasmids and viruses, often forming higher order filaments in these cases (Figure 1-2B).

INTRODUCTION

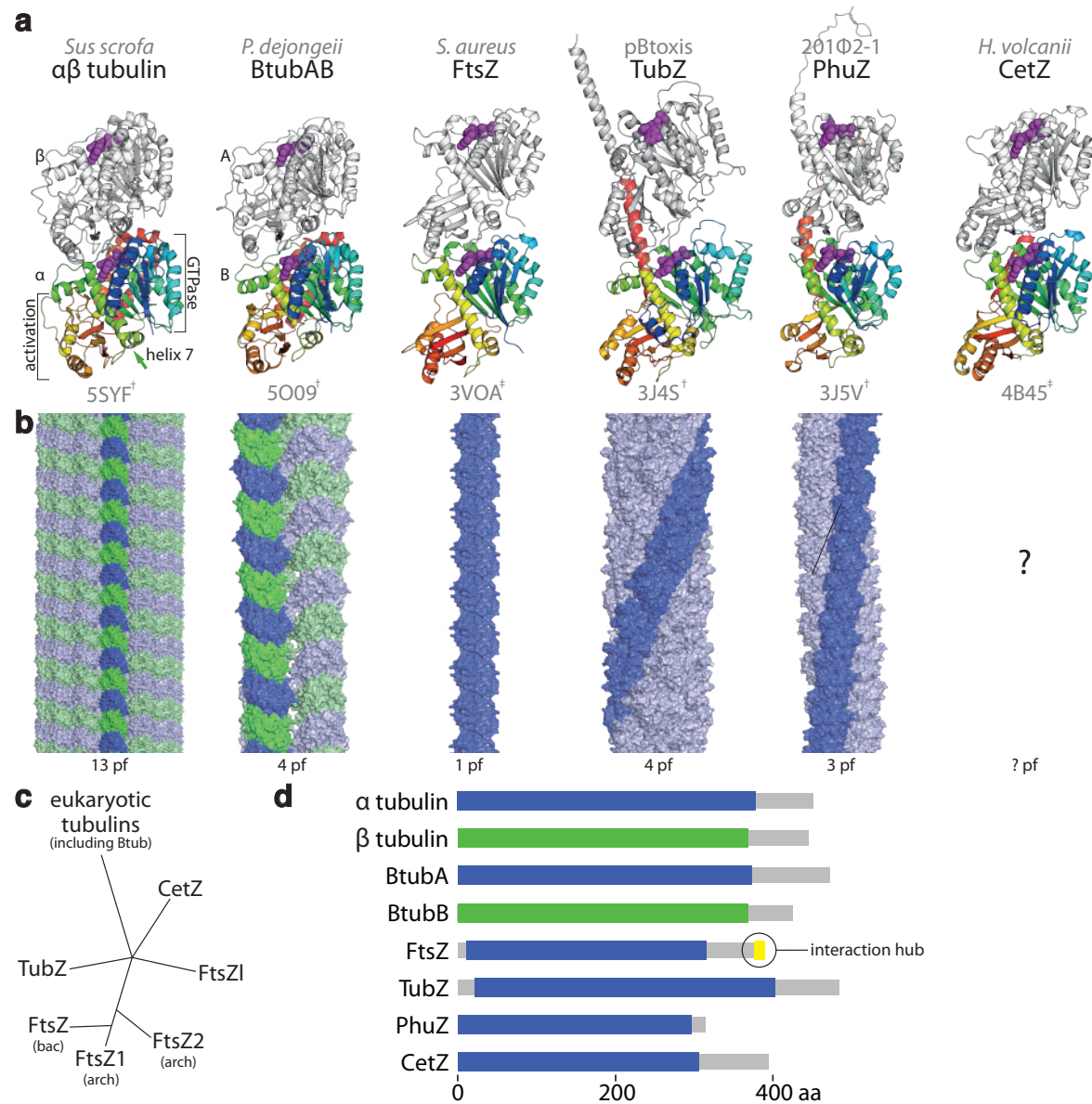
Figure 1-2 – Tubulin superfamily filaments

A Subunit structures and longitudinal contacts in tubulin superfamily protofilaments. Pairs of monomers are shown in cartoon representation, with nucleotides as magenta spheres. In each case the lower subunit is coloured blue to red, N terminus to C terminus, and the upper subunit is white. The lower monomer in each case was aligned to FtsZ's lower monomer. The PDB ID of the model used to generate the interface (and the filament structure) is given below each dimer. CryoEM derived structures indicated with †, X-ray structures with ‡.

B Diverse tubulin superfamily filament structures, shown as surface representations. An individual protofilament in each filament is highlighted in darker colour(s). A/ α subunits of heterodimers are coloured blue, B/ β are green. All protofilament interfaces are in roughly the same vertical orientation as those in A. The number of protofilaments (pf) forming each filament is given below. CetZ filament structure remains unknown. The microtubule is at a smaller scale.

C Schematic inferred phylogeny of the tubulin superfamily, a conservative consensus based on two analyses (Duggin et al., 2015; Makarova and Koonin, 2010). The base of the tree is poorly resolved and not possible to root confidently.

D Domain schematics for the representative family members presented here. The sequence region corresponding to the conserved globular domain is shown in blue, other regions are thought to be unstructured in all cases. The FtsZ interaction hub is highlighted – this is the short sequence which folds-upon-binding to FtsA, ZipA, MinC, and others.



INTRODUCTION

1.2.1 FtsZ – the organiser of bacterial cell division

FtsZ was the first component of a prokaryotic cytoskeleton to be suggested as such (Bi and Lutkenhaus, 1991; de Boer et al., 1992; Löwe and Amos, 1998; RayChaudhuri and Park, 1992). FtsZ is composed of the common bipartite globular tubulin domain at the N-terminus which is separated by a disordered linker of variable length from a short, conserved, C-terminal region responsible for mediating most interactions with other proteins (reviewed (Erickson et al., 2010)).

FtsZ is localised near but not bound to the membrane at future division sites in almost all bacteria and most archaeal phyla (Lindås and Bernander, 2013; Wang and Lutkenhaus, 1996) as a ring-like structure, the so-called Z-ring. During cytokinesis, the Z-ring contracts. In bacteria, FtsZ is amongst the first molecules to arrive during the assembly of a poorly characterised macromolecular complex known as the divisome, which incorporates many of the enzymatic activities and other functional modules needed to carry out cytokinesis and remodel the cell wall (reviewed (Haeusser and Margolin, 2016)). The central role of FtsZ in cell division of bacteria, although well established (Haeusser and Margolin, 2016), has recently been characterised using new light microscopy techniques that have changed perspectives somewhat (Bisson-Filho et al., 2017; Coltharp et al., 2016; Loose and Mitchison, 2014; Strauss et al., 2012; Yang et al., 2017). Higher resolution imaging (in time and space) of the Z-ring, including in live bacteria, and improved pulsed labelling of newly synthesised peptidoglycan, suggest a model for FtsZ function whereby relatively short FtsZ filaments treadmill circumferentially around the division plane, and in doing so drive cell-wall remodelling divisomes around with them. Divisome procession would therefore result in the laying-down of peptidoglycan around the septum, ultimately leading to scission of daughter cells. Treadmilling is a theoretically well understood property of multi-stranded filaments but until recently it was not clear how a single-stranded filament like FtsZ could show this behaviour (Wagstaff et al., 2017). Recent electron cryotomography of whole cells from many species early in division (Yao et al., 2017) shows that division often initiates asymmetrically, at a single position on the division plane, and initial ingression of the cell wall is able to proceed with only short FtsZ filaments present at the point of ingression on the interior of the cell, presumably locally organising wall remodelling.

This emerging picture conflicts with previous suggestions that overlapping FtsZ filaments, probably encircling the entire cell, directly drive division of, at least, the plasma membrane, by maximising overlap or via iterative bending (Erickson et al., 2010; Szwedziak et al., 2015).

Although many questions remain unanswered it now seems likely that FtsZ filaments in bacteria are probably required mostly for organising the machinery of division in space and time, rather than manipulating membranes directly - although the two are certainly not mutually exclusive (Bisson-Filho et al., 2017). An appealing hypothesis is that an ancient function of FtsZ to shape membranes has been complemented or largely replaced with its role in divisome orchestration in bacteria. The mechanism of FtsZ function in archaea remains almost totally unexplored, although many euryarchaeal genomes additionally encode a member of a divergent group of FtsZs, termed FtsZ₂ (Vaughan et al., 2004) (Figure 1-2C), which are also involved in division. Most plastids (Osteryoung and Pyke, 2014) and many mitochondria (Kiefel et al., 2004) also use FtsZs during division, these are unsurprisingly most closely related to bacterial FtsZs.

Some magnetotactic bacteria contain an additional FtsZ-like protein, termed FtsZ_m which does not have the C-terminal extension required for interaction with many partners, including FtsA (Richter et al., 2007; Uebe and Schüler, 2016). The role of FtsZ_ms is unclear, although they apparently copolymerise with standard FtsZ and are thus recruited to the Z-ring, and they have been implicated in redox dependent regulation of magnetosome biogenesis (Müller et al., 2014).

1.2.2 CetZ – a divergent tubulin used for cell shape determination in some archaea

A distinct group of tubulin superfamily genes are found in some Euryarchaeal genomes coexisting with division-related FtsZ(s), often several examples are present per genome (archaeal tubulins reviewed (Aylett and Duggin, 2017)). Their sequences cluster away from both eukaryotic tubulins and bacterial and archaeal FtsZs, and share features with both. These proteins were recently investigated in the model Haloarchaeum *Haloferax volcanii* (Duggin et al., 2015), and the group are now named ‘CetZ’ after the prototypical member characterised in that work: ‘cell structure-related Euryarchaeota tubulin/FtsZ homologue 1’. CetZ₁ is required in *H. volcanii* for differentiation of the typically irregular plate-shaped cells into a rod-form required for efficient swimming motility. CetZ₁ forms dynamic cytoplasmic filaments, including at the membrane, which are required for its function in cell shape control. The mechanism by which CetZ proteins modulate cell shape is unknown, although localisation of the protein was shown to be related to membrane curvature.

INTRODUCTION

1.2.3 TubZ – tubulins used for segregation of non-chromosomal DNA in bacteria

TubZs are a diverse but likely monophyletic group of tubulin superfamily members predominantly encoded on bacterial plasmids and in phage genomes (reviewed (Fink and Aylett, 2017)). They include the type III systems of plasmid segregation (Larsen et al., 2007; Tinsley and Khan, 2006), and the PhuZ subfamily of phage encoded proteins which act during viral assembly to position viral DNA and virions within the host cell before lysis (Chaikeeratisak et al., 2017; Kraemer et al., 2012). Both classes act as one dimensional molecular motors, although in opposite modes: plasmid encoded TubZs probably drag copies of their host plasmid to cell poles via depolymerisation (Fink and Löwe, 2015) while PhuZs push phage particles to the middle of the cell using the growth of dynamically unstable filaments (Erb et al., 2014). While we still do not know whether or how FtsZ and CetZ protofilaments might associate to form higher order structures in cells, in the case of TubZs, several parallel protofilaments associate to form the functional cytoplasmic filaments. TubZ from the *Bacillus thuringiensis* plasmid pBtoxis forms four-stranded helical filaments (Montabana and Agard, 2014), while PhuZ from *Pseudomonas chlororaphis* phage 201φ2-1 forms three-stranded helical filaments (Zehr et al., 2014) with an inside-out topology as compared to both TubZ helices and microtubules (Figure 1-2). The additional filament stability conferred by lateral interactions between protofilaments may be necessary for these cytomotive functions where filament integrity across very large length scales (as compared to FtsZ) is required. Multi-protofilament helical architecture, in general, ensures equal rigidity in all directions and restricts polarity to the longitudinal direction, all properties ideally suited to filaments that reach through cytoplasmic space, such as eukaryotic F-actin and microtubules, but also TubZ and the prokaryotic actins ParM and MamK. TubZ proteins have a C-terminal extension which reaches along the protofilament to the next monomer, and in all examples studied has been critical for robust filament formation and for wild-type filament dynamics.

1.2.4 Other prokaryotic tubulins

Other members of the tubulin superfamily are found scattered across bacteria and archaea, identifiable by the highly conserved sequence motifs of the GTPase domain.

So-called bacterial tubulin genes, BtubAB, more similar in sequence (Jenkins et al., 2002) and structure (Schlieper et al., 2005) to eukaryotic tubulins than to FtsZs, are found

coexisting with FtsZ in several *Prothescobacter spp.*, members of the Verrucomicrobia phylum (Jenkins et al., 2002). BtubAB have been observed to form tubular structures *in vivo* but these are much smaller in cross section than microtubules (Pilhofer et al., 2011). Btubs are most likely the product of a horizontal gene transfer event from a eukaryote to a *Prothescobacter* ancestor. Recent work characterising BtubAB filament structure and dynamic behaviour supported this hypothesis (Deng et al., 2017). *In vitro*, BtubAB forms 4-stranded ‘mini microtubules’ (Figure 1-2) exhibiting both a seam and dynamic instability, two hallmarks of eukaryotic microtubules. The function of Btubs is unknown, but it presumably involves a third protein, BtubC, which was shown to bind the mini-microtubules and reduce their dynamics. BtubC was necessary to find the register of the heterodimer repeat in the cryoEM structure – analogous to the use of kinesin in solving (early) microtubule structures by cryoEM.

Some members of the Thaumarcheota (within the TACK superphylum) encode a eukaryotic tubulin-like protein denoted ‘artubulin’ (Yutin and Koonin, 2012). It is not clear whether artubulins are the product of a horizontal gene transfer event, or represent a vertically inherited orthologue of eukaryotic tubulin. More convincing putative ‘ancient tubulin’-like genes are found in recently published archaeal genomes assembled from metagenomic sequence data (Zaremba-Niedzwiedzka et al., 2017).

Two groups of proteins with homology only to the GTPase domain of the tubulin superfamily have been identified in bacterial and archaeal genomes; both groups have been termed FtsZl (FtsZ-like) (Makarova and Koonin, 2010). Genome context suggests that these proteins may be involved in membrane remodelling (Makarova and Koonin, 2010), although they will be unable to form filaments in the same way as other tubulin superfamily members because of the missing or differing C-terminal domains.

1.3 The actins

Actins, like tubulins, are incredibly versatile cytoskeletal building blocks, able to form robust cellular scaffolds but also offering dynamic properties that can be harnessed for cytomotive functions. The actin ATP-binding fold (SCOP: 53067) is ancient, and widely distributed across the tree of life in proteins that both do and do not form filaments, for example in the non-polymerising proteins Hsp70/DnaK and hexokinase (Bork et al., 1992). The filament forming actins are probably monophyletic, i.e. polymerisation evolved only once (Figure 1-3C). Actin protofilaments share a fundamentally conserved, although

INTRODUCTION

variable, mode of longitudinal interaction (Figure 1-3A) whilst the protofilament itself has been repurposed many times in evolutionary history, forming a fascinating variety of higher order filament architectures and performing many different cellular roles (Figure 1-1, Figure 1-3B). The actin globular domain is typically composed of four subdomains (labelled either IA, IB, IIA, IIB or 1-4) which function as two pairs (I and II, or 1-2 and 3-4), the adenosine nucleotide is held in a binding pocket at the centre of the molecule. The two halves of the protein rotate relative to one another upon nucleotide hydrolysis and polymerisation, linking nucleotide state to polymerisation properties and lending the protofilament intrinsic dynamics (reviewed (Dominguez and Holmes, 2011)).

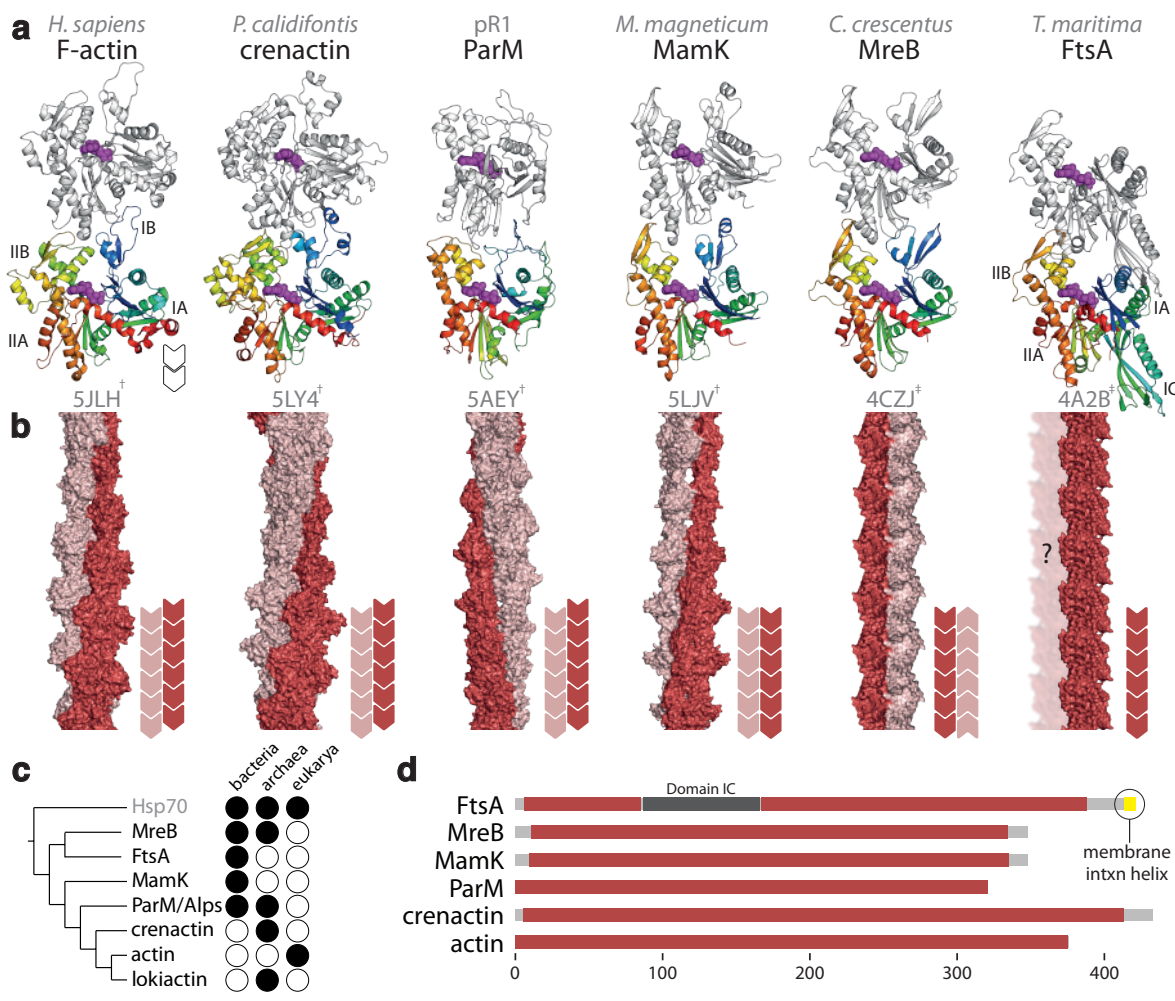
Figure 1-3 – Actin superfamily filaments

A Subunit structures and longitudinal contacts in actin superfamily protofilaments (strands). Pairs of monomers are shown in cartoon representation, with nucleotides as magenta spheres. In each case the lower subunit is coloured blue to red, N terminus to C terminus, and the upper subunit is grey. The lower monomer in each case was aligned to F-actin's lower monomer. The PDB ID of the model used to generate the interface (and the filament structure) is given below each dimer. CryoEM derived structures indicated with †, X-ray structures with ‡. Subdomains are labelled for F-actin and FtsA. Overall, the protofilament contacts are clearly related, but they also show significant differences, especially in sub-domains IB.

B Diverse actin superfamily filament structures, shown as surface representations. Individual protofilaments are shown in a single colour. Cartoons indicate protofilament polarity and subunit alignment (staggered or juxtaposed).

C Distribution and inferred phylogeny of the actin superfamily. Schematic consensus phylogeny derived from three analyses (Derman et al., 2009; Ettema et al., 2011; Spang et al., 2015)

D Domain schematics for the family representatives presented here. Sequence regions corresponding to the conserved globular domain are shaded in red, other regions (grey) are thought to be unstructured in all cases. Domain IC of FtsA, and that protein's amphipathic membrane-interacting helix, are highlighted.



INTRODUCTION

1.3.1 MreB – control of bacterial cell wall synthesis

MreB is the prototypical bacterial actin (van den Ent et al., 2001; Jones et al., 2001), found in almost all walled bacteria with elongated shapes (reviewed (Errington, 2015)). MreB is essential for normal cell wall synthesis in these organisms, responsible for organising a multi-enzyme complex known as the elongasome (Szwedziak and Löwe, 2013). Controversial for a long time, a consensus is now forming about how MreB functions. MreB forms anti-parallel, in-register, double filaments close to the membrane, binding it directly (van den Ent et al., 2014; Salje et al., 2011). Their unusual architecture allows MreB filaments to bend in one particular direction, unlike helical F-actin. Although it was once thought that long MreB filaments organised cell wall synthesis globally by forming a cell-spanning helical structure, this view is now unpopular. Newer imaging techniques suggest that short MreB filaments move circumferentially in concert with the cell wall synthesis enzymes of the elongasome, organising synthesis locally (Billaudeau et al., 2017; Domínguez-Escobar et al., 2011; Garner et al., 2011; Teeffelen et al., 2011). Unlike the comparable motion of FtsZ in the division plane which is apparently driven by polymer dynamics (namely, treadmilling), MreB motion is driven by cell wall synthesis itself (Garner et al., 2011; Teeffelen et al., 2011). We have recently gained further insight into how MreB organises cell wall synthesis. Membrane bound MreB filaments have an intrinsic curvature tighter than the curvature of the wall and as a result become aligned perpendicular to the long axis, this alignment is then transmitted to cell wall synthesis enzymes and the glycan polymers they produce (Hussain et al., 2018).

Some organisms have multiple copies of MreB, in some cases with distinct but overlapping roles (Fenton et al., 2010a; Kawai et al., 2009). In FtsZ- and, almost, wall-less Chlamydiales MreB and associated cell wall machinery have been co-opted for the synthesis of a vestigial septum which divides the cell (Jacquier et al., 2014; Ouellette et al., 2012). In other organisms, MreB filaments are used for functions independent of cell wall patterning, for instance as a cytoplasmic component of the gliding motility machinery of *Myxococcus spp.* (Em et al., 2010; Schumacher and Søgaard-Andersen, 2017) (and possibly also in more diverse members of the Alpha- and Delta-proteobacteria (Luciano et al., 2011)). More dramatically, MreB is associated with the cell-spanning cytoskeletal ‘ribbon’ of the wall-less Mollicute *Spiroplasma spp.* (Trachtenberg et al., 2008). MreB has been implicated in segregation of chromosomes in *Caulobacter crescentus* (Gitai et al., 2005) and other species, although it has been difficult to validate how direct this role may be, given the tight and complex

associations between nucleoid, cell wall, and the filament forming proteins that pattern cell wall deposition – an ongoing challenge for bacterial cell biology. Archaeal actins whose closest homologues are MreB have been identified but remain unstudied (Ettema et al., 2011).

1.3.2 FtsA – an unusual bacterial actin that cooperates with the tubulin FtsZ

FtsA links FtsZ filaments to the membrane and also to other components of the divisome in many bacteria, although other FtsZ membrane anchors exist (reviewed (Haeusser and Margolin, 2016) and see SepF below). FtsA is itself able to form filaments, and polymerisation is required for wildtype function (Shiomi and Margolin, 2007; Szwedziak et al., 2012). Although FtsA was long ago identified as a putative member of the actin superfamily (Bork et al., 1992), it was not clear whether it would be able to polymerise as the amino acids corresponding to subdomain IB in actin/MreB are missing, and a large insertion is present within subdomain IA. Crystal structures and negative stain electron microscopy revealed that FtsA does have a recognisable, although unusual, actin fold which can polymerise to form actin-like protofilaments (Ent and Löwe, 2000; Fujita et al., 2014; Szwedziak et al., 2012). Domain IB is indeed missing and the insertion in IA forms an alternative subdomain 'IC', which contributes to polymerisation as if it were the IB from the adjacent monomer in a canonical protofilament (Figure I-3).

FtsA and FtsZ copolymerise *in vitro* to form a variety of dynamic structures (Loose and Mitchison, 2014), and inside liposomes they can cooperate to produce constrictions (Osawa and Erickson, 2013; Szwedziak et al., 2015). Similar structures can be seen in cryoelectron tomograms of cells overexpressing both proteins (Szwedziak et al., 2015), however it is still not known when and how copolymerisation is used to regulate the divisome. One proposal is that FtsA plays a role directly analogous to MreB in elongation (Szwedziak and Löwe, 2013). Although we don't know if a FtsA double filament would be curved like an MreB one, and thus be able to act as a rudder orienting division in the correct plane, the fact that SepF, an alternative Z-ring anchor, is highly curved is suggestive. A recent report showed that *E. coli* FtsA can form small rings *in vitro* (single-stranded, and on a flat surface), the significance of this is unclear (Krupka et al., 2017).

INTRODUCTION

1.3.3 MamK – a protein scaffold for a bacterial compass needle

MamK forms filaments used by magnetotactic bacteria in the alignment and segregation of magnetosomes (Komeili et al., 2006; Scheffel et al., 2006): inner membrane invaginations containing biomineralised iron compounds, which enable orientation of motility relative to the earth's magnetic field (reviewed (Uebe and Schüller, 2016)). MamK is found in all magnetotactic bacteria studied but appears to have slightly different roles even in the two well studied and closely related model species *Magnetospirillum gryphiswaldense* MSR-1 (MSR) and *Magnetospirillum magneticum* AMB-1 (AMB). In both species MamK forms cytoplasmic filaments that connect ordered chains of magnetosomes. Deletion of *mamK* in MSR results in a dramatic disorganisation of magnetosomes into short chains which do not segregate efficiently at division (Katzmann et al., 2011), whereas Δ *mamK* AMB magnetosomes are still found in long chains, although they are less organised and cytoplasmic filaments are no longer visible (Komeili et al., 2006).

The structures of both filamentous and monomeric MamK from MSR were solved (Löwe et al., 2016), providing mechanistic insight into filament dynamics, thought to be important in function (Toro-Nahuelpan et al., 2016). The conformational changes through MamK's polymerisation cycle are highly reminiscent of those seen for eukaryotic actin (Oda et al., 2009), ParM (Gayathri et al., 2012) and to some extent MreB (van den Ent et al., 2014) (see Results section 2.4). MamK filaments are right-handed, parallel, and two-stranded, and unusually with juxtaposed subunits (Figure 1-3).

Some magnetotactic bacteria, including AMB, additionally encode a MamK homologue, "MamK-like", which assists in magnetosome alignment and also forms filaments, alone and with MamK (Abreu et al., 2014; Rioux et al., 2010).

1.3.4 ParM and the Alps – actin-based spindles for efficient DNA segregation in bacteria

As well as the three well-studied chromosomally-encoded bacterial actins described above, there exists a large number of extremely diverse plasmid- and phage-borne actins (Derman et al., 2009) (reviewed (Gayathri and Harne, 2017)). While the abundance and diversity of this group of bacterial 'actin like proteins', or Alps, was not recognised until more recently (Derman et al., 2009), the most prominent member of the group has been the subject of study for many years: the protein ParM, prototypically found on the *Escherichia coli* R1 plasmid (Gerdes et al., 1985). The R1 Par locus is the founding member of the type II plasmid

segregation systems, which confer stability on their host plasmids by enforcing active segregation of plasmid copies into daughter cells. Type II segregation depends on actin-like ParM, a DNA binding protein ParR, and a ‘centromeric’ DNA region *parC* (Møller-Jensen et al., 2003). The molecular details of ParMRC plasmid segregation were resolved recently (Bharat et al., 2015), building on decades of genetic, biochemical, and structural data (reviewed (Salje et al., 2010)). Briefly: after plasmid replication, several copies of ParR assemble along two *parC* regions. Each ParRC complex recruits a left-handed, staggered, parallel, double-helical ParM filament, via the ‘barbed end’ (by analogy with eukaryotic F-actin). Antiparallel ParRC-bound ParM filaments associate (forming a four protofilament bundle via the pointed ends) (Gayathri et al., 2012) to form a bipolar spindle which pushes ParRC complexes, and plasmids, apart via incorporation of ParM subunits at the ParRC-bound barbed ends. There is some evidence that ParMs form a *bona fide* family, with conserved properties despite relatively low sequence similarities (Rivera et al., 2011); nevertheless some Alps with apparently divergent properties have also been labelled ParM (Popp et al., 2010).

Aside from ParMs only one other plasmid-borne Alp has been extensively characterised: AlfA, found on *Bacillus subtilis* pBET31. Like ParM, AlfA functions as part of a type II segregation system (AlfB acts as DNA adaptor, the centromeric region is known as *parN*) although the mechanism of segregation appears to be somewhat different (Becker et al., 2006; Polka et al., 2009, 2014; Tanaka, 2010). On the basis of sequence, AlfA seems to be missing actin subdomain IIB, which is part of the canonical longitudinal filament interface. Two recent high-resolution filament structures confirmed this observation and revealed how filament topology adjusts to accommodate the differences (Szewczak-Harris and Löwe, 2018; Usluer et al., 2018).

A few other Alps have been partially characterised. These include the phage-encoded AlpC (Donovan et al., 2015), two phage-encoded Alps from *Bacillus pumilus* (Yuan et al., 2015), Alp12A from a *Clostridium tetani* plasmid (Popp et al., 2012), Alp7A from a *Bacillus subtilis* plasmid (Derman et al., 2012), and the divergent ‘ParM’ from *Staphylococcus* multidrug resistance plasmid pSK41 (Popp et al., 2010; Schumacher et al., 2007). These investigations suggest that there may be a significant degree of diversity in the mechanisms of action, and possibly functions, to be found amongst the Alps. One archaeal actin, Tao583 from *Thermoplasma acidophilum*, most closely related to the bacterial Alps, is probably the result of a horizontal gene transfer event (Ettema et al., 2011; Hara et al., 2007).

INTRODUCTION

1.3.5 Crenactin – archaeal evidence that eukaryotic F-actin architecture is ancient

Crenactins are archaeal actins found in members of the Thermoproteales class of the phylum Crenarchaea within the TACK superphylum (Ettema et al., 2011) (archaeal actins reviewed (Lindås et al., 2017)). The eukaryote lineage is rooted close to the TACK clade (Hug et al., 2016). Thermoproteales have no known filament or membrane remodelling system except for crenactin (Makarova et al., 2010), and immunofluorescence data suggest that the protein may play a cytoskeletal role, including in division (Ettema et al., 2011). Despite previous evidence to the contrary, it was recently shown that the structure of the crenactin filament is almost identical to that of eukaryotic F-actin (Izoré et al., 2016) – and forms right handed, staggered, parallel, double helical filaments with a ‘hydrophobic plug’ between the two strands, a hallmark of F-actin (Figure 1-3).

Recent metagenomics studies have revealed the existence of archaea (the so-called Asgard superphylum) with actins likely to be even more similar to eukaryotic F-actin than crenactin, as well as apparent actin-related proteins (Arps) and gelsolin-like domain homologues (Spang et al., 2015; Zaremba-Niedzwiedzka et al., 2017). Future investigation of these molecules will be exciting in the context of understanding the evolution of actin dynamics at membranes required for phagocytosis/engulfment – an event in the evolution of the eukaryotic lineage which may have been required for a eukaryogenic endosymbiosis.

1.4 Coiled coil filaments

Aside from actins and tubulins, the most widely distributed cytoskeletal building block is the coiled coil, formed via parallel or antiparallel association of, often long, alpha helices that twist around each other. Although not ‘conserved’ as such, coiled coil cytoskeletal proteins appear to function using common principles derived from their shared structure (nucleotide independent prokaryotic cytoskeletons reviewed (Lin and Thanbichler, 2013)). Coiled coil cytoskeletons typically function as (minimally dynamic) scaffolds in the cell, performing structural roles or promoting specific subcellular localisations of other molecules, or both.

Eukaryotic intermediate filaments (IF) are the prototypical example of a cytoskeletal component that assembles via coiled coil interactions. IF sequence architecture is well defined and partially understood structurally (Figure 1-4A) (reviews (Chernyatina et al., 2015; Herrmann and Aebi, 2016)): a central all-helical ‘rod’ domain is capped by poorly

ordered ‘head’ and ‘tail’ domains. Rod domains (like all coiled coils) can be identified with reasonable confidence from sequence alone due to the strict heptad-based periodicity, which ensures compatible residues are bridging associated alpha helices (Crick, 1952). IF monomers dimerise in parallel to form a coiled coil and higher order interactions are then also at least partly mediated by the coiled regions, although assembly mechanisms differ between IFs. IFs are a well-defined class of coiled coil filaments – but importantly there are other ways of using coiled coils to build cytoskeletons (many are catalogued in (Walshaw et al., 2010)).

While actins and tubulins form intrinsically dynamic, filaments, made dynamic through their in-built nucleotide hydrolase activity, IFs have no such activity and often use additional factors to facilitate remodelling of cytoskeletal structures via post-translational modification (Snider and Omary, 2014). Prokaryotic coiled coil filaments that exhibit dynamics presumably have analogous factors although in most cases these have not been identified. So far, observed coiled coil dynamics have not extended to a function that could be considered cytomotive at the molecular level.

1.4.1 Crescentin – an IF-reminiscent determinant of cell shape

Crescentin (CreS) is a filament-forming coiled coil protein found in abundance on the cytoplasmic face of the *Caulobacter* inner curve (Ausmees et al., 2003). The sequence and *in vitro* assembly characteristics of crescentin are highly reminiscent of eukaryotic IF proteins, with likely disordered head and tail regions, and a rod domain with analogous coil regions and even a distinctive break in periodicity known as the stutter (Ausmees et al., 2003; Cabeen et al., 2011) (Figure 1-4A). CreS is required for *Caulobacter* cell curvature, and is sufficient to generate curvature when ectopically expressed in *Escherichia coli* (Cabeen et al., 2009). Control of curvature is probably via modulation of cell wall synthesis resulting from mechanical strain on the cell envelope applied by elastic CreS assemblies (Cabeen et al., 2009) however the molecular details of this remain unclear. Importantly, overexpression of other polymeric membrane-binding proteins can also generate curved *E. coli* (Deng et al., 2019). One confounding factor is that CreS induced curvature is also somehow dependent on the metabolic enzyme CTP synthase (CtpS), which is filament-forming in *Caulobacter* but also in almost all organisms studied including man (Ingerson-Mahar et al., 2010; Lynch et al., 2017) (CtpS polymerisation is probably primarily a way to regulate enzymatic activity).

INTRODUCTION

1.4.2 Scy, FilP and others – is there a broader class of IF-like proteins?

Scy and FilP (along with coiled coil DivIVA, see below, reviewed (Kelemen, 2017)) are required for normal development of hyphae in the filamentous bacteria *Streptomyces spp.*, localising to and specifying the growing tip and future branching sites, although FilP is also found in rod-shaped Actinobacteria (Bagchi et al., 2008; Holmes et al., 2013), which also exhibit polar growth. Like CreS, their sequences and *in vitro* assembly properties bear basic similarities to those of IF proteins, although the arrangement of coiled coil regions and repeat architecture in the rod domain is quite different from both CreS and IFs (Figure 1-4A) (Walshaw et al., 2010). CreS, FilP and Scy are the best studied examples of a large group of bacterial proteins which could arguably be considered IF-like (Kelemen, 2017; Walshaw et al., 2010), although discriminating a cohesive and meaningful IF-like group from a broader coiled coil rich class (see below) is not straightforward and probably not feasible using sequence data alone.

1.4.3 Bacterial Coiled Coil Rich Proteins (CCRPs) – a cytoskeletal motif, not a cytoskeletal family

I adopt the imperfect umbrella term Bacterial Coiled Coil Rich Proteins (CCRP) to discuss any coiled coil rich protein for which a better classification is not available (after Refs (Kelemen, 2017) and (Waidner et al., 2009)), i.e. members do not belong in a widely distributed and functionally well understood family (e.g. DivIVA, below) nor do they exhibit unambiguous IF-like properties (as for those examples above). Very few of the CCRPs identifiable from sequence (Walshaw et al., 2010) have been studied in depth.

Filament-forming CCRPs in *Helicobacter spp.* are important for maintaining the distinctive (and virulence associated) helical shape of these pathogens (Specht et al., 2011; Waidner et al., 2009). *Leptospira spp.* (spiral-shaped Spirochetes) contain DNA-binding CCRPs which may be involved in organisation of the nucleoid into a cell-spanning rod (Mazouni et al., 2006; Raddi et al., 2012). In *Myxococcus spp.* normal gliding motility is dependent on filament-forming CCRPs AglZ (Yang et al., 2004) and FrzS (Ward et al., 2000) which are involved in, respectively, linking transmembrane gliding motility machines to cytosolic components with MreB, and regulating exopolysaccharide secretion at the cell pole (Berleman et al., 2011) (gliding motility reviewed (Schumacher and Søgaard-Andersen, 2017)). A CCRP has been identified in the related bacterial predator *Bdellovibrio bacteriovorus* which appears to have a limited role in maintaining cell shape integrity (Fenton et al.,

2010b). It remains to be seen if the diverse functions of CCRPs are united by common molecular mechanisms beyond polymerisation. Mechanistic studies of polymerising coiled coil proteins remain technically challenging due to the hard to control polymerisation process.

1.4.4 DivIVA – a coiled coil determinant of cell polarity and division site

DivIVA is distributed widely amongst Gram positive bacteria (not just those exhibiting polar growth), and localises variously to cell poles, hyphal branching sites and future division sites, playing somewhat diverse roles, including modulating activity of the Min system (Cha and Stewart, 1997; Marston et al., 1998) (reviews (Kaval and Halbedel, 2012; Kelemen, 2017; Lin and Thanbichler, 2013)). DivIVA binds the membrane directly and polymerises to form higher order structures with intrinsic curvature (Oliva et al., 2010; Stahlberg et al., 2004), probably thereby generating/sensing/localising to high membrane curvatures (Lenarcic et al., 2009; Ramamurthi and Losick, 2009). DivIVA activity, in *Streptomyces spp.* and *Mycobacteria* at least, is regulated by site-specific phosphorylation (Hempel et al., 2012; Kang et al., 2005; Saalbach et al., 2013). In the MreB-less rod-shaped actinobacterium *Corynebacterium spp.* DivIVA is not phosphorylated but functions synergistically with another coiled coil protein, RsmP, which is phosphorylated at specific sites (Fiuza et al., 2010). No direct effect of phosphorylation on polymerisation has yet been identified in either case, although modulation of phosphorylation *in vivo* has dramatic phenotypes in both cases.

1.4.5 ESCRTIII relatives in archaea – membrane scission by a polymer of coiled coils

Homologues of the eukaryotic endosomal sorting complexes required for transport (ESCRT) system have been identified in diverse archaea (Obita et al., 2007) (reviewed (Makarova et al., 2010; Samson et al., 2017)). ESCRT systems use multiple proteins to perform regulated scission of membranes, including during some archaeal cell divisions (Lindås et al., 2008), as visualised by electron cryotomography of the FtsZ-less Crenarchaeon *Sulfolobus solfataricus* (Figure 1-4B) (Dobro et al., 2013). In eukaryotes, coiled coil ESCRTIII proteins polymerise at membranes leading to membrane scission, however the molecular mechanism of this process remains incompletely understood (Schöneberg et al., 2017). Depolymerisation and recycling of ESCRTIII subunits is achieved by the action of a separate AAA⁺ hexameric ATPase, the prototypical example being Vps4 from

INTRODUCTION

Saccharomyces cerevisiae. Archaeal homologues of ESCRTIII/Vps4 pairs have been identified in many genomes, the best-studied examples being CdvB (ESCRTIII) and CdvC (Vps4) in *Sulfolobus spp.* In eukaryotes, ESCRTIII recruitment is dependent on additional factors (ESCRT0, I and II), archaeal homologues of which have been identified only in genomes assembled from metagenomic sequences thought to represent lineages which are sister groups to the eukaryotic lineage (Spang et al., 2015; Zaremba-Niedzwiedzka et al., 2017). In contrast, in *Sulfolobus spp.* an unrelated protein CdvA is required (Samson et al., 2011).

1.4.6 CrvA – a periplasmic cytoskeleton

A periplasmic filament forming protein in *Vibrio cholerae*, CrvA, has recently been identified and characterised (Bartlett et al., 2017). CrvA localises to the inner face of cell curvature where it slows down peptidoglycan synthesis on that side so as to establish or reinforce pathogenicity-associated vibrioid cell morphology. CrvA filament formation is dependent on the presence of a predicted coiled coil domain, although the molecular mechanism by which CrvA modulates peptidoglycan patterning remains unclear, similar to CreS. Improved live cell peptidoglycan labelling and imaging methods, such as those developed during work on CrvA (Bartlett et al., 2017), should be helpful in many cases to help disentangle the many mechanisms by which bacterial cytoskeletons modulate cell wall patterning.

1.5 Other prokaryotic cytoskeletons

Many protein filaments with cytoskeletal functions are not actins, tubulins, or coiled coils. This reflects the relative ease of evolving filament formation (or the difficulty in avoiding it) (Barry and Gitai, 2011): the three groups above are the best studied examples, and are somewhat distinguished by their especially wide distributions and fundamental roles in cell biology, but not by polymerisation *per se*.

Bactofilins are a poorly understood family of bacterial filament forming proteins, yet they are highly conserved, broadly distributed within bacteria, and abundant in cells (Kühn et al., 2010; Lin and Thanbichler, 2013). They have been found to play a cytoskeletal role in several organisms, often via modulation of cell wall properties (Hay et al., 1999; Kühn et al., 2010; Mk et al., 2011; Sycuro et al., 2010). A BacA monomer from *Caulobacter crescentus* was resolved in the first ever *ab initio* solid-state NMR solution structure, and shown to form a

right-handed beta helix (Figure 1-4C) (Shi et al., 2015). Filaments and sheets are seen *in vitro* and *in vivo*, but how monomers come together to form these architectures remained unclear until very recently when cryoEM, X-ray crystallography, and sequence analysis were combined to show that the functional bactofilin unit is a single apolar protofilament, with the ability to bind membranes (Deng et al., 2019).

SepF was originally identified as a component of the divisome in *Bacillus subtilis* (Hamoen et al., 2006). Subsequently SepF was shown to bind membranes, recruit FtsZ to the membrane, and itself form curved filaments (Duman et al., 2013). Structural analysis suggests that filaments are non-polar polymers of head-to-head SepF dimers. SepF is found in many Gram positive bacteria (and also Cyanobacteria), where it complements and in some cases replaces FtsA function as a FtsZ membrane anchor (Gola et al., 2015; Gupta et al., 2015; Hamoen et al., 2006; Ishikawa et al., 2006; Marbouty et al., 2009). SepF is also found in all FtsZ containing archaea, and as such seems a good candidate for an archaeal FtsZ anchor – indeed no other known bacterial Z-ring anchors have widespread archaeal homologues (Makarova et al., 2010).

PopZ is a proline-rich protein which forms filaments that associate to form an irregular mesh at cell poles in *Caulobacter* and other Gram negative bacteria (Bowman et al., 2008; Ebersbach et al., 2008). The mesh appears to function as a molecular ‘hub’, with intrinsically disordered regions of PopZ responsible for recruiting at least 11 different proteins (Holmes et al., 2016). PopZ has inferred helical regions but these are not predicted to form coiled coils.

SpoIVA is a Walker-A type ATPase which forms a filamentous coat around *Bacillus subtilis* forespores (Tocheva et al., 2011), and assembles into filaments in an ATP hydrolysis dependent manner *in vitro* (Ramamurthi and Losick, 2008). There is considerable uncertainty as to whether other Walker-A type ATPases (e.g. MinD, Soj/ParA, SopA, ParF – all have been previously denoted Walker A cytoskeletal ATPases (WACAs) (Michie and Löwe, 2006)) form functional filaments *in vivo*, and therefore whether they should also be considered cytoskeletal. Recently, a cryoEM structure of MinCD filaments from *Pseudomonas aeruginosa* was determined, several features of which appear to support the idea that these filaments are in fact functional (Szewczak-Harris et al., 2019). Though this is in the face of convincing genetic evidence suggesting otherwise (Park et al., 2015). Further work is certainly required in this somewhat controversial area.

INTRODUCTION

Spirochetes (including the Lyme disease pathogen *Borrelia burgdorferi*) achieve an unusual mode of motility using periplasmic flagella (PF) anchored at either end of the inner membrane compartment, which produce backward-moving waves that propel the bacterium forwards (reviewed (Charon et al., 2012)). The flagella are in some cases responsible for generating the helical (or 'flat wave') cell morphology, as well as motility, and so have a cytoskeletal function. Some Spirochetes (Treponemes) have an additional, cytoplasmic, filament system which also appears to generate helical morphology (Izard et al., 2003; You et al., 1996).

The cell-spanning cytoskeletal ribbons of *Spiroplasma spp.* (with which MreB associates, see above) are composed largely of 'fibril' proteins, with no known homologues, which are crucial for maintaining cell shape and in some cases needed for motility (reviewed (Trachtenberg et al., 2008)).

Several unidentified cytoskeletal elements have been observed *in vivo* via electron microscopy methods (some examples are collected in (Dobro et al., 2017)). These might simply be unrecognised examples of proteins mentioned above, but they may also be as yet undiscovered filament forming proteins.

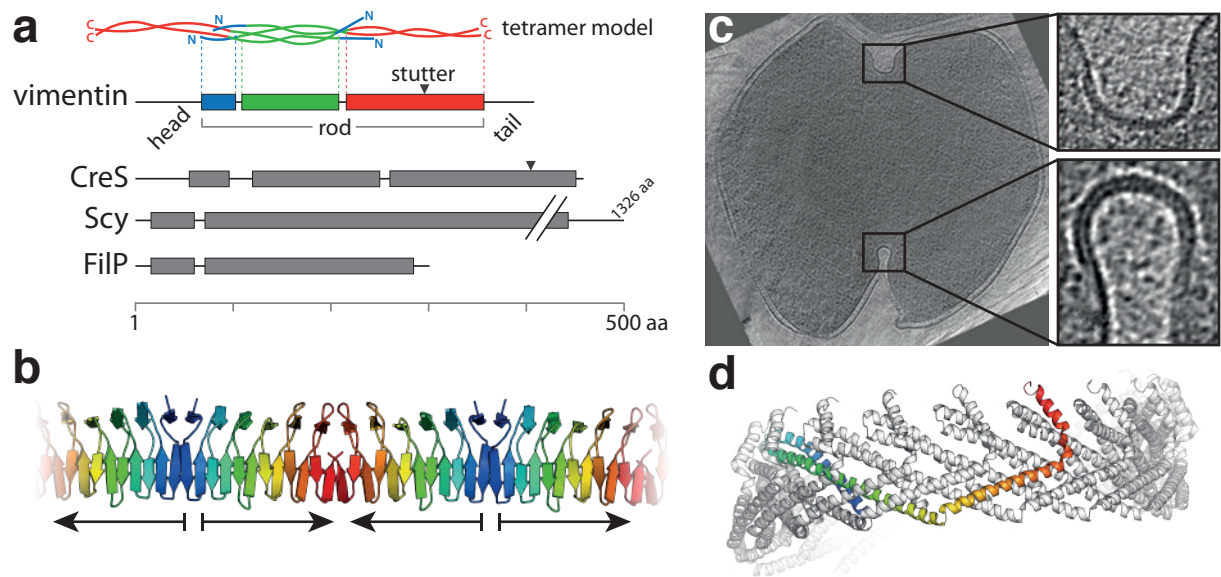


Figure 1-4 – Towards structural understanding of diverse prokaryotic cytoskeletal filaments

A Some prokaryotic coiled coil proteins, which may be part of an intermediate filament-like family. Human vimentin is shown as an example of IF sequence properties and proposed IF architecture. The schematic vimentin tetramer model is derived from the atomic model in (Herrmann and Aebi, 2016), it illustrates how both dimerisation and higher order associations are mediated by the coiled coil rod region. Sequence schematics of vimentin, CreS, Scy and FilP, show verified (vimentin) or predicted (CreS (Ausmees et al., 2003), FilP and Scy (Walshaw et al., 2010)) coiled coil regions as boxes.

B Apolar bactofilin filament structure PDB ID 6RIB, determined via cryoEM.

C,D Archaeal ESCRT systems. **(C)** electron cryotomogram of a dividing *Sulfulobus solfataricus* cell, showing the cytokinetic protein belt thought to be composed of ESCRTIII homologues and associated proteins. Scale bar 200 nm. Reproduced from (Dobro et al., 2013). **(D)** eukaryotic ESCRTIII helical assembly (McCullough et al., 2015) illustrates coiled coil-like filament formation by this family of proteins (from PDB ID 3JC1).

1.6 Perspective on prokaryotic cytoskeletons

The various prokaryotic filaments and their cellular functions are fascinating in their own right, but collectively they demonstrate how conserved proteins and their filaments have persisted during evolution for astonishingly long periods of time because of their usefulness in the many different processes that require long-range organisation. Crucially, for a given family, filament-forming properties are conserved, while specific functional contexts are typically not. However, diverse cells have similar needs for organisation at large length scales and the filament-based solutions to any given problem can be strikingly similar in overall mechanism, despite employing evolutionarily distant proteins. Prokaryotic cytoskeletons and the protein filaments that form them are variations on a theme: filaments give individual proteins access to larger length scales.

To emphasise this point, the convergent use of diverse filaments in four fundamental cellular processes is briefly discussed below.

1.6.1 Cell division

Many cells divide (and therefore replicate) via constriction of the plasma membrane and other cell envelope components. Different filaments are used in different ways to achieve constriction. In many eukaryotic cells a contractile ring of actin coupled to myosin motors powers cytokinesis. In most bacteria, FtsZ filaments perpendicular to the long axis of the cell organise cell wall remodelling at division sites (Haeusser and Margolin, 2016). FtsZ rings around division sites have also been visualised in some (wall-less) Euryarchaeota (Wang and Lutkenhaus, 1996). In FtsZ-less and almost wall-less Chlamydiales MreB is required for division, organising synthesis of a vestigial septum (Jacquier et al., 2014; Ouellette et al., 2012). In Thermoproteales (phylum Crenarchaea) division-plane rings of the archaeal actin crenactin have been seen, importantly no filament-associated molecular motors have been identified in these organisms (Ettema et al., 2011). In the Sulfolobales (also Crenarchaea) a division plane band of ESCRTIII homologue CdvB at the membrane appears to organise or power plasma membrane scission (Lindås et al., 2008). ESCRTIII based division is also commonplace in metazoa – ESCRTIII filaments deliver the final cut to the midbody (Carlton and Martin-Serrano, 2007). Division where the plasma membrane is not divided from the outside-in can also rely on filaments, for instance assembly of the cell plate in plants has a well understood dependence on microtubules (Rasmussen et al., 2013).

1.6.2 Cell shape determination

For a single celled organism, cell shape is a critical determinant of interaction with the environment. In many cases, non-spherical cell shapes are dependent on protein filaments. For instance, the role of the actin cytoskeleton in determining the shape of many animal cells is well known. In walled bacteria, cell shape is typically maintained by the properties of the rigid cell wall – although these properties are often modulated indirectly by the action of cytoskeletons on the activity of cell wall synthesis and remodelling enzymes. Interaction between cytoskeleton and cell wall synthesis is not limited to prokaryotes either, as plant cell wall synthesis machinery is aligned by cortical microtubules (Bringmann et al., 2012). In many rod-shaped bacteria MreB filaments control the insertion of new cell wall to maintain shape. Dynamic MreB filaments lie at the membrane perpendicular to the long axis of the cell and are associated with key cell wall synthesis enzymes (Eun et al., 2015). Although poorly characterised, bactofilins in several organisms control cell morphology via modulation of cell wall properties (Lin and Thanbichler, 2013). The cytoplasmic coiled coil protein crescentin (CreS) in *Caulobacter crescentus* assembles on the inner face of the curved cell and retards cell wall synthesis relative to the outer face (Cabeen et al., 2009). A periplasmic polymer, CrvA, functions similarly in *Vibrio spp.* (Bartlett et al., 2017). In some Euryarchaeota the tubulin superfamily protein CetZ regulates a morphological switch between plate- and rod-shapes via unknown mechanisms (Duggin et al., 2015). In the wall-less *Spiroplasma spp.* a cytoskeletal ribbon composed largely of fibril protein is the determinant of the helical cell shape (Trachtenberg et al., 2008). Similarly, cell-spanning periplasmic flagella (PF) in the distantly related (and walled) Spirochaete bacteria enforce helical morphology as well as producing motility (Charon et al., 2012). Within archaea one analysis showed that the presence of actin family genes (crenactin or MreB orthologues) correlated perfectly with rod-shaped morphologies (Ettema et al., 2011) – although no specific mechanism for control of cell shape by these genes is known.

1.6.3 DNA segregation

Segregation of chromosomes by the tubulin-based mitotic spindle, ensuring stable inheritance, is a striking example of a cytomotive filament function in eukaryotes. Segregation of chromosomes by filaments has not been observed in prokaryotes. In contrast, spindle-based segregation of non-chromosomal DNA by filaments is a broadly distributed and well-studied phenomenon. Bacterial plasmids with both actin- (ParM and Alps) and tubulin-based (TubZ) spindles have been extensively characterised (reviewed

INTRODUCTION

(Fink and Aylett, 2017; Gayathri and Harne, 2017)). Some phage use tubulin filaments (PhuZ) to ensure correct positioning, and subsequent packaging, of virions and genomes (Erb et al., 2014).

1.6.4 Organisation of intracellular components

The long-range organising potential of filaments is also realised in the general case of positioning other cytoplasmic molecules. Perhaps the most striking example of this is the MamK actin family filament which organises membrane-bound magnetosome organelles in magnetotactic bacteria into linear arrays apparently scaffolded by the helical filaments (Komeili et al., 2006). PopZ, which forms filaments *in vitro*, assembles into a branching filament network near cell poles in some Gram negative bacteria which recruits a specific set of polar determinants via unstructured regions (Holmes et al., 2016). DivIVA, a coiled coil protein, polymerises on the membrane at the poles of some Gram positive bacteria where it is involved in modulating Min system behaviour via recruitment (Bramkamp et al., 2008; Patrick and Kearns, 2008), and apparently promoting membrane curvature (Ramamurthi and Losick, 2009).

1.6.5 The cytomotive distinction

As has been alluded to several times above there is a crucial distinction between those “cytomotive” protein filaments which are able to couple hydrolysis of nucleotides to their (de)polymerisation cycle in order to directly pushing or pulling other molecules around, and the protein filaments which act to impose order over long distances but do so without intrinsic dynamics. The term “cytomotive” was proposed by Löwe and Amos in 2009, but the ability of protein filaments to act as one-dimensional motors has been recognised for much longer (reviewed (Theriot, 2000)). The importance of this distinction, and a possible mechanistic explanation for it is discussed further in Section 2.4.

1.7 Motivation and outline

I began my PhD by working on trying to understand the polymerisation of cytomotive FtsZ filaments better. I then moved on to working on two FtsZ-polymerisation related projects: (1) looking at ZapA, a protein which interacts with FtsZ filaments, and (2) looking at how we might be able to develop better FtsZ inhibitors by exploiting our understanding of polymerisation. Finally, I circled back to trying to rationalise the basis of cytomotivity in other protein filaments.

2 RESULTS AND DISCUSSION

2.1 Polymerisation-coupled conformational switching in FtsZ

Much of the work constituting section 2.1 has been published as Wagstaff et al., 2017. Some sections are quoted verbatim. Where experiments were carried out by my collaborators this is indicated with a note in italics at the start of the subsection, like this one.

Cell division in many bacteria relies on a constricting cytokinetic ring that is orchestrated by the tubulin-like protein FtsZ. FtsZ forms dynamic filaments close to the membrane at the site of division that have recently been shown to treadmill around the division ring, apparently guiding septal wall synthesis.

Here, using X-ray crystallography of *Staphylococcus aureus* SaFtsZ I reveal how an FtsZ can adopt two functionally distinct structural conformations: open and closed. The open form is found in SaFtsZ filaments formed in crystals and also in soluble filaments of *Escherichia coli* FtsZ as deduced by cryoEM. The closed form is found within several crystal forms of two non-polymerising SaFtsZ mutants and corresponds to many previous FtsZ structures from other organisms.

I argue that FtsZ's conformational switch is polymerisation-associated, driven by the formation of the longitudinal inter-subunit interfaces along the filament. I show that such a switch provides explanations for both how treadmilling may occur within a single-stranded filament, and why filament assembly is cooperative.

2.1.1 Background

FtsZ is an ancient, filament forming, tubulin-like GTPase protein found in the vast majority of bacteria and archaea, where it acts as a central component of the cell division machinery (Bi and Lutkenhaus, 1991; Löwe and Amos, 1998; Mukherjee and Lutkenhaus, 1994). FtsZ is localised to the plasma membrane at future division sites resulting in the emergence of a ring structure around the centre of the cell, the Z-ring. FtsZ is anchored to the plasma membrane by other proteins, most often FtsA but also ZipA and/or SepF (Hale and de Boer, 1997; Hamoen et al., 2006; Lutkenhaus, 2007). FtsA is a divergent actin homologue that forms copolymers with FtsZ and contains an amphipathic helix that facilitates membrane attachment (Szwedziak et al., 2012).

RESULTS AND DISCUSSION

After the localisation of FtsZ, a large number of other proteins are recruited to the division site. These proteins carry out remodelling and synthesis of cell wall during the division process. Together these proteins have been termed the divisome, although it is currently not known whether there is a stable multi-subunit complex at the heart of the divisome.

The precise molecular architecture of the Z-ring remains unclear, although it is probably composed of dynamic overlapping filaments along the circumference of the ring, at least during the later stages of the division process in rod-shaped model organisms such as *Escherichia coli* (Szwedziak et al., 2015). It was already clear from early fluorescence microscopy studies that during the cell division process the Z-ring contracts with the constricting septum (Sun and Margolin, 1998). *In vitro* reconstitution experiments of FtsZ and FtsA with membranes showed that these two components alone deform membranes (Osawa and Erickson, 2013; Szwedziak et al., 2015). Together with homology to force-generating eukaryotic tubulins this prompted the suggestion that FtsZ has a role in generating forces required for constriction. In contrast, observations of constrictions and divisions of cells with helical Z-rings, incomplete Z-rings, and divisomes with modified FtsZ properties, support the opposing idea that FtsZ does not provide an indispensable driving force for constriction (Addinall and Lutkenhaus, 1996; Bendezú et al., 2009; Fu et al., 2010; Monahan et al., 2009). The alternative candidate for force generation is cell wall remodelling, such that the activated substrate turnover driven accumulation of cell wall material works to push the plasma membrane inwards. A third option is that cell wall remodelling and Z-ring dynamics are interlinked processes that work together from the inside and outside of the plasma membrane to generate the forces needed for division to occur robustly and efficiently under many circumstances.

Treadmilling is a property of certain cytomotive filaments characterised by subunit addition at one filament end and subunit loss at the other, allowing the filament to move along a matrix, without any polymerised subunits themselves moving. Treadmilling requires a difference in the rate of net polymerisation and de-polymerisation at the so-called plus and minus ends of the filaments (such that filaments have a kinetic polarity as well as a structural polarity).

Recently, *in vitro* treadmilling of FtsZ filaments has been reported on supported bilayers with (Loose and Mitchison, 2014) and without FtsA (Ramirez et al., 2016), and also *in vivo* where FtsZ filaments were found to treadmill with components of the divisome around the division site (Bisson-Filho et al., 2017; Yang et al., 2017). These findings have resurrected an

old model of bacterial cell division: the template model, in which the closing septum constricts by new cell wall material being deposited in concentric rings on the inside of old material by moving synthesis machinery (altogether, the “divisome”), which in turn is guided or organised into a ring by dynamic FtsZ filaments (Bramhill and Thompson, 1994). This idea fits into the third category of ideas listed above about the role of FtsZ: FtsZ dynamics and cell wall synthesis working together to facilitate constriction.

FtsZ, until relatively recently, had not been considered a good candidate for treadmilling behaviour. This is largely because it is currently not known if any functionally relevant FtsZ structures are formed in cells beyond single-stranded protofilaments (Li et al., 2007; Szwedziak et al., 2015), and treadmilling has been proposed to be a property restricted to multistranded filaments only (Narita, 2011). However, given that treadmilling is seen in multiple organisms *in vivo*, and *in vitro*, in the latter case including observation of single protofilaments treadmilling (Loose and Mitchison, 2014), it seems very likely that treadmilling is an intrinsic property of FtsZ protofilaments, at least.

Surprisingly, knowledge of FtsZ filament structure is limited. Only one FtsZ crystal form, from *Staphylococcus aureus* (SaFtsZ, PDB IDs 3VOA, 3VO8), has revealed a straight protofilament of FtsZ, as might be expected from electron micrographs of many different FtsZ filaments and by analogy to eukaryotic tubulins (Matsui et al., 2012). The conformation of SaFtsZ subunits in those straight filaments showed an unusually (as compared to FtsZ structures from other organisms) open conformation, with the N-terminal GTP binding domain (NTD) and C-terminal GTPase activation domain (CTD) being rotated and shifted apart (~27°, compared to e.g. *Bacillus subtilis* structure PDB ID 2VAM). Subsequent crystallisation efforts using SaFtsZ constructs with large changes to the critical T7 loop that normally contacts the GTP/GDP nucleotide bound to the next subunit were successful in generating crystals where SaFtsZ adopted a different ‘closed’ conformation, more similar to FtsZs from other species (PDB IDs 3WGK, 3WGL) (Matsui et al., 2014). These crystals also contained straight protofilaments. Currently, it remains unclear what causes the conformational switch seen in these T7 mutants. It is possible the switch was promoted by non-specific crystal contacts or by the alterations of the T7 loop. Also unknown is whether an unmodified SaFtsZ can adopt a closed conformation.

SaFtsZ has also been crystallised in an open conformation in complex with the FtsZ functional inhibitor and filament stabiliser PC190273 (PDB IDs 3VOB, 4DXD), the drug is bound in the cleft between the N- and C-terminal domains, only possible in the open

RESULTS AND DISCUSSION

conformation – suggesting that the mechanism of drug action is to lock the protein in this state (Elsen et al., 2012; Matsui et al., 2012; Tan et al., 2012). Isolated, open form SaFtsZ monomers relax into the closed conformation during molecular dynamics simulations (Ramírez-Aportela et al., 2014). Fluorescent analogues of PC190723 have recently been used to monitor apparent opening and closing of the inter-domain cleft in solution as a function of FtsZ polymerisation state (Artola et al., 2016). Together, these results hinted that the closed form of different FtsZs seen in many crystals is the predominant conformation of monomeric FtsZs and, *vice versa*, that filamentous FtsZ in solution is in the open conformation seen in SaFtsZ filament crystals. What was lacking was robust structural evidence that this is the case.

FtsZ shares two properties with actin and tubulin that until now have been hard to explain. Firstly, FtsZ exhibits cooperative assembly, with a critical concentration and a lag phase for assembly. This is not possible for a single-stranded, isodesmic filament with rigid subunits, and an assembly switch has long been hypothesised as a way to explain this cooperativity (Huecas et al., 2008; Michie and Löwe, 2006; Miraldi et al., 2008). Secondly, filament treadmilling is presumed to require multi-strandedness (Narita, 2011), while FtsZ is apparently single-stranded.

2.1.2 SaFtsZ-T66W and -F138A are polymerisation and GTPase compromised.

The experiments referred to in 2.1.2 were carried out by María A. Oliva and Alba García-Sánchez, both at Centro de Investigaciones Biológicas, CSIC, Madrid, Spain.

Previously, there was no pair of native-like structures showing an FtsZ molecule in the closed and open states, as discussed above. In this work we set out to generate an SaFtsZ structure with the molecule in the closed form, which we suspected to be found in monomeric FtsZs, by introducing single point mutations inhibiting polymerisation, in regions of the structure thought to be far away from regions involved in nucleotide binding or conformation switching. Specifically, two SaFtsZ mutations, F138A and T66W were designed to inhibit SaFtsZ filament formation, based on equivalent mutations inhibiting assembly of *Methanocaldococcus jannaschii* FtsZ (M164A (Martín-Galiano et al., 2010) and T92W (Díaz et al., 2001) respectively; polymerisation inhibition of T92W unpublished data). Both mutation sites are located on the ‘top’ surface of FtsZ, on the N-terminal, GTP-binding domain and are part of the longitudinal protofilament interface seen in crystals.

Full-length, untagged, SaFtsZ wildtype, F138A, and T66W proteins were purified and characterised biochemically (Figure 2-1). Filament formation in both SaFtsZ mutated proteins was compromised since no filament formation was detected by sedimentation (Figure 2-1A) or negative stain electron microscopy (Figure 2-1C) for either T66W or F138A in the presence of GTP or guanosine-5'-[(α,β)-methyleno]triphosphate (GMPCPP), a slowly-hydrolysable analogue of GTP. FtsZ GTPase activity is largely dependent on polymerisation as one subunit provides catalytic residues to the active site of the next subunit through residues in loop T7. Both mutants have weak GTPase activity (Figure 2-1C), indicating that monomers may at least associate to form transient but functional active sites. In support of this, on addition of PC190723, the mutant proteins did form filaments detectable by sedimentation and electron microscopy in the presence of GTP and GMPCPP. We concluded that SaFtsZ T66W and F138A are polymerisation and GTPase compromised but retain some residual activities.

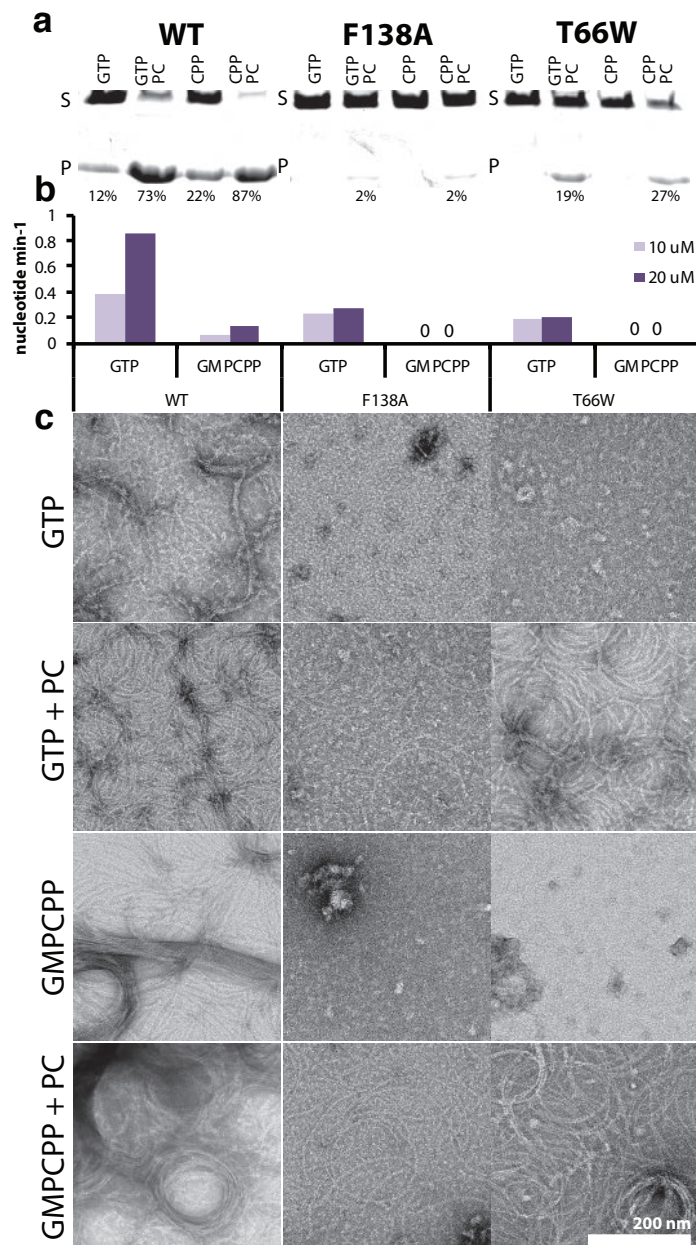


Figure 2-I – SaFtsZ mutants T66W and F138A have compromised polymerisation and GTPase activities.

A Polymerisation of FtsZ proteins at 10 μ M was assayed by sedimentation in the presence of GTP and GMPCPP (CPP) with and without FtsZ functional inhibitor PC190723 (PC). Pelleted (P) and soluble (S) protein was run in the same lane of an SDS-PAGE gel with a delay. Percentage of pelleted protein was estimated from integration of band intensities.

B GTPase activity of FtsZs at 10 and 20 μ M in the presence of GTP/GMPCPP.

C Polymerisation of FtsZ proteins in the presence of GTP and GMPCPP with and without FtsZ inhibitor PC190723 (PC) was assessed by negative stain electron microscopy. All images are at the same magnification (scale bar 200 nm).

2.1.3 SaFtsZ adopts either a closed or an open conformation in crystals

Crystallography of SaFtsZ mutants was begun by Matthew Tsim and Danguole Kureisaite-Ciziene. Diffraction data from two crystals was collected before I took over the project. I carried out all subsequent work including protein purification, further crystallisation trials, all subsequent data collection, and all refinement and model building.

I solved five crystal structures of the globular domains of SaFtsZ T66W and F138A (Table 2, Figure 2-2) (See Appendix, Principles of X-ray Crystallography, p. 137). SaFtsZ constructs truncated to residues 12-316 were used to remove the N and C-terminal tails of FtsZ previously found to inhibit crystallisation. For easier reference, the five SaFtsZ structures are named herein in the form #XXx: number (1-5), mutation (F for F138A, T for T66W), monomer conformation (O for open, C for closed), and finally the arrangement of monomers within the crystal (m for monomeric, f for filamentous, single protofilament and s for split/domain swapped).

One structure, 1FOF, was in the open form and essentially identical (crystallographically isomorphous) to previously published wildtype SaFtsZ open conformation structures (C α RMSD versus PDB 3VOA: 0.33 Å) (Figure 2-2A, top). FtsZ molecules in 1FOF form completely straight single-stranded filaments (protofilaments) with a 44 Å repeat extending throughout the crystal. Four of the polymerisation compromised FtsZ point mutant structures (2TCM, 3FCM, 4FCs, 5FCM) were in closed conformations similar to that previously seen in SaFtsZ after extensive mutation of the T7 loop (e.g. C α RMSD 2TCM vs PDB ID 3WGL: 1.50 Å). Indeed, the closed structures were successfully solved by molecular replacement with one of the previous T7 loop replacement mutant structures (PDB 3WGL) as the starting search model. Unlike the closed form T7 mutant SaFtsZ crystals, none of the closed crystal forms here contained straight filaments running through the crystals.

When I analysed the conformations of all of the available nucleotide-bound SaFtsZ structures it became clear that they fall into two discrete groups (Figure 2-2B-D). I excluded SaFtsZ apo structures (e.g. PDB ID 3VO9), which are very different and are unlikely to be physiologically relevant given the high concentration of GTP/GDP in cells. The two conformations, open and closed, are distinguished by the change of the interdomain angle between the N- and C-terminal domains. If one considers the NTD to be fixed in space, the switch to the open conformation is best defined (as determined by the model-free algorithm implemented in the program DynDom (Hayward and Berendsen, 1998)) as a $\sim 27^\circ$ rotation

RESULTS AND DISCUSSION

of the CTD versus the closed conformation, around an axis of rotation as indicated by the circled dot in Figure 2-2B, right. This rotation is accompanied by a downward shift of the central helix 7 (H7, yellow in Figure 2-2) by almost one helical turn (Figure 2-2B, left).

It is important to note that, including previous work and my work described here, there are now available SaFtsZ structures with all permutations of open/closed conformations and bound GTP/GDP nucleotide – making it difficult to imagine that the open/closed conformational state and nucleotide state are linked (as has been proposed by some (Erickson et al., 2010)). Also, for the first time, with this work we have structures showing a single, essentially unmodified, FtsZ molecule in multiple conformations: SaFtsZ F138A crystallised in the open conformation in straight filaments as 1FOf, in the closed form as a monomer in two different space groups in 3FCm and 5FCm and as a split/domain-swapped closed form monomer in 4FCs. Domain swapping has been seen before for FtsZ (Oliva et al., 2004), and highlights the surprising independence of the N- and C-terminal domains that probably reflects a gene fusion in the evolutionary history of the protein.

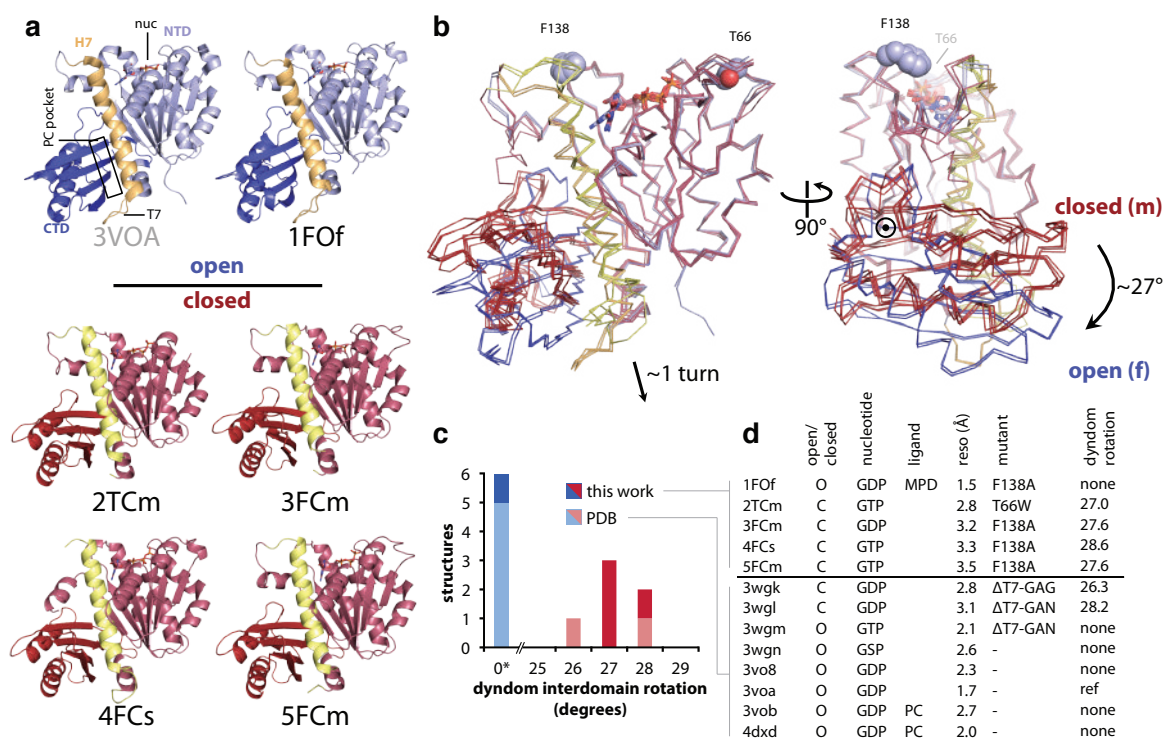


Figure 2-2 – Nucleotide-bound SaFtsZ crystal structures group into two conformations: open and closed.

A The five SaFtsZ (truncated to residues 12-316) structures determined here and PDB ID 3VOA are shown in cartoon representation, with nucleotides as sticks coloured by element. MPD molecule in IFOF is shown as green sticks. The structures are coloured according to conformation. Closed structures are shown in red, with the N-terminal GTP-binding domain in light red, and the C-terminal GTPase activation domain in dark red, central helix H7 is highlighted in yellow. Open structures are shown in blue, with the N-terminal domain in light, and the C-terminal domain in dark blue, central helix H7 is highlighted in orange. All structures shown in the same orientation, after alignment to the N-terminal domain of 3VOA (residues 13-165). 4FCs domain-swapped pseudomonomer is formed of two polypeptides. Note the different position of the C-terminal domain in the two sets of structures. The position of the PC190723 binding pocket is indicated on the 3VOA molecule.

B Superposition of the six structures in (A) shown in C α ribbon representation, after alignment as for (A), with the same colour scheme. Nucleotides are shown as sticks. Sidechains of residues F138 and T66 of wildtype structure are shown as spheres, non-carbon atoms coloured by element. (left) the same view as in (A), (right) molecules rotated 90° as indicated. Axis of interdomain rotation is indicated by the circled dot and the curved arrows

C, D Census of available nucleotide-bound SaFtsZ structures. **C** Bar chart indicating that DynDom, model-free assessment of dynamic protein domains, reveals two groups when comparing SaFtsZ structures to PDB ID 3VOA: no interdomain rotation, or a ~27° shift (around the axis in (B, right)).

D Table with information about nucleotide-bound SaFtsZ structures. Horizontal line separates structures determined here (above) from previously deposited structures in the PDB. (MPD: 2-methyl-2,4-pentanediol, PC: PC190723, GSP: guanosine 5'-O-[gamma-thio]triphosphate).

RESULTS AND DISCUSSION

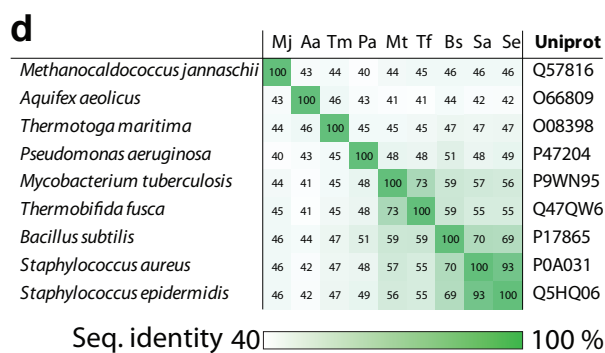
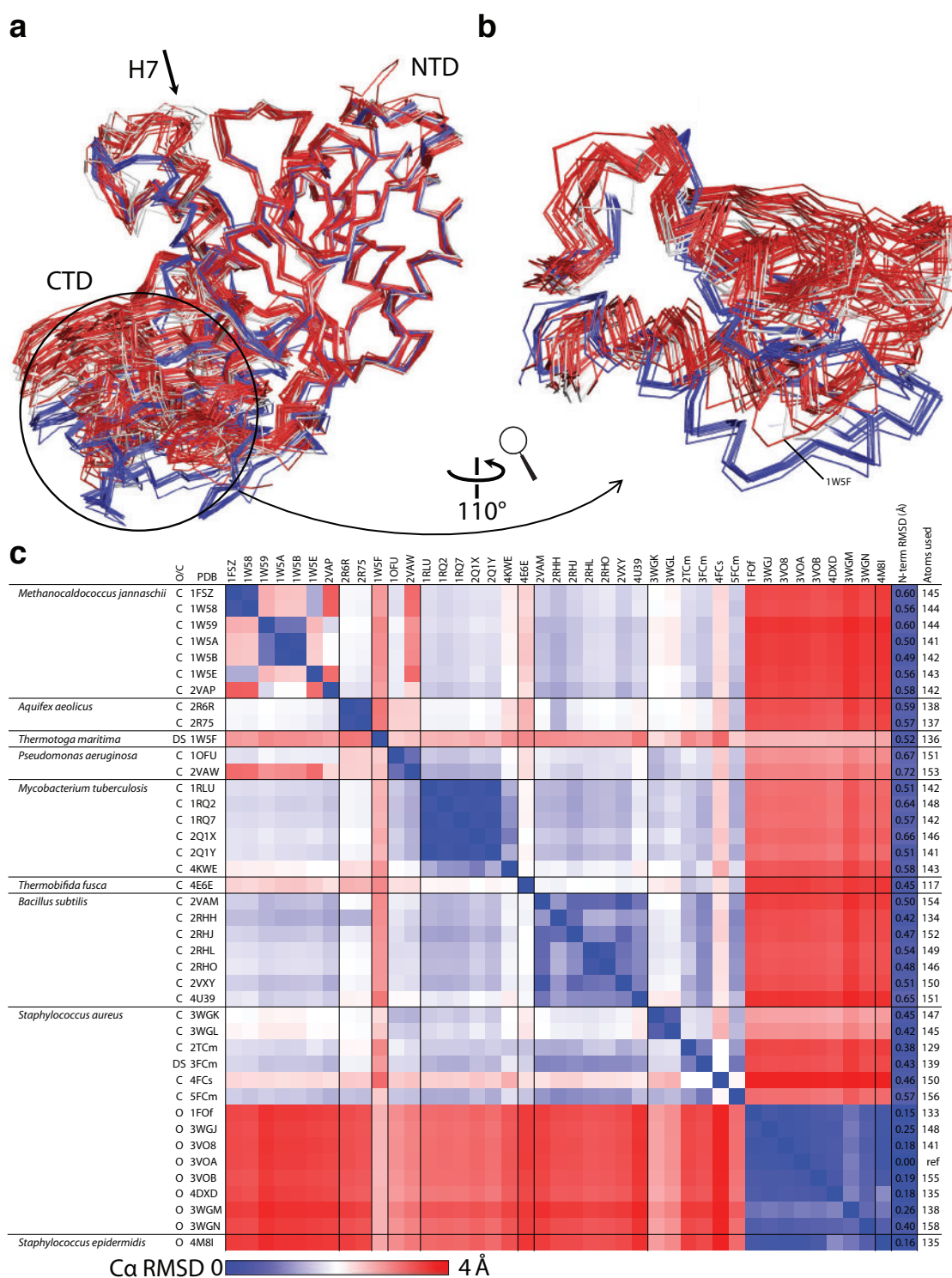
Figure 2-3 – All FtsZ structures can be placed in one of two groups: open and closed.

A All previous FtsZ structures were obtained from the PDB in October 2016 as listed in (B). Chain A from each downloaded structure, and the five structures determined here, was extracted and aligned to the N-terminal domain (residues 12 -176) of 3VOA using the PyMOL align command (which matches residues via sequence then minimises RMSD (root mean square distance) over matched residues, with 5 cycles of outlier rejection; except for PDB ID 1W5F and my structure 4FCs which are both domain-swapped, in these cases a pseudomonomer was generated for each, also *S. aureus* apo-structures (PDB IDs 3VO9, 3VPA), which have a very different conformation (Matsui et al., 2012), were excluded. N- and C- terminal extensions were removed, and the aligned structures are shown in ribbon representation from the same view as in Figure 2B. Closed structures are coloured red, except for closed *S. aureus* structures which are in white, open structures are coloured blue. The structural conservation of FtsZs is clear from the quality of alignment at the N-terminal domain (the outlier-excluded RMSDs, and the number of C α used is given in the last two columns of (C)). The two groups of structures can be distinguished because of the relative motion of the C-terminal domain - the open blue structures are separated from the closed white and red ones.

B The discrete distinction between the two groups is made clearer by zooming in on the C-terminal domain as indicated.

C C α RMSDs were calculated for all structures vs all structures, using the PyMOL align command with 0 cycles of outlier rejection (i.e. all residues matched via sequence are included in RMSD calculation). The RMSD for each pair of structures is indicated with a linear 3 colour gradient as indicated below the matrix. Within each species sets of highly similar structures are found (blue squares on the diagonal filling the black lines), with the exception of *S. aureus* where the two conformations, open and closed, align poorly. The *S. aureus* closed structures are more similar to FtsZs from other species than they are to open *S. aureus* structures, indicating that all existing non-*S. aureus* FtsZ structures are in similar, closed, conformations.

D Sequences of the FtsZs for which crystal structures were compared were aligned using Clustal Omega and pairwise similarity scores are shown.



2.1.4 Comparison of all deposited nucleotide-bound FtsZ structures

Based on previous work that established that all FtsZ structures are broadly similar (Oliva et al., 2007) I decided to again compare all FtsZ structures to all others, including the ones presented here and those published since 2007. The striking similarity of all FtsZ structures, except SaFtsZ open forms, is illustrated in Figure 2-3. There are many interesting results in Figure 3C, but the most significant is the fact that SaFtsZ closed forms have a more similar conformation to other FtsZs, even evolutionarily distant archaeal ones, than to SaFtsZ open structures. The most obvious outlier to the overall trend is PDB ID 1W5F, the previously published structure of a domain-swapped FtsZ from the extremophile bacterium *Thermotoga maritima*. In the structural alignment in Figure 2-3A and B the 1W5F structure can be easily identified as it falls approximately between the two clusters. Also, our domain-swapped structure 4FCs aligns relatively poorly to the other closed structures, although is much more similar to closed structures than open ones. Both cases are perhaps unsurprising, as domain swapping will clearly impose additional constraints on the conformational freedom of the protein. In the case of 1W5F the two swapped monomers contact one another via their CTDs, so it is unlikely to represent a functionally relevant intermediate form.

I concluded that SaFtsZ exists in two distinct conformations, open and closed, and that the closed form is much more similar to all other FtsZ structures than to the SaFtsZ open conformation.

2.1.5 Crystal structures of polymerisation compromised SaFtsZ mutants reveal structural features of the conformational switch.

In order to exist in two conformations, SaFtsZ must clearly have structural features that rearrange during switching. The large rotation of the C-terminal domain (CTD) versus the N-terminal domain (NTD) requires local rearrangement of residues in order to maintain hydrophobic contacts, side chain solvation state and generally favourable intramolecular interactions in both states. The degree of local rearrangement required is reduced by the movement of H7, which moves as to stagger rearrangement across the interior faces of the two domains. Displacement of the C-terminal portion of H7 versus the CTD is facilitated by a large hydrophobic region on the interior face of the CTD's beta-sheet being able to rotate against hydrophobic residues on H7. Side chain rearrangements here are relatively minor. Regions of greater rearrangement around H7 are highlighted in Figure 2-4, where structures 1FOF and 5FCM are compared (and measurements refer to this pair) although all of the changes discussed are similar in any pair of open/closed structures. Figure 2-4A and B show rearrangements at the NTD-facing side of H7, around the nucleotide pocket. Notably, when shifting from closed to open Arg 29 moves from the solvent exposed side of H7 to become slotted between H7 and the NTD in the open state (a 6.5 Å displacement of the guanidinium carbon), interacting directly with both guanosine and Asp 187 (on H7, in the closed state itself interacting with the base). Reassuringly, R29-D187 is a conserved ion pair in many FtsZs (Martín-Galiano et al., 2010). Despite the downward movement of H7, Phe 183 (also on H7) maintains favourable π -stacking with guanosine, because the base rotates around the C1'-N9 bond. The switch from closed to open leads to disruption of ionic interactions across the C-terminal part of H7 and NTD residues, however a subtle rearrangement takes place to maintain a base-base interaction (Heyda et al., 2010) between Arg 191 and His 33 (Figure 2-4B, inset): the flexibility and length of the Arg sidechain is used to allow the head group to remain almost fixed despite the ~4 Å movement of the C α atom.

Figure 2-4C and D illustrate rearrangement in the three-way interactions between the N-terminal part of H7, the NTD, and the CTD. While the residues from the NTD involved in the three-way contact remain relatively fixed in the shift from closed to open, e.g. Leu 169, residues from the CTD beta-sheet and H7 move downward in a coordinated fashion and a loop (246-258) from the CTD loosens allowing residues 248-250 to move towards H7, maintaining solvent exclusion from the hydrophobic pocket.

RESULTS AND DISCUSSION

The conformational switch in SaFtsZ does not involve structural changes around the phosphate-binding region of the nucleotide-binding pocket (Figure 2-4A). In particular, the T₃ loop can be ordered in all permutations of nucleotide (GDP/GTP or GTP γ S) and conformation (open/closed) (1FOF, 3FCM, 5FCM, PDB ID 3WGN), and can even be disordered when GTP-bound (2TCM). These observations appear inconsistent with a mechanism where a conformation change is associated with nucleotide hydrolysis state (Diaz et al., 2001; Li et al., 2013), although the terminal phosphate may modulate protein dynamics in a non-obvious way.

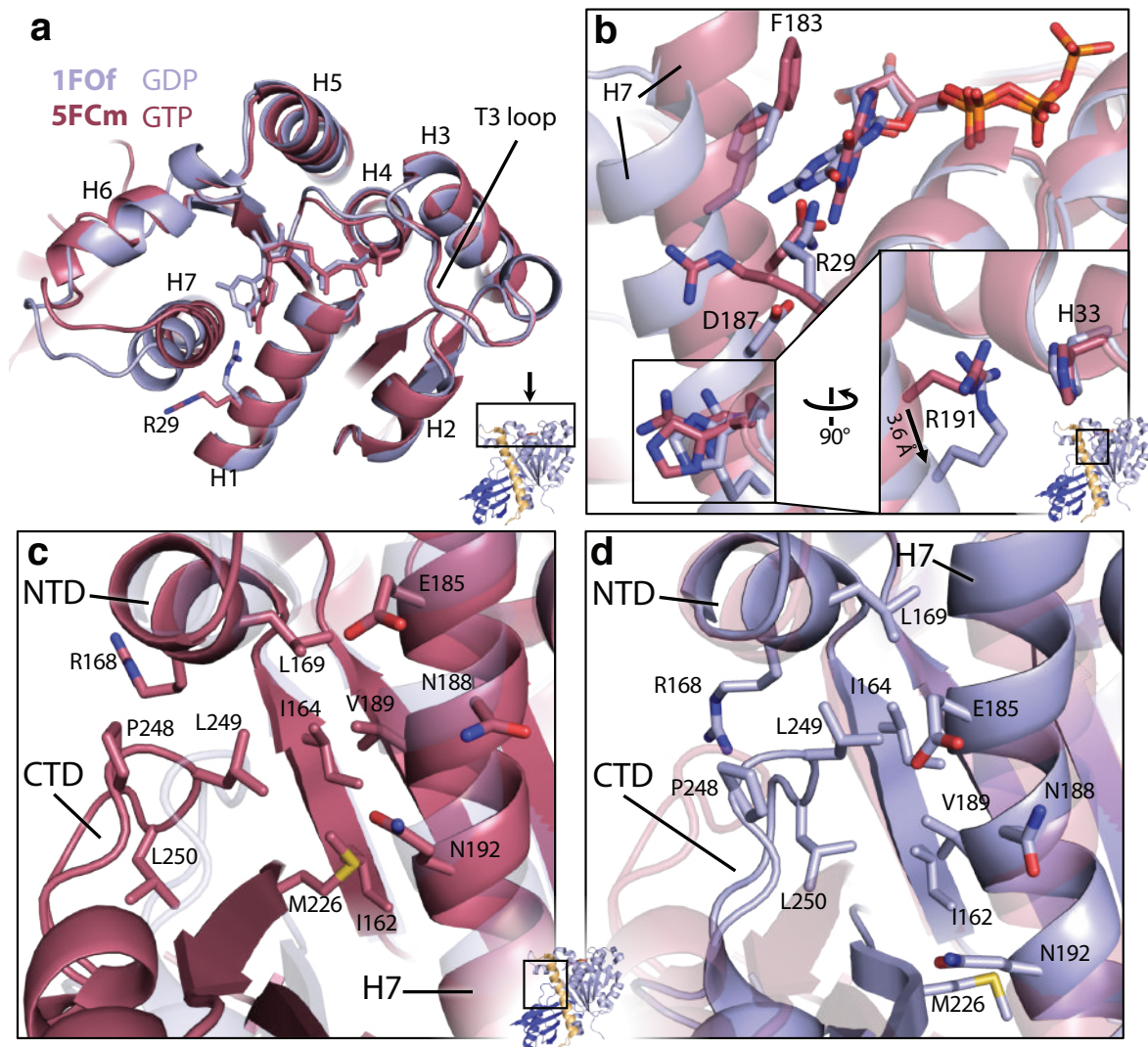


Figure 2-4 – Atomic details of the SaFtsZ regions allowing the conformational switch.

Structures IFOF (open, blue) and 5FCm (closed, red) are shown superposed in cartoon representation after alignment on the N-terminal domain (NTD). Nucleotides and labelled residues are shown as sticks. Non-carbon atoms are coloured by element, except in (A). Viewpoint is indicated in small cartoons, colouring as for Figure 2.

A Top view of FtsZ N-terminal domain. Helices are numbered. Note the very minimal rearrangements in this region after both conformational switch and nucleotide hydrolysis.

B View of the top of H7 and into the nucleotide binding pocket. Cartoons are semi-transparent. Inset is at same scale and shows molecule 90° rotated as indicated. 3.6 Å is shift of R191 Ca. Note rearrangement of individual sidechains between conformations.

C, D Identical views of the three-way interaction between the NTD, C-terminal domain (CTD), and H7, at the top of H7. In (C) IFOF is semi-transparent with no sidechains, in (D) 5FCm. Identical sidechains are shown in both. The three-way interaction is different in each conformation but solvent is excluded from the hydrophobic core in both cases.

2.1.6 Closed forms of FtsZs correspond to the free monomer, and open forms to the polymerised subunit.

The five polymerisation-compromised mutant SaFtsZ structures can be classified into two groups on the basis of having closed or open conformations, but they can also be grouped according to how they are found in relation to other molecules in the crystal. SaFtsZs in iFOF, and in previously published open forms (PDB IDs 3WGM, 3VOA, 3VOB, 3VO8, 4DXD) are arranged in straight, single, tubulin-like filaments extending through the crystal – indicated in our naming scheme by the second, lower-case, ‘f’ in iFOF. Adjacent subunits from iFOF, extracted from the crystal lattice (constructed using crystallographic symmetry operators), are shown in Figure 2-5A. As in tubulin, the nucleotide forms a large part of the interface between subunits, and it is thought that nucleotide hydrolysis is used to modulate interface affinity: an interface with a GTP is stronger (more binding enthalpy) than one with GDP (Erickson et al., 2010). The SaFtsZ crystalline filaments have a 44 Å repeat, which corresponds well to repeat intervals seen in electron microscopy negatively stained FtsZ filaments from a number of species. As a result, it has been hypothesised that the iFOF-like crystal filaments resemble soluble FtsZ filaments (Matsui et al., 2012).

As discussed, previous work generated SaFtsZ structures in a closed conformation by extensive alteration of the T7 loop (PDB IDs 3WGL, 3WGK) (Matsui et al., 2014). These structures contain SaFtsZs that are clearly in the closed conformation (Figure 2-2D, Figure 2-3), and are arranged in straight filaments in the crystal. However, these filaments are not the same as the open form filaments, with a much smaller interface buried surface area of ~700 Å² as compared to ~1200 Å² for iFOF and PDB ID 3VOA (calculated with PDBe PISA server (Krissinel and Henrick, 2007)), and a repeat of 45 Å. A dimer from a 3WGL pseudofilament is shown in Figure 2-5. The longitudinal contact is made between residues from the bottom subunit at the N-terminus of H5 and the preceding loop (including residue F138), and the loop between H6 and H7. From the top subunit the T7 loop (replaced in these structures), one face of S9, and the loop at the N-terminus of H10 are involved. Interaction does not involve any of the residues on the other side of the interface, towards the phosphates of the nucleotide.

In contrast, this work yielded four crystal forms where, for the first time, SaFtsZ is not arranged in straight, infinitely long filaments. In three of these, 2TCm, 3FCm and 5FCm, we find in each case that one of the molecules in the ASU forms what looks superficially like a filament interface via its top face, and the other molecule in the ASU equivalently

contributes a bottom face to another pseudo-interface. The crystals are therefore composed of pairs of poorly-interacting FtsZs (shown in Figure 2-5B) which pack via further crystal contacts that do not resemble interfaces in any way. The pseudo-interfaces have a subunit-subunit buried surface area (BSA) of 670-800 Å², and look similar to the interfaces seen in the closed T7 mutant structures, only including residues from one side of the top face.

Given that: (1) the F138A and T66W proteins have compromised filament formation (Figure 2-1), and (2) they adopt the closed conformation, and (3) they fail to form *bona fide* interfaces in crystals; it seems very likely that these closed forms correspond to the conformation of monomeric SaFtsZ in solution. The pseudo-interfaces seen are probably best thought of as a consequence of crystallisation, a process that explicitly employs conditions intended to enhance protein-protein interactions. If the protein will crystallise it is extremely likely that one of the major crystal contacts will imitate the longitudinal interface, as the interface regions are most likely sticky and more complementary than other surface regions. However, we cannot formally rule out the possibility that this minimal interface (*in silico* repetition of which generates a highly curved filament) is a functionally relevant and/or stable way for FtsZs to interact in solution, for example representing an initial capture state that precedes filament formation.

The fact that the phosphate end of the interface is not formed in any of the F138A closed form crystals supports the idea that it is the closed conformation that is not compatible with formation of *bona fide* interfaces, not the mutation per se – because the F138A mutation is within the pseudo-interface.

The fourth closed form structure, 4FCs, is arranged very differently within the crystal. There are two molecules of FtsZ present in the asymmetric unit (ASU) although the N- and C-terminal domains of each polypeptide have become disengaged and reformed in domain-swapped FtsZ molecules with the corresponding domains of crystallographic-symmetry related molecules (Figure 2-5). The two pseudo-FtsZs formed by each pair of polypeptides in the ASU both adopt the closed conformation (C α RMSD for comparable atoms in pseudo-monomer vs 2TCm 1.0 Å). The domain-swapped FtsZs do not make any crystal contacts that resemble filament interfaces. That a domain swap can happen, and that a domain-swapped FtsZ adopts a closed conformation, suggests that the two domains have a significant degree of independence and, more importantly here, that when SaFtsZ conformation is not modulated by polymerisation or pseudo-interfaces, the molecule

RESULTS AND DISCUSSION

adopts the closed conformation, as implied previously by molecular dynamics (Ramírez-Aportela et al., 2014).

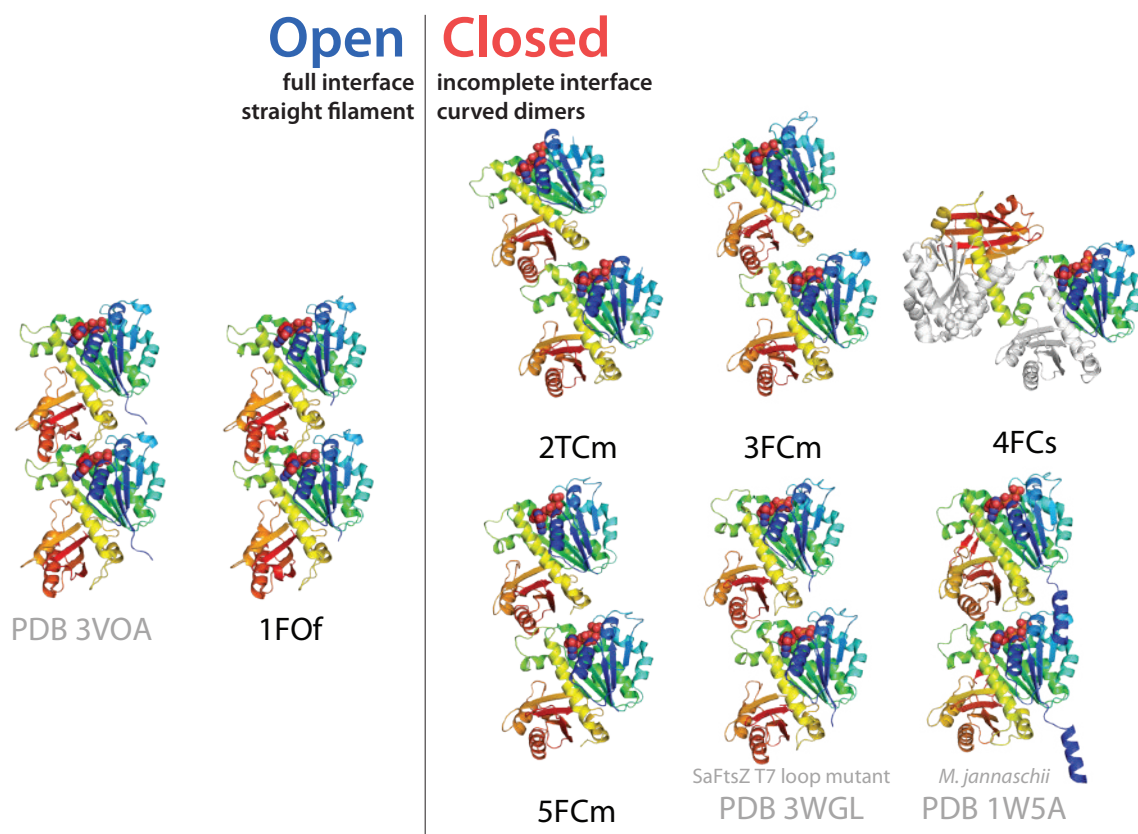


Figure 2-5 – Crystallised pairs of FtsZ molecules show the differences in longitudinal interactions between open and closed structures

Pairs of FtsZs were extracted from the indicated crystal structures. Structures are shown in cartoon representation, each chain is rainbow coloured blue to red, N terminus to C terminus. Nucleotide atoms are coloured by element. In each case the view is from the same orientation after the lower molecule is aligned to the NTD of the lower subunit from 1FOF. 4FCs is shown with one chain coloured and the other in white to highlight the domain swap.

2.1.7 CryoEM of SaFtsZ and EcFtsZ filaments reveals open conformation subunits

In order to reinforce the case that polymerisation into a straight filament is the driving force for the conformational switch within crystal structures I turned to cryoEM (See Appendix Principles of Electron Cryo-Microscopy (CryoEM), p. 147) to analyse the conformation of subunits within frozen-hydrated FtsZ filaments, i.e. not in crystals.

I began working on filaments of full length SaFtsZ. It was challenging to generate suitable cryoEM samples of well dispersed filaments in thin ice due to the antagonistic effects of the relatively “lazy” polymerisation of SaFtsZ monomers to form protofilaments and the highly cooperative assembly of higher order structures from those protofilaments. Some of the higher order structures observed during the long process of sample optimisation are shown in Figure 2-6A-D, ranging from tubes (A), double filaments (B), toroids (C), to thick bundles (D).

Eventually I was able to generate a usable sample, shown in Figure 2-6E. Although these images have significant background noise (from unpolymerised protein) I was able to obtain 2D classes of filament segments with clear secondary structure details, one of these is shown in Figure 2-6F. Unfortunately, all of the 2D classes looked like this one – the sample suffers from severe preferred orientation – a relatively common problem in cryoEM, and one that regularly makes progress impossible or extremely difficult. The problem is most often due to the interaction between the sample and the air-water interface at the surfaces of the thin film of solvent which exists in the time between blotting and vitrification. That we face the problem in this case is perhaps unsurprising: because FtsZ filaments do not (or, hardly) twist any hydrophobic patch on the surface of the subunit, when polymerised, will be presented in a long, co-linear, array which will interact strongly with the hydrophobic air water interface due to avidity.

In an attempt to move forwards I tried a wide selection of common approaches to improving orientation distribution, including various supports (e.g. graphene oxide and thin carbon) and a variety of detergents, as well as changing the buffer conditions. None of these were successful, 2D classes resulting from two of these attempts are shown in Figure 2-6, G & H. Despite this failure, it was possible to gain some confidence in the conclusions from crystallography, as the one projection I did recover was consistent with the simulated

RESULTS AND DISCUSSION

projection of the straight SaFtsZ filaments found in crystals (Figure 2-6, I, J & K). A full set of simulated projections are shown in Appendix Figure 4-5, p. 157.

After somewhat exhausting my options for improving the SaFtsZ filament data I decided to try imaging FtsZ filaments from another species, the distantly related Gram-negative γ -proteobacterium *Escherichia coli* (interestingly *E. coli* FtsZ has stubbornly resisted crystallisation, despite significant efforts). EcFtsZ and SaFtsZ have a pairwise identity of only ~45% (ClustalOmega). Optimisation of EcFtsZ polymerisation for cryoEM was relatively straightforward, although, as for SaFtsZ, higher order filament assembly was highly buffer dependent. I was able to generate much better images (Figure 2-7A), and although the data still suffer from severe preferred orientation (preferred orientation shown in Figure 2-7B), it was possible to reconstruct a medium (~8 Å) resolution map of wildtype, full-length *E. coli* FtsZ straight filaments (Figure 2-7C). The map suffers from information anisotropy due to the poor recovery of certain orientations (Figure 2-5C). However, the map clearly reveals an FtsZ filament with a 44 Å repeat and a density envelope into which SaFtsZ open conformation filaments can be fitted very satisfactorily (Figure 2-7D,E), and closed form structures cannot be fitted well at all (Figure 2-7F) Figure 2-7. The *M. jannaschii* closed conformation dimer structure PDB ID 1W5A is also shown and poorly fitting as it has previously been suggested to represent the conformation of FtsZ filaments (Oliva et al., 2004). Several secondary structure elements can be unambiguously identified in the reconstruction, including H7 and, crucially, the planes of both N- and C-terminal domain beta sheets – showing that the molecule is in the open conformation.

Given that all FtsZ crystals where *bona fide* straight filaments are seen in the crystal have FtsZs in the open conformation, and that the inverse is also true – SaFtsZ filament crystals contain open subunits, and that our intermediate resolution EcFtsZ cryoEM structure also contains open subunits, we propose that a polymerisation-driven conformational switch is a general property of all FtsZs. One of the consequences of such a switch, namely: permitting cooperative assembly of a single-stranded filament, has been discussed previously (Elsen et al., 2012; Huecas et al., 2008; Martín-Galiano et al., 2010; Michie and Löwe, 2006; Miraldi et al., 2008), however, such a switch confers additional surprising properties on a model filament.

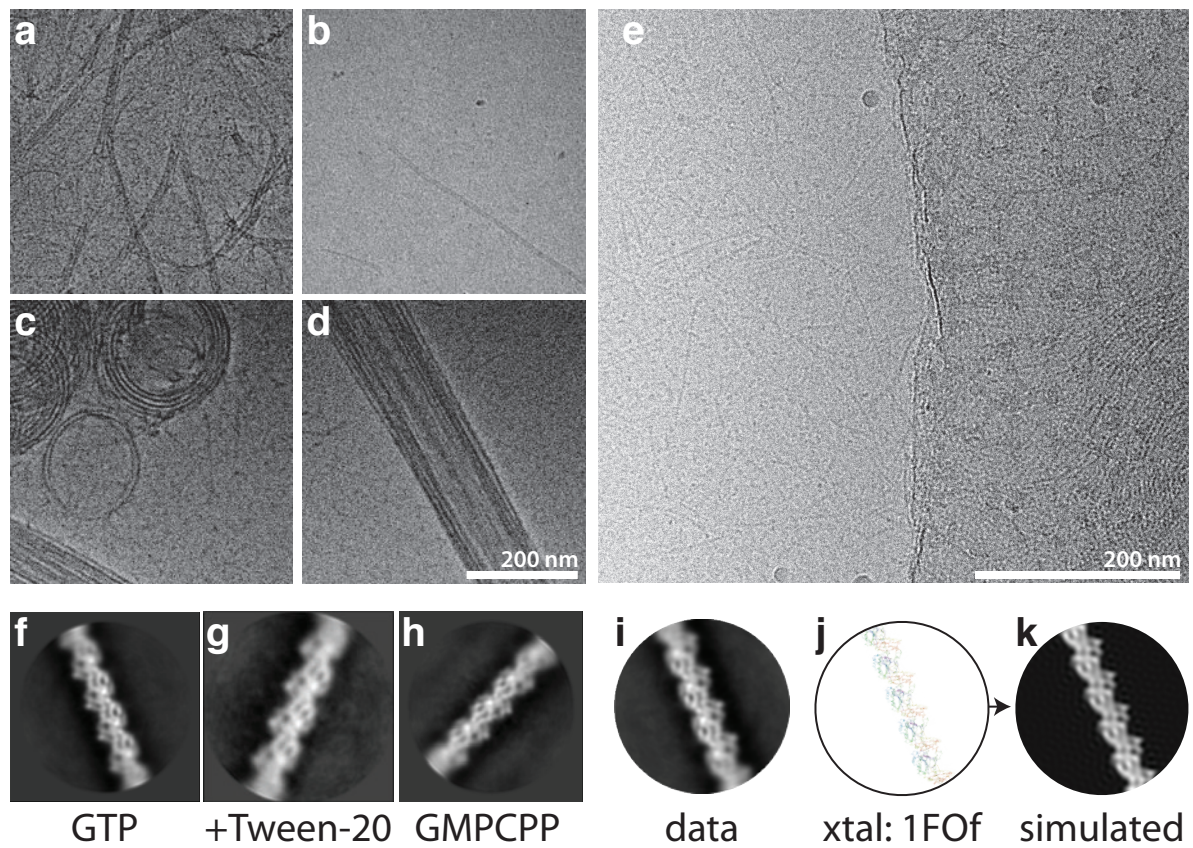


Figure 2-6 – CryoEM of *S. aureus* FtsZ filaments

A-D Higher order SaFtsZ structures seen by cryoEM.

E Representative micrograph of SaFtsZ polymerised in the presence of GTP.

F-H Representative 2D classes of SaFtsZ filaments imaged in the conditions indicated.

I-K Comparison of the preferred projection of SaFtsZ to a simulated projection of the straight SaFtsZ filaments found in some crystal forms.

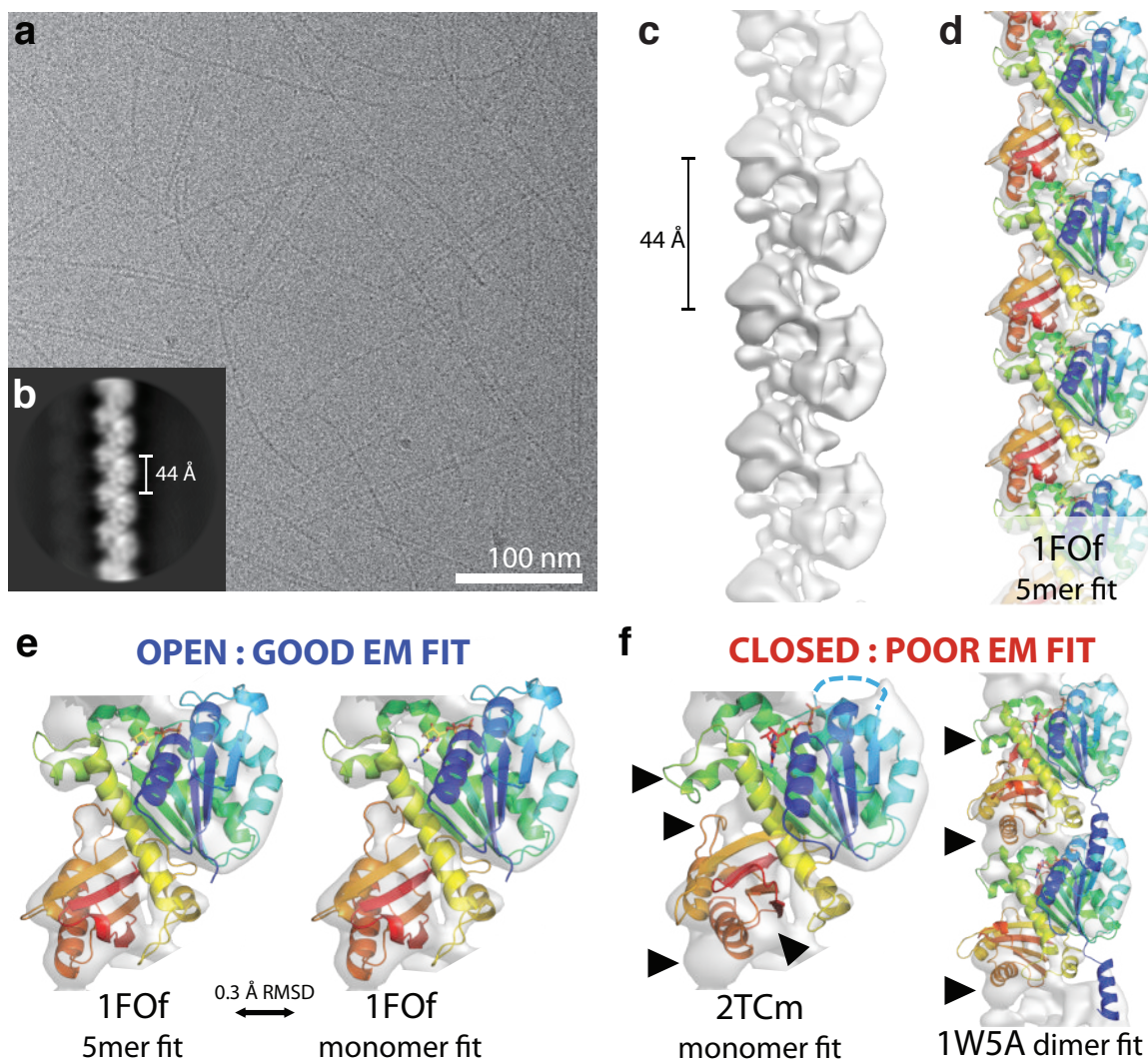


Figure 2-7 – CryoEM of *E. coli* FtsZ filaments

A Typical micrograph of frozen-hydrated EcFtsZ.GMPCPP filaments. Curved, straight, single and double/bundled filaments are seen.

B Representative EcFtsz filament 2D class produced by RELION

C EcFtsZ filament cryoEM density is shown at a threshold of 7.5 σ (left), and also with a 1FOF filament fitted into it (right)

E, F FtsZ structures as indicated were fitted into the EcFtsZ cryoEM density using the CHIMERA volume viewer fitting tool. The flexible T3 loop region is indicated. **(E)** A 1FOF 5-mer fits very well into the density, as does a 1FOF monomer – with both fits extremely similar. RMSD is for middle subunit in rigidly fitted 5-mer and monomer fitted into middle subunit density **(F)** Closed structures do not fit well into the electron density, and certainly not so that a repeating filament can be constructed. Some regions of especially poor fit are indicated with black arrowheads. 2TCm was fitted using only the NTD, which fitted into the same position as the open structure NTDs.

2.1.8 The FtsZ conformational switch between monomer and filament provides filament-end asymmetry necessary for treadmilling

Theoretical considerations of treadmilling can be fraught with intellectual traps. Having thought hard about these potential pitfalls I present simplified, yet robust, schema to explain how a polymerisation-associated conformational switch provides the end-asymmetry necessary for treadmilling within a single stranded filament. I focus on the specific case where the nucleotide forms part of the filament interface (i.e. in a tubulin-like fashion). In these, solvent exposed NDPs (nucleoside diphosphates) are quickly exchanged with NTPs (nucleoside triphosphates), NTP hydrolysis is not immediate, and NTP interfaces are stronger than NDP interfaces; although many of the conclusions are the same for filaments where nucleotide is buried inside subunits and likely has an allosteric effect on interface strength (i.e. in an actin-like fashion).

Treadmilling of cytoskeletal filaments is a useful dynamic property. Treadmilling filaments can be used to push or pull molecules in the cell without motor proteins as long as end-tracking mechanisms or co-factors exist, and these behaviours can be made switchable with high flux through the filament (e.g. in eukaryotic anaphase microtubules (Maddox et al., 2003)). Recently it has been shown that individual FtsZ filaments can treadmill *in vitro* with FtsA (Loose and Mitchison, 2014) and also alone (Ramirez et al., 2016), and that FtsA/Z treadmill in cells guides septal cell wall remodelling (Bisson-Filho et al., 2017; Yang et al., 2017). Treadmilling can also be useful without tight end-tracking, via a diffusion-and-capture mechanism, as has recently been suggested for FtsA/Z and a putative end-tracker, FtsN (Baranova et al., 2018). However, as has been noted previously (Löwe et al., 2004), a single-stranded filament with the above properties and rigid subunits, without conformational changes, cannot do robust treadmilling.

Such a hypothetical filament with rigid subunits is shown in Figure 2-8A. Note that the location (top/bottom) of nucleotide binding to the monomer is not important. This filament treadmills if a nucleotide gradient along the filament exists, and the kinetic plus end (net growth) will be at the end with more NTP. On-rates cannot differ at the two ends because they are the same reaction, but off-rate at the minus (NDP) end will be greater than at the plus end, so a situation of net growth at one end and net shrinkage at the other can be produced at certain monomer concentrations (addition reaction is 1st order with respect to monomer, loss is 0 order). This does not represent robust treadmilling however, as breakdown of terminal GDP interfaces is equivalent to breakdown of a GDP interface

RESULTS AND DISCUSSION

anywhere in the filament – and these processes will occur at the same rate as they are all zero order. As noted previously (Bisson-Filho et al., 2015), filament breakage and annealing could be an important facet of FtsZ dynamics (analogous to the idea of filament breakage and seeding in, for example, tauopathies), but the filament in Figure 2-8A has a more fundamental limitation on its biological usefulness: the direction of treadmilling is determined entirely by the history of the filament (the direction of the initial NTP-NDP gradient), so there is no coupling of kinetic and structural polarity – and the same filament could just as easily treadmill in either structure-defined direction.

Coupling of kinetic and structural polarity requires subunit addition and or loss to proceed via different stereochemical pathways at each structure-defined end of the filament. This is not the case in Figure 2-8A, the difference in off-rates (the kinetic polarity) is set by the nucleotide gradient and not the structural polarity, and we have already seen that there can be no difference in on-rates at either end. Filament systems can generate different stereochemistry for subunit addition at either end by being multi-stranded and having staggered subunits, such as actin (Wegner, 1976), or by using a longitudinal hooking mechanism, such as TubZ (Fink and Löwe, 2015).

Figure 2-8B shows our model for how a single filament very similar to the case in Figure 2-8A can also couple its structural polarity to a defined kinetic polarity and thus usefully, and robustly, treadmill. The crucial difference between the filament in Figure 2-8A and that in B is the existence of a polymerisation-associated conformational switch, i.e. subunits are no longer rigid, but can exist in one of two conformations – one form associated with the polymer, the other adopted in the free monomer. The free energy cost of the conformational switch from closed to open is paid for by binding to a filament end, and in the other direction through nucleotide hydrolysis and exchange that makes the longitudinal NDP intersubunit interface unfavourable. Although formation of a NTP interface at either structurally-defined end has the same net energy change, the reaction pathways are stereochemically different, and will occur at different rates because two different pairs of molecular surfaces are involved in each case initially. This difference is illustrated in the context of our structures in Figure 2-9– but note we are not making a prediction about which end of a single-stranded FtsZ filament is the kinetic plus end.

Importantly, the scheme in Figure 2-8B also allows breakage at NDP interfaces within the filament to be different to loss of NDP subunits from each end: NDP interfaces in the filament are stronger because the energetic cost of losing subunits from ends only is paid

for by the favourable switch to the monomer conformation, which the ‘new’ end subunits of two halves of a broken filament cannot do because they remain in filaments through one remaining interface. Especially important to note here that the scheme in Figure 2-8B can also be drawn with nucleotide on the other side of the monomer. Recently, Joe Lutkenhaus and co-workers provided convincing evidence that FtsZ has the opposite kinetic polarity to eukaryotic tubulin (Du et al., 2018), which may not be as surprising as it sounds as microtubules can in fact treadmill in either direction, under certain conditions, (Grego et al., 2001).

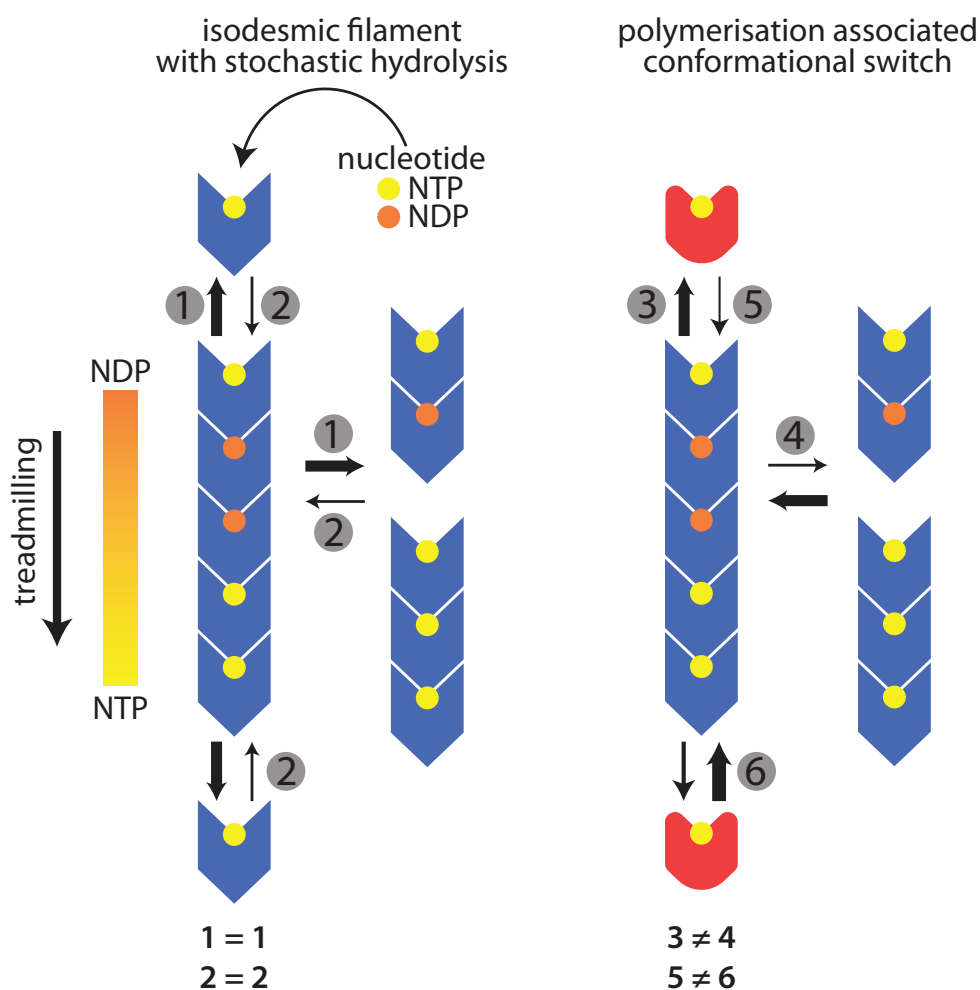


Figure 2-8 – A polymerisation-associated conformational switch allows treadmilling of single-stranded filaments.

Black arrows indicate rates roughly in proportion to their width, similarly sized arrows in (A) indicate rates that are exactly equivalent. See main text for discussion of limitations and assumptions of these simplified models, particularly regarding implied orientation of molecules.

A An idealised rigid (lacking a conformational switch), tubulin-like, filament forming protein, for which addition/loss of a given NXP is isodesmic. This filament cannot do robust treadmilling, as breakage is the same as minus end subunit loss, and it cannot couple structural and kinetic polarity

B A single-stranded version of (A) with a polymerisation-associated conformational switch (between blue and red forms), able to treadmill robustly and with coupled kinetic and structural polarities. The conformational switch allows filament breakage and subunit loss from ends to be different, and for the stereochemistry of subunit addition at either end to be different – meaning that addition will take place at different rates in a manner defined by structural polarity.

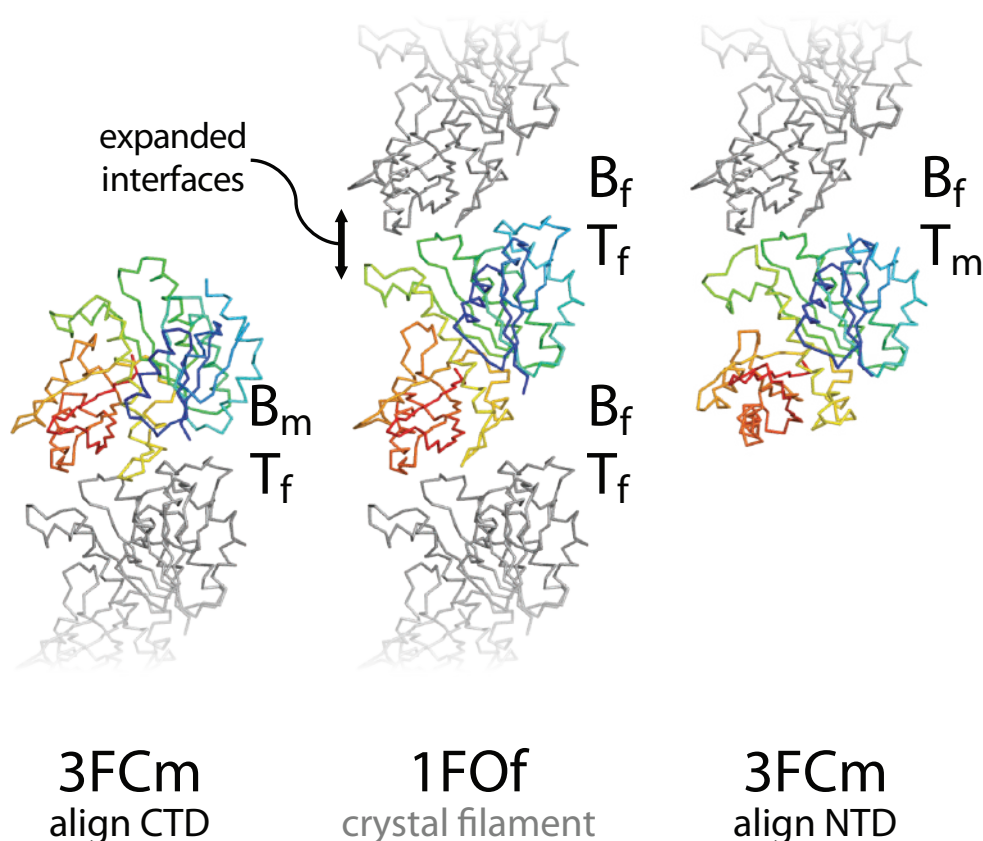


Figure 2-9 – A polymerisation-associated conformational switch generates asymmetry between filament end interfaces.

(Middle) 3 molecules from the open form IFOF crystal filament, slightly separated for clarity, are shown as C α ribbons. The middle subunit is rainbow coloured blue-red, N- to C-terminus, the top and bottom subunits are coloured grey. (Right, left) The middle subunit is replaced with a closed form 3FCm molecule, aligned to the middle subunit N-terminal domain (NTD) (right) or C-terminal domain (CTD) (left). The different pairs of approaching surfaces are labelled B/T_{m/f} : bottom/top, monomer/filament. These modelled closed-open interfaces will not represent the transition state of subunit addition at either end of a filament (nor even any position on the reaction pathway), but they illustrate the fact that the conformational switch will necessarily lead to stereochemically different reaction pathways at each end that allow the two ends to have different rates of subunit addition, linking structural and kinetic polarity.

2.1.9 Conclusion

Here we have shown that FtsZs adopt two different conformations: open and closed. The open form is adopted by FtsZ in straight filaments, the closed form by FtsZ monomers. The implication is that the polymerisation-associated switch from closed to open is made favourable by the free energy gain of interface formation of the subunits in the filament. Such a polymerisation-associated conformational switch explains how a single-stranded filament can show cooperativity in polymerisation, and how it can avoid breaking apart when treadmilling. This switch also explains how a single-stranded filament with tubulin-like properties can couple structural and kinetic polarities to enable robust treadmilling, with plus and minus ends being defined by the polarity of the filament. The switch is placed in a wider context in Section 2.4.

At this point it should be highlighted that although single-stranded FtsZ is frequently considered the functional unit of the protein *in vivo*, the potential of the conformational switch to generate end-asymmetry could also be exploited in multi-stranded treadmilling, and treadmilling in conjunction with the many FtsZ-interacting proteins *in vivo*. In addition to this, we have not directly addressed the structural basis of filament bending – an outstanding question in the field. Indirectly, cryoEM of *E. coli* FtsZ filaments assembled with GMPCPP and frozen after a 20-30 second incubation show some degree of bending in almost all single filaments, and segments from bent filaments are included in the reconstruction showing subunits in the open form - apparently directly undermining previous ideas that all bent FtsZ filaments are GDP-bound and/or in a closed or related conformation.

2.2 ZapA cross-links FtsZ filaments

This work is unpublished.

2.2.1 Background

FtsZ filaments are used to organise cell division but can only do this via interactions with other proteins (Haeusser and Margolin, 2016). Known FtsZ filament interacting proteins come in several flavours: membrane tethering (required for cell division), severing and capping (probably negative regulators of polymerisation), and cross-linking (probably positive regulators of polymerisation) (reviewed in Ortiz et al., 2016) (Figure 2-10A).

The roles of membrane tethering proteins such as FtsA, ZipA, and SepF are relatively well understood – they all serve to transmit the spatial information encoded in FtsZ filaments to the membrane (exactly why this needs to happen, and which information is important, is still not clear, however), and at least one membrane anchor protein is required in cells which use FtsZ to divide. All of the known membrane tethers bind to FtsZ via the conserved C-terminal “interaction hub”.

The roles of the severing and capping proteins, such as MinCD, SlmA, SulA and MciZ appear to be self-explanatory – they all act to reduce the length of FtsZ filaments (in response to a variety of cues), and so inhibit cell division either locally or globally.

Less clear is the role, or roles, of filament cross-linking proteins. This group includes some of the “Z-associated proteins”, or “Zaps”: ZapA, ZapC, and ZapD. These proteins are all thought to be oligomeric in the cell, with more than one FtsZ-binding per oligomer, and therefore be able to cross-link (or “bundle”) FtsZ filaments (Durand-Heredia et al., 2012; Low et al., 2004; Ortiz et al., 2015).

Here it is worth mentioning that FtsZ literature greatly suffers from usage of the word “bundling” to describe a wide spectrum of effects. Essentially, all FtsZ-modulating processes are at one point or another investigated via negative-stain EM, and the extent of “bundling” assayed, usually in a qualitative manner. One problem inherent in this approach is that FtsZ filaments already associate with one another – i.e. bundle, and so essentially any change to polymerisation conditions is able to perturb this process: to exacerbate or reduce the extent of interaction between filaments (via e.g. change in pH, osmolarity, ion balance, etc.). Another problem is that polymerisation (and GTPase activity)

RESULTS AND DISCUSSION

and filament bundling, are highly cooperative processes. As a result, the dynamic range of any assay which uses the extent of bundling as a readout is necessarily very narrow (this motivated me to work on developing better approaches to finding FtsZ inhibitors, see Section 2.3, p. 81). Together these problems mean that reports of FtsZ regulation (or chemical inhibition) via modulation of bundling should be treated with caution. I refer to “cross-linking” of FtsZ filaments when I think that a particular molecule is forming specific interactions with two different FtsZ filaments – this will of course often lead to bundling *in vitro*. Nevertheless, it appears that all of ZapA, C, and D, are *bona fide* FtsZ filament cross-linkers.

ZapC and ZapD are thought to interact with the FtsZ C-terminal interaction hub, while ZapA has been proposed to bind to the globular domain within FtsZ polymers (Roseboom et al., 2018). I was interested in the possible analogy between this mode of FtsZ filament binding and the many Microtubule Associated Proteins (MAPS) such as End Binding 3 (EB3) that interact only with polymerised tubulin.

ZapA, much like the other crosslinking proteins, has generally been described as promoting the assembly of mature Z-rings e.g. (Gueiros-Filho and Losick, 2002; Monahan et al., 2009), and more recently has been attributed the role of “focussing” the Z-ring (Buss et al., 2013; Woldemeskel et al., 2017). The Δ ZapA phenotype is weak, although the gene becomes essential in a low FtsZ background (Gueiros-Filho and Losick, 2002). ZapA functions in concert with another coiled coil protein, ZapB, though the details of how this works remain unclear (Buss et al., 2017; Galli and Gerdes, 2010, 2012). Very recently the role of ZapA was carefully investigated *in vitro* by Caldas et al. in the group of Martin Loose, they found that addition of ZapA lead to more coherent FtsA:FtsZ dynamics on a lipid surface, and that it did so without reducing the speed of treadmilling (Caldas et al., 2019).

Two crystal structures of ZapA have been solved, corresponding to the proteins from *Pseudomonas aeruginosa* (Low et al., 2004; Roach et al., 2014) and *E. coli* (Roach et al., 2014). In both, ZapA forms a tetramer with 3 \sim C2 symmetry axes (one axis is crystallographic, two are approximate as there are two monomers in the asymmetric unit, overall the tetramer has \sim D2 symmetry) (Figure 2-10B). There is substantial biochemical and genetic evidence that the tetramer is a functional form, and that it is the N-terminal head region which binds FtsZ (Caldas et al., 2019; Low et al., 2004; Pacheco-Gómez et al., 2013). The implications of the high ZapA symmetry for filament binding were discussed by Low et al. in 2004 but have not been explicitly investigated since then. It is hard to imagine that none of the ZapA

symmetries is used to impose order on the FtsZ filament. Some of the possibilities are illustrated in Figure 2-10C. The key uncertainties are: how many of the ZapA symmetries are used, and to what extent the ZapA molecule distorts from the almost perfect D₂ symmetric crystallised tetramers to facilitate a crosslinking mode which breaks any of the symmetries. I attempted to answer these questions by using cryoEM to visualise the interaction of FtsZ and ZapA from *E. coli*, first though, I was interested in how commonly ZapA is found in bacterial genomes.

RESULTS AND DISCUSSION

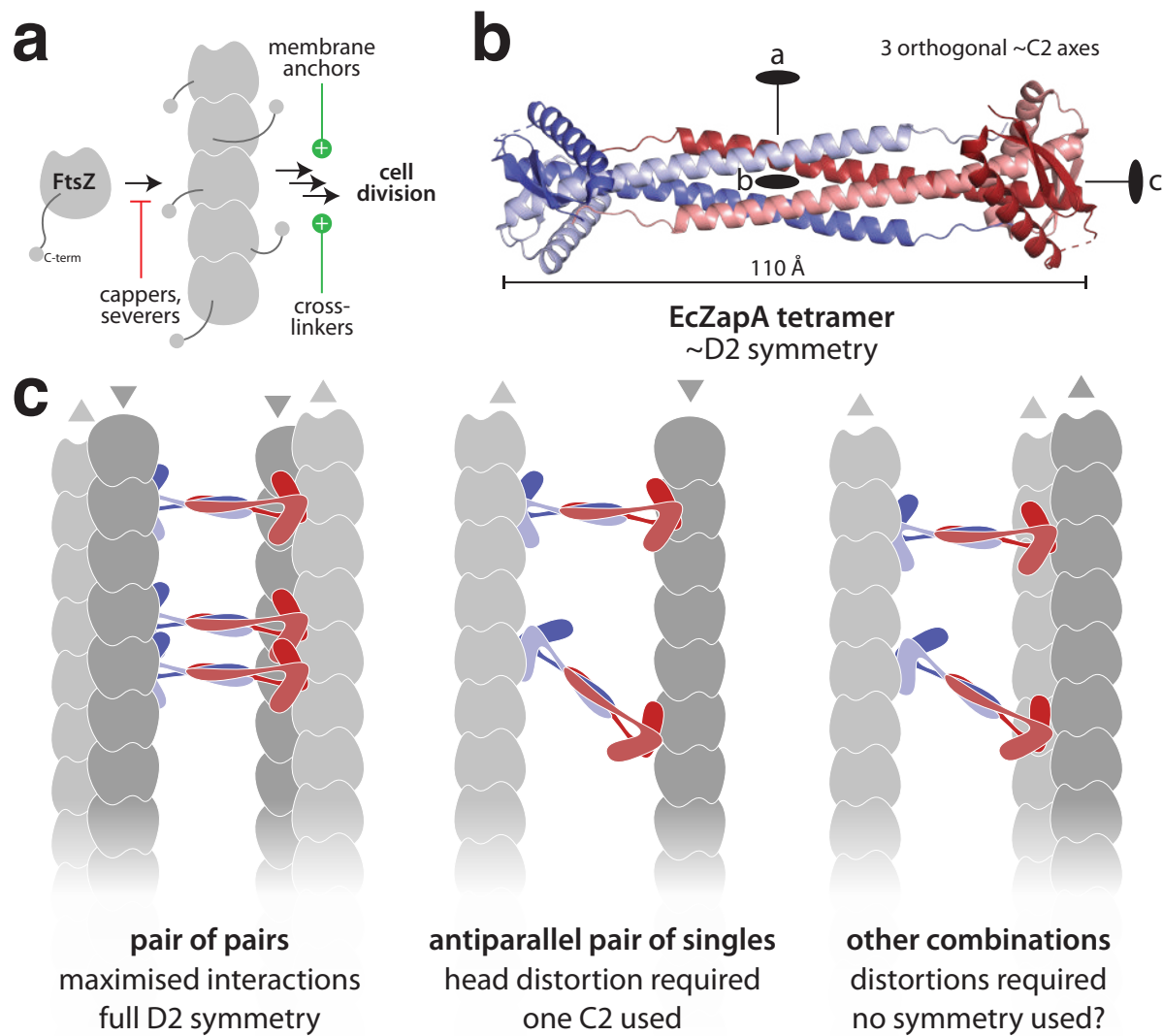


Figure 2-10 – Proposed role of ZapA

A Model for roles of Z-interacting proteins. FtsZ polymerises, which ultimately leads to cell division. Capping and severing proteins reduce the number or length of filaments and inhibit division. Membrane anchors attach filaments to membranes, allowing filaments to organise division processes. Cross-linking proteins somehow also promote division processes.

B Structure of EcZapA tetramer (PDB 4PIM). The ASU of the crystal contains pairs of ZapA monomers related by approximate $C2$ axis “c”, which are further paired, and related via (crystallographic) $C2$ axis “b”, to form tetramers which have an additional approximate $C2$ axis “a”. Overall, the tetramer has approximate $D2$ symmetry.

C Schematics showing some of the plausible ways that ZapA tetramers could cross-link FtsZ filaments, with an indication of whether the ZapA heads would have to distort to bind, and to what extent the symmetry of the tetramer is used in the interaction.

2.2.2 ZapA is widespread amongst bacteria

The presence of ZapA has been reported and experimentally verified in several bacterial clades, including many mitochondria (Buss et al., 2013; Gueiros-Filho and Losick, 2002; Low et al., 2004; Woldemeskel et al., 2017; Yoshida et al., 2009). In order to assess further ZapA distribution I searched for the presence of the conserved ZapA domain (described by PFAM entry PF05164 (El-Gebali et al., 2019)) in a curated set of non-redundant prokaryotic genomes (Mendler et al., 2018), annotated with a standardised phylogenomic taxonomy (GTDB v86) (Parks et al., 2018). Using a standardised taxonomy allows for a meaningful assessment of the distribution of individual genes across clades, because clades of equal taxonomic rank represent roughly comparable levels of genomic divergence. I found that ZapA was “common” (present in more than 20% of genomes) in 74 of the 114 phylum-level clades in the standardised taxonomy. Hence, ZapA is very widely distributed within bacteria. ZapA is virtually ubiquitous within several major clades, including Proteobacteria and Bacteroidota (roughly equivalent to NCBI taxonomy phylum Bacteroidetes). I was not able to find any evidence of ZapA in the domain Archaea.

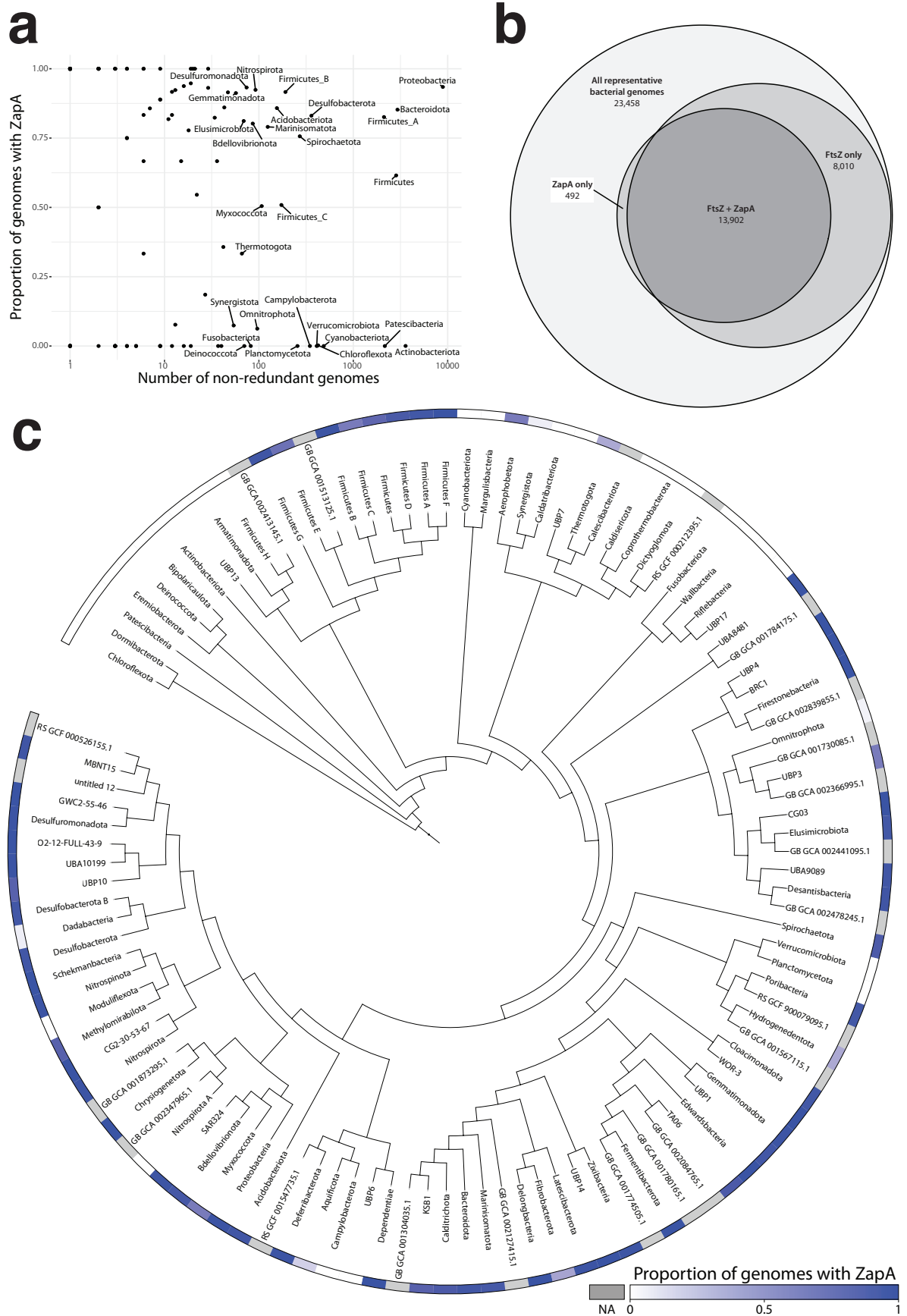
RESULTS AND DISCUSSION

Figure 2-11 – Distribution of ZapA across Bacteria

A Phylum level clades from the GTDB taxonomy v86 (Parks et al., 2018) of bacteria are plotted as points with the number of non-redundant genomes in the clade against the proportion of genomes with at least one ZapA hit. ZapA hits were HMMSEARCH results with PFAM PF05164, using an E-value cutoff of $1E-7$. Pre-computed HMMSEARCH results were retrieved from the Annotree server v1.1 (Mendler et al., 2018).

B Euler diagram showing distribution of representative bacterial genomes containing FtsZ-encoding genes (search HMM: TIGR00065, E-value cutoff $1E-5$) and ZapA-encoding genes (PFAM PF05164, $1E-5$). ZapA hits are very rare in genomes with no detectable FtsZ homologue. GTDB taxonomy v89 results available at Annotree were used for panel B.

C Phylogenomic tree of GTDB taxonomy v86 (Parks et al., 2018) (downloaded from Annotree server) showing the phylum level clades which are plotted as points in (A). Tips are positioned at the first branchpoint within each clade. Outer ring shows proportion of genomes with at least one ZapA hit, as for (A). Grey colour indicates that the clade only has one genome (and the proportion of hits is not shown).



2.2.3 CryoEM shows ladders of EcZapA crosslinking FtsZ filaments

Although ZapA is thought to crosslink FtsZ filaments the way in which this happens has not been directly visualised. Figure 2-12A shows wildtype, full-length, FtsZ and ZapA proteins imaged via cryoEM after incubation with GMPCPP (similar structures are visible with GTP).

The two proteins form ladder-like structures. 2D classification and averaging of ladder segments reveals the basic architecture of these copolymers: ZapA tetramers link parallel FtsZ filaments via interaction with, or close to, the globular domain (a set of interesting 2D classes, ordered by descending occupancy from top left to bottom right, is shown in Figure 2-12B). We can infer the gross architecture from the FtsZ-like 44 Å repeat along the outside bars and the recognisable ZapA secondary structure elements linking them. In both micrographs and 2D classes, most of the views of the copolymer correspond to orientations where ZapA's long axis is perpendicular to the beam (indicated with a '‡' in Figure 2-12A, and most of the classes in Figure 2-12B), but there are apparently some side-views corresponding to looking along ZapA's long axis (indicated with a '*' in Figure 2-12A, and labelled (i) and (xi) in Figure 2-12B). However, there are not very many intermediate views (perhaps (xii) and (xiv) in Figure 2-12B). To try and counter this preferred orientation, and increase the likelihood of generating a high quality 3D map, I collected several datasets while tilting the microscope stage.

From 2D information alone we can begin to infer something further about the architecture of the cofilaments. As discussed, one way to make use of a ZapA symmetry axis would be for a pair of heads related by the C₂ symmetry axis labelled 'c' in Figure 2-10B to interact with an antiparallel pair of FtsZ filaments. The projection of an antiparallel pair of FtsZ filaments when imaged with the two filaments one on top of each other should have 1) twice the intensity of a single filament and 2) a mirror plane perpendicular to the long axis. Several of the 2D classes in Figure 2-12B (e.g. (iii), (xiii)) have one side much brighter than the other, and although it is difficult to be sure, one side (e.g. the bottom in (xiii) and the top in (iii)) appears to have a mirror plane. Other classes show apparently asymmetrical FtsZ filaments, which are probably singles (although they could, potentially, be a pair of parallel filaments), examples include both sides of (xvi), the top of (x), and the bottom of (vii). One side could also appear brighter than the other if there was flexibility in the ZapAs connecting them, such that high quality alignment could only be achieved for one side:

blurring suggesting this is seen in several of the classes (e.g. (vii) and (viii)). I think it is likely that there is a mix of one- and two-stranded FtsZ filaments along the sides of the ladder.

There appears to be further heterogeneity within the filaments, as the angle between ZapA tetramers and the Z-filaments varies significantly, from approximately perpendicular in (x) to about 20° off axis in (iv), with intermediate angles visible (e.g. ~10° in (xiv)). Importantly these projections cannot be produced by simply rotating a structure with perpendicular bars: there really must be significant flexibility either in the ZapA:FtsZ interaction, or within the ZapA dimerisation/tetramerisation interface (or both). In some cases there appears to be a C₂ symmetry axis parallel to the beam, e.g. in class (xvi).

The possibility of heterogeneity in the interaction mode has been raised before, as genetic and MS cross-linking experiments have produced some confusing results (e.g. (Nogueira et al., 2015; Roach et al., 2014; Roseboom et al., 2018)). Also, I was not able to recover any evidence of specific pairwise interactions from a direct coupling analysis (DCA) of 9,000 FtsZ/ZapA pairs, suggesting that the interaction could be driven by more general surface properties spread over a larger area of one or both molecules – as has been suggested previously e.g. Low et al. proposed a charge-based interaction via the conserved acidic residues on the ZapA head (although they proposed an interaction with a basic C-terminal unstructured region of FtsZ).

Despite the significant heterogeneity in the sample I attempted to generate a 3D reconstruction to gain further insight into the interaction.

RESULTS AND DISCUSSION

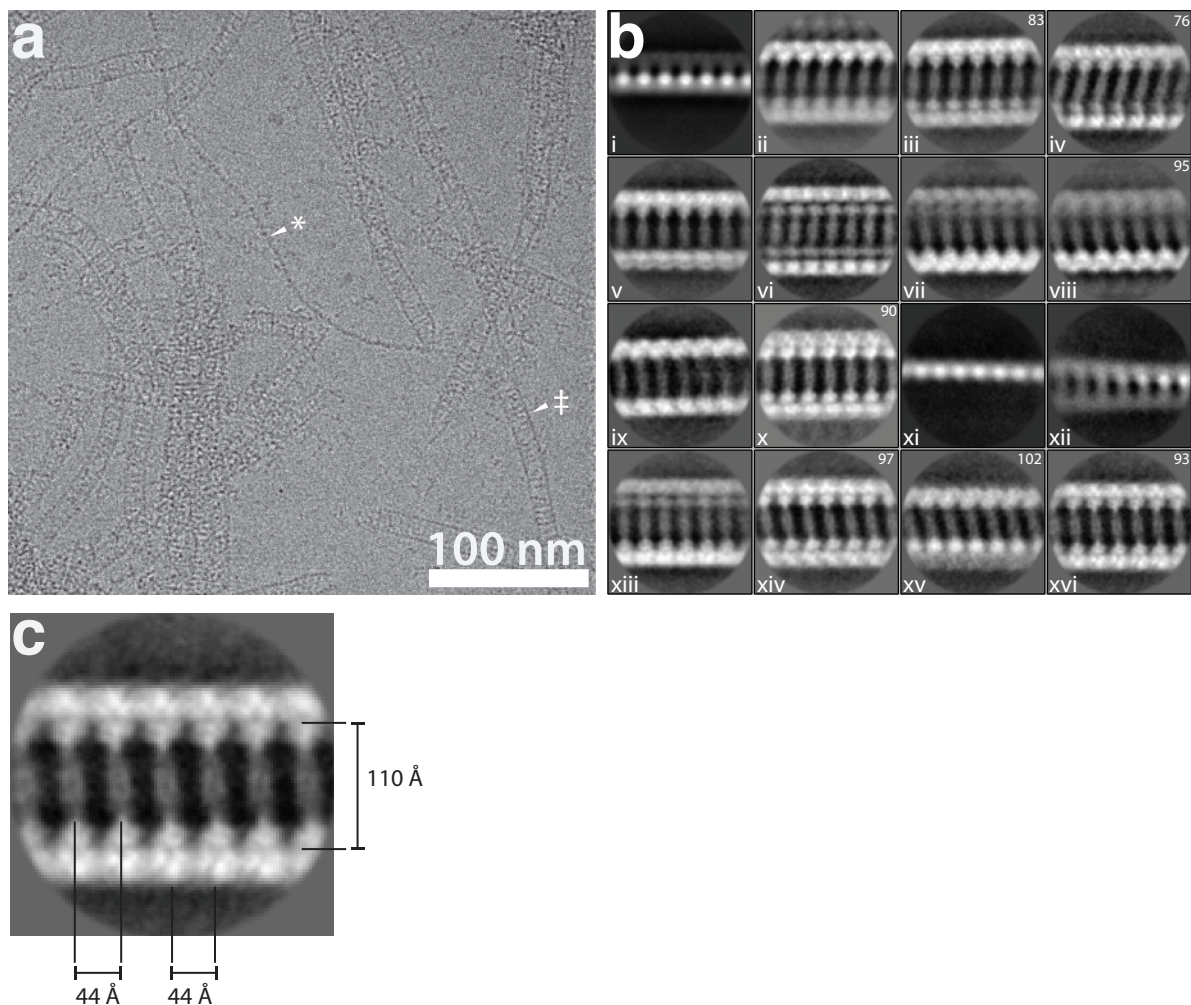


Figure 2-12 – “Ladders” of FtsZ and ZapA are seen in cryoEM

A Representative micrograph. Symbols: * indicates a putative side view, ‡ a top view.

B Selected 2D classes, labelled as discussed in text. Box size is 301.4 Å. The figures in the top right of selected panels is the angle between the long axis of the side filaments and the approximate long axis of the ZapA “rungs”, crucially, this number varies greatly.

C Expanded view of panel xvi from **B** with key distances marked. The 110 Å between the “sides” of the ladder distance corresponds well to the length of crystallised ZapA tetramers (see Figure 2-10), the 44 Å longitudinal repeat corresponds well to the FtsZ filament repeat (see Figure 2-7)..

2.2.4 3D reconstruction of FtsZ:ZapA copolymer

I tried many different strategies for generating a 3D reconstruction of the FtsZ:ZapA copolymer, attempting to compensate for the apparent heterogeneity. I was unable to get to a high resolution structure, however. An example strategy is shown in Figure 2-13A, and briefly discussed here.

Despite the heterogeneity in the sample it seemed clear from the 2D classes that most of the copolymers have a helical symmetry, with a 44 Å repeat corresponding to the repeat in an FtsZ filament. For this reason I decided to put all 111,000 manually picked particles into an initial 3D refinement while imposing helical symmetry (He and Scheres, 2017). This produced a map with the expected overall “ladder” geometry, although one side was thicker than the other. I used the Euler angles determined in 3D refinement to carry out a 2D classification of particle images. I discarded particle images which did not contribute to classes containing well defined secondary structure, leaving 70,000 particles. I carried out another 3D refinement, this time imposing both helical symmetry and C2 symmetry with the axis along the helical axis. This choice of symmetry axis would be appropriate if the Z-filaments along each edge are parallel (Figure 2-13B). I don’t think is the case, but as the direction of FtsZ filaments is hard to distinguish at low resolution I was hoping this would help to get all the other angles approximately correct. I then carried out a symmetry expansion operation, using the same C2 axis. Symmetry expansion duplicates all the particles, and generates Euler angles for each duplicate which correspond to putting the symmetry related parts of the molecule into the same position in the reconstruction. This is useful if the symmetry is not absolute, as further refinement can be carried out on the symmetry-related copies independently. Using the expanded particle set (140k asymmetric units) I carried out a further 3D refinement, masking on one side. I then carried out a 3D classification using the angles assigned during this refinement. As hoped, I was able to separate classes in which filaments were apparently running in the two opposite directions, suggesting that the symmetry expansion broadly worked (Figure 2-13C). However, I was not able to refine these classes further to deliver any confident insight into how the ZapA:FtsZ interface is arranged. This is most likely because the data were too weak relative to the small mass I was attempting to refine.

I tried many combinations of possible symmetries in refinement, and I also tried hard to isolate just those filaments with highly ordered structure throughout, but none of these strategies were successful.

RESULTS AND DISCUSSION

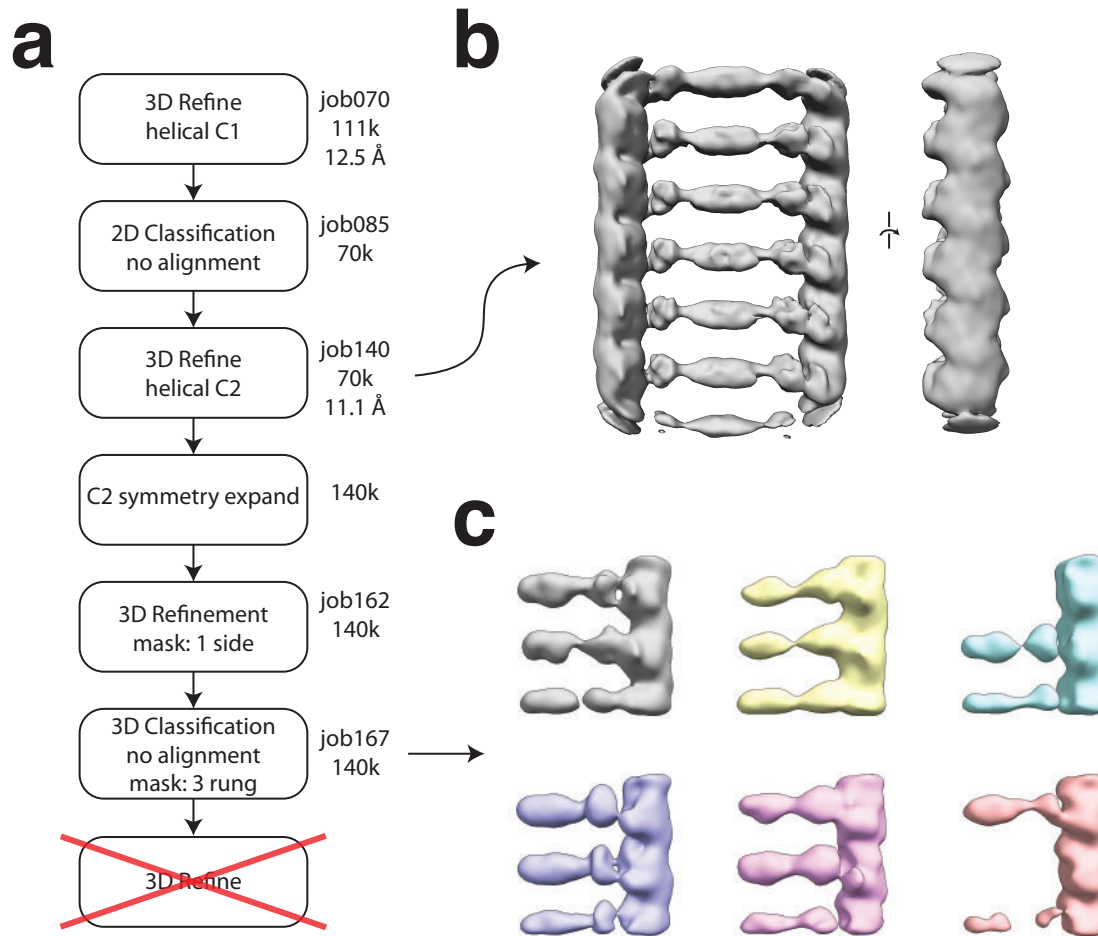


Figure 2-13 – Attempted 3D reconstruction of FtsZ:ZapA copolymer

A Example processing scheme. “k” numbers refer to thousands of particles. Resolutions are approximate.

B Map after helical/C2 symmetry imposed refinement.

C 6 classes from masked 3D refinement.

2.2.5 Comment and future work

Although it is disappointing that I am unable to present a detailed structure of the FtsZ:ZapA interaction, this is the first time that the interaction has been directly visualised. In particular, the suspicion that the ZapA head domain contacts the FtsZ globular domain was broadly confirmed. Because of this, it is likely that the ZapA:FtsZ interaction is indeed somewhat dependent on the dramatic conformational change in the FtsZ globular domain upon polymerisation. The heterogeneity observed in the interaction may be functionally relevant in allowing ZapA to mediate several, topologically distinct, kinds of FtsZ-FtsZ interactions. Exactly why FtsZ needs cross-linkers is not immediately apparent, as Z-filaments alone form bundles, in a way that is mediated by the disordered C-terminal tails (Huecas et al., 2017). It is possible that ZapA is particularly responsible for bringing filaments parallel, in a way that might not be possible through forming contacts via the disordered tails. Some support for this idea can be found in the recent *in vitro* experiments indicating that ZapA increases the collinearity of treadmilling FtsZ filaments (Caldas et al., 2019).

I think that high resolution structural information about FtsZ:ZapA could be gained through the approach begun here, but will require significantly more, and most likely higher quality, data. Alternative approaches would include trying to reduce sample heterogeneity by creating ZapA heterotetramers with putative FtsZ interfaces mutated away, or by generating mutant FtsZs which do not form pairs of filaments. Subtomogram averaging may also be a sensible approach. It is hard to see how a crystallographic approach could work.

2.3 An assay to find better FtsZ inhibitors

This work is unpublished but some passages are taken verbatim from an (successful) application to the MRC/Astra Zeneca Centre for Lead Discovery (MRC reference: MR/S026150/1)

2.3.1 Background

Every year more and more people are dying from bacterial infections which are resistant to existing therapeutics (OECD, 2018). There are simply not enough antibiotics available to clinicians, and this will not change in the near future, without radical improvements, because there are not enough molecules in development to fill the ever-widening gap between what's available and what's needed (The Review on Antimicrobial Resistance, 2015). In Europe alone, the disease burden of antibiotic resistant infections is already equal to that of influenza, TB and HIV/AIDS combined (Cassini et al., 2019). If current trends continue there will have been more than 1 million needless deaths in Europe by 2050 (OECD, 2018). As is often pointed out there has been only a single truly novel class of antibiotics brought to market (the oxazolidinones, discovered in 1978) since the “golden age” ended in the 1980s. Especially worrying is the fact that essentially no new drugs whatsoever for treating Gram negative infections have entered the pharmacopoeia since the 1960s (Fair and Tor, 2014).

Importantly, several analyses have determined that the “innovation gap” is caused not by a severe scientific difficulty in developing novel therapeutics, but instead by a failure of economic and policy incentives to stimulate enough effort in this area (OECD, 2018; The Review on Antimicrobial Resistance, 2015). The UK based Review on Antimicrobial Resistance has estimated that a radical overhaul of the antibiotic pipeline, which would likely be enough for antimicrobial innovation to outpace the spread of resistance, would cost \$16-37 billion over 10 years. To put this in context, resistant infections in the US alone cost the healthcare system \$20 billion annually (Centres for Disease Control and Prevention, 2013). So, the challenge for citizens and politicians is to figure out how to mobilise that sort of spending, and the challenge for scientists is to be clear on what should be done with it.

Crudely, the ongoing search for antibacterial compounds is split in two. Many, perhaps most, believe that the most efficient way to find new antibiotics is to screen molecules (from one of two sources: organic chemists or nature) for their effects on bacterial phenotypes

(Wohlleben et al., 2016). Conversely, the major alternative approach is to identify a molecular target and attempt to find those molecules that perturb the target biochemically. There are also hybrid approaches using well designed reporter strains, e.g. (Stokes et al., 2005). Target based approaches have fallen out of fashion in antibiotic discovery, although they remain the predominant framework for discovery in most other therapeutic areas (Knowles and Gromo, 2003). This unpopularity stems largely, it seems, from many (expensive) failures in the late 1980s through the 1990s (Mohr, 2016). Personally, I am yet to be convinced that target-based approaches are fundamentally flawed: previous failures, particularly in the case of FtsZ, are not difficult to explain in addressable ways. In particular, technical capabilities and biological understanding have advanced dramatically since much of the work that is used to dismiss the feasibility of finding antibiotics via rational approaches. I am an optimist in this regard, and this section of my dissertation describes the development of a biochemical assay designed to efficiently find effective inhibitors of FtsZ from *Staphylococcus aureus*.

2.3.2 Why FtsZ from *S. aureus*?

As discussed, the most terrifying prospect of increasing resistance amongst pathogenic bacteria to antibiotics is that of pathogens which are resistant to all existing therapies – bugs with no drugs. In Europe, in 2015, 39% of resistant bacterial infections were resistant to the current last line antibiotic (Cassini et al., 2019). Indeed, many pathogenic species have acquired multi-drug resistance phenotypes including *S. aureus*, a firmicute, which is a normal component of a healthy microbiome but can also cause fatal systemic infections. The World Health Organisation designated *S. aureus* as one of its seven ‘bacteria of international concern’ in 2014, largely due to the increase in resistant infections and the associated high mortality (Tacconelli et al., 2018). Recently *S. aureus* isolates resistant to vancomycin, currently the drug of last resort, have been identified, highlighting the urgent need for novel therapies (Foster, 2017).

Almost all bacteria require a functional FtsZ to perform cell division and replicate (Haeusser and Margolin, 2016). Inhibition of FtsZ has been proposed as an antibacterial therapy for the treatment of many different infections (including *S. aureus*, (Foster, 2017)), leading to many efforts to target the protein (comprehensively reviewed in (Hurley et al., 2016)), and several FtsZ inhibitors with potent antibacterial activity (e.g. (Kaul et al., 2015)). So why then, when: (1), FtsZ is a popular target for antibiotic discovery with significant effort expended already on finding inhibitors, and (2), existing FtsZ inhibitors have potent cell

RESULTS AND DISCUSSION

killing activity; is any further effort justified? Because: no anti-FtsZ molecule has been approved for therapeutic use against *S. aureus* or any other bacterial species (Hurley et al., 2016; Kaul et al., 2015). This is for two reasons related to the two statements above: (1) most of the efforts to find FtsZ inhibitors have been flawed (and reports of biochemical success have often been incorrect - see discussion of “bundling” p.69), and (2), the few validated biochemical inhibitors of FtsZ are rapidly escaped via spontaneous mutation. We have developed an approach designed to be better both from the perspective of biochemical tractability, and to pre-empt the evolution of spontaneous resistance.

2.3.3 Designing a better FtsZ assay

Many of the previous efforts to develop biochemical assays for the inhibition of FtsZ have been fundamentally limited by their choice of readout: using either filament formation or GTPase activity (which is a consequence of polymerisation). Both assays are necessarily kinetic, and polymerisation is a highly cooperative process (Hurley et al., 2016; Wagstaff et al., 2017), meaning that these assays have an extremely limited dynamic range. Furthermore, polymerisation can be difficult to distinguish from aggregation with many experimental approaches.

Instead, I decided to isolate a single, essential, biochemical aspect of FtsZ function: GTP binding. This idea has been tried on a small scale before, with a few putative GTP-competitive compounds being identified (Artola et al., 2015; Keffer et al., 2013; Ruiz-Avila et al., 2013). Choosing to readout GTP-binding allows us to confidently screen for inhibition using a sensitive and robust assay with a wide dynamic range. In addition, and in common with those who have pursued this idea before, I anticipate that a molecule which competes directly with GTP and has a high enough affinity for FtsZ will be a potent inhibitor of FtsZ polymerisation and cell division (Figure 2-14A,B). Indeed, genetic and biochemical evidence suggests that small amounts of inhibited FtsZ may be able to poison cell division (Araújo-Bazán et al., 2016; Hurley et al., 2016; Margalit et al., 2004), including (Du et al., 2018) showing that some dominant-negative mutations inhibit cell division at a 1:20 mut:WT ratio.

As mentioned there is (only) one class of well-characterised small molecule FtsZ inhibitors, the benzamide family similar to PC179023 (Hurley et al., 2016; Kaul et al., 2013). The benzamides bind in the interdomain cleft of FtsZs (annotated “PC Pocket” in Figure 2-2A, p. 49), disrupting filament dynamics by locking the conformation of FtsZ in the open/filament state, stabilising filaments and reducing the critical concentration required

for polymerisation (Andreu et al., 2010). Taxis Pharmacaeuticals Inc. (NJ, USA) have stated an aim to enter Phase I clinical trials with their benzamide derivative TXA709 in 2018 (this does not appear to have happened). These molecules are highly effective *in vivo* inhibitors of *S. aureus* cell division, but they appear to be of very limited clinical use as in infection models spontaneous resistance rapidly arises (Kaul et al., 2013). The binding site does not seem to be under strong sequence constraints (PC binding site indicated in Figure 2-2, p.49), and indeed resistance to TXA709 emerges at a high frequency of $\sim 1 \times 10^{-8}$ cells in MRSA isolates via mutations in the pocket (Kaul et al., 2015). There is an extremely high degree of conservation across FtsZ GTP binding pockets (see alignment Figure 2-14C), suggesting that evolution of resistance via mutation of the pocket will be unlikely, at least in comparison. For the same reason I am cautiously optimistic that compound families which inhibit *S. aureus* FtsZ via the GTP pocket may offer opportunities for optimisation so as to target other bacterial species.

In the context of the work presented here in Section 2.1, I think there is also a strong possibility that a GTP competitive inhibitor would have an analogous effect to the benzamides, i.e. locking the conformation of FtsZ (as per cartoon Figure 2-14A). As shown in Figure 2-4, p. 54, there are a set of interactions between H7 residues and the guanine moiety which change upon switching, and these could be targeted during a medicinal chemistry campaign to try and lock the conformation from the other side, relative to the benzamides.

Having designed the assay in principle (Figure 2-14B) I began assembling the necessary components.

RESULTS AND DISCUSSION

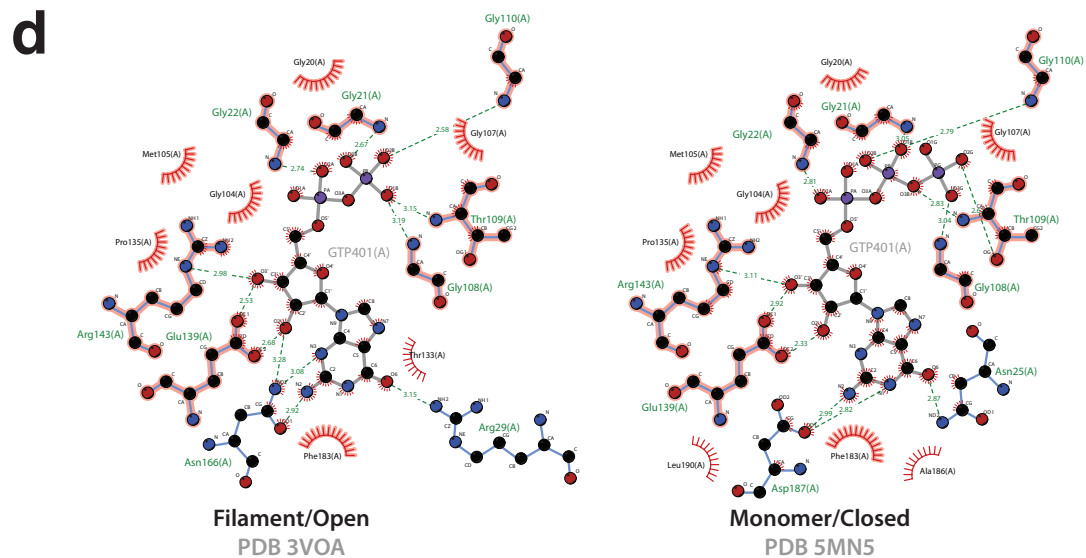
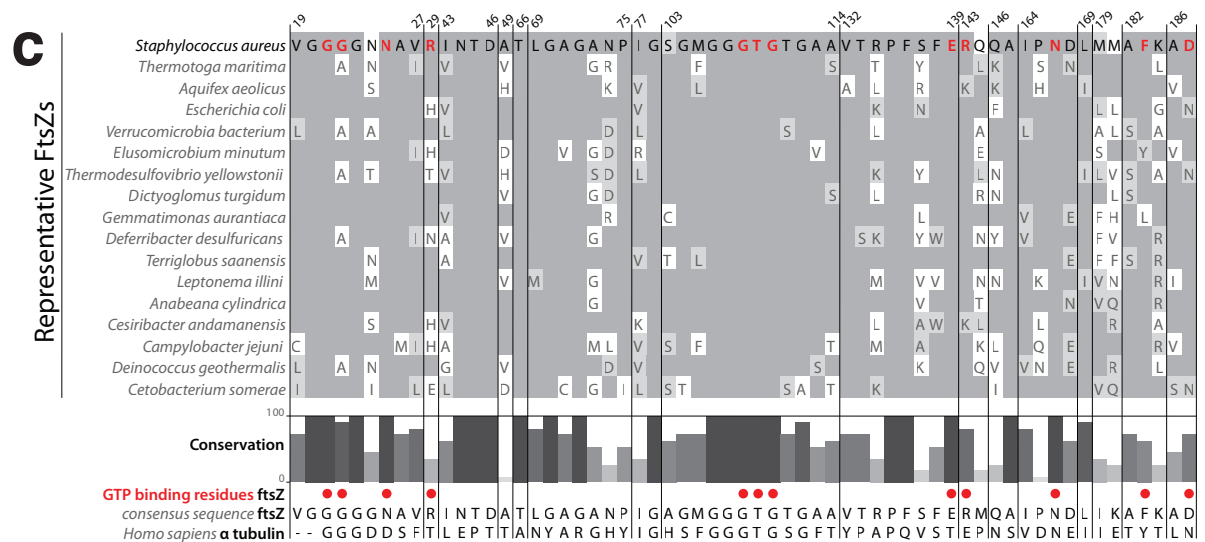
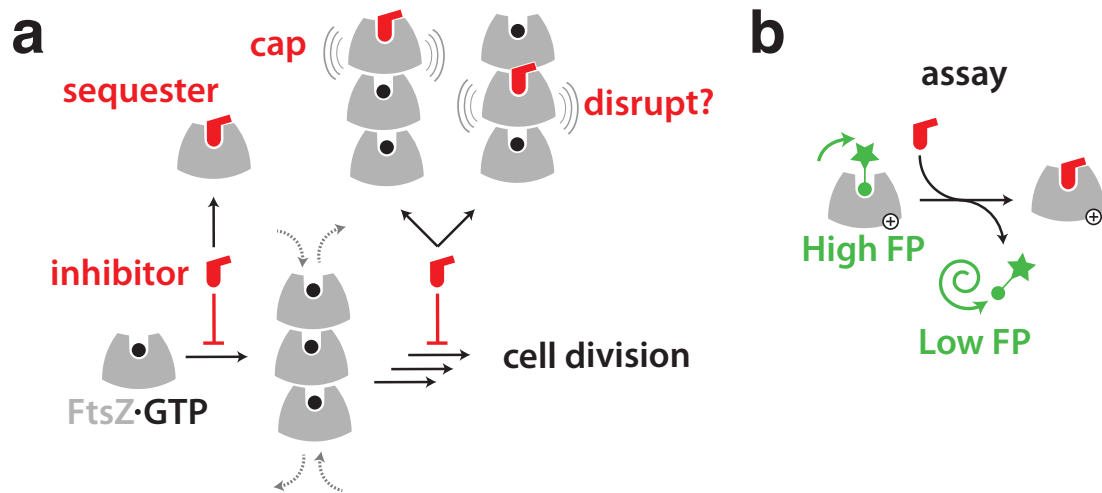
Figure 2-14 – Rationale for a GTP-competitive FtsZ inhibitor

A Models for how a GTP-competitive FtsZ inhibitor could work.

B Schematic of assay principle: non-polymerising (L272D) apoSaFtsZ⁺ is incubated with a fluorescently labelled GTP (green). The slow-tumbling complex yields high fluorescence polarisation (FP). When a competitive inhibitor (red) displaces fluorescent GTP, the small labelled nucleotide tumbles more rapidly and yields a low FP signal.

C Alignment of FtsZ and human alpha tubulin sequences showing only residues which align with residues close to GTP in *S. aureus* FtsZ (within 8Å of GTPγS in PDB 3WGN). FtsZ sequences are representative of all culturable bacterial lineages which have FtsZ. Residues with direct contacts to GTP (to GDP in PDB 3VOA, and/or to GSP in PDB 3WGN) are shown in red, and their positions are marked with dots below the conservation chart. Residue numbering at top refers to *S. aureus* sequence (Uniprot FTSZ_STAAU). Background colouring is by agreement (BLOSUM 62 score) with bacterial consensus sequence, dark grey means match to consensus residue, light grey means similar residue.

D Ligplot (Laskowski and Swindells, 2011) diagrams showing interactions between GTP/GDP and *S. aureus* FtsZ in both open and closed conformations. Residues which form contacts in both forms are highlighted in pink. Hydrogen bonds are shown in green, hydrophobic contacts are indicated with red “waves”. These plots provide context for the alignment panel above (C).



2.3.4 A Fluorescence Polarisation assay for GTP-competitive inhibitors of SaFtsZ

For the assay protein, I reused the SaFtsZ crystallography construct (12-316), as the protein is well behaved and crystallises readily, although I added a C-term His-tag. I also introduced a point mutation designed to entirely ablate polymerisation (L272D – L272 is located on the tip of the C-terminal sub-domain, within the longitudinal interface c.f. (Du et al., 2018)); ensuring that I was always working with a monomeric sample, even at the relatively high concentrations required for some assay validations. Crucially, it was necessary to purify the protein without nucleotide, in the “apo” state, to allow binding of the fluorescent probe. A pure apo-protein sample on SDS-PAGE is shown in Figure 2-15A. The sample was stable (as measured using the final assay) for several days at 4 °C, and more than 24 h at room temperature, and (un)freezes well.

Purification in the apo state required a very slow size-exclusion step (ion exchange over Q resin was also partially effective). The apo-protein was extremely unstable in the typical buffers used for size-exclusion/Q, a finding that has been replicated by Jose Manuel Andreu and Sonia Huecas (CSIC Madrid, personal communication). They identified that the apo protein is stabilised by crowding agents and can be worked with more easily in buffers with e.g. 20% glycerol. In these crowded solutions the affinity for GTP is greatly increased (or the off-rate is decreased) because size-exclusion in these cases is unable to separate the protein from the nucleotide. I found that adding DMSO to the assay buffer also increased the apparent affinity for GTP (data not shown), presumably via the same mechanism. Other buffer components were chosen for similarity to SaFtsZ polymerisation buffers. The final buffer used for all of the experiments presented here was 9 mM Tris-HCl, 45 mM KCl, 18% v/v glycerol, 10% v/v DMSO, at pH 7.5, with 0.01% casein.

Previously published fluorescence assays for GTP-replacing FtsZ inhibitors have all used 2'/3'-mant-GTP as the fluorescent probe (Artola et al., 2015; Ruiz-Avila et al., 2013). The affinity of FtsZs for mant-GTP is much lower than for GTP (in my hands, mant-GTP:SaFtsZ affinity $\sim 20 \text{ uM}^{-1}$, similar to published value (90 uM^{-1}) for mantGTP:FtsZ from *Methanocaldococcus jannaschii* (Schaffner-Barbero et al., 2010), versus $\sim 7 \text{ nM}^{-1}$ and 10 nM^{-1} for GTP in each case). This can be rationalised by examining the arrangement of residues around guanosine nucleotides in crystal structures of SaFtsZ: the 2' and 3' hydroxyls (where the Mant moiety is conjugated) are pointing into the pocket (Figure 2-15B). After trying several other attachment points, I chose to use a probe with the dye conjugated to the sp2-

hybridised C8 of the guanine, in place of the hydrogen, which points straight out of the pocket into the solvent (Figure 2-15B).

After trying several dyes attached at C8 which increased the affinity of FtsZ to the probe relative to GTP (presumably by interacting directly elsewhere on the surface of FtsZ), I settled on the dye ATTO-550, which did not have this problem. The probe, with dye and linker, was therefore 8-[(6-amino)hexyl]-amino-GTP-ATTO-550, see Figure 2-15C inset. ATTO-550 is a bright and photostable dye, structurally related to Rhodamine 6G and Rhodamine B (see, www.atto-tec.com). ATTO-550 has optimal properties for fluorescence polarisation in the regime required for this assay (appropriate fluorescence life-time and tumbling coefficient relative to FtsZ monomer). The long emission wavelength (576 nm) minimises the risk of assay interference by library compounds in a screening setting.

I measured a dissociation constant (K_d) of ~ 7 nM of ATTO-550-GTP for apo-FtsZ by titrating protein into a fixed concentration of probe (saturation binding curve in Figure 2-15C). The reverse titration was done initially also, to determine the reasonable range for probe concentration to ensure a good signal-to-noise ratio, I found that signal was hard to interpret below ~ 1 nM of probe. For competition assays I used a protein concentration of 25 nM ($\sim 70\%$ binding) and a probe concentration of 2 nM. Competition with unlabelled GTP indicated a inhibition constant (K_i , in this case equal to the dissociation constant) of ~ 8 nM (see Appendix: Principles of Fluorescence Polarisation, p. 152). Results of this experiment for three different apoSaFtsZ purifications are shown in Figure 2-15D. Thus, the affinity of apoSaFtsZ to the probe is essentially the same as that to GTP (both measurements are probably only accurate to within a fold change). The very high affinity for the probe, and the sufficient brightness of the dye, mean that the assay has a high dynamic range, allowing detection of inhibitors with a broad range of affinities for FtsZ (Xinyi Huang, 2003).

During assay development I also worked to miniaturise the assay to 384-well plate format. All data shown here was recorded in 384-well plates, with a final well volume of 20 μ L.

RESULTS AND DISCUSSION

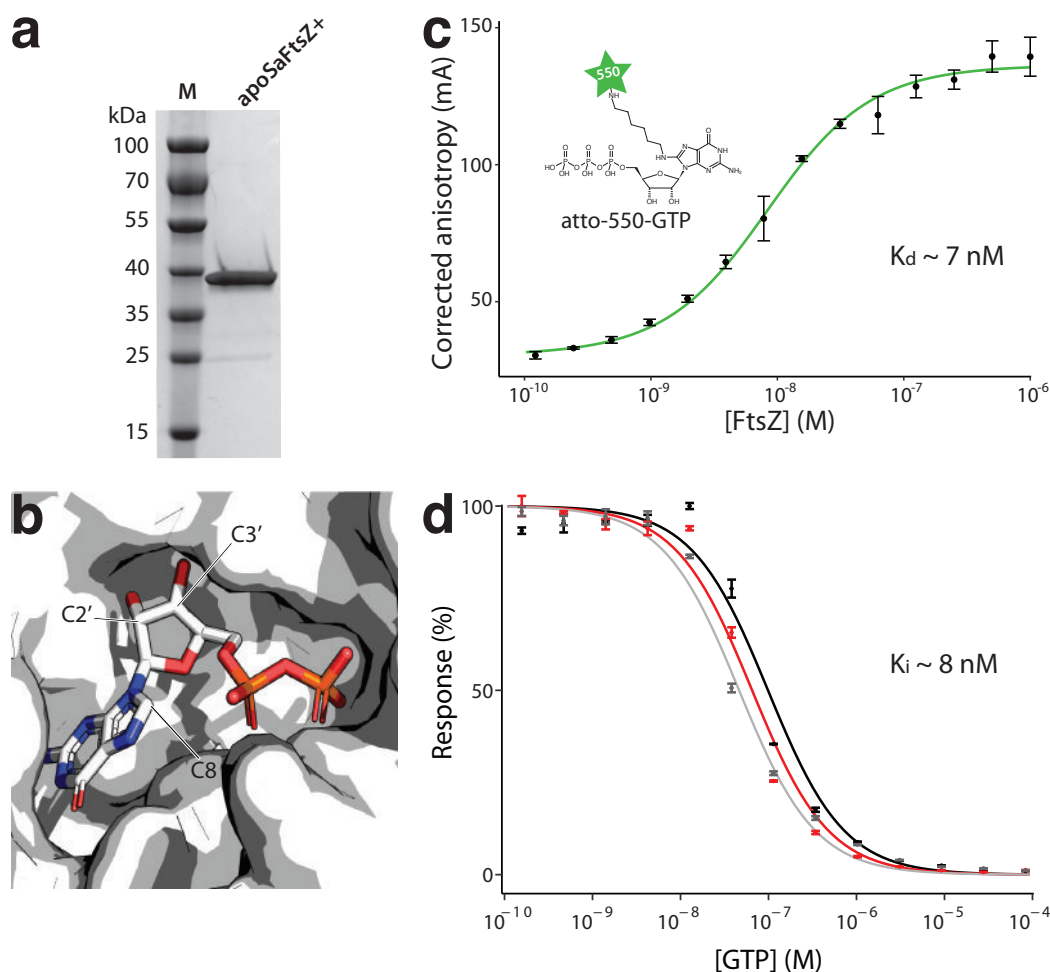


Figure 2-15 – An FP assay for GTP-competitive FtsZ binding molecules

A SDS-PAGE gel showing purified nucleotide free *S. aureus* FtsZ⁺ (12-316, L272D, C-6xHis) assay sample.

B Shape of GTP binding pocket on SaFtsZ. Surface representation of the region surrounding GDP in PDB id 3VOA is shown. The nucleotide is shown in stick representation, coloured by element, with the atoms mentioned in the text labelled.

C Saturation binding curve. ATTO-550-GTP binds apoSaFtsZ⁺ tightly with a K_d of ~ 7 nM, giving the assay an excellent expected dynamic range. Values plotted here are the mean of three with standard deviations shown as error bars. Values are adjusted for gain in fluorescence upon binding and ligand depletion as per (Schaffner-Barbero et al., 2010). Final buffer conditions for (C) and (D) are 9 mM Tris-HCl pH 7.5, 45 mM KCl, 18% v/v glycerol, 10% v/v DMSO, 0.01 % casein. Inset: Structure of probe, ATTO-550-GTP. ATTO-550 structure is not disclosed by ATTO-TEC GmbH but is related to the dyes Rhodamine 6G and Rhodamine B.

D XC50 assays for displacement of ATTO-550-GTP by unlabelled GTP. 3 independent replicates are shown (each using an independent protein preparation), giving pXC50 values within ± 0.3 log units. ApoSaFtsZ⁺ at 25 nM ($\sim 70\%$ response in main panel), ATTO-550-GTP at 2 nM. pXC50 values imply a K_i of ~ 8 nM (calculated as per (Nikolovska-Coleska et al., 2004)).

2.3.5 SaFtsZ interaction with GTP analogues

I used the FP assay to determine the affinity of apoSaFtsZ for several nucleotides (Figure 2-16).

GTP and GTP γ S, (guanosine 5'-O-[gamma-thio]triphosphate) had similar, high, affinities for SaFtsZ (low nM⁻¹). The GTP analogue GMPCPP had an affinity ~ 2 logs lower. Interestingly, I was never able to get SaFtsZ to polymerise in the presence of GTP γ S (whereas it polymerises readily with GMPCPP).

The gamma phosphate appears to have a major contribution to GTP:SaFtsZ affinity, as the affinity for GDP is 3 logs lower than GTP (contrary to the findings for FtsZ from the archaeon *Methanocaldococcus jannaschii*, where affinities for GTP and GDP were very similar (Schaffner-Barbero et al., 2010)). As expected, the affinity for ATP is much lower, in the micromolar range.

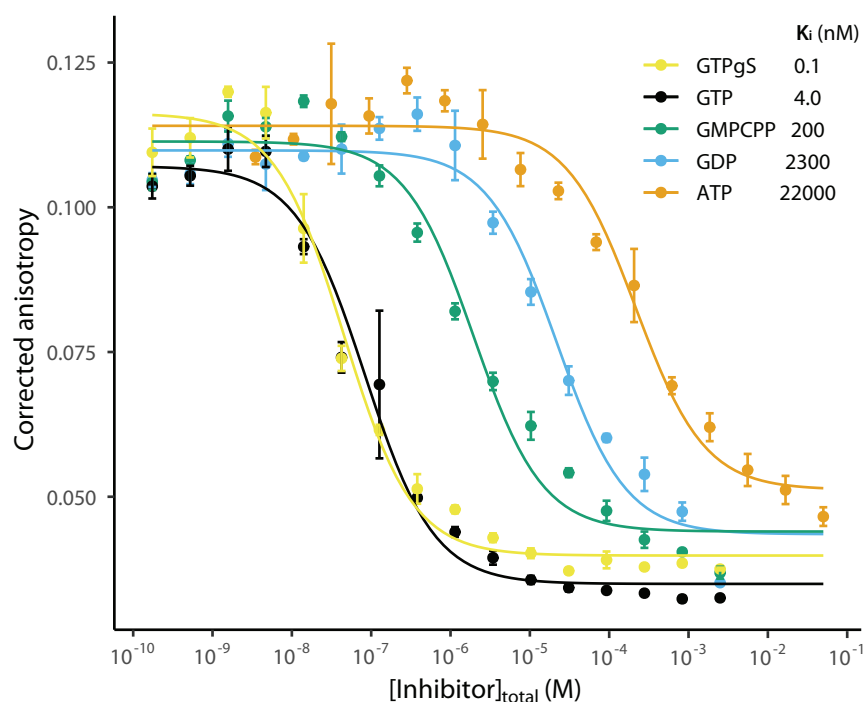


Figure 2-16 – Interaction of SaFtsZ with GTP analogues

Corrected fluorescence anisotropy is plotted against the concentrations of the five nucleotides in an assay mixture containing 25 nM apoSaFtsZ and 2 nM ATTO-550-GTP. Points plotted are the average of three measurements and error bars show one standard deviation. Curves and corresponding K_i values were fitted as described in the text.

2.3.6 Assay validation for high throughput screening

Before embarking on a high throughput screen it is necessary to conduct several validations of the proposed assay. Because in most screening campaigns the primary screen will only be carried out once per library molecule, a key question is the ability of an assay to cleanly and reproducibly separate positive and negative results. A popular metric to summarise this ability is the Z' (“Z-prime”) score, given by:

$$Z' = 1 - \frac{3 \cdot (\sigma_{neg} + \sigma_{pos})}{|\mu_{pos} - \mu_{neg}|}$$

Where σ and μ are the standard deviation and mean, respectively, of several measurements of positive (“pos”, i.e. 100% response) and negative (“neg”, i.e. background) controls for the assay. This score is calculated per plate, and ranges between 0 and 1; “good” scores are above 0.5 (if standard deviations for both controls are equal, a Z' of 0.5 means that controls are separated by 12 standard deviations). The data for one assay plate with wells containing only positive or negative controls is shown in Figure 2-17A, the Z' score for this plate was 0.82. I performed this test for 10 plates, obtaining a mean Z' of 0.82, ranging between 0.79 and 0.84. This is an excellent score, and a very good consistency of scores.

While moving towards carrying out high throughput screening with the assay I began using a lab automation system (Biomek, Beckman Coulter). This required significant troubleshooting, including the addition of a blocking agent to minimise interaction of the protein with plasticware. After trying several options I chose to use 0.01% casein, which is largely disordered and is thought to bind to fewer library compounds than BSA, another popular choice. Addition of casein to the assay buffer effectively reduced losses due to non-specific binding to polypropylene surfaces.

Using the robot I carried out a small pilot screen of ~4,000 compounds from the Dundee Drug Discovery Unit’s “Small Polar” collection. This was useful to highlight the practical issues of managing throughput, and led to some small optimisations of the assay protocol. The results are shown in Figure 2-17B. The usefulness of being able to simultaneously record fluorescence anisotropy (FA) and total fluorescence intensity (FI) is clear: in this small set of compounds all of the apparent hits, with reduced FA, were in fact compounds which lead to aggregation, visible by the increase in FI. The compounds causing the largest drops in FA were rescreened in XC50 experiments, which confirmed that they were all aggregating the protein.

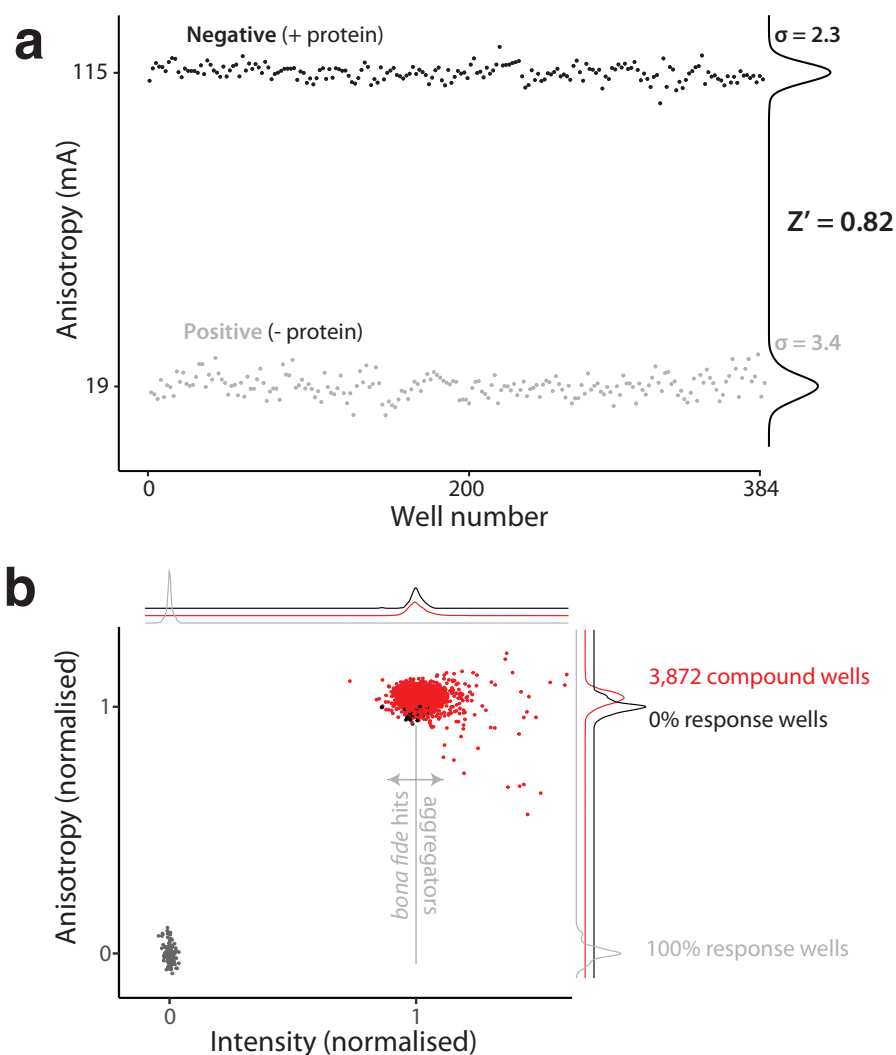


Figure 2-17 – Validation of FP assay for High Throughput Screening

A FP measurements were performed on wells with 2 nM ATTO-550-GTP with (negative, black dots) or without (positive, grey dots) 15 nM apoSaFtsZ+. Kernel density estimates are shown at right with standard deviations for the two control groups. Values on y-axis are mean values for each group. Z' score (0.82) is for plate shown. The average Z' across 10 plates was also 0.82, ranging from 0.79 - 0.88.

B Data from an 11 plate proof-of-principle screen are shown, with both per-well anisotropy and intensity plotted, normalised to on-plate control values. Fluorescence intensity (FI) provides useful QC data for FP assays as bona fide hits should not significantly change FI (if anything, they should reduce it), allowing false positives by FP measurement (causing e.g. aggregation) to be discarded early on.

2.3.7 Future work

After validating the final assay for high throughput screening I and my supervisor, Jan Löwe, applied to the Astra Zeneca (AZ) – MRC Centre for Lead Discovery (CLD). The CLD is a collaborative project in which AZ performs screens using assays developed by MRC scientists. Our application was successful and in late 2019 the AZ compound collection (c. 2 million molecules) will be screened against the assay described here.

2.4 Polymerisation-coupled conformational switching across the actin and tubulin superfamilies

This work is unpublished.

After investigating the polymerisation-coupled conformational switch in FtsZ and identifying the potential role of the switch in generating kinetic end-asymmetry required for robust treadmilling I became interested in how cytomotive filaments function, in general.

2.4.1 Looking for a mechanistic basis of cytomotivity

As discussed in the introduction, there are a very large number of protein filament systems scattered across the tree of life. Some of these protein filaments are used in cells to position other molecules in space and time – but not all of them. For instance, many enzymes appear to form filaments for purely regulatory reasons e.g. CTP synthase in organisms spanning *E. coli* to man (Lynch et al., 2017) (Figure 2-18A). I have, and have argued, the view that the term “(prokaryotic) cytoskeletons” can be usefully employed to encompass those protein filaments which are responsible for positioning other molecules inside cells (Wagstaff and Löwe, 2018), although the term has been used in other ways e.g. (Pilhofer and Jensen, 2013). In my preferred framework any given filament system forms a single “cytoskeleton”, and any given cell may contain several of these cytoskeletons (i.e. a casual description of the “eukaryotic cytoskeleton” is not consistent, it would be necessary to specify, for example, the “microtubule cytoskeleton”).

Within the large class of cytoskeletal filaments there are several different ways in which filaments are used to position other molecules. One important subclass is that of the “cytomotive” filaments (Figure 2-18A) (Löwe and Amos, 2009). Cytomotive filaments make use of the plentiful supply of free energy available in the cell by catalysing nucleotide hydrolysis in a way that is coupled to their (de)polymerisation cycle, and so are able to do the useful work of pushing and pulling of other molecules around via dynamic filament growth or shrinkage. This can be done in two modes: treadmilling, or dynamic instability (Löwe and Amos, 2009; Mogilner and Oster, 2003; Theriot, 2000). So far, we know of only two families of proteins which can form filaments that act as one-dimensional motors in this way: the actins and tubulins. There are other systems which come close to being cytomotive, inasmuch as they couple polymerisation and nucleotide hydrolysis in order to

RESULTS AND DISCUSSION

manipulate other molecules, but these systems have the coupled functionalities spread across several proteins (at least one of which does not polymerise). Two prominent examples of this mode of decoupled activities are the ESCRT-III like systems, in which polymerised ESCRT-III homologues are disassembled by Vps4 ATPase homologue (reviewed (Schöneberg et al., 2017)); and MinCD filaments whose intrinsic ATPase activity is activated by MinE (reviewed (Szwedziak and Ghosal, 2017)); details in both cases remain unclear).

Given the obvious usefulness of cytomotive filaments, as evidenced by their ubiquity in essential cellular processes (see “Perspective on prokaryotic cytoskeletons”, Section 1.6, p. 37), it is tempting to ask the question: why is it (only) the actin and tubulin superfamilies that make these dynamic structures? Asking “why” in biology should be a disguise for a smarter question, of course. In this case I think the corresponding question is: which evolutionary regime is life in with respect to cytomotive filaments. The observed biology can be explained in probably three ways:

1. Cytomotive filaments are easy to evolve
 - a. but two families are enough, or,
 - b. but we have not looked hard enough yet
2. Cytomotive filaments are hard to evolve: actin and tubulin are special

Some evidence that (1) may well be the case comes from the fact that the most salient features of the cytomotive filaments, namely: filament formation and nucleotide hydrolysis, both appear to be easily accessible in evolutionary space, and not obviously counter-selected (e.g. CTP synthase (Ingerson-Mahar et al., 2010)). Of course, these features must be integrated so that they are coupled, but again it would seem that this could be straightforward if done in the same way as tubulin, for example, where the presence/absence of the γ -phosphate within the filament interface simply regulates interface strength and therefore the propensity to depolymerise. Filament formation in particular is so easy to evolve that it has been designed, by David Baker’s group and others (Garcia-Seisdedos et al., 2017; Shen et al., 2018).

Evidence that (1a) may be unlikely includes the observation that the actin and tubulin systems have been repurposed so many times, clearly implying that there can be a selective advantage in getting a new cytomotive filament system. The proposition that we simply have not found other extant cytomotive filament systems (1b) will remain a possibility for a

long time, as we know from metagenomic sequencing efforts that we have characterised very little of cell-biological diversity (for example, both the Candidate Phyla Radiation in bacteria and the DPANN clade in archaea remain essentially unstudied despite their constituting huge chunks of the diversity within their respective domains (Hug et al., 2016)). On the other hand, it does seem unlikely that there is an unknown, widespread, cytomotive filament system with important roles in cell biology in the organisms we understand reasonably well.

The tempting explanation of (2) (even more tempting if you work on these proteins, of course), implies that, in fact, the two features of cytomotive filament-forming proteins mentioned above are not sufficient for cytomotility, or that their integration to produce cytomotility is not straightforward. I think that both of those things are possible. The fact that we cannot easily rule (2) out clearly suggests that we do not understand cytomotility well – and, whether or not it is “special”, we should invest energy in doing so.

Obviously, many people have worked on trying to understand the molecular bases of the remarkable properties of both eukaryotic actin filaments and microtubules. However, both eukaryotic actins and tubulins are extremely homogenous, in terms of sequence, structure, and function (even so, I think it would be a stretch to describe either system as fully understood). Both filaments are highly optimised for their roles in eukaryotic cells. As a result, while working on these proteins it is unavoidably hard to distinguish what is an important feature of eukaryotic actin/tubulin, and what is an important feature of a cytomotive actin/tubulin filament *per se*. Luckily, a much smaller group of people, many of them my predecessors or contemporaries in Jan Löwe’s group at the MRC LMB, have invested serious efforts into understanding the structure and function of actin and tubulin superfamily members from outside the narrow slice of biological diversity within eukaryotes.

The expanding zoo of well characterised prokaryotic actin and tubulin superfamily filaments from across bacterial and archaeal phyla, discussed in the Introduction, offers an opportunity to try and identify the general mechanistic principles by which these proteins function. My usage of the word “superfamily” in the remainder of this section is illustrated in Figure 2-18B. In words: a set of related sequences, and structures, with potentially diverse functions united by a common mechanistic underpinning. This is a slight narrowing of the definition of Murzin et al., who wrote “families, whose proteins have low sequence identities but whose structures and, in many cases, functional features suggest that a

RESULTS AND DISCUSSION

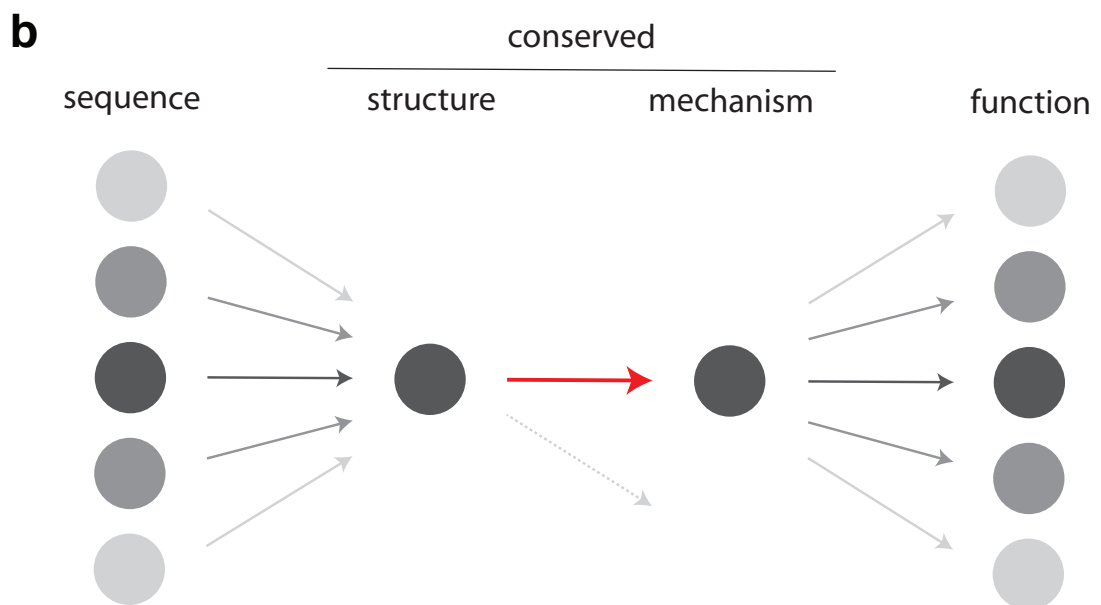
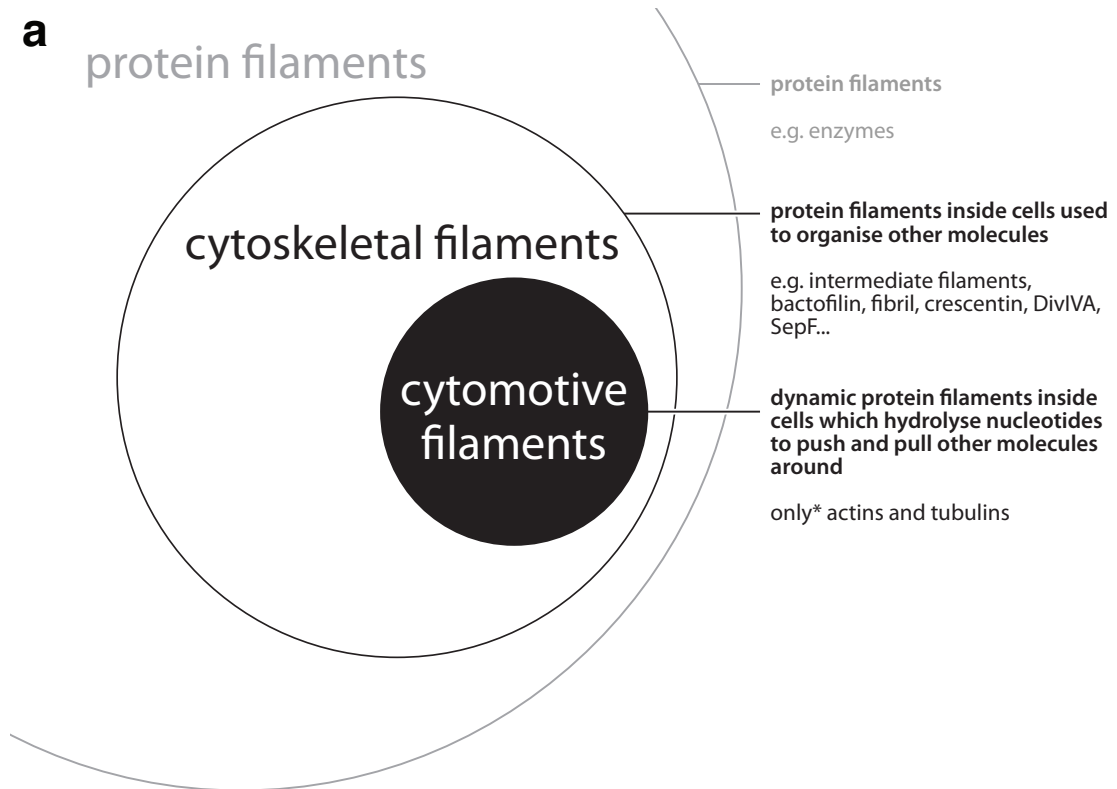
common evolutionary origin is probable, are placed together in superfamilies” (Murzin et al., 1995).

In order to try and better understand the structure → mechanism principles (the red arrow in Figure 2-18B) of the actin and tubulin superfamilies, in both of which the shared mechanism is the formation of cytomotive filaments, I analysed the available structural data in each case.

Figure 2-18 – Investigating the conserved basis of cytomotivity

A Schematic showing the relationship between different classes of protein filaments.

B Schematic illustrating the concept of a protein superfamily, as the term is used here. Members of a superfamily will have many different functions, encoded within their diverse sequences, but they will share a structure and also a mechanism, as determined by the structure. The structure and mechanism are what is conserved within the superfamily. The actin and tubulin superfamilies share a common mechanism – they form cytomotive filaments. The dashed grey arrow goes to the structurally related proteins which use a different mechanism (i.e. they would be superfamily members in the Murzin et al. framework).



2.4.2 Looking at superfamily filaments

An obvious place to look for clues as to a conserved basis for the remarkable functional properties of the cytomotive filament-forming proteins is in the structures of the filaments themselves. Within oligomer-forming superfamilies it is indeed common for quaternary structure to be conserved (Levy et al., 2008). However, in the case of both actins and tubulins this is only partially the case.

Often, interactions between subunits within protein filaments are considered in terms of being either “longitudinal” or “lateral”, reflecting the fact that a filament structure can frequently be understood as being formed of protofilaments: one-subunit thick filaments in which subunits interact via longitudinal interfaces, and which associate with one another via lateral interfaces. This is typically a useful model, but it is important to remember that there are other ways to understand the helical symmetries of these objects, which are sometimes more relevant to biology – rigorously discussed in (He and Scheres, 2017).

The ways in which protofilaments come together in the actin and tubulin superfamilies are strikingly diverse (see Figure 1-2B and Figure 1-3B, p. 18 and p. 24). Within the tubulins, known filament architectures range from single FtsZ filaments to ~13 stranded microtubules, via 4-stranded mini-microtubules, and viral tubulin filaments with 3- (PhuZ) and 4- (TubZ) protofilaments; with a concomitant variation in lateral contacts (or lack thereof). Within actins there is a propensity for double filaments (possibly a consequence of the likely domain duplication in the evolutionary history of actin cf. (Bork et al., 1992; Levy et al., 2008)), but the relative arrangement of the paired-protofilaments varies greatly, as illustrated by the topology cartoons at the bottom of Figure 1-3B, p. 24, as do the lateral contacts which facilitate them.

Longitudinal filament contacts in both actin and tubulin superfamilies are similar across the subfamilies, with approximately equivalent subunit surfaces coming together, but there are significant variations in both cases. This is very clearly so in the actin superfamily where certain subdomains involved in the longitudinal interface have been replaced or lost entirely (in the cases of Alfa, and FtsA, respectively (Szewczak-Harris and Löwe, 2018; Szwedziak et al., 2012)).

In summary, it is hard to pull together an explanation for the shared cytomotive properties of actin and tubulin filaments from the conserved properties of the filaments themselves within each superfamily.

2.4.3 Looking at superfamily subunits

Beyond the filaments formed by actin and tubulin superfamily members, especially in the context of having worked on the conformational switch in FtsZ, an obvious place to look for a conserved basis of cytomotivity is within the highly conserved subunits themselves, and the conformational dynamics thereof. Indeed, many of the studies on individual actin and tubulin superfamily members have focussed on conformational changes, but surprisingly none have systematically tried to relate these together, in either case. I have attempted to do this.

The approach I have taken to synthesise conformational information from across superfamilies is illustrated in Figure 2-19A, and the steps briefly discussed below:

- (i) In order to understand how or whether conformational dynamics are conserved across a set of diverse sequences it is necessary to establish a common frame of reference for the sequences: an alignment. Structure-based approaches to aligning sequences are considered the gold-standard, as they are able to recover relationships between residues that cannot be found using sequences alone (these approaches are used as approximations of ground truth to benchmark sequence alignment algorithms). There are many structure-based alignment algorithms to choose from, with the key distinction being between those that allow for structural flexibility and those that perform only a global superposition to guide sequence alignment. I have used both varieties as discussed below, and typically within an overall alignment algorithm which can incorporate both structure and sequence-derived constraints (e.g. PROMALS3D and T-Coffee (Notredame et al., 2000; Pei et al., 2008)).
- (ii) Assuming that all of the superfamily members work the same way, positions with gaps are residues that do not contribute to the core mechanism and can be removed from the alignment. This also permits further analysis by e.g. PCA, which requires a full matrix. The remaining, ungapped residues, form the structurally conserved core of the superfamily fold.
- (iii) To compare structures a different frame of reference is required: a defined invariant region (distinct from a sequence based structural alignment, because it requires a sequence alignment to mark equivalent residues). I used the approach of Gerstein et al., implemented within the `bio3d` package for the statistical programming language R. (Gerstein and Altman, 1995; Gerstein and

RESULTS AND DISCUSSION

Chothia, 1991; Grant et al., 2006). This approach performs iterative rounds of global alignment, removing the worst aligned residues as determined by the volume of an ellipsoid with dimensions corresponding to the lengths of the 3 principal eigenvectors of the aligned coordinates for that residue, until all of the volumes fall below a threshold.

- (iv) After superposition on the invariant region, sequence-aligned residues can be compared with one another on the basis of their position in space by various methods including Principal Component Analysis (PCA). The basis of PCA is illustrated in Figure 2-19D. PCA in particular is a powerful technique for reducing dimensionality of data and allowing the largest sources of variance to be effectively visualised, and has been successfully applied to the analysis of protein structures many times (Grant et al., 2006).

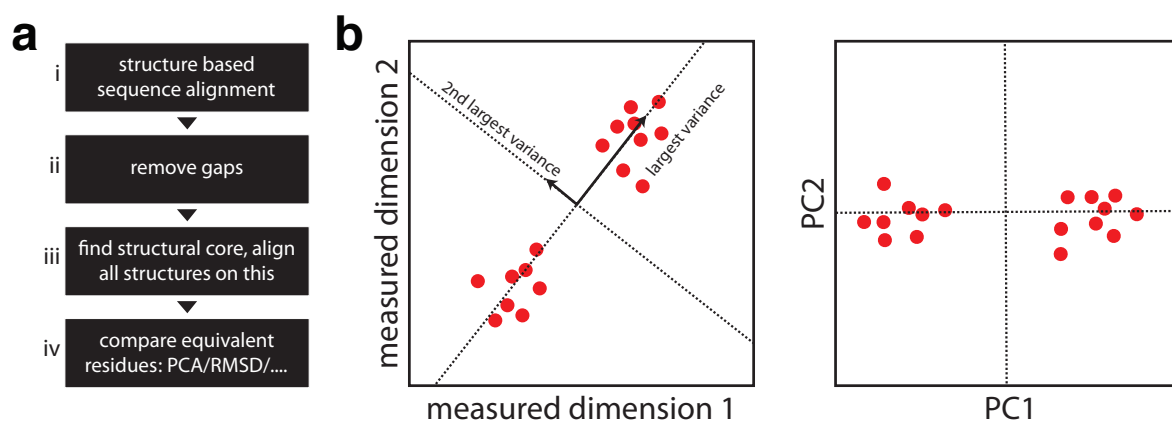


Figure 2-19 – Approach for analysing conservation of conformational dynamics

A Workflow used for analysing conservation of conformational dynamics within a superfamily.

B Schematic illustration of Principal Component Analysis (PCA) in a 2D space. Individual observations are made of two variables. PCA determines the linear combination of those variables which describes the direction of maximum variance (PC1), and the subsequent vector orthogonal to it which describes the second largest variance (PC2). These vectors are also eigenvectors of the data matrix.

2.4.4 Tubulin superfamily members have a conserved polymerisation-coupled conformational switch

In order to investigate conformational changes in the tubulin superfamily I assembled a dataset of protein structures from the Protein Data Bank (PDB). I decided to focus on the tubulin superfamily members for which we have a good understanding of subunit structures both within and outside of the filaments formed. This decision limited the analysis to FtsZs, alpha tubulins, and beta tubulins.

In total, I analysed 1007 chains, from a total of 266 deposited structures. I selected a non-redundant set of chains (one from each conformation cluster, RMSD < 0.5 Å, within each deposition), maximising resolution and minimising the number of gaps in the representative structures. I removed all structures worse than 5 Å, and all structures without a bound nucleotide/nucleotide analogue. The final dataset used here contained 551 chains, and can be found in Table 4, p.164.

After a structure-based sequence alignment of the selected structure sequences, 258 un-gapped positions were identified: the structurally conserved core of the tubulin fold (for reference, these residues covered 84% of the SaFtsZ globular domain (aa 12-316)). The invariant region was defined as the set of Cα with an eigenvector ellipsoid volume < 1.5 Å, this was 43 residues, all located in the beta sheet at the centre of the N-terminal domain. The core and invariant region are shown in Appendix Figure 4-6A, p. 148.

PCA was carried out per subfamily on the matrix of Cα Cartesian coordinates for the structurally conserved core residues, after alignment on the invariant region. The results of this procedure are shown in Figure 2-20. As discussed, PCA determines the linear combination of measured dimensions which maximises the amount of variance in the input data that can be explained by moving along that vector; Figure 2-20A shows the proportion of the variance that is explained by each of the first five principle components of each subfamily analysis. Strikingly, and this is generally true, a very large proportion of the variance within a set of homologous protein structures can be explained by very few principle components. For instance, 90% of variance in the entire ensemble of FtsZ Cα positions is explained by just three principle components. PCA is very good at capturing ~rigid body motions, which constitute a significant fraction of protein dynamics. Overall this means that the high dimensional space of structures (e.g. the space which describes the Cαs of the tubulin structurally conserved core has 774 dimensions, the number of residues

(258) multiplied by the number of spatial dimensions (3)) can be meaningfully reduced to a smaller number of richly descriptive dimensions permitting further analysis.

A visualisation of PC1 for each subfamily is depicted in Figure 2-20B. Arrows (red) are drawn from mean C α positions (black) for the subfamily, the length/direction of the arrows are defined by the loadings for the x,y,z components at that position (as vectors with origin at the mean C α position). The position of the points in the positive direction along the x-axis in the PC subspace plot in Figure 2-20C (see below) corresponds to adding increasing amounts of the red arrows to the mean positions of the C α s. All three subfamily PC1s look reasonably similar with the variance in the structures being distributed along a vector that involved a coordinated, and approximately coaxial, movement of the C-terminal subdomain and helix 7. See below and Figure 2-21 for discussion of how similar these PCs are, but first it is worth asking whether there is a functional correlate for these PC1s, which explain so much of the variance within each subfamily.

In Figure 2-20C the results of the PCAs are plotted in their respective PC1-PC2 subspaces. Each point is one structure, coloured by polymerisation state. Rather dramatically, it is immediately obvious that PC1 in all three cases is a discrete classifier for polymerised versus monomeric conformations; i.e. a very large proportion of the variation amongst the structures linearly describes a conformational change upon polymerisation. In all three cases the change corresponds to moving along the red arrows in Figure 2-20B in a filament-to-monomer conformational change. In Appendix Figure 4-7 p. 159 there is a version of Figure 2-20C with the points coloured instead by the hydrolysis state of the nucleotide bound – showing that there is no clear relationship between hydrolysis state and position in the PC1-PC2 subspace. In essence this pair of observations is a re-affirmation of the (finally!) prevailing view of microtubule formation: the “lattice model”, as opposed to the “allosteric model”. The lattice model is usually described in terms of the transition from kinked heterodimers in solution, to straight ones inside microtubules (reviewed (Brouhard and Rice, 2018)). Less often discussed (although certainly noted!) is the fact that a significant component of the overall conformation change of the heterodimer arises from the relative movement of the subdomains within each of the two subunits (not just movement of the monomers relative to one another). To put this consensus differently, both alpha and beta tubulins undergo a polymerisation associated conformational change – just like FtsZs.

RESULTS AND DISCUSSION

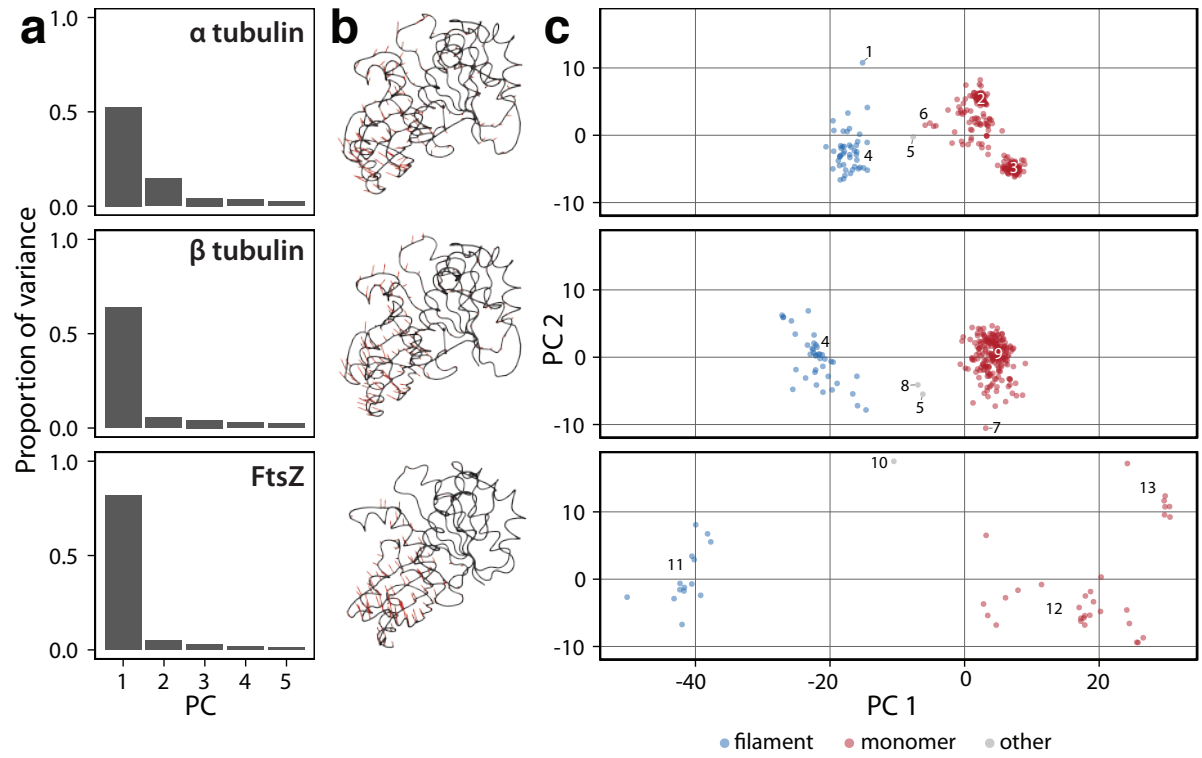
Figure 2-20 – PCA of tubulin superfamily structures

A Proportion of variance explained by first 5 principal components.

B PC1 component vectors (red) plotted on mean structure (black) for each subfamily.

C Results of PCA plotted in PC1-PC2 subspace. Individual structures are coloured as to whether the conformation is found in filaments or unpolymerised monomers. Numbered structures, and groups of structures are as follows:

1. 3J8X:A 5Å structure of kinesin bound to MT
2. Bottom alpha tubulins in stathmin-stabilised-like tetramers
3. Middle alpha tubulins in stathmin-stabilised-like tetramers
4. CryoEM MT structures
5. 5NJH:A/B Triazolopyrimidine bound tetramer
6. RB3 stathmin like tetramers
7. 5LOV:B DZ2384:tubulin complex
8. Low resolution (incorrect) structure 3J8Y
9. Beta tubulins in stathmin-stabilised-like tetramers
10. 5H5I:A SaFtsZ R29A mutant
11. SaFtsZ filament crystals
12. Various bacterial FtsZs
13. *Methanocaldococcus jannaschii* FtsZs



RESULTS AND DISCUSSION

An obvious question is whether the change in each case is the “same” one. There are several approaches for assessing this, two are shown in Figure 2-21. Because the per-subfamily PCAs were carried out on the structurally conserved core residues, and all the structures were aligned on the invariant region, it is possible to project the coordinates from one subfamily’s structures into the PC space of another. The result of projecting beta tubulin and FtsZ structures into the alpha tubulin PC1-PC2 subspace is shown in Figure 2-21A and B. The alpha tubulin PC1 effectively separates the beta tubulin and FtsZ polymerised/monomeric states. The FtsZ structures have a different midpoint through which the conformational change goes, but the vector which separates the two states is similar in all cases. We can also ask what proportion of the variance in the projected structures is explained by the PC subspace, for example 21% of variance amongst FtsZ structures is described by the alpha tubulin PC1.

A second way to assess the similarity of the vectors is demonstrated in Figure 2-21A, which shows the overlap (dot product) of the per-family PC1s and 2s (overlap of one means that vectors are parallel, overlap of zero that they are orthogonal – such as the beta-beta overlaps in the top right quadrant). The pairwise overlaps between all the PC1s are high, indicating that these vectors, which explain the bulk of variance amongst each subfamily’s structures, are similar. As we know that each PC1 describes the conformational change upon polymerisation within each subfamily, we can begin to conclude that not only do all of the families have such a change, but that it is the same change in each case. Perhaps more surprisingly, there is also fairly good overlap between the PC2s in each case, which typically describe differences between species (or in the case of alpha tubulin, the difference between being at the top of, or in the middle of, a stathmin-stabilised dimer of heterodimers). In contrast, there is very poor overlap of PC1-PC2 pairs taken from any two subfamilies: supporting the idea that the PC1s are similar, because they are orthogonal to not only their own PC2 (which they must be, by definition), but also those of the other subfamilies. It is worth noting that the similarity of the conformational changes has been noted before, but not systematically, e.g. (Buey et al., 2006), and has so far not been widely acknowledged.

So, there is a polymerisation-associated conformational change within each subfamily, and it appears to be the same change. An important question is whether the change reflects a switch. Switches are pairs of low energy states separated by high energy transition pathways. The low probability of moving from one state to another is exploited in biological systems to generate non-linear behaviours. In Section 2.1 I argued that FtsZ switches

conformation upon polymerising, drawing on the evidence that we observe just two, discreet, states (in that section using the pairwise RMSDs) – and no intermediates, suggesting that those intermediates are unstable. The discrete nature of FtsZ conformational states is recapitulated in the PCA analysis. The argument can be extended to the alpha and beta tubulins. Again, in all cases, the monomeric and polymerised conformations are separated into discrete clusters in the PC space, with no intermediates.

The argument that the conformational changes are switches is based on the assumption that the conformational space is sufficiently sampled by the available structures. This is impossible to know for sure, although the extensive structural biology efforts to understand both eukaryotic tubulin and FtsZ should give us hope. There is additional evidence in both cases, however:

Another research group has recently shown via Hydrogen-Deuterium Exchange Mass Spectrometry (HDX-MS) that FtsZ from *Caulobacter crescentus* exists in solution in two discrete conformations corresponding to the crystal structures (Laura Corrales Guerrero and Martin Thanbichler, personal communication). As discussed in Section 2.1.5, p. 52, and illustrated in Figure 2-4B, there is an arginine residue (R29 in SaFtsZ) which rearranges during the polymerisation associated conformational change from packing against helix 7 from the “outside” in the monomer to packing against it from the “inside” in the filament, a journey which appears to require transition through unlikely looking intermediates, and is a candidate for a switch residue, ensuring the bistability of the transition. A paper investigating the SaFtsZ conformational switch, Fujita et al., 2017, (published simultaneously with our paper, Wagstaff et al. 2017, arising from the work outlined in Section 2.1) went further and showed that an R29A mutant in fact did crystallise in an intermediate conformation (PDB ID 5H5I:A) – the grey dot numbered ‘10’ in Figure 2-20A .

Examining existing evidence for a bistable switch in tubulin subunits is complicated by the previously discussed fact that models for tubulin typically emphasise the importance of conformational changes across the entire heterodimer, which are dominated by the inter-alpha-beta angle. Interestingly, although many tubulin assembly models have posited the importance of a kinked-straight assembly switch (as measured by inter alpha beta angle), there are at least two molecular dynamics papers which suggest that such a barrier may not exist (i.e. that flexibility across the heterodimer hinge is continuous) (Gebremichael et al., 2008; Igaev and Grubmüller, 2018). However, there are clues in both that a within-subunit conformational switch may exist. Some more convincing evidence comes from a recent

RESULTS AND DISCUSSION

study of a beta tubulin mutation on helix 7 (*S. cerevisiae* T238A), which modulates MT dynamics in a way consistent with a conformational switch within beta tubulin (Geyer et al., 2015). Further work is required, to establish the conformational (energy) landscape of eukaryotic tubulins.

The functional consequences of a having a polymerisation associated conformational switch are discussed below, after the conformational dynamics of actins have been examined.

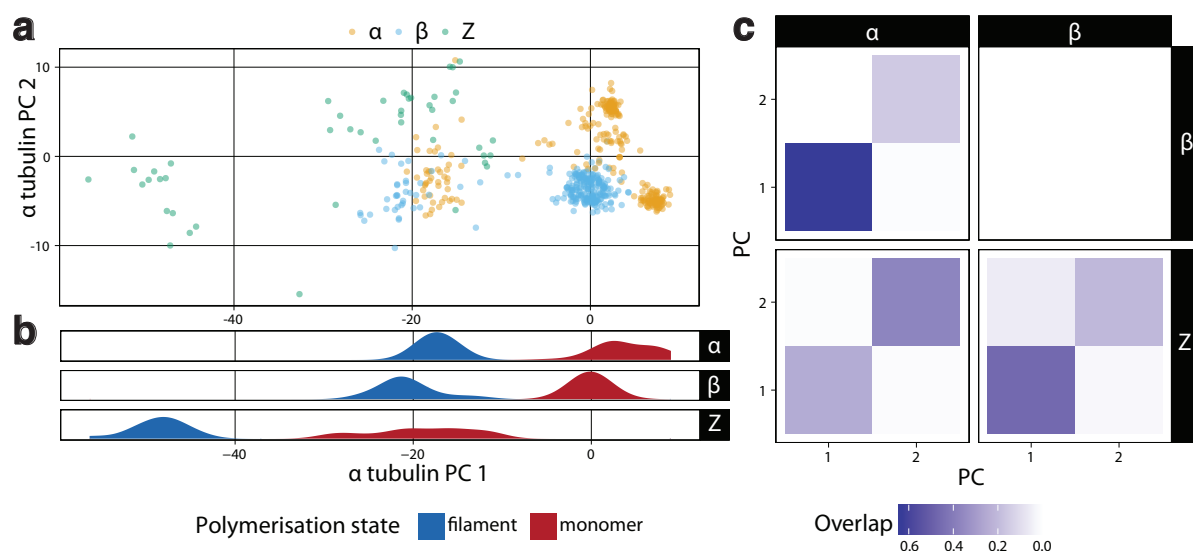


Figure 2-21 – The conformational switches within tubulin subfamilies are similar

A Projection of all structures into the alpha tubulin PC1-PC2 subspace.

B Kernel density estimation showing distribution of all structures, coloured by polymerisation state, projected along alpha tubulin PC1.

C Overlap between PCs 1 and 2 of the three subfamilies.

RESULTS AND DISCUSSION

2.4.5 Cytomotive actin superfamily members also have a conserved conformational switch

I analysed the filament forming actin superfamily members in a similar way to the tubulins. Again, I selected the subfamilies with well-characterised structures corresponding to both polymerised and monomeric states, limiting the analysis to: eukaryotic actin, crenactin, MamK, ParM from the *E. coli* R1 plasmid, and MreB.

I initially downloaded 888 chains, from a total of 251 deposited structures. I selected a non-redundant set of chains (one from each conformation cluster, RMSD < 0.5 Å, within each deposition), maximising resolution and minimising the number of gaps for the representative structures. I removed all structures worse than 5 Å, and all structures without a bound nucleotide/nucleotide analogue. The final dataset used here contained 209 chains, listed in Table 5, p.172.

After a structure-based sequence alignment of the selected chain sequences, 177 un-gapped positions were identified: the structurally conserved core of the actin fold. This core encompasses eukaryotic subdomains IA, IIA and some of IIB, but does not include IB. The core corresponds well to the most minimalistic actin identified so far: AlfA from the *Bacillus* plasmid pLS32 (Szewczak-Harris and Löwe, 2018). The invariant region was then defined as the set of Cα with an eigenvector ellipsoid volume < 1 Å, this was 26 residues, mostly located in the subdomain IIA beta sheet beneath the nucleotide. The core and invariant region are shown in Appendix Figure 4-6B.

PCA was carried out per subfamily on the Cα Cartesian coordinates for the structurally conserved core residues after alignment on the invariant region. The results of this are shown in Figure 2-22. As for the tubulins, in all cases the first few PCs describe the total conformational variability well. Visualisation of PCs on the mean structures for each subfamily illustrates that the major structural transitions occur in subdomain IIA, as it moves in or out relative to the rest of the molecule, and in some cases also rotating around an axis approximately passing through the centres of subdomains IA and IIA. In MreB and ParM there are also some larger PC1 loadings at residues on the IIA/B half.

As for the tubulins, when the actin structures are plotted in their respective PC1-PC2 subspaces and coloured by their polymerisation state (Figure 2-22C) it is clear that PC1 cleanly separates monomeric from polymerised conformations – with one exception: MreB. The MreB PC1 describes the relatively small conformational differences between the

monomeric and single filament states (negative PC₁ values) and the double filament state (positive PC₁ values). As for the tubulins, there is no obvious relationship between PC₁-PC₂ subspace position and the hydrolysis state of the bound nucleotide (Appendix Figure 4-8). The conformational change upon polymerisation in eukaryotic actin is well characterised as the “propeller twist” of subdomains IA/B versus IIA/B (reviewed (Dominguez and Holmes, 2011)). One interesting point is the structure labelled ‘4’, this is a cryoEM structure of an actin filament bound with the severing protein cofilin, as can be seen this structure lies in the monomeric portion of PC₁ – recapitulating the depositing authors’ conclusions that cofilin binding forces the actin subunit into a conformation less compatible with polymerisation (Tanaka et al., 2018).

Within the framework of the PCA we can ask whether the changes upon polymerisation in actin are similar across the subfamilies using the same analyses as for tubulins (Figure 2-23). In Figure 2-23A all of the structures are projected into the eukaryotic actin PC₁-PC₂ subspace. Remarkably the actin PC₁ cleanly separates monomeric and polymeric structures for all of the subfamilies, with the exception of MreB, for which all of the structures are placed on the polymeric side of the plot. Figure 2-23B shows the overlap of the first three PCs for all of the subfamilies, again the pairwise PC₁ overlaps are generally very high. PC₂ and PC₃ (which mostly seem to encode species differences) are a little scrambled but in many cases overlap well pairwise. The exception, again, is MreB whose PCs show limited overlap with the other subfamilies.

So, like the tubulins, the actins subfamilies all undergo a polymerisation associated conformational change, and it appears to be the same change – with the caveat that none of this seems to be true for MreB. And, again, like the tubulins, the conformational change has the appearance of a switch, exhibiting two apparently discrete states.

Very recently, a group produced a structural survey of eukaryotic actin structures, similar to that presented here (and with similar conclusions), but also molecular dynamics evidence that the polymerised and monomeric subunit conformational ensembles are indeed separated by high-energy transition pathways (Oda et al., 2019). Remarkably, this appears to be the first time that anyone has proposed the existence of an assembly switch in actin polymerisation.

RESULTS AND DISCUSSION

Figure 2-22 – PCA of actin superfamily structures

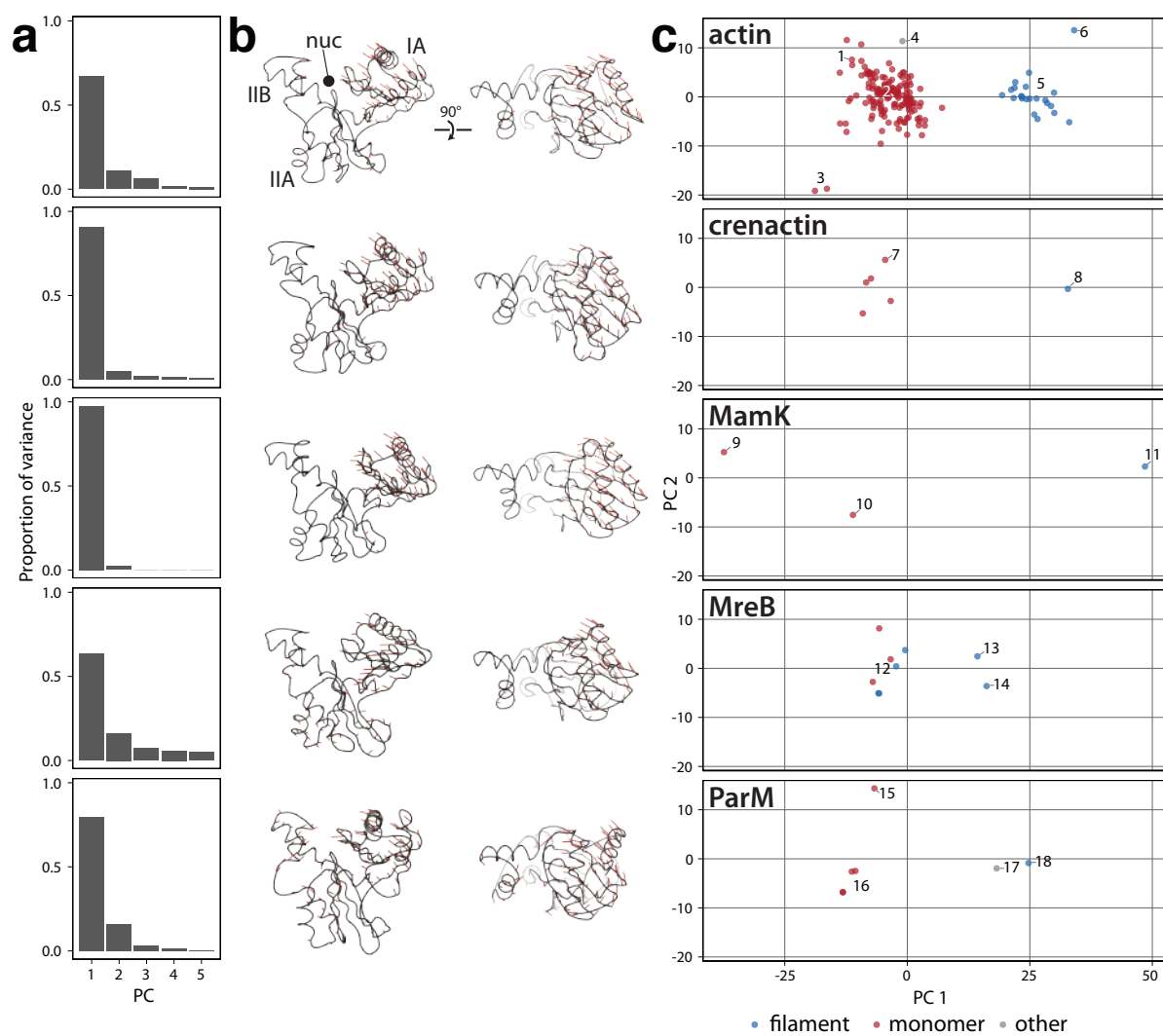
A Proportion of variance explained by first 5 principal components.

B PC1 component vectors (red) plotted on mean structure (black) for each subfamily.

C Results of PCA plotted in PC1-PC2 subspace. Individual structures are coloured as to whether the conformation is found in filaments or unpolymerised monomers.

Numbered structures and groups of structures are as follows:

1. 2HMP:A uncomplexed actin monomer (cleaved between residues 42/43)
2. Mostly complexed actins (e.g. with gelsolin)
3. Two structures with very wide open clefts c.f. MamK monomer #9
4. 5YU8 cryoEM structure of a cofilin (actin disassembler) decorated actin filament
5. cryoEM structures of actin (co)-filaments
6. 2ZWH first F-actin model derived from fibre diffraction
7. 5LY3:A crenactin in complex with arcadin-2 peptide
8. 5MWI cryoEM structure of crenactin filament
9. 5LJW:B wide open MamK monomer
10. 5LJW:A less open MamK monomer
11. 5LJV cryoEM structure of MamK filament
12. *Caulobacter* MreB monomeric and single filament structures
13. 4CZJ *Caulobacter* MreB double filament
14. 1JCG *Thermotoga* MreB single filament
15. 4A61:A *E. coli* ParM in complex with AMPNPP
16. Monomeric ParMs
17. 4A62:A *E. coli* ParM in complex with ParR peptide (polymerisation nucleator)
18. 5AEY cryoEM structure of ParM filament



RESULTS AND DISCUSSION

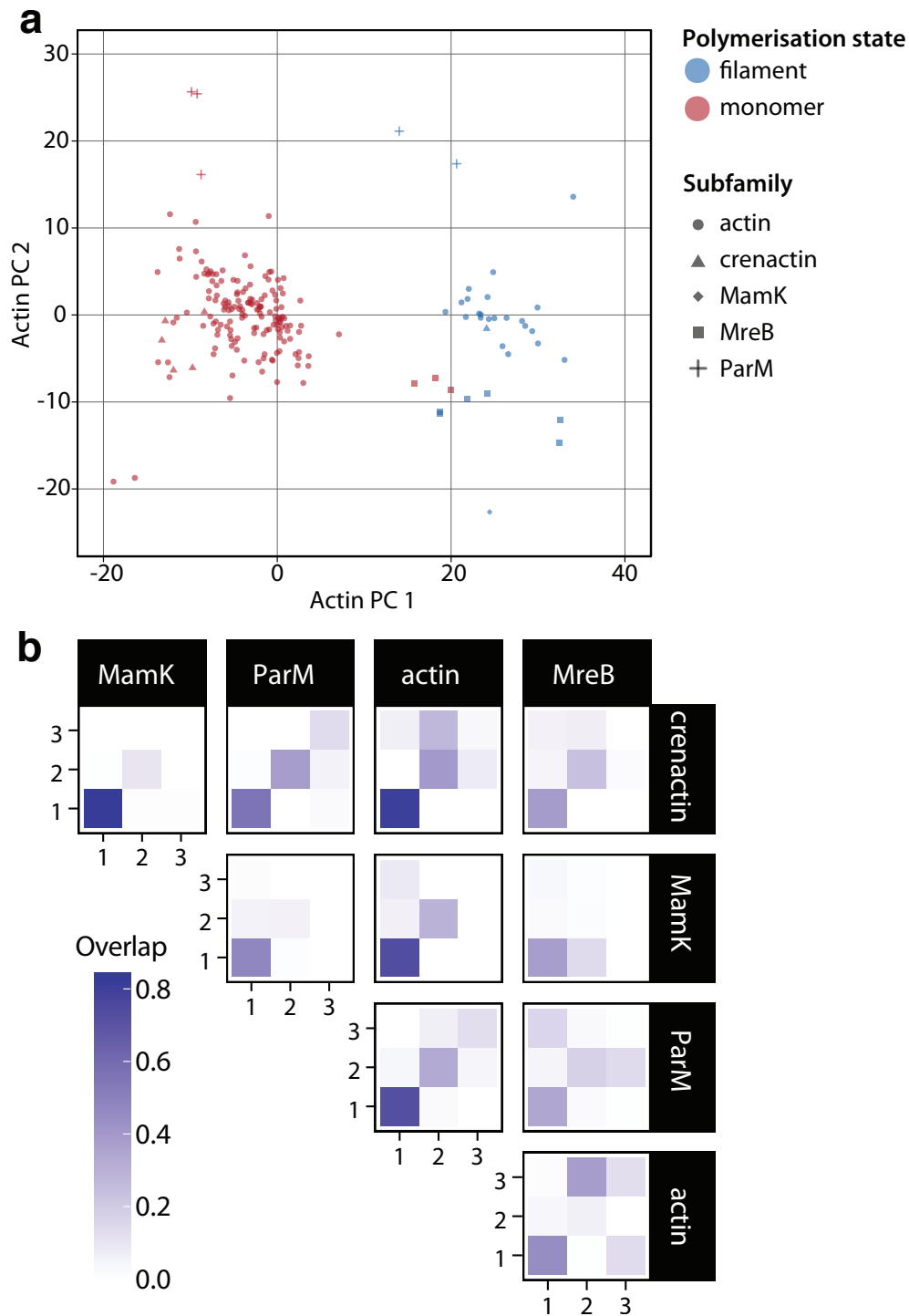


Figure 2-23 – The conformational switches within cytomotive actin subfamilies are similar

A Projection of all structures into the eukaryotic actin PC I-PC2 subspace.

B Overlap between PCs 1, 2 and 3 of the subfamilies.

2.4.6 What is the role of conformational changes upon polymerisation?

The fact that conformational changes happen upon polymerisation has been noted in actin and tubulin superfamily systems, here I am making the case that these changes are switches, that they happen in essentially all of the studied subfamilies, and that within each subfamily it is the same switch. Some of the mechanistic consequences of subunit-intrinsic conformational changes upon polymerisation have been recognised in the context of various systems. In particular:

1. The straightening of the kinked soluble tubulin heterodimer upon polymerisation into MTs has been extensively discussed, and the most common explanation for this is that lateral interactions between protofilaments (PFs) pay for the unfavourable straightening, storing strain within the MT lattice (Buey et al., 2006).
2. The flattening of the eukaryotic actin monomer in the G to F (polymerisation) transition has also been extensively discussed. The most common explanation for this is that the change is important for stimulating the intrinsic NTPase activity of the monomer, by positioning the catalytic glutamine (and histidine) correctly (Chou and Pollard, 2019; Merino et al., 2018; Oda et al., 2009). Of course, in tubulins the potentiation of NTPase activity is also achieved via polymerisation, by the enforced proximity of the catalytic T7 loop from the next subunit to the bound NTP.
3. The importance of a switch for cooperative assembly of a single stranded filament (FtsZ) has been rigorously modelled by Miraldi et al. (2008), although the principle was first introduced (to my knowledge) by Michie and Löwe (2006). This is essentially equivalent to (1), but invoking the importance of longitudinal interactions (rather than lateral ones) to pay for the otherwise unfavourable switch.

My proposal is that the switch is important for all of these things, and that it is also critical for coupling of kinetic and structural polarities, as introduced in Section 2.1.8 for FtsZ.

2.4.7 How are structural and kinetic polarities coupled across the actin and tubulin superfamilies?

Cytomotive filaments are thought of as working in one of two ways: by treadmilling, or by exhibiting dynamic instability. Both actins and tubulins have been ascribed the ability to do each of these. I would argue that these two modes are not as different as they appear, with the minus end of a treadmilling filament being somewhat equivalent to a de-capped end of a dynamically unstable filament undergoing catastrophe. This idea has recently also

RESULTS AND DISCUSSION

been proposed by Harold Erickson (Erickson, 2019). The feature which unites the two mechanisms is the directed 1D motor of (de)polymerisation.

The ability of nucleotide-hydrolysing filament-forming proteins to do useful work as 1D motors has been formally treated in energetic and kinetic terms in a series of historic papers, beginning with the seminal work on actin treadmilling by Albrecht Wegner, or as he termed it, “head-to-tail polymerisation” (Wegner, 1976). Wegner’s conclusions were extended and generalised to include microtubules and to incorporate the effects of resistance at filament ends on filament dynamics by Terence Hill and Mark Kirschner (Hill and Kirschner, 1982). These, and subsequent, models all assume the fact that the 1D-filament-motors have slow- and fast-growing ends, also referred to as the minus- and plus-ends, respectively, but these models do not themselves explain the origin of this kinetic polarity, nor how it is coupled to structural polarity (as it clearly is, and needs to be to be useful).

Some, though surprisingly few, attempts have been made to rationalise the origin of kinetic polarity, and its observed coupling to structural polarity in both eukaryotic actin filaments and microtubules.

In the case of microtubules, the difference in growth rates at the two ends is typically attributed to the fact that minus ends are thought to be blunt while plus ends form open, ragged, funnels (as reviewed in, for example, (Brouhard and Rice, 2018)) and incoming subunits will therefore traverse different addition pathways at either end (permitting different on-rates). Note that this argument for structural end-differences is dependent on the multi-strandedness of the microtubule. The paradigm of the two different end-structures has recently faced a significant challenge from a very thorough study of microtubule ends which suggests that polymerisation and depolymerisation at both plus- and minus-ends takes place in α -subunit thick single protofilaments, *in vivo* and *in vitro* (McIntosh et al., 2018). I expect to see significant efforts to settle this question of end structures in the near future, but for now it remains a very real possibility that, at their ends, microtubules polymerise and depolymerise as single protofilaments.

In eukaryotic actin, one study purports to show that the pair of subunits at the minus-end (“pointed end”) of the double filament adopt an alternative structure (alternative to both monomeric or within-filament polymerised subunits) which enforces a slower binding regime on incoming monomers (Narita et al., 2011). The evidence presented there consists

of a low resolution (~ 20 Å) cryoEM reconstruction and is not convincing, but illustrates the unmet need for an explanation. Whereas, in one of the two recent papers (Chou et al. (2019), the other being Merino et al. (2018)) describing the structures of an apparently full set of eukaryotic actin filament structures (all of: ATP-, ADP-Pi-, and ADP-bound structures), the authors put forward an explanation for the origin of kinetic polarity essentially identical to that presented here for FtsZ (and previously published by us (Wagstaff et al., 2017)), i.e. that it is the difference between the pairs of interfaces interacting at each end (top of monomer, in monomer conformation, and bottom of filament subunit, in polymerised conformation, at one end, and *vice versa* at the other) that explains the difference in kinetics at the two ends. Again, this argument does not directly depend on the multi-strandedness of the actin filament, but is compatible with it.

I hope that it is now becoming clear that the argument put forward in Section 2.1.8 for single-stranded FtsZ: that the generation of kinetic end-polarity, and its coupling to structural polarity, can be achieved robustly via a polymerisation-associated conformational switch; is consistent with the data available for many of the actin and tubulin superfamily members discussed here. And, that this argument could fill a gap in our understanding of these remarkable dynamic protein assemblies. In summary, I am proposing that the requirements of a protein to form a useful cytomotive filament are the following:

1. Binds nucleotide
2. Can polymerise
3. Polymer stability is linked to nucleotide state
4. Has intrinsic NTPase activity, activated by polymerisation
 - a. Creates NTP/NDP gradient
5. Limited nucleotide (NTP for NDP) exchange after hydrolysis
6. Conformational switch upon polymerisation
 - a. Enforces cooperative assembly
 - b. Imposes kinetic end-asymmetry and sets direction of NTP/NDP gradient, thus coupling kinetic and structural polarity

(1,2,3) are clearly necessary. (4) sets up the NTP/NDP gradient, (5) maintains it. (6) is crucial for enforcing cooperative assembly during nucleation, and as proposed here (and Wagstaff et al., (2017)), for setting the direction of the NTP/NDP gradient by coupling structural and kinetic polarities, and preventing single-stranded filaments from falling apart at the same rate as end subunits are lost.

2.4.8 MreB

The arguments laid out here are preliminary, although I am optimistic that further work will bear out the conclusions. During the course of the superfamily analysis I was very interested in the case of MreB. As noted above, MreB does not appear to undergo a polymerisation associated conformational switch (Figure 2-22), instead it appears to be “locked” in the conserved filament state. This would appear to be a stumbling block for the ideas above, as MreB has regularly been described as a cytomotive filament (e.g. (Aylett et al., 2011)). However, the emerging picture (as briefly discussed in the Introduction) is that MreB does not in fact, form cytomotive filaments. Instead, the filaments are thought to act as “rudders” for cell wall synthesis enzymes, using their tight curvature to align perpendicular to the long axis of the cell, and transmitting this orientation to the rod complex/elongasome (Garner et al., 2011; Hussain et al., 2018; Teeffelen et al., 2011). This should perhaps not come as a surprise, given the importance of directionality in the application of cytomotivity: as we know that MreB forms antiparallel double filaments, which are inherently non-polar (van den Ent et al., 2014). The fact that a filament we know to be not cytomotive does not have a polymerisation associated switch adds to the circumstantial evidence that this is a relevant observation.

2.4.9 Conclusions and future work

The proposition laid out here is qualitative and will require a rigorous mathematical treatment by both coarse-grained modelling of systems with the properties defined here, and also high-quality molecular dynamics approaches. Key uncertainties are:

- Just how necessary bistable conformational switches are (as opposed to continuous conformational changes)?
- Whether the role of multistrandedness is more than just potentiation of the payoff from longitudinal contact formation?
- How to integrate these ideas with the mass of literature covering the post-hydrolysis states of subunits within filaments: both eukaryotic actin filaments and MTs apparently have functionally relevant, and structurally distinct, NDP.Pi and NDP states (Alushin et al., 2014; Merino et al., 2018)? (Although as can be seen from the analysis above, these changes are far smaller than the changes associated with polymerisation itself)

If indeed the switch is shown to be important, it will be crucial to understand the molecular basis of bi-stability: which residues are responsible for the energy barrier. Ways to approach this would include analysing pairs of high quality structures within each family to try and identify conserved (or not) residues which undergo noticeable changes in torsion angles, contact networks; and by analysing large sets of sequences for correlation with coevolutionary relationships and/or raw conservation. It may be necessary to use a higher level of abstraction to define equivalence, e.g. secondary structure units, as the precise position of critical residues may vary even if the mechanistic principle is conserved.

Returning to the question of whether evolving cytomotivity is easy or hard, as far as it is possible to say, it does seem that the two cytomotive folds do indeed contain a set of functionalities that might be difficult to integrate in such small domains. More importantly though, the idea that polymerisation-coupled conformational switches are the conserved basis for the coupling of kinetic and structural polarities in these filament forming superfamilies is an attractive one, which appears to explain a large amount of historical data, and I am excited about going further in demonstrating that this really is the case.

3 MATERIALS AND METHODS

3.1 General methods

All reagents were purchased from Sigma Aldrich unless stated otherwise.

3.1.1 Preparation of electrocompetent cells and transformation

Electrocompetent cells were prepared as follows. Frozen stocks were streaked out on TYE plates with no antibiotics and incubated overnight at 37 °C. The next day a 10 mL 2xTY starter culture was inoculated with a single colony, and incubated overnight with shaking at 37 °C. On the third day, the overgrown 10 mL culture was added to 1 L 2xTY and incubated with shaking (200 rpm) at 37 °C until OD₆₀₀ of 0.35-0.4 was reached at which point the flask was immediately surrounded with ice. The flask was allowed to chill for 20-30 minutes with occasional swirling to ensure even cooling. The 1 L culture was then split and transferred to four ice-cold centrifuge bottles and spun at 1000 g for 20 minutes at 4 °C. The supernatant was discarded and the pellets resuspended in 200 mL each ice-cold ddH₂O. The centrifugation was repeated, and the pellets resuspended in 100 mL each ice-cold ddH₂O, before combining into two bottles and centrifuging again. These two pellets were resuspended in 40 mL each ice-cold 10% glycerol before transferring to ice-cold, pre-washed, 50 mL Falcon tubes. The centrifugation step was then repeated. Pellets were resuspended in 1 mL ice-cold 10% glycerol by swirling for a final OD₆₀₀ of ~200-250. The suspension was aliquoted (25-100 µL) into 1.5 mL Eppendorf tubes on ice before snap freezing in LN₂, and stored at -80 °C. Competence was tested for each batch using a control plasmid, using the transformation protocol below.

Electrocompetent cells were transformed with plasmids or Gibson reaction products as follows. Aliquots of cells were thawed on ice before 25 µL was added on top of 1 µL DNA in a chilled electroporation cuvette (2 mm gap, Flowgen Bioscience) and gently mixed by tapping. A voltage of 2500 V was applied using an Eppendorf Eporator, and 900 µL of SOC was quickly added. The transformed cells were incubated at 37 °C for 30 minutes to allow expression of resistance genes, before plating on agar with appropriate antibiotics.

3.1.2 Cloning procedures

All the plasmids used here are listed in Table 1, p.161. All cloning by me was done in *Escherichia coli* MAX Efficiency™ DH5α™ cells (Thermofisher Scientific). See Section 3.2 Strains, below.

All Polymerase Chain Reactions (PCR) were done with Q5 Hot Start High-Fidelity DNA Polymerase (NEB) in accordance with the manufacturer's instructions. All oligonucleotides were synthesised by Sigma Aldrich, and stored at 100 mM in ddH₂O at -20 °C.

Plasmids were assembled using the isothermal assembly method, also known as Gibson Assembly (Gibson et al., 2009), using a kit (NEB), and following the manufacturer's instructions. Appropriate primers were designed using the NEBuilder Assembly Tool (v1, NEB).

Mutagenesis was achieved via blunt end ligation using the Q5 Site-Directed Mutagenesis Kit (NEB) according to the manufacturer's instructions.

Plasmids were purified using a QIAprep Spin Miniprep Kit (QIAGEN NV), and quality was checked using a NanoDrop Microvolume Spectrophotometer (Thermofisher Scientific) by assessing 230/260/280 nm absorbance ratios. All plasmids were sequenced through coding regions by GATC GmbH (now Eurofins Genomics) with appropriate primers.

3.1.3 Agarose gel electrophoresis

DNA was visualised on agarose gels made by dissolving 1.5% w/v agarose (Biogene.com) in 1 x TBE buffer with 1:1000 v/v SYBR Safe (Invitrogen). Samples were mixed with dye (GelPilot DNA Loading Dye, 5x (Qiagen)) before loading. Agarose gels were run at 100 V for 45 minutes before imaging of UV fluorescence with a Gel Doc XR+ imaging system (Bio-rad).

3.1.4 SDS-PAGE

Protein samples were visualised via SDS-PAGE. Samples were mixed with protein loading dye and loaded onto an SDS-PAGE gel (10-20% gradient, Bio-Rad). The gel was typically run at 300 V for 30 minutes in 1x SDS-PAGE buffer before staining with Quick Coomassie stain (Generon) and imaging with a Gel Doc XR+ imaging system (Bio-rad).

MATERIALS AND METHODS

3.1.5 Electrospray ionisation mass spectrometry

All protein samples were analysed by electrospray ionisation mass spectrometry to confirm expected molecular weights (accurate to 1 in 10,000). Solubilisation in an appropriate solvent mix (e.g. 50 % MeOH with 1 % formic acid *or* 50 % acetonitrile with 1 % formic acid) was achieved using the procedure of (Whitelegge et al., 1999). Samples were analysed on a Micromass LCT Classic TOF instrument (Waters).

3.2 Strains

<i>Strain</i>	<i>Genotype</i>	<i>Reference</i>
<i>Escherichia coli</i> C41 (DE3)	BL21(DE3) derivative	(Miroux and Walker, 1996)
<i>Escherichia coli</i> MAX Efficiency TM DH5 α TM	F- ϕ 80lacZ Δ M15 Δ (lacZYA-argF) U169 <i>recA1 endA1 hsdR17</i> (rk-, mk+) <i>phoA supE44</i> λ - <i>thi-1 gyrA96 relA1</i>	ThermoFisher Scientific

3.3 Growth Media and Standard Solutions

3.3.1 TYE Plate

10 g tryptone

5 g yeast extract

8 g NaCl

15 g agar

Formedium TYEA09L premix used. Final pH 7.0 at 25 °C, made up to 1 L with milliQ water then autoclaved and poured. Antibiotics added after autoclaving at around 55 °C if needed.

3.3.2 SOB liquid media

28 g SOB ready mix (VMR)

Made up to 1 L with milliQ water, pH adjusted to 7.0 before autoclaving. For SOC media 18 mL / L 20% Glucose was added.

3.3.3 2xTY liquid media

16 g tryptone

10 g yeast extract

5 g NaCl

MATERIALS AND METHODS

Formedium YBD20L premix used. Made up to 1 L with milliQ water, and pH adjusted to 7.4 before autoclaving.

3.3.4 1x SDS running buffer

30 g Trizma Base

144 g glycine

10 g SDS

Made up to 10 L with distilled water.

3.3.5 10X TBE

108 g Trizma Base

9.3 g EDTA

55 g boric acid

Made up to 1 L with MilliQ water, autoclave.

3.3.6 Protein loading buffer

0.6 g Trizma Base

0.77 g DTT

2 g SDS

10 g sucrose

0.095 g EDTA

0.25% w/v bromophenol blue

Made up to 50 mL with MilliQ water and pH adjusted to 6.8.

3.4 Expression and purification of proteins

All chromatography steps were carried out using an Äkta purifier system (GE Healthcare) at 6 °C (in a cold room) unless stated otherwise. All proteins I purified were expressed in *Escherichia coli* C41 cells (details in Section 3.2, p.122).

3.4.1 Full-length SaFtsZ (I) and mutants

Protocol carried out by María A. Oliva and Alba García-Sánchez at Centro de Investigaciones Biológicas, CSIC, Madrid, Spain for the biochemistry experiments discussed in section 2.1.2, p.44.

Full-length (FL) *SaFtsZ* (Uniprot ID: FTSZ_STAAU) was amplified using PCR from genomic DNA and cloned into the NdeI and SapI sites of pTXB1 (NEB IMPACT system, NEB Ipswich, MA), generating a C-terminal fusion to the *Mxe* intein/chitin binding domain which self-cleaves upon the addition of DTT. PCR mutagenesis using this vector as a template generated mutants T66W and F138A.

Full-length fusion proteins were expressed in *E. coli* BL21 (DE3) cells, which were grown in LB media with ampicillin (100 mg/L) at 37 °C with 200 rpm shaking to an OD₆₀₀ of 0.6. Cultures were then shifted to 16 °C and after 1 hour expression was induced by the addition of 0.4 mM isopropyl-β-D-1-thiogalactopyranoside (IPTG), before overnight incubation. Cells were collected by centrifugation and resuspended in buffer FL.A (50 mM HEPES-KOH, 50 mM NaCl, 20mM EDTA, pH 8.5) with 100 µg/mL lysozyme, 10 µg/mL DNase and 4 mg/mL PMSF, before lysis via 2-3 passes through a French press. Lysate was clarified by centrifugation at 100,000 g and 4 °C for 1 hour. Soluble protein was captured on a chitin column (NEB) equilibrated and washed with buffer FL.A. Intein activity and release of the untagged, full-length protein was initiated by overnight incubation in buffer FL.B (buffer FL.A with 50 mM DTT) at 4 °C followed by elution. Eluate was further purified by anion-exchange chromatography on a 5 mL HiTrap Q column (GE Healthcare, Little Chalfont, UK). The column was equilibrated and washed with buffer FL.Q.A (50 mM Tris-HCl, 1 mM EDTA, pH 7.5) and bound protein was eluted with a linear gradient of buffer FL.Q.B (FL.Q.A with 1 M NaCl). Peak fractions were further purified by size-exclusion on a 70 mL Sephadex 75 (GE Healthcare) column in Buffer FL.GF (20 mM Tris-HCl, 150 mM NaCl, 10% glycerol, pH 8.0). Peak fractions were pooled and concentrated using centrifugal concentrators (Vivaspin, Sartorius, Epsom, UK) to 5-8 mg/mL before freezing in liquid nitrogen and storage at -80 °C. Protein integrity was confirmed by electrospray mass spectrometry.

MATERIALS AND METHODS

3.4.2 Full-length Sa FtsZ (II)

The protocol carried out by me to generate protein for cryoEM experiments at MRC LMB. Early iterations were developed by Tim Nierhaus.

Full-length (FL) SaFtsZ (Uniprot ID: FTSZ_STAAU) was amplified using PCR from genomic DNA and cloned into a pHis17 plasmid derivative, with no tag, via Gibson assembly. This plasmid was a gift from Tim Nierhaus (herein pJW1). FL SaFtsZ was expressed in *E. coli* C41 (DE3) cells (Lucigen) grown in 2xTY media with ampicillin (100 mg/L) at 37 °C with 200 rpm shaking to an OD₆₀₀ of 0.6. Cultures were then shifted to 16 °C and after 1 hour expression was induced with the addition of 0.5 mM IPTG, before overnight incubation. Cells were collected by centrifugation and resuspended in Buffer FL.Q.A2 (50 mM Tris-HCl, pH 7.5). 1 cOmplete protease inhibitor tablet (Roche, IN USA) per L was added, as well as DNase I. Cells were lysed by passing through a cell disruptor (Constant Systems, Daventry, UK) at 25 kpsi. The lysate was clarified by centrifugation at 100,000 g and 4 °C for 30 minutes. The soluble fraction was loaded onto Blue Sepharose (GE Healthcare) resin (40 mL bed volume, packed in a XK50 column (GE Healthcare)) equilibrated in Buffer FL.Q.A2, before elution with a gradient of Buffer FL.Q.B2 (Buffer FL.Q.A2 with 1M KCl). Fractions with protein were pooled and concentrated using centrifugal concentrators (Vivaspin, Sartorius) before further purification by size-exclusion chromatography on a HiLoad Sephacryl S300 16/60 column (GE Healthcare) in Buffer FL.GF2 (50 mM PIPES-KOH, 250 mM KCl, 1 mM NaN₃, pH 6.8). Fractions with protein were diluted 10-fold in Buffer FL.Q.A2 before being loaded onto a Mono Q 4.6/100 (1.7 mL) PE column (GE Healthcare) equilibrated and washed with Buffer FL.Q.A2 before elution with a linear gradient of Buffer FL.Q.B2. The cleanest fractions were pooled and concentrated using centrifugal concentrators (Vivaspin, Sartorius) before freezing in liquid nitrogen and storage at -80°C. Protein integrity was confirmed by electrospray mass spectrometry.

3.4.3 Untagged Sa FtsZ 12-316, and mutants

Truncated (TR) (12-316), SaFtsZ (Uniprot ID: FTSZ_STAAU) was cloned into a pHis17 plasmid derivative, with no tag, via Gibson assembly (Gibson et al., 2009). PCR mutagenesis using the resulting plasmid (herein pJW3) as a template generated mutants T66W (herein pJW4) and F138A (herein pJW5). These plasmids were a gift from Matthew Tsim.

Truncated SaFtsZ proteins were expressed in *E. coli* C41 (DE3) cells (Lucigen) grown in 2xTY media with ampicillin (100 mg/L) at 37 °C with 200 rpm shaking to an OD₆₀₀ of 0.6. Cultures

were then shifted to 16 °C and after 1 hour expression was induced by the addition of 0.5 mM IPTG, before overnight incubation. Cells were collected by centrifugation and resuspended in Buffer TR.A (50 mM Tris-HCl, 30 mM NaCl, pH 8.0) before lysis by passing through a cell disruptor (Constant Systems, Daventry, UK) at 25 kpsi. 1 cOmplete protease inhibitor tablet (Roche, IN USA) per L was added, as well as DNase I. The lysate was clarified by centrifugation at 100,000 g and 4 °C for 30 minutes. The soluble fraction was loaded onto a HiTrap Q anion-exchange column (GE Healthcare), washed with Buffer TR.Q.A, and eluted with a linear gradient of Buffer TR.B (TR.A with 1 M NaCl). Peak fractions were pooled, and protein was precipitated by adding saturated ammonium sulphate to 35% v/v. Precipitated protein was centrifuged at 28,000 g and 4 °C for 30 minutes, and the pellet resuspended in Buffer TR.A. Resuspended protein was further purified by size-exclusion chromatography on a HiLoad Sephacryl S300 16/60 column (GE Healthcare) in Buffer TR.A. Peak fractions were pooled, concentrated to 15-25 mg/mL using centrifugal concentrators (Vivaspin, Sartorius) before freezing in liquid nitrogen and storage at -80°C. Protein integrity was confirmed by electrospray mass spectrometry.

3.4.4 Full-length Ec FtsZ

Full length, untagged, *E. coli* FtsZ (Uniprot ID: FTSZ_ECOLI) was cloned into the BamH/NdeI sites of pET9a (Novagen), with no tag. This plasmid (pSZ65) was a gift from Piotr Szwedziak, herein named pJW18. Purification of *E. coli* FtsZ (EcFtsZ) was by a modified version of established protocols (Rivas et al., 2000). Protein was expressed in *E. coli* C41 (DE3) cells (Lucigen) grown in 2xTY media with kanamycin (50 mg/L) at 37 °C with 200 rpm shaking to an OD₆₀₀ of 0.6. Cultures were then shifted to 20 °C and, after 1 hour, expression was induced by the addition of 0.5 mM IPTG, before overnight incubation. Cells were collected by centrifugation and resuspended in Buffer PEM (50 mM PIPES-KOH, 5 mM MgCl₂, 1 mM EDTA, pH 6.5) before lysis by passing through a cell disruptor (Constant Systems) at 25 kpsi. 1 cOmplete protease inhibitor tablet (Roche, IN USA) per L was added, as well as DNase I. The lysate was clarified by centrifugation at 100,000 g and 4 °C for 30 minutes. FtsZ was separated by GTP and calcium-induced precipitation, as follows. Lysate was adjusted to pH 7 with acetic acid then GTP and CaCl₂ were added to 1 mM and 20 mM respectively. This mixture was then centrifuged at 11,000 g and 4 °C for 15 minutes. The pellet, containing FtsZ, was resuspended in buffer PEM and insoluble debris was removed by centrifugation at 100,000 g and 4 °C for 30 minutes. FtsZ was further purified by anion exchange chromatography over a Mono Q 4.6/100 (1.7 mL) PE column (GE Healthcare)

MATERIALS AND METHODS

equilibrated and washed with Buffer ECZ.Q.A (50 mM Tris-HCl, 50 mM KCl, 1 mM EDTA, 10% glycerol, pH 8.0), bound protein was eluted with a linear gradient of Buffer ECZ.Q.B (Buffer ECZ.Q.A with 1 M KCl). Peak fractions were pooled, concentrated to 20 mg/mL using centrifugal concentrators (Vivaspin, Sartorius) before freezing in liquid nitrogen and storage at -80°C. Protein integrity was confirmed by electrospray mass spectrometry.

3.4.5 EcZapA

Full length *E. coli* ZapA (Uniprot ID: ZAPA_ECOLI) was cloned into a pTXB1 backbone (NEB) (Chong et al., 1997), as a C-terminal fusion to a self-cleaving intein / Chitin Binding Domain (CBD) tag, via Gibson assembly (Gibson et al., 2009), to make plasmid pJWI9. Full length *E. coli* ZapA (EcZapA) was expressed in *E. coli* C41 (DE3) cells (Lucigen) grown in 6L 2xTY media with ampicillin (100 mg/L) at 37 °C with 200 rpm shaking to an OD₆₀₀ of 0.6. Cultures were then shifted to 20 °C and, after 1 hour, expression was induced by the addition of 0.5 mM IPTG, before overnight incubation. Cells were collected by centrifugation and resuspended in buffer ZAPA.C (20 mM Tris-HCl, 500 mM NaCl, pH 8.5) before lysis by passing through a cell disruptor (Constant Systems, Daventry, UK) at 25 kpsi, twice. 1 cOmplete protease inhibitor tablet (Roche, IN USA) per L was added, as well as DNase I. The lysate was clarified by centrifugation at 100,000 g and 4 °C for 30 minutes, then filtered through a 0.45 µm PVDF mesh. The ~200 mL soluble fraction was loaded onto ~65 mL of chitin binding resin packed in a XK50 column (GE Healthcare) at a flow rate of 2.5 mL/min, before washing with 250 mL of buffer ZAPA.C. Cleavage on the column was achieved by washing with 180 mL of buffer ZAPA.D (ZAPA.C with 50 mM DTT), followed by incubation overnight. Liberated full-length, untagged, EcZapA was collected in fractions. Fractions containing EcZapA were concentrated to 2.5 mL using centrifugal concentrators (Vivaspin, Sartorius). 1 mL of concentrated eluate was further purified by size-exclusion chromatography over a Superdex 75 pg 16/600 column (GE Healthcare) in Buffer ZAPA.GF (50 mM Tris-KOH, 50 KCl, 1 mM EDTA, 5% v/v glycerol, pH 7.9). The peak fractions were pooled and concentrated using centrifugal concentrators (Vivaspin, Sartorius) to 500 µL of ~10 mg/mL, before freezing in liquid nitrogen and storage at -80°C. Protein integrity was confirmed by electrospray mass spectrometry.

3.4.6 Nucleotide-free SaFtsZ 12-316 L272D C-His6

A series of mutations designed to prevent SaFtsZ polymerisation (11 combinations in total) were introduced into pJWI (full length WT SaFtsZ in pHis17 with no tag). These full-length

constructs were then truncated to residues 12-316 by various PCR and Gibson assembly steps (Gibson et al., 2009) to make untagged, N-terminally His6-tagged, and C-terminally His6-tagged versions of each. Small scale expression of all of these was carried out and the L272D C-His6 construct (pJW62) was chosen for further work due to its high level of expression and predicted strong inhibition of polymerisation. Purification of the protein in the apo state (without bound nucleotide) was carried out, as follows.

SaFtsZ 12-316 L272D C-His6 was expressed in *E. coli* C41 (DE3) cells (Lucigen) grown in 2xTY media with ampicillin (100 mg/L) at 37 °C with 200 rpm shaking to an OD₆₀₀ of 0.5. Expression was induced by the addition of 0.5 mM IPTG, before a 5 hour incubation. Cells were collected by centrifugation and resuspended in Buffer HisA (50 mM Tris, 300 mM NaCl, pH 8.0) before lysis by passing through a cell disruptor (Constant Systems, Daventry, UK) at 25 kpsi. The lysate was clarified by centrifugation at 100,000 g and 4 °C for 30 minutes, then filtered through a 0.45 µm PVDF mesh. The soluble fraction was loaded onto a 5 mL HisTrap HP column (GE Healthcare). The column was washed extensively with Buffer HisA before elution with 2% Buffer HisB (Buffer HisA plus 1M imidazole). Fractions with FtsZ were pooled and diluted 10-fold in cold ddH₂O before loading onto a HiTrap Q HP (GE Healthcare) in Buffer APO.A (25 mM Tris-KOH, 25 mM NaCl, pH 8.0). Elution was by gradient of Buffer APO.B (Buffer A, 1M NaCl), two peaks of FtsZ were visible, the first is apoFtsZ, the second still had nucleotide bound. Both peaks were collected, pooled and concentrated using centrifugal concentrators (Vivaspin, Sartorius). The protein at this stage was rather unstable and had to be kept on ice, and sharp motions avoided, to prevent precipitation. Concentrated FtsZ was loaded onto a Superdex 200 16/60 column (GE Healthcare) in Buffer APO.GF (50 mM PIPES-KOH, 250 mM KCl, 20 mM EDTA, pH 6.8) which was run very slowly (0.1 mL/min) to gradually separate the nucleotide from the protein. The apoFtsZ peak (very low 260/280 nm absorption) was pooled and concentrated using centrifugal concentrators (Vivaspin, Sartorius) before exchanging with a spin column (Zebaspinn) into the final Buffer APO.GLY (10 mM Tris-HCl, 50 mM KCl, 20% v/v glycerol, pH 7.5), in which apoFtsZ is stable. Aliquots were snap frozen in 1 N₂ and stored at -80°C. Protein integrity was confirmed by electrospray mass spectrometry. Absence of nucleotide was confirmed by UV/Vis spectroscopy of samples after precipitation with 0.5 N cold HClO₄.

3.5 X-ray crystallography

3.5.1 Protein crystallisation

Crystallisation conditions were found using the LMB in house high-throughput crystallisation platform, by mixing 100 nL truncated *SaFtsZ* T66W or F138A solution at 5 or 10 mg/mL, with GTP at 10 mM, with 100 nL of 1920 different crystallisation reagents in MRC vapour diffusion sitting drop crystallisation plates (Gorrec and Löwe, 2018). Conditions yielding crystals were optimised, and crystals from either the initial screens or subsequent optimization were selected for data collection. Conditions giving the crystals for which structures are presented are in Table 2, p. 162.

3.5.2 Crystallographic data collection and structure determination

Diffraction images were collected from single frozen crystals at beamlines at either DLS (Diamond Light Source, Harwell, UK) or ESRF (European Synchrotron Radiation Facility, Grenoble, France) as indicated in Table 2, at 100 K. Diffraction images were processed with **XDS**, **POINTLESS** and **SCALA** software (Evans, 2006; Kabsch, 2010). Initial phases were determined by molecular replacement using **PHASER** with search models as indicated in Table 2 (McCoy et al., 2007). Models were rebuilt manually using **MAIN** and refined using **REFMAC** and **PHENIX . REFIN** alternately and iteratively (Afonine et al., 2018; Murshudov et al., 1997; Turk, 2013). Ramachandran plots and **MOLPROBITY** statistics were used to validate the structures as per Table 2, p. 162 (Williams et al., 2018).

3.6 Electron cryo-microscopy (cryoEM)

3.6.1 SaFtsZ

For collection of the datasets from which 2D classes shown in Figure 2-6 were produced, SaFtsZ was prepared at a final concentration of 0.2 mg/mL in Buffer SAZAB₂ (100 mM KCl, 10 mM magnesium acetate, 50 mM PIPES-KOH, pH 6.8), with or without 0.005 % TWEEN-20. GTP or GMPCPP was added to 5 or 0.1 mM respectively, and the solution was mixed and incubated for 8 minutes before 2.5 μ L sample was applied to freshly glow-discharged Quantifoil Cu R2/2 200 mesh grid and plunge frozen using a Vitrobot Mark III (FEI Company, OR) into liquid ethane maintained at 93.0 K using an ethane cryostat (Russo et al., 2016). The Vitrobot chamber temperature was set to 10 °C and humidity to 100 %.

Micrograph movies of FtsZ filaments were collected with an FEI Tecnai G2 Polara microscope operating at 300 kV. Data were acquired on a Falcon III direct electron detector prototype at a calibrated pixel size of 1.34 Å and an approximate total dose of 40 e⁻/Å² using the automated acquisition software EPU (FEI Company). Images were processed with the helical pipeline implemented in RELION (He and Scheres, 2017).

3.6.2 EcFtsZ

For cryoEM, *E. coli* FtsZ was prepared at 0.5 mg/mL in Buffer ECZAB₃ (50 mM HEPES-KOH, 100 mM potassium acetate, 5 mM magnesium acetate, pH 7.7), at 20 °C. GMPCPP was added to 0.1 mM. 2.5 μ L sample was immediately applied to freshly glow-discharged Quantifoil Cu R2/2 200 mesh grid and plunge frozen using a Vitrobot Mark III (FEI Company, OR) into liquid ethane maintained at 93.0 K using an ethane cryostat (Russo et al., 2016). The Vitrobot chamber temperature was set to 10 °C and humidity to 100 %. The time between GMPCPP addition and vitrification was ~30 s.

Micrograph movies were collected as for SaFtsZ. A total of 3688 movies were collected at -1 to -4 μ m defocus in 46 frames during each 1.5 s exposure.

All image processing was carried out within RELION 2.0 (Scheres, 2012). Micrograph movies were motion corrected using MotionCor2 (Zheng et al., 2016) with 5 x 5 patches and a grouping of 10 frames. Helical autopicking in RELION was used in order to find segments along the filaments at 4.3 nm intervals with confidence. Boxes of 190 x 190 pixels were extracted around each segment. After 2D classification, a 3D autorefinement of the

MATERIALS AND METHODS

remaining 943,277 filament segments was performed in RELION using helical reconstruction options (He and Scheres, 2017), against an atomic protofilament model derived from PDB ID 3VO8, filtered to 20 Å (similar results were obtained with a smooth cylinder, they just took longer to converge). The resulting two half maps were used in post processing to sharpen the map (B-factor -360 Å⁻¹) and to obtain a gold standard FSC-based resolution estimate of 6.7 Å (0.143 FSC criterion), however the map is anisotropic, preventing interpretation of features at this resolution.

In the absence of an *E. coli* FtsZ crystal structure, CHIMERA (Pettersen et al., 2004) was used to determine that the SaFtsZ filament structure, showing the open conformation, fits very well into the *E. coli* filament density, as opposed to any other structure containing closed conformations (see Figure 2-5, p.58).

3.6.3 EcFtsZ with EcZapA

EcFtsZ (0.04 mg/mL final) and EcZapA (0.2 mg/mL final) were prepared for cryoEM in Buffer ECZAB₃ (50 mM HEPES-KOH, 100 mM potassium acetate, 5 mM magnesium acetate, pH 7.7), with TWEEN-20 (5.6 µL, 0.05% stock, 0.007% final), on ice in 28 µL aliquots. GMPCPP (2 µL, 0.1 mM, 0.02 uM final) was added, the solution was transferred to 20 °C, incubated for 1 minute (total time from addition to freezing) before 2.5 µL was applied to freshly glow-discharged Quantifoil Cu R2/2 200 mesh grid and plunge frozen using a Vitrobot Mark III (FEI Company, OR) into liquid ethane maintained at 93.0 K using an ethane cryostat (Russo et al., 2016). The Vitrobot chamber temperature was set to 10 °C and humidity to 100 %.

Four datasets were merged for the analysis shown in Section 2.2.3. These are summarised in the table below:

Name	Microscope	Pixel size (Å)	Stage tilt (°)	# images	# particles
Pol1	Polara	1.37	35	494	30941
Pol3	Polara	1.37	0	1175	37701
Diao	Krios	1.34	0	1673	26033
Dia25	Krios	1.34	25	1895	17026

Polara: FEI Tecnai G2 Polara microscope operating at 300 kV, with Falcon III direct electron detector prototype. Krios: FEI Titan Krios microscope operating at 300 kV, with K3 detector.

In all cases movies were collected with a total dose of ~ 40 electrons/ \AA^2 . Between- and within-frame motion was corrected with **MotionCor2**, and approximate dose weighting was done at the same time (Zheng et al., 2017). Defocus/CTF estimation was using **CTFFIND4** (Rohou and Grigorieff, 2015), and for tilted datasets refined using **GoCtf** (Su, 2019). All subsequent processing was using **RELION3** (Zivanov et al., 2018). Ends of helices were picked manually and segments extracted at 45 \AA intervals, to yield the '*# particles*' in the table above. Particles were extracted and scaled to a consistent pixel size of 2.74 $\text{\AA}/\text{pix}$ in 110 x 110 pixel boxes. An initial model for 3D refinement was constructed using the published structures of ZapA and FtsZ, before filtering to 60 \AA . As described in the text a wide variety of refinement and classification strategies were attempted within the Relion framework.

3.7 Fluorescence polarisation assay for GTP-competitive inhibitors of FtsZ

3.7.1 Fluorescence polarisation assay

Assay mixture components were combined in an order so as to minimise the concentration of DMSO to which the protein was exposed. Final buffer in all cases was: 9 mM Tris-HCl, 45 mM KCl, 18% v/v glycerol, 10% v/v DMSO, 0.01 % casein, pH 7.5. Unless otherwise stated in figure legends, the concentration of *S. aureus* FtsZ 12-316 L272D (apoSaFtsZ) was 15 nM, and the concentration of 8-[(6-Amino)hexyl]-amino-GTP-ATTO-550 (Jena Bioscience NU-830-550) was 2 nM.

20 µL volumes of assay mixtures were dispensed into wells of black, low volume, Corning 384-well plates (CLS4514), with a non-binding surface and a U-bottom using the Span8 head of a Biomek FXp liquid handling system (Beckman Coulter) using 50 µL tips, or by hand, and mixed by pipetting up and down by 10 µL 5 times. Plates were centrifuged at 100 g for 1 minute and then incubated at 25 °C for 30 minutes, allowing equilibrium to be reached (in actuality this happens much faster). All of these steps were carried out in low lighting to minimise photo-bleaching of the probe.

FP measurements were made with a BMG Pherastar FSX instrument using a “FP 540-20 590-20 590-20” filter block, with 200 flashes per well.

3.7.2 Pilot screen

For the pilot screen, assay plates were stamped with concentrated DMSO solutions of library compounds at the Dundee Drug Discovery Unit before being sealed, frozen and sent to LMB, where I stored them at -20 °C. Assay solutions were pipetted on top of the compounds to bring the final concentration of library compounds to 30 µM and mixed as above.

3.7.3 Binding analysis

All analysis was carried out using custom R scripts, which made extensive use of the `tidyverse` (Wickham, 2017). Non-linear least squares estimates of model parameters (as per Appendix: Principles of Fluorescence Polarisation p.152) were determined using the `nls` function in R's `stats` package.

3.8 Superfamily analysis

All analysis was carried out using custom scripts written in R, making extensive use of the `bio3d` (Grant et al., 2006) and `tidyverse` (Wickham, 2017) packages. Many of the details of the method are described in the main text.

3.8.1 Datasets

Structure datasets were collected programmatically from the PDB by running individual `phmmer` (Eddy, 2011) searches of PDB sequences with a representative from each of the subfamily investigated.

3.8.2 Alignment

Sequences from the downloaded PDB depositions were extracted and aligned as follows. Firstly, a high-quality representative structure was selected for each subfamily, and these were aligned for each superfamily via a hybrid approach combining structural and sequence alignments, including information from large alignments of homologues, with the `PROMALS3D` web server with defaults (Pei et al., 2008). Sequences were then aligned within each subfamily to the representative, using `MUSCLE` (Edgar, 2004) (with some manual adjustments), before all sequences were combined into a super alignment on the basis of the representative alignment (with some manual adjustments).

3.8.3 Structure annotation

Structures were annotated by downloading the Uniprot entry listed in the PDB annotation. Polymerisation state was assigned semi-automatically on the basis of experimental technique, but checked manually. Similarly, nucleotide state was assigned semi-automatically on the basis of ‘ligand’ annotation in the PDB.

3.8.4 Structural analysis

Structure analysis was carried out as described in Section 2.4.3, p.100. The structurally conserved core was found using the `bio3d::core.find` routine. The structures were aligned on the core using `bio3d::fit.xyz`. PCA was done using `bio3d::pca.pdbs`.

4 APPENDICES

4.1 Principles of X-ray Crystallography

We are very lucky to be living in the best period of human history so far. Every day we benefit from a vast array of technologies which exploit our knowledge of the universe to improve our lives. There have been many advances in natural science to bring us to this point, but few have had an impact as large as that of X-ray crystallography.

X-ray crystallography, for the first time, allowed us to visualise the structure of matter at the smallest scale – that of atoms. Information about how atoms are arranged relative to one another underpins our ability to understand and manipulate substances, including those in biological systems. The very first atomic structure, solved by Lawrence Bragg in 1913, revealed the now-familiar fact that sodium chloride was not, in fact, composed of Na-Cl molecules. This was the first of many insights into the world to be gained from shining X-rays through regular arrays of atoms. The principles by which structural information is obtained in this way are briefly outlined below.

4.1.1 Molecular imaging

In order to get some information about the structure of an object using another one the two must interact. The diffraction limit tells us that the interrogating object must be, at largest, of a similar scale to the smallest features on the interrogated object we want to resolve. If we wish to interrogate atomic structures we typically turn to subatomic particles, notably: electrons, neutrons, or photons; this is for two reasons. Firstly, these particles do interact with the components of atoms (protons, neutrons, and electrons, though not in all combinations), and secondly these particles have sizes, or wavelengths, similar to or smaller than the scales of interatomic interactions. This scale is on the order of 10 billionths of a metre (10^{-10} m), or 1 ångström (*abbrev.* Å), for instance, the Van der Waals radius of a Carbon atom is 1.70 Å, and the typical length of a C-C bond is 1.54 Å. All of electrons, neutrons, and photons can be coerced to form waves of appropriate wavelengths to resolve atomic features. In particular, neutrons and electrons must be accelerated to high energies, while similarly high energy photons, in the hard X-ray part of the spectrum or beyond must be used.

APPENDICES

When these interrogating particles pass through a molecule of interest one of three things can happen. The most likely of these is: nothing. In the case of X-rays almost all of the photons will not interact with the molecule. When interaction does occur, we call this scattering and this can happen in two ways. An inelastic scattering event results in deposition of energy in the molecule, resulting in radiation damage and the re-emission of a particle different in energy, and, in wave-speak, phase to the incoming one. An elastic scattering event results in the re-emission, without energy loss or a change in phase, of a particle much like the incoming one, but in a direction that is dependent on the structure of the molecule. Both kinds of scattering events can be used to infer information about molecular structure, but it is elastic scattering events which are useful in X-ray diffraction experiments.

The inverse linear relationship between energy and wavelength (given by the Planck-Einstein relationship for photons, and the De Broglie relationship for matter waves of electrons and neutrons) results in the fact that waves of sufficiently short wavelength to interrogate atomic structures also carry energy that is in the regime that will destroy atomic interactions via inelastic scattering events. It is therefore impossible to repeatedly irradiate an individual molecule until sufficient information has been recovered to generate a structure. In most cases, for a single molecule of interest, it is difficult to record even one interaction because the molecule is destroyed so quickly. One solution is to use very short (tens of femtoseconds), and very bright, pulses of X-ray photons in X-ray Free Electron Laser (XFEL) experiments. In these experiments the photon-matter interaction finishes before the molecule has had time to disintegrate. Even in an XFEL, though, only a single image can be obtained, which is rarely enough to generate a structure. Also, XFELs are amongst the most expensive scientific instruments ever built.

While we cannot repeatedly irradiate a single molecule we can approximate doing so by looking at many copies of that molecule. In the case of single particle imaging approaches (such as single particle XFEL imaging, or single particle analysis of electron micrographs), as the name suggests, information from many noisy images of single molecules is combined. The combination step can be very challenging, due to the noise (See Principles of Electron Cryo-Microscopy (CryoEM), below). In the case of crystallographic diffraction methods we exploit the special interaction between waves and regular arrays of molecules (in particular, Bragg's Law) to keep the quantity of scattering events constant, both damaging inelastic ones, and useful elastic ones, but increase the amount of information we extract from each

elastic collision. Changing the ratio between the damage done and the information extracted can, in the best cases, allow us to record enough information to generate a structure.

4.1.2 Diffraction by an object yields its Fourier transform

As alluded to above, whilst it is helpful to think about the interaction between irradiating subatomic particles and matter in terms of collisions of particles, in fact crystallographic theory requires us to consider the wave-like properties of incident radiation. The interaction of waves and matter is governed by diffraction theory.

A wave consists of many (infinitely) small regions of space which oscillate with respect to some property. Each point can be considered as the source of a propagating spherical wave. For a propagating plane wave, points in a plane oscillate together, and the planar waveform can be explained by the sum of the spherical waveforms over space. When a wave interacts with scattering medium, each part of the scattering object itself acts as a point source, with the amplitude corresponding to the strength of the interaction with the incident wave. Although within the scattering medium the interactions between the scatter sources are complex due to interference between non-parallel waves, further from the object parallel waves dominate and the radial pattern is another plane wave (the scattered/diffracted wave), with properties determined by the structure of the scattering object.

In particular, the intensity of the scattered wave in any direction is determined largely by two things: the scattering density (the real space distribution of scattering potential), and the relative phase between scattered waves, which governs their interference and hence the measured intensity.

Figure 4-1 illustrates how we can derive an expression for the phase difference, $\Delta\varphi$, at a position \mathbf{r} away from the origin O, for a given scattering vector, \mathbf{S} . $\Delta\varphi$ is given by:

$$\Delta\varphi = \mathbf{S} \cdot \mathbf{r}$$

After weighting for the distribution of the scattering potential, $\rho(\mathbf{r})$, we can integrate over real space to get an expression for the scattered waveform, $F(\mathbf{S})$:

$$F(\mathbf{S}) = \int \rho(\mathbf{r}) \cdot e^{(2\pi i \mathbf{S} \cdot \mathbf{r})} d\mathbf{r}$$

APPENDICES

The introduction of the imaginary component into this formulation arises from the accounting trick of using Euler's formula to incorporate the phase of a wave into calculations in terms of vectors.

Importantly, this expression is in the form of a Fourier transform of the distribution of scattering potential in real space: the structure! Performing the inverse Fourier transform (something which is eminently tractable thanks to Fast Fourier Transform algorithms) on the scattered waveform, measured in frequency/reciprocal space, will therefore yield the scattering density:

$$\rho(\mathbf{r}) = \int F(\mathbf{S}) \cdot e^{(-2\pi i \mathbf{S} \cdot \mathbf{r})} d\mathbf{S}$$

Critically, to do this reverse transform we will need both the real valued amplitudes of the scattered waveform $F(\mathbf{S})$ and the complex-valued phases. Unfortunately, in simple X-ray diffraction experiments we are only able to measure the amplitude of scattered waveforms, this is the origin of the infamous “phase problem” in crystallography, whose solution will be discussed below.

In practical terms, because of radiation damage as discussed above, we are not able to reconstruct $\rho(\mathbf{r})$ from the X-ray diffraction pattern of a single molecule (even if we could recover phase information), which is why we instead measure scattering by crystals.

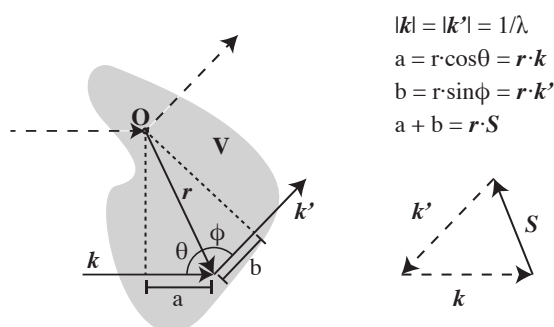


Figure 4-1 - Diffraction by an arbitrary object

See text for description.

4.1.3 Diffraction by a crystal

Crystals are highly symmetric objects. Symmetry describes a property of an object such that a geometric transformation can be applied to it and the returned object is indistinguishable from the original. The fundamental symmetry possessed by all crystals is the translational symmetry defined by the “lattice group”. This symmetry is described in terms of a set of three vectors, **a**, **b**, and **c**, each of which shifts any point in the lattice to an equivalent one, and together also describe the boundaries of the “unit cell”. There is a limited set of possible lattice symmetries in three dimensions, these are known as the 14 Bravais lattices. They are distinguished by the relationships between **a**, **b**, and **c**. For instance, in a tetragonal lattice $|a|=|b|\neq|c|$, and all three are perpendicular to one another.

Crystals also very often possesses additional “point group” symmetries within the unit cell, which describe symmetry operations relating copies of the asymmetric unit, of which there may be many within the unit cell, to each other. For chiral molecules, such as peptides and nucleic acids, the possible point group symmetry operations are limited to rotations and screw axes (which combine rotation with displacement by real fractions of the unit cell vectors). Only certain combinations of lattice and point groups are possible, for achiral asymmetric units there are 230 possibilities, known as “space groups”. For chiral asymmetric units, this is reduced to 65. Importantly, an asymmetric unit may contain several identical molecules, related by additional symmetry operations (this is known as non-crystallographic symmetry, or NCS).

At first glance we might imagine that the diffraction pattern observed in the waves scattered by a crystal would simply be a multiplication of the diffraction pattern of the unit cell, as we are simultaneously irradiating many identical copies of that unit cell, in identical orientations. However, this is not the case, again due to the effects of interference between scattered waves.

In a large ensemble of scattered waves, only those separated in phase by a whole number of wavelengths, i.e. precisely in phase, will constructively interfere, and all others will destructively interfere. In the context of a crystal this restriction is the key to recovering interpretable information. Bragg’s law succinctly describes when waves diffracted by equivalent points within each unit cell in the lattice (which will lie on a set of regularly spaced planes, see Figure 4-2) will be in phase, in terms of the distance between those

APPENDICES

planes, d , the angle between the incident beam and the plane family, θ , and the wavelength, λ :

$$n = d \cdot \frac{2\sin\theta}{\lambda}$$

Scattered waves will only constructively interfere for integer values of n . Clearly the set of conditions which will generate integer n is rather small, and we can work them out, as follows. The concepts are illustrated in 2D in Figure 4-2.

The families of planes on which equivalent points lie can be conveniently described by a set of indices, h, k , and l , denoted Miller indices, which have several derivations. The Miller indices for a plane family, hkl , are the number of times planes intersect each of the unit cell vectors \mathbf{abc} . There are an infinite number of plane families for any lattice. More importantly, and less intuitively, the Miller indices are also related to the “reciprocal lattice”. The reciprocal lattice is defined by the reciprocal lattice vectors, \mathbf{a}^* , \mathbf{b}^* , and \mathbf{c}^* , which are of reciprocal lengths relative to their real space counterparts, and to which their relative orientations are defined in trigonometric terms. A given integer reciprocal lattice vector, \mathbf{d}_{hkl}^* , can be decomposed as $h\mathbf{a}^* + k\mathbf{b}^* + l\mathbf{c}^*$, and corresponds to the normal to a lattice plane with Miller indices hkl .

If we now extend Bragg’s Law to 3 dimensions, we can see that constructive interference by the waves scattered by a plane family will only occur when the scattering vector \mathbf{S} is equal to \mathbf{d}_{hkl}^* . This condition is expressed geometrically in the Ewald’s Sphere construction, depicted in Figure 4-2. The usefulness of the reciprocal lattice now becomes clear, because when we do a diffraction experiment we know \mathbf{S} , we can index the diffraction pattern in terms of hkl , and this will correspond to one slice of the reciprocal lattice. By rotating the crystal relative to the incident waveform, and with it the reciprocal lattice, and measuring the scattered waves at a plane (the detector) we can systematically record the entirety of the reciprocal lattice (which is really just the Fourier transform of the real lattice).

So far, we have only considered diffraction by lattice points, but the same conclusions hold for arbitrary scattering density in the unit cell. Due to the properties of the Fourier transform, the diffraction pattern of a crystal corresponds to a convolution of the Fourier transform of the lattice and the unit cell. Point group symmetries within the unit cell, have a different effect, that of producing “systematic absences” in the diffraction pattern. The

reasons for this are not discussed here, but these absences are critically important for inferring the space group and ensuring a correct structure solution.

In summary, by recording the X-rays scattered by a crystal we are recording the Fourier transform of the electron density distribution in the crystal.

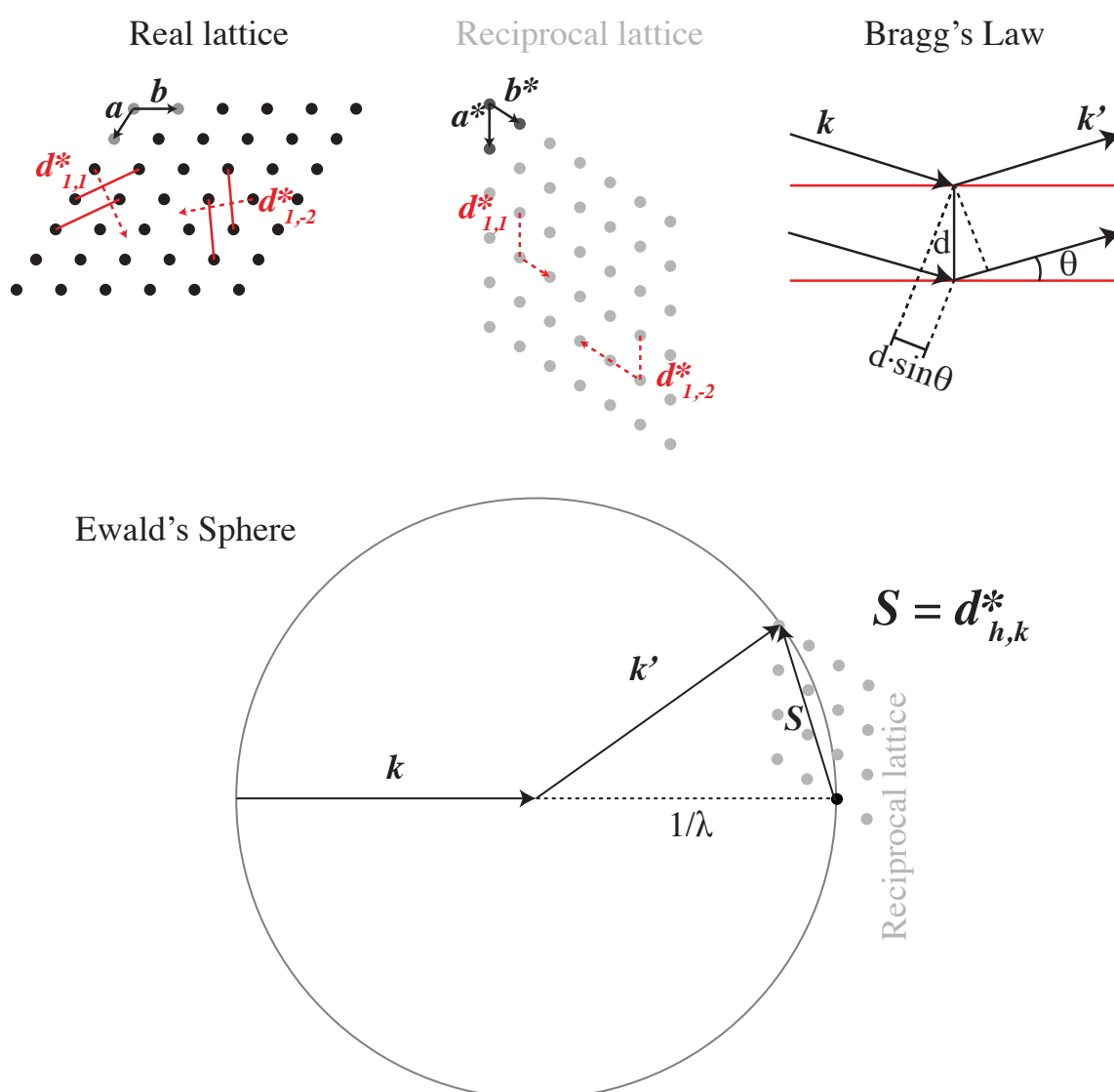


Figure 4-2 - Diffraction by a lattice

See text for description.

4.1.4 The phase problem

So, if we can collect measurements of $F(S)$ (the amplitudes and phases of the scattered rays) for a crystalline array of the molecule we are interested in, we will be able to do the Fourier transform to recover an approximation for the electron scattering density for the asymmetric unit. However, we are not out of the woods yet, as we cannot typically measure the phase component of $F(S)$. There are two ways to experimentally derive the relative phases of scattered waves: “isomorphous replacement” and “anomalous dispersion”, both make use of heavy atoms (often incorporated via soaking crystals in salt solutions, or by replacement of methionine with selenomethionine during protein production) in the crystal, and I will not discuss them further as I did not do them. For the crystal structures determined here I was able to use the non-experimental approach of “molecular replacement”, which allows the approximation of the unknown phases with calculated phases from a homologous molecule.

Even without phases, the way forward is to carry out a Fourier transform of the measured amplitudes of $F(S)$, to yield the Patterson Map. This 3-dimensional, real-valued, map has the interesting property of being an autoconvolution of the unit cell electron scattering density, with peaks corresponding to vectors between regions of high scattering density. For simple molecules the Patterson Map can be interpreted directly, and this is how the first crystal structures were solved, however for more complex molecules such as proteins this is not possible.

During molecular replacement, the number of copies of the homologous structure in the unit cell is estimated and a Patterson Map simulated for this number of copies, in various relative positions. These relative positions are optimised to maximise the similarity of the observed and calculated Patterson Maps. This search is greatly accelerated by the fact that Patterson Maps are centrosymmetric meaning that independent rotational and translational searches can be carried out. When a good agreement is found between the synthetic and measured maps, phases can be approximated for the observed $F(S)$ amplitudes, to give the “structure factors” which are used for model building and further refinement. These downstream processes are not discussed here.

4.2 Principles of Electron Cryo-Microscopy (CryoEM)

As discussed above, molecular structure can also be probed by firing electrons at a sample of interest. Here, I will discuss the basic principles of electron cryo-microscopy for single particle analysis (SPA).

4.2.1 Transmission electron microscopy

Transmission electron microscopy (TEM) is highly analogous to light microscopy, with optics based on lenses which can be thought of as being able to bend and focus rays and therefore generate magnified projection images. A typical optical scheme is shown in Figure 4-3. One important difference in the two modalities is the charge carried by the imaging particle, this causes many additional complications not discussed here. As is often mentioned, the wavelength of electrons used for electron microscopy is very small and the diffraction limit is rarely (never, for biological experiments) the limiting factor for the resolution ultimately obtained (e.g. λ of a 300 keV electron is 1.96 pm). Instead, resolution is limited by the comparatively poor quality of electron lenses, and, in the case of native biological specimens, by the rate of radiation damage.

CryoEM experiments for SPA use the TEM in bright field mode. Projection images are collected, with the intensity measured at any point on the detector corresponding to a line integral of the electron scattering (Coulomb) potential at a position in the sample. As we will see, by collecting images of many copies of a molecule of interest a 3-dimensional reconstruction of the electron scattering potential throughout the object can be calculated.

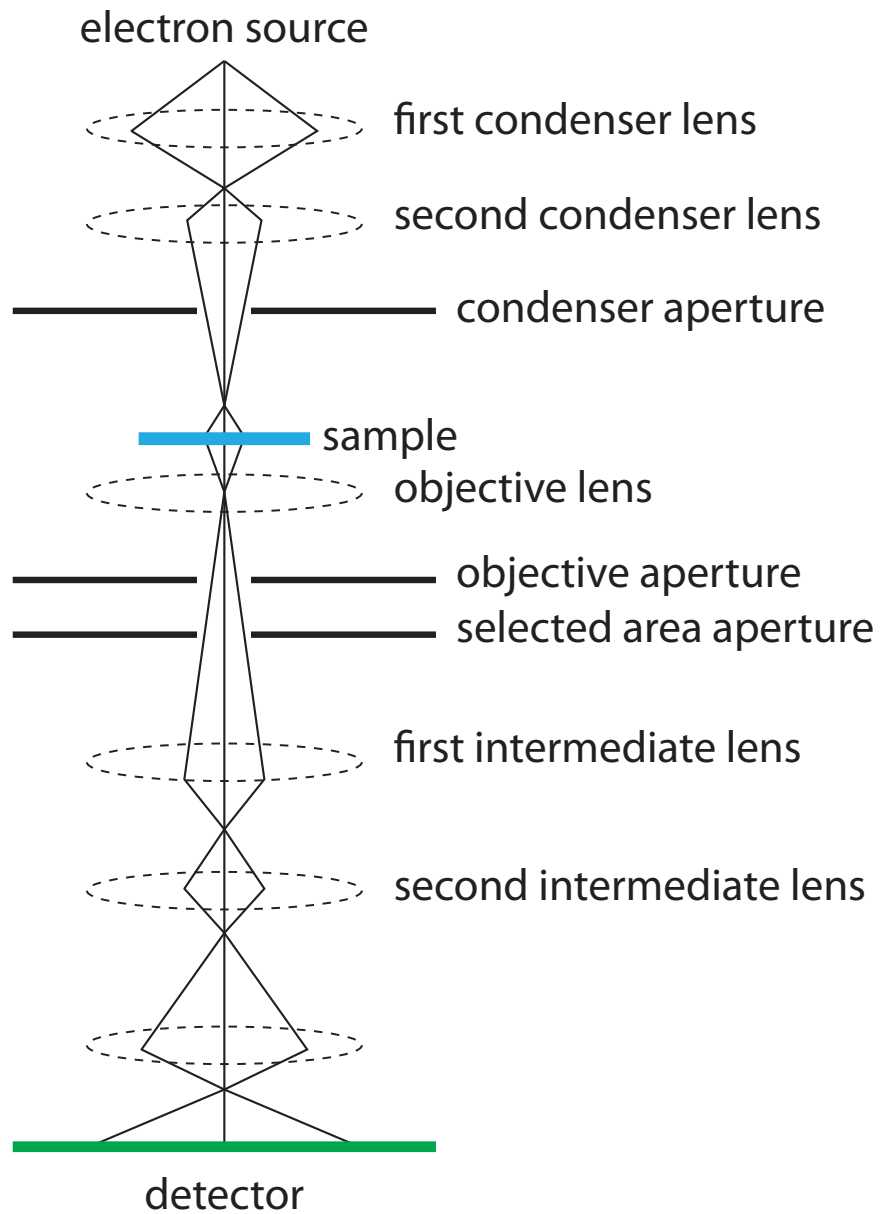


Figure 4-3 – Typical electron microscope optics

After Williams and Carter.

4.2.2 Cryo methods for biological samples

As alluded to, a major limitation for the imaging of native biological material is the radiation sensitivity of molecules built from low Z atoms. There are additional problems associated with working on biological material in a TEM, not least the fact that biological systems are typically functional in the aqueous phase (not compatible with the high vacuum required within the TEM column). A major breakthrough in biological EM was made by Jacques Dubochet and colleagues with the perfection of methods to freeze biological molecules in a thin layer of vitreous (amorphous) ice. In this “frozen hydrated” state molecular structure and solvent interaction is apparently preserved, and the low temperatures are radiation protective. For amorphous ice to remain so it must be kept below ~136 K, which necessitated the development of elaborate experimental procedures to ensure the sample is always cold.

4.2.3 Generating contrast for low Z specimens

Not only are low-Z atoms radiation sensitive, they generate very poor contrast – there is not much difference in the electron scattering potential of a biological carbon and a water oxygen. To generate additional contrast cryoEM images are typically collected with an applied defocus. This has the unfortunate consequence that the projection image of the Coulomb potential is convoluted with the so-called Contrast Transfer Function (CTF), a quasi-periodic sine function, in reciprocal space. The CTF must be modelled and corrected for during image processing, this is now possible to a very high degree of accuracy. The CTF also absolutely limits resolution, with greater defocus leading to a tighter limit, and data should be collected with the minimum defocus that still permits accurate particle alignment.

4.2.4 Projection matching

Given a collection of CTF-corrected images corresponding to many projections of the Coulomb potential distribution in the molecule of interest, all that is required is to accurately assign a set of “Euler angles” to the experimental images such that a consensus 3D reconstruction can be calculated. This task is somewhat complicated by several factors, however.

Firstly, sample heterogeneity will clearly prevent the finding of a single solution for angle assignment, and some classification scheme must be employed (several exist). Secondly, all of the reconstruction algorithms are local optimisers, and the initial model must be chosen

APPENDICES

carefully to avoid becoming trapped in a local minimum of refinement. Additionally, even with the various advances in direct electron detectors, microscope optics, and data collection strategies, cryoEM data are extremely noisy and recovering useful information is not a foregone conclusion, even for a well behaved sample.

Nevertheless, cryoEM reconstructions can now be determined to resolutions approaching those achieved via crystallography – the current record is ~ 1.5 Å. All high resolution cryoEM reconstructions are generated via iterative projection matching approaches. This can be carried out in real space but there are several computational advantages to carrying out the equivalent procedure in reciprocal space. A scheme illustrating this process is shown in Figure 4-4.

Figure 4-4 - Iterative projection matching and the central slice theorem

Adapted from (Nogales and Scheres, 2015).

A The central slice theorem states that 2D slices of the 3D Fourier transform of a volume are also 2D Fourier transforms of a 2D projection image of that volume. As mentioned in the text, many image processing operations are computationally easier in reciprocal space (notably, the specification of the smoothness prior which guards against overfitting in RELION).

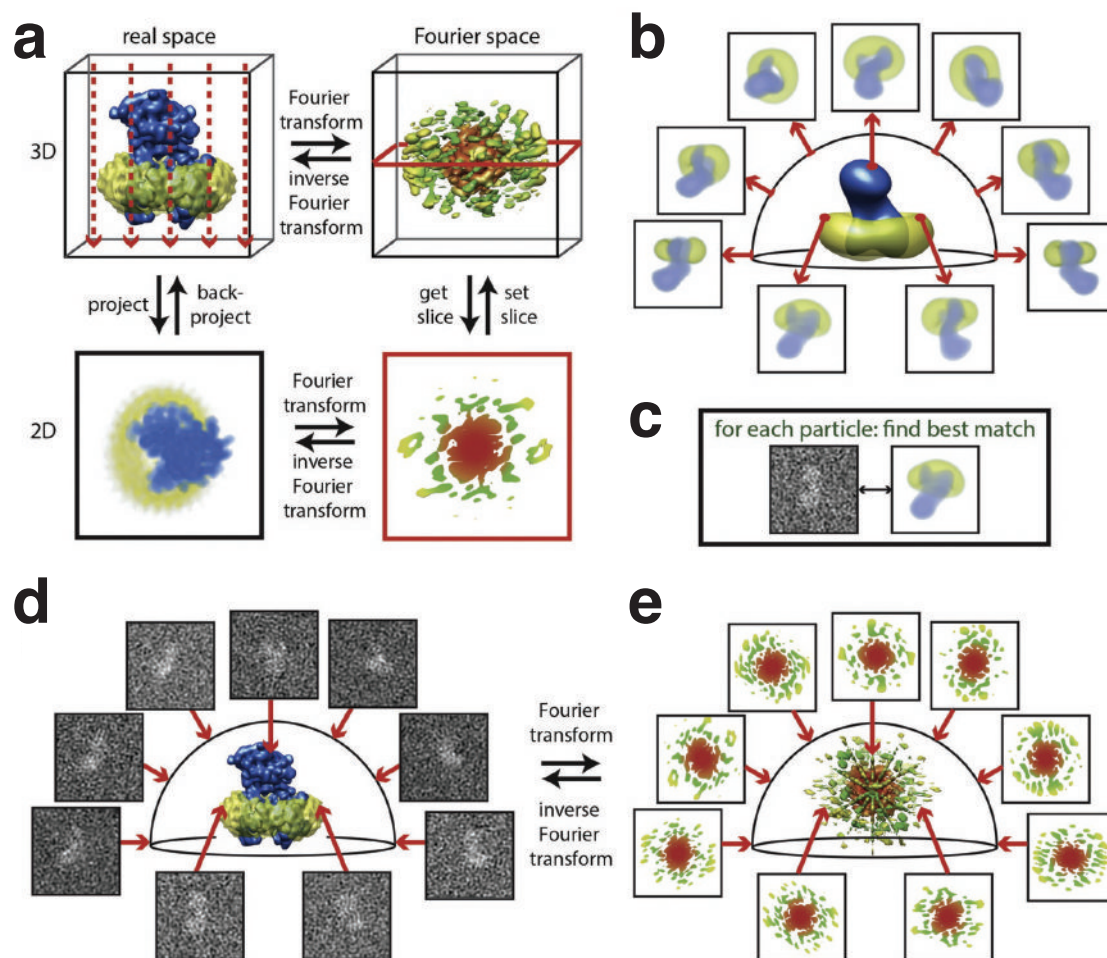
B In the first instance an initial model is generated, and projections from many possible viewpoints, with defined Euler angles, are generated *in silico*.

C For each image, or “particle”, in the dataset the best matching simulated projection is identified, and an approximate set of Euler angles is assigned (In RELION, probabilities that a particle corresponds to each of the viewpoints are assigned instead)

D In real space, an improved model (essentially, a tomographic reconstruction) is then generated using the angles assigned to the particle images.

E As implied by the central slice theorem, this process of reconstruction can be carried out very effectively in reciprocal space.

By iterating over steps B-E, an improved model is generated, and, in the best cases, this iterative approach can drive the resolution of the reconstruction down to that required to resolve atomic details.



4.3 Principles of Fluorescence Polarisation

The Invitrogen Fluorescence Polarisation Technical Resource Guide (Invitrogen, 4th edition) is an extremely useful practical guide to carrying out calculations for FP assays and guided me to the analysis strategies outlined here.

4.3.1 Fundamentals

Fluorescence polarisation (FP) is a powerful technique for monitoring interactions between a fluorescent probe and another molecule, largely developed for this purpose by Gregorio Weber (Jameson, 2001). The FP of a fluorophore is calculated after excitation with polarised light by measuring the intensity of the light emitted in two channels, one parallel to the electric vector of the excitation light (I_{\parallel}) and one perpendicular (I_{\perp}) to it. The FP (P) is given by the difference in these two channels normalised by their sum:

$$P = \frac{I_{\parallel} - I_{\perp}}{I_{\parallel} + I_{\perp}}$$

The difference can also be normalised by the total fluorescence (I_T), given by:

$$I_T = I_{\parallel} + 2I_{\perp}$$

This gives the fluorescence anisotropy (FA, A):

$$A = \frac{I_{\parallel} - I_{\perp}}{I_{\parallel} + 2I_{\perp}}$$

Which is related simply to the FP:

$$A = \frac{2P}{3 - P}$$

FA is preferred for calculations (because it makes them simpler) but the technique is usually referred to as FP. In typical regimes the two numbers are extremely similar. FP and FA values are often expressed in milli-units (mP and mA), these are simply the raw values multiplied by 1000.

FP (the technique) generates useful information because not all of the individual (identical) fluorophores in solution will respond the same way to the polarised excitation light.

Fluorophores with their absorption transition dipole more closely aligned with the electric vector of the excitation light are more likely to absorb light, and will then emit it, all else being equal, also polarised parallel to the excitation light. This is known as “photoselection”. Because fluorophores in solution are randomly orientated there is a maximum observable FA of 0.4. The observed FA value can depend on other factors however – which is why FP can be useful.

For a spherical (fluorescent) molecule, the observed FA is given by the Perrin equation (Perrin, 1926):

$$A = \frac{A_0}{1 + \tau/\theta}$$

Where A_0 is the fluorophore’s intrinsic anisotropy (for a molecule with parallel excitation and emission dipoles, i.e. most common fluorophores, this is 0.4), τ is the fluorescence lifetime, and θ is the rotational correlation time (the time taken to rotate through one radian). The rotational correlation time is itself a function of several variables:

$$\theta = \frac{\eta V}{k_b T}$$

Where η is the viscosity of the solution, V is the volume of the fluorescent molecule, k_b is the Boltzmann constant, and T is the temperature.

FP’s usefulness in biology stems from the fact that the differences in rotational correlation times arising from typical differences between the volumes of biological macromolecules are on the same order of magnitude as the fluorescence lifetimes of common fluorophores (Hall et al., 2016). This means that changes in the volume of fluorescent molecules, for instance the binding/unbinding of a fluorescent probe to a protein can be sensitively measured via FP.

4.3.2 Compensation for changes in fluorescence intensity upon binding

The quantum yield of many fluorophores is highly dependent on the chemical environment. In the context of FP this usually means that the FI of bound fluorophores is higher than unbound ones. This can be corrected for, however.

APPENDICES

Measurements of total FI over a titration of the non-fluorescent binding partner (the “receptor”) against a constant concentration of the fluorescent molecule (the “probe”) can be used to determine the quantum yield ratio (Q) of fluorescence emission intensities for bound (I_b) and free (I_f) fluorophore ($Q = I_f/I_b$). If the titration curve is sigmoid when plotted on a semi-log scale then the FI changes upon binding ($Q \neq 1$) and must be corrected for. I_b and I_f are the asymptotes of a simple one-site binding model:

$$I = I_f + (I_b - I_f) \cdot \frac{R_T}{K_d + R_T}$$

Where I is observed FI and R_T is total receptor concentration. Fitting this model will yield accurate values of I_b and I_f (but not of the other parameters!), and allow calculation of Q .

We also need estimates of the FA for the bound (A_b) and free (A_f) probe, which we can get from the same data, as these values are the asymptotes of a model which describes the measured anisotropy during titration of the receptor:

$$A = A_f + (A_b - A_f) \cdot \frac{R_T}{K_d + R_T}$$

With these values in hand the corrected anisotropy ($A_{corrected}$) can be calculated from the “apparent” anisotropy (A) using the relationship (Dandliker et al., 1981):

$$A_{corrected} = \frac{\frac{A - A_f}{A_b - A_f} \cdot Q \cdot A_b - A_f}{1 + \frac{A - A_f}{A_b - A_f} \cdot Q}$$

4.3.3 Estimation of K_d from binding isotherm

The corrected FA signal is shown for the titration of SaFtsZ into a fixed concentration of ATTO-550-GTP in Figure 2-15, p.88. An accurate K_d can be estimated from this experiment by fitting a binding model which corrects for receptor depletion (Swillens, 1995):

$$A_{corrected} = A_f + (A_b - A_f) \cdot \frac{(L_T + K_d + R_T) - \sqrt{(-L_T - K_d - R_T)^2 - 4 \cdot L_T \cdot R_T}}{2 \cdot L_T}$$

Where L_T is the total concentration of the probe, R_T is the total concentration of receptor, K_d is the dissociation constant, and anisotropy values are as above.

4.3.4 Estimation of K_i from IC50

Calculating K_i (in this case equal to K_d) values for FP-based competition assays is non-trivial when the affinity of inhibitors and probes is close to the concentration of the receptor and/or probe. A set of robust equations for this purpose were derived in (Nikolovska-Coleska et al., 2004). The key points are laid out here.

For a system where receptor, R , and ligand, L , bind with 1:1 stoichiometry to form a complex RL , and a competitive inhibitor, I , is added, at any time:

$$[R]_T = [R] + [RL] + [RI]$$

$$[L]_T = [L] + [RL]$$

$$[I]_T = [I] + [RI]$$

And where K_d and K_i are the dissociation constants of RL and RI , respectively, we also know that at equilibrium:

$$K_d = \frac{[R][L]}{[RL]}$$

$$K_i = \frac{[R][I]}{[RI]}$$

Working through from fundamental principles of FP (when corrected for fluorescence changes upon binding) it can be shown (non-obviously) that:

$$[RL]_{50} = \frac{[RL]_0}{2}$$

Where $[RL]_{50}$ is the concentration of protein:probe complexes at 50% inhibition and $[PL]_0$ is the concentration of the complex in the absence of an inhibitor. Using this and substituting in the obvious relationships described above it can be shown that:

$$K_i = \frac{[I]_{50}}{\frac{[L]_{50} + [R]_0}{K_d} + 1}$$

All of the numbers required to compute this can be calculated: $[I]_{50}$, the free inhibitor concentration at 50% inhibition, $[L]_{50}$, the free ligand at the same time, and $[R]_0$, the concentration of free protein in the absence of inhibitor.

APPENDICES

Considering the 0% inhibition scenario it can be shown that $[R]_0$ is the positive root of a quadratic equation, such that:

$$[R]_0 = \frac{-(K_d + L_T - R_T) + \sqrt{(K_d + L_T - R_T)^2 - 4 \cdot (-R_T \cdot K_d)}}{2}$$

$[RL]_0$ and $[L]_0$ are then easily determined:

$$[RL]_0 = [R]_T - [R]_0$$

$$[L]_0 = L_t - [RL]_0$$

And we can then solve for the concentrations at the 50% inhibition point (IC_{50} is the total concentration of inhibitor at this point):

$$[RL]_{50} = \frac{[RL]_0}{2}$$

$$[L]_{50} = [L]_T - [RL]_{50}$$

$$[I]_{50} = IC_{50} - R + \frac{K_d \cdot [RL]_{50}}{[L]_{50}} + [RL]_{50}$$

Finally allowing calculation of K_i ! This is the approach used for the K_i values shown in Figure 2-15B, p.88, and Figure 2-16, p.90, after IC_{50} is determined by fitting the competition model:

$$A_{corrected} = A_f + \frac{A_b - A_f}{1 + \frac{[I]_T}{IC_{50}}}$$

4.4 Additional figures

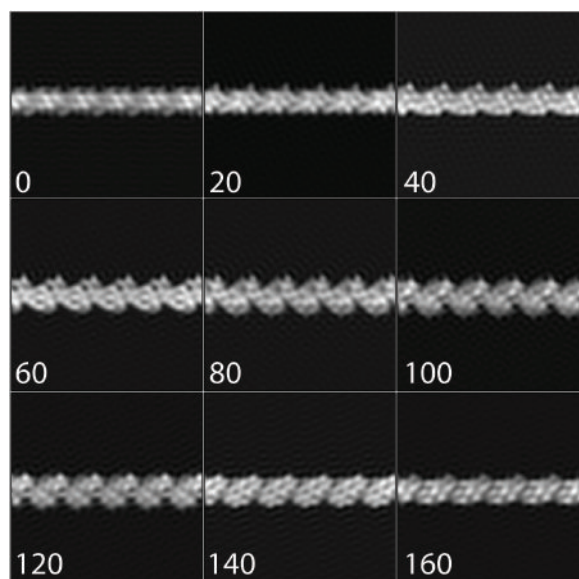


Figure 4-5 – Calculated projections of SaFtsZ crystal filaments

Projections of a SaFtsZ protofilament model constructed using the coordinates and symmetry of PDB entry 5MN4 (iFOF as per Section 2.1). Simulated EM density was generated using the EMAN2 script `e2pdb2mrc.py`, and the projections generated using `relion_project` with a maximum resolution of 10 Å. The filament is rotated along its long axis by the number of degrees indicated.

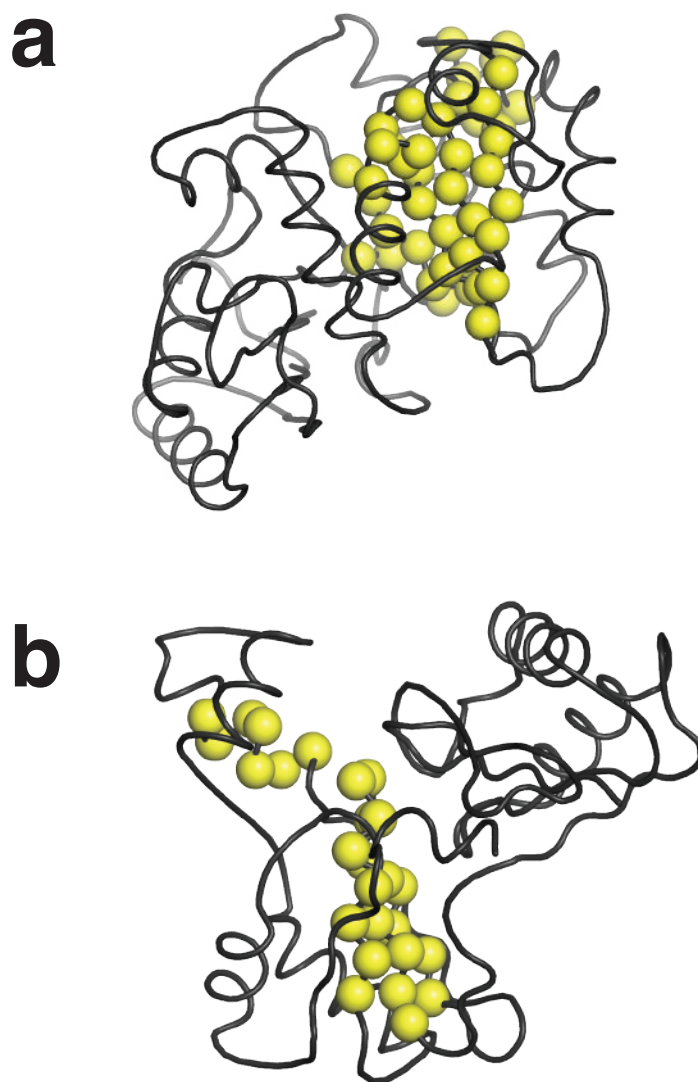


Figure 4-6 – Invariant regions plotted on conserved structural cores

Conformationally invariant residues (see text) are shown as yellow spheres on a black C α pseudo-ribbon joining residues which form the structurally conserved core of the tubulin (**A**) and actin (**B**) superfamilies.

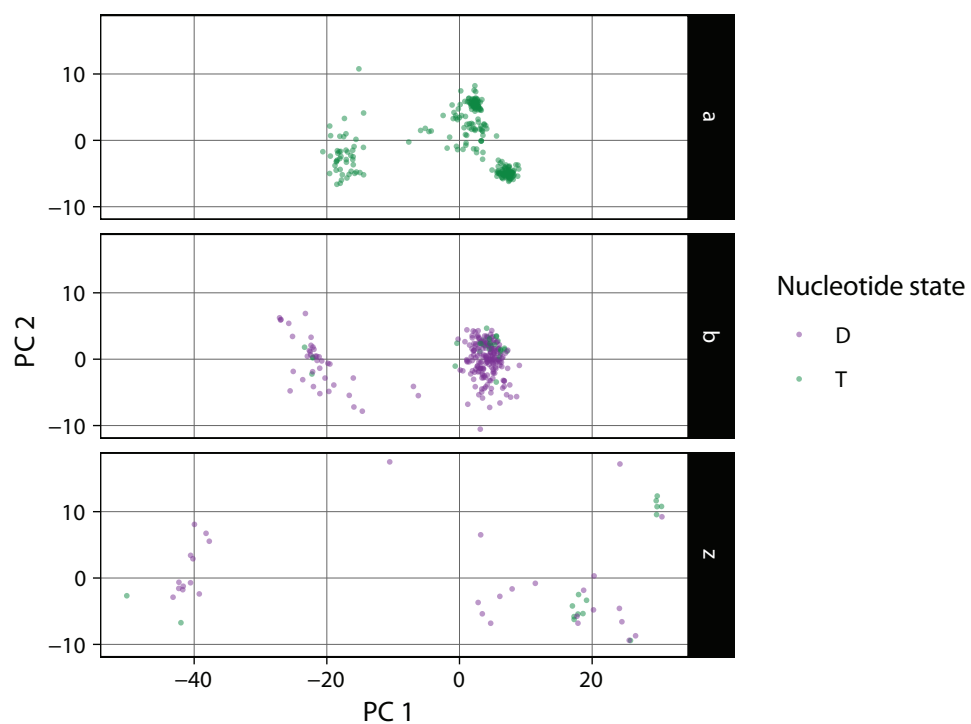


Figure 4-7 – PCA of tubulin subfamilies, coloured by nucleotide state

Same plot as Figure 2-20, with structures coloured instead by the hydrolysis state of the bound nucleotide, as indicated.

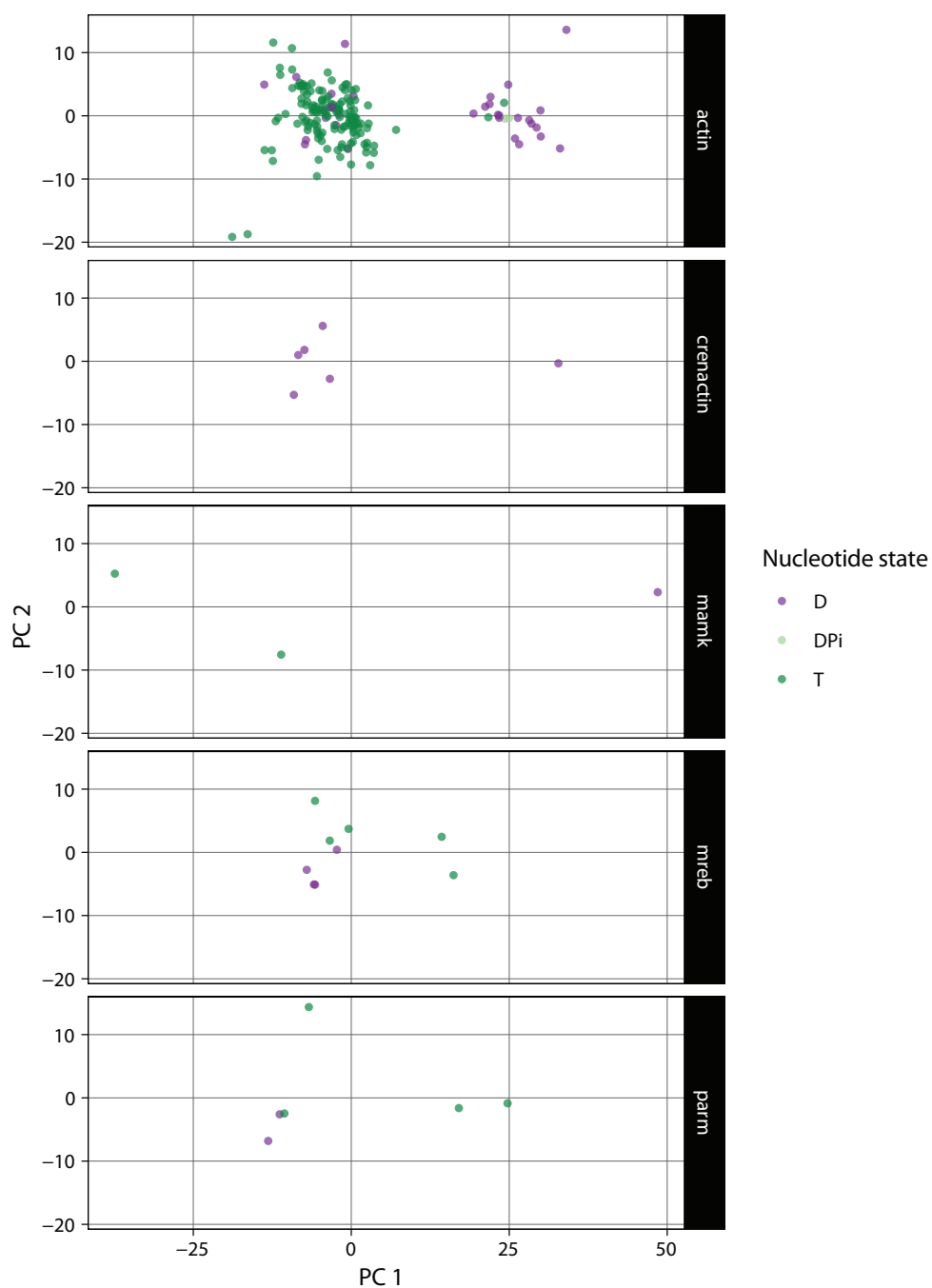


Figure 4-8 – PCA of actin subfamilies, coloured by nucleotide state

Same plot as Figure 2-22, with structures coloured instead by the hydrolysis state of the bound nucleotide, as indicated.

5 TABLES

Table 1 – Plasmids

<i>Plasmid</i>	<i>Source</i>	<i>Backbone</i>	<i>Gene</i>	<i>Construct</i>	<i>Tag</i>	<i>Resistance</i>	<i>Inducer</i>
pJW1	Tim Nierhaus	pHis17	SaFtsZ	Full length	None	Amp	IPTG
pJW3	Matt Tsim	pHis17	SaFtsZ	12-316	None	Amp	IPTG
pJW4	Matt Tsim	pHis17	SaFtsZ	12-316, F138A	None	Amp	IPTG
pJW5	Matt Tsim	pHis17	SaFtsZ	12-316, T66W	None	Amp	IPTG
pJW18	Piotr Szwedziak	pET9a	EcFtsZ	Full length	None	Kan	IPTG
pJW19	This work	pTXB1	EcZapA	Full length	C-intein-Chitin Binding Domain	Amp	IPTG
pJW62	This work	pHis17	SaFtsZ	12-316, L272D	C-His6	Amp	IPTG

Table 2 - Crystallographic and cryoEM data for section 2.1

Statistics		iFOF	2TCm	3FCm	4FCs	5FCm	cryoEM
		FtsZm3-SaF38A/rb2_9 Staphylococcus aureus FtsZ (F38A)	3D ₀ T66W_E8 Staphylococcus aureus FtsZ (T66W)	FtsZm3-SaF38A/rb4_5 Staphylococcus aureus FtsZ (F38A)	1L_L1MB9_H4_dL3_1 Staphylococcus aureus FtsZ (F38A)	1L_L1MB9_C8_d2_2_1 Staphylococcus aureus FtsZ (F38A)	Escherichia coli FtsZ
Sample							
UniProt ID		FTSZ_STA0U	FTSZ_STA0U	FTSZ_STA0U	FTSZ_STA0U	FTSZ_STA0U	FTSZ_ECOLI
Constructs		12-316, no tag F38A mutation	12-316, no tag T66W mutation	12-316, no tag F38A mutation	12-316, no tag F38A mutation	12-316, no tag F38A mutation	no tag full length,
Crystallisation/grids		10 mg/ml; 12.5 % w/v PEG 1k, 12.5 % w/v PEG 350, 12.5 % v/v MPD, 0.1 M bicine/Tris pH 8.5, 0.03 M NaF, NaBr and NaI; cryo 30 % ethylene glycol	10 mg/ml; LiCl 1.136 M, PEG 6,000 31.4 %, 0.1 M MES pH 6; cryo 20 % PEG 200	10 mg/ml; 12.5 % w/v PEG 4,350, 12.5 % w/v PEG 1k, 12.5 % v/v MPD, pH 6.5, 0.04 M MES/midazole, 0.03 M NaF, NaBr and NaI; cryo 30 %	10 mg/ml; 40% PEG monomethyl ether 350, 0.05 M MES pH 6; cryo 20 % glycerol	5 mg/ml; 1.6 M ammonium sulfate, 0.5 M LiCl; cryo 20 % glycerol	0.5 mg/ml in 50 mM HEPES/KOH, 100 mM K-acetate, 5 mM Mg- acetate, pH 7.7; Quantifoil Cu R2/2 200 mesh
Method		crystallography molecular replacement model 3VO8	crystallography molecular replacement model 3WGL	crystallography molecular replacement model zTCm	crystallography molecular replacement model zTCm	crystallography molecular replacement model zTCm	cryoEM single particle model 1FOF @ 20 Å
Data collection							
Beamline/microscope		ESRF id3zeht	ESRF id29	ESRF id3zeht	Diamond Iq4-1	Diamond Iq4-1	FEI Polara G2
Wavelength / energy		0.93 Å	0.9792 Å	0.93 Å	0.9282 Å	0.9282 Å	300 kV
Crystal / helical							
Space / point group		C2	P2 ₁ 2 ₁ 2 ₁	P2 ₁ 2 ₁ 2 ₁	1222	P3 ₂ 2 ₁	
Cell (Å)		71.8, 51.1, 88.1, 111°	43.8, 59.9, 187.7	41.1, 68.2, 207.9	116.1, 130.0, 134.1	69.8, 69.8, 295.5	
Twist / rise							
Data							
Resolution (Å)		15	2.8	3.2	3.3	3.5	7.8 Å, anisotropic
Completeness (%) ^a		98.5 (97.9)	98.2 (95.5)	99.9 (100)	94.5 (94.3)	98.3 (99.6)	
Multiplicity ^a		3.4 (3.4)	4.4 (4.3)	9.9 (8.8)	3.6 (3.6)	4.8 (5.1)	
(I) / σ(I) ^a		14.1 (1.7)	11.4 (3.0)	10.6 (1.7)	11.6 (1.9)	6.8 (1.4)	
R _{merge} ^a		0.045 (0.652)	0.109 (0.554)	0.132 (1.107)	0.098 (0.719)	0.146 (1.226)	
R _{int} ^a		0.045 (0.411)	0.056 (0.286)	0.043 (0.389)	0.055 (0.408)	0.073 (0.606)	
CC1/2		0.999 (0.740)	0.995 (0.781)	0.998 (0.737)	0.997 (0.696)	0.998 (0.853)	
Images, pixel size							1834, 1.34 Å
Defocus range, dose							-1.5 - -4.0 μm, 40 e/Å ²
Segments							511,000
Refinement							
R / R _{int} ^b		0.178 / 0.212	0.217 / 0.263	0.216 / 0.299	0.211 / 0.268	0.2649 / 0.3137	not refined
FSC (REFMAC)							
Models		1 chain/ASU; 12-315, 1 GDP, 1 MPD, 251 waters	2 chains/ASU; A13-62, 74-315, B13- 62, 74-202, 209-315, 2 GDP, no waters	2 chains/ASU; A13-201, 209-315, B12-315 2 GDP, no waters	2 chains/ASU; A/B13-315, 2 GTP, 2 Mg, no waters	2 chains/ASU; A/B13-202, 207-315, 2 GTP, no waters	
Bond length rmsd (Å)		0.009	0.006	0.010	0.002	0.002	
Bond angle rmsd (°)		1.58	0.946	1.573	0.505	0.575	
Favoured (%) ^c		99.6	99.6	100	99.8	99.8	
Disallowed (%) ^c		0.4	0	0	0.2	0.2	
MOLPROBITY score		99th percentile	99th percentile	98th percentile	100th percentile	100th percentile	
PDB ID		5MN4	5MN5	5MN6	5MN7	5MN8	

^a Values in parentheses refer to the highest recorded resolution shell. ^b 5% of reflections were randomly selected before refinement. ^c Percentage of residues in the Ramachandran plot (PROCHECK 'most favoured' and 'additionally allowed' added together).

Table 3 – Protein sequences

<i>Protein</i>	<i>Sequence</i>
SaFtsZ <i>Uniprot PoAo3I</i>	MLEFEQGFNHLATLKVIGVGGGGNNAVNRMIDHGMNNVEFIAINTDGQ ALNLSKAESKIQIGEKLTRGLGAGANPEIGKKAEEESREQIEDAIQGA DMVFVTSGMGGGTGTGAAPVVAKIAKEMGALTVGVVTRPFSFEGKRKQ TQAAAGVEAMKAAVDTLIVIPNDRLLDIVDKSTPMMEAFKEADNVLRQ GVQGISDLIAVSGEVNLDFAADVKTIMSNQGSALMGIGVSSGENRAVEA AKKAISSPLLETSIVGAQGVLMNITGGESLSLFEAQEAADIVQDAADE DVNMIFGTVINPELQDEIVVTVIATGFDDKPTSHGRKSGSTGFGTSVN TSSNATSKDESFTSNSSNAQATDSVSERTHTTKEDDIPSFIRNREERR SRRTTR
EcFtsZ <i>Uniprot PoA9A6</i>	MFEPMELTNDAVIKVIGVGGGGGNAVEHMRERIEGVEFFAVNTDAQA LRKTAVGQTIQIGSGITKGLGAGANPEVGRNAADEDRDALRAALEGAD MVFIAAGMGGGTGTGAAPVVAEVAKDLGILTVAVVTKPFNFEGKKRMA FAEQGITELSKHVDLITIPNDKLLKVLGRGISLLDAFGAANDVLKGA VQGIAELITRPGLMNVDFADVRTVMSEMGYAMMGSGVASGEDRAEEAA EMAISSPLLEDIDLSGARGVLVNITAGFDLRLDEFETVGNTIRAFASD NATVVIGTSLDPDMNDELRVTVVATGIGMDKRPEITLVTNKQVQQPVM DRYQQHGMAPLTQEKPVAKVVNDNAPQTAKEPDYLDIPAFLRKQAD
EcZapA-Intein-CBD <i>Cleavage site: “ ”</i> <i>ZapA Uniprot PoADS2</i>	MSAQPVDIQIFGRSLRVNCPDQRDALNQAADDLNQRLQDLKERTRVT NTEQLVFIAALNISYELAQEAKATRDYAASMEQRIRMLQQTIEQALLE QGRITEKTNQNF CITGDALVALPEGESVRIADIVPGARPNSDNAID LKVLDRHGPNVLADRLFHSGEHPVYTVRTVEGLRVGTGTANHPLLCLVD VAGVPTLLWKLIDEIKPGDYAVIQRSFVSVCAGFARGKPEFAPTTYT VGVPGLVRFLEAHHRDPDAQIADELTDGRFYAKVASVTDAGVQPVY SLRVDTADHAFITNGFVSHATGLTGLNSGLTTNPGVSAWQVNTAYTAG QLVTYNGKTYKCLQPHTSLAGWEPSNVPALWQLQ

TABLES

Table 4 – Deposited structures used for tubulin superfamily analysis

<i>PDB ID</i>	<i>Family</i>	<i>Polymerisation state</i>	<i>Nucleotide state</i>
5syc_A	a	f	T
5syg_A	a	f	T
5syf_A	a	f	T
5syf_A	a	f	T
5ijo_A	a	f	T
5n5n_G	a	f	T
5ij9_A	a	f	T
4drx_A	a	m	T
5lp6_A	a	m	T
5lp6_C	a	m	T
5gon_A	a	m	T
5gon_C	a	m	T
6evw_A	a	f	T
5kmg_A	a	f	T
5c8y_A	a	m	T
5c8y_C	a	m	T
5xi7_C	a	m	T
5xi7_A	a	m	T
5xi5_C	a	m	T
5xi5_A	a	m	T
5cb4_A	a	m	T
5cb4_C	a	m	T
5xhc_A	a	m	T
5xhc_C	a	m	T
5ca1_C	a	m	T
5ca1_A	a	m	T
5yl4_C	a	m	T
5yl4_A	a	m	T
5ezy_A	a	m	T
5ezy_C	a	m	T
6bry_A	a	m	T
6bry_C	a	m	T
6br1_C	a	m	T
6br1_A	a	m	T
6brf_A	a	m	T
6brf_C	a	m	T
5h74_C	a	m	T
5h74_A	a	m	T
6bs2_A	a	m	T
6bs2_C	a	m	T
5h70_C	a	m	T
5h70_A	a	m	T
4i4t_A	a	m	T
4i4t_C	a	m	T
4ihj_A	a	m	T
4ihj_C	a	m	T
5jh7_C	a	m	T
5jh7_A	a	m	T
5xlz_C	a	m	T
5xlz_A	a	m	T
5njh_C	a	NA	T
5njh_A	a	m	T
5xlt_C	a	m	T
5xlt_A	a	m	T
4i55_C	a	m	T
4i55_A	a	m	T
5fnv_A	a	m	T
5fnv_C	a	m	T
4i50_A	a	m	T
4i50_C	a	m	T
5j2t_A	a	m	T
5j2t_C	a	m	T
507a_C	a	m	T
507a_A	a	m	T
4o4l_A	a	m	T
4o4l_C	a	m	T

5lov_C	a	m	T
5lov_A	a	m	T
5iyz_C	a	m	T
5iyz_A	a	m	T
5itz_A	a	m	T
4o4h_C	a	m	T
4o4h_A	a	m	T
5lxt_C	a	m	T
5lxt_A	a	m	T
5nm5_A	a	m	T
5ogc_A	a	f	T
4o4i_A	a	m	T
4o4i_C	a	m	T
4o2b_A	a	m	T
4o2b_C	a	m	T
6fkl_A	a	m	T
6fkl_C	a	m	T
6fjm_A	a	m	T
6fjm_C	a	m	T
5eib_C	a	m	T
4tv9_C	a	m	T
4tv9_A	a	m	T
5nqt_A	a	m	T
5m5c_A	a	f	T
4iij_C	a	m	T
4iij_A	a	m	T
5lxs_A	a	m	T
5lxs_C	a	m	T
4tv8_A	a	m	T
4tv8_C	a	m	T
5m7g_C	a	m	T
5m7g_A	a	m	T
5m8g_A	a	m	T
5m8g_C	a	m	T
5bmv_C	a	m	T
5bmv_A	a	m	T
5osk_A	a	m	T
5osk_C	a	m	T
4o2a_A	a	m	T
4o2a_C	a	m	T
5jvd_C	a	m	T
5jvd_A	a	m	T
5nfz_A	a	m	T
5nfz_C	a	m	T
6ff_C	a	m	T
6ff_A	a	m	T
5m7e_A	a	m	T
5m7e_C	a	m	T
4yj2_A	a	m	T
4yj2_C	a	m	T
4yj3_C	a	m	T
4yj3_A	a	m	T
6fii_A	a	m	T
6fii_C	a	m	T
5m8d_A	a	m	T
5m8d_C	a	m	T
5la6_A	a	m	T
5la6_C	a	m	T
5xag_C	a	m	T
5xag_A	a	m	T
5j2u_A	a	m	T
5j2u_C	a	m	T
4wbn_A	a	m	T
4wbn_C	a	m	T
5mio_A	a	m	T
6fkj_C	a	m	T
6fkj_A	a	m	T
5ngt_C	a	m	T
5ngt_A	a	m	T
6bbn_A	a	m	T

TABLES

6bbn_C	a	m	T
4tuy_A	a	m	T
4tuy_C	a	m	T
ijff_A	a	f	T
5nqu_A	a	m	T
5lyj_C	a	m	T
5lyj_A	a	m	T
5ov7_C	a	m	T
5ov7_A	a	m	T
4o4j_C	a	m	T
4o4j_A	a	m	T
5xaf_A	a	m	T
5xaf_C	a	m	T
5nd4_A	a	f	T
5mf4_A	a	m	T
5mf4_C	a	m	T
3j8x_A	a	f	T
3jas_A	a	f	T
5yls_C	a	m	T
5yls_A	a	m	T
6evy_A	a	f	T
6dpv_A	a	f	T
6bjc_A	a	f	T
3jat_A	a	f	T
6evz_A	a	f	T
3jak_A	a	f	T
6dpw_A	a	f	T
5cao_A	a	m	T
5cao_C	a	m	T
6ewo_A	a	f	T
5xkg_A	a	m	T
5xkg_C	a	m	T
6boc_A	a	m	T
6boc_C	a	f	T
3jal_A	a	f	T
6dpu_A	a	f	T
3jar_A	a	f	T
6boi_A	a	f	T
6cvn_B	a	f	T
5ylj_A	a	m	T
5ylj_C	a	m	T
6evx_A	a	f	T
5xkf_C	a	m	T
5xkf_A	a	m	T
5yl2_C	a	m	T
5yl2_A	a	m	T
4zhq_C	a	m	T
4zhq_A	a	m	T
4zi7_C	a	m	T
4zi7_A	a	m	T
3j8y_A	a	f	T
5xiw_C	a	m	T
5xiw_A	a	m	T
5jcb_C	a	m	T
5jcb_A	a	m	T
5xkh_C	a	m	T
5xkh_A	a	m	T
5xp3_C	a	m	T
5xp3_A	a	m	T
5jqg_C	a	m	T
5jqg_A	a	m	T
3jaw_A	a	f	T
6cvj_A	a	f	T
5xke_A	a	m	T
5xke_C	a	m	T
4zol_A	a	m	T
4zol_C	a	m	T
6bol_A	a	f	T
3ryc_A	a	m	T
3ryc_C	a	m	T

3ryf_A	a	m	T
3ryf_C	a	m	T
4f61_C	a	m	T
4f61_A	a	m	T
3ryi_C	a	m	T
3ryi_A	a	m	T
4eb6_C	a	m	T
4eb6_A	a	m	T
3ut5_A	a	m	T
3ryh_C	a	m	T
3ryh_A	a	m	T
4hna_A	a	m	T
4f6r_A	a	m	T
4lnu_A	a	m	T
5eyp_A	a	m	T
1sao_A	a	m	T
1tvk_A	a	f	T
1sa1_A	a	m	T
3e22_A	a	m	T
1z2b_A	a	m	T
1tub_A	a	f	T
3j6f_A	a	f	T
3j6e_A	a	f	T
5mm4_A	a	f	T
1ffx_A	a	m	T
5jco_A	a	f	T
3hkb_A	a	m	T
3n2k_A	a	m	T
4x1y_A	a	m	T
4x1y_C	a	m	T
4x20_C	a	m	T
4x20_A	a	m	T
3hkd_A	a	m	T
3hkc_A	a	m	T
4xi1_A	a	m	T
4xi1_C	a	m	T
3hke_A	a	m	T
3n2g_A	a	m	T
4x1k_C	a	m	T
4x1k_A	a	m	T
5kx5_C	a	m	T
5kx5_A	a	m	T
5ucy_A	a	f	T
4u3j_A	a	m	T
4ffb_A	a	m	T
5w3h_A	a	f	T
5w3j_A	a	f	T
5w3f_A	a	f	T
5mjs_E	a	f	T
5mlv_B	a	f	T
5syc_B	b	f	D
5syg_B	b	f	D
5syf_B	b	f	D
5ij9_B	b	f	D
5ij9_B	b	f	D
4drx_B	b	m	T
5lp6_D	b	m	D
5lp6_B	b	m	D
5gon_B	b	m	D
5gon_D	b	m	D
5kmg_B	b	f	D
5c8y_B	b	m	D
5c8y_D	b	m	D
5xi7_B	b	m	D
5xi7_D	b	m	T
5xi5_D	b	m	T
5xi5_B	b	m	D
5cb4_D	b	m	D
5cb4_B	b	m	D

TABLES

5xhc_B	b	m	D
5xhc_D	b	m	T
5cat_B	b	m	D
5cat_D	b	m	D
5yl4_B	b	m	D
5yl4_D	b	m	T
5ezy_B	b	m	D
5ezy_D	b	m	T
6bry_D	b	m	D
6bry_B	b	m	D
6br1_D	b	m	D
6br1_B	b	m	D
6brf_D	b	m	D
6brf_B	b	m	D
5h74_D	b	m	T
5h74_B	b	m	D
6bs2_B	b	m	D
6bs2_D	b	m	D
5h7o_B	b	m	D
5h7o_D	b	m	T
4i4t_B	b	m	D
4i4t_D	b	m	D
4ihj_D	b	m	D
4ihj_B	b	m	D
5jh7_D	b	m	D
5jh7_B	b	m	D
5xlz_D	b	m	T
5xlz_B	b	m	D
5njh_B	b	NA	D
5njh_D	b	m	D
5xlt_B	b	m	D
5xlt_D	b	m	D
4i55_D	b	m	D
4i55_B	b	m	D
5fnv_B	b	m	D
5fnv_D	b	m	T
4i5o_D	b	m	D
4i5o_B	b	m	D
5j2t_D	b	m	D
5j2t_B	b	m	D
5o7a_B	b	m	D
5o7a_D	b	m	D
4o4l_D	b	m	D
4o4l_B	b	m	D
5lov_B	b	m	D
5lov_D	b	m	D
5iyz_D	b	m	D
5iyz_B	b	m	D
5itz_B	b	m	D
4o4h_B	b	m	D
4o4h_D	b	m	D
5lxt_B	b	m	D
5lxt_D	b	m	D
5nm5_B	b	m	D
5ogc_B	b	f	D
4o4i_D	b	m	D
4o4i_B	b	m	D
4o2b_D	b	m	D
4o2b_B	b	m	D
6fkl_B	b	m	D
6fkl_D	b	m	D
6fjm_B	b	m	D
6fjm_D	b	m	D
5eib_D	b	m	T
4tv9_D	b	m	D
4tv9_B	b	m	D
5nqt_B	b	m	D
5m5c_B	b	f	D
4iij_B	b	m	D
4iij_D	b	m	D

5lxs_B	b	m	D
5lxs_D	b	m	D
4tv8_B	b	m	D
4tv8_D	b	m	D
5m7g_B	b	m	D
5m7g_D	b	m	D
5m8g_D	b	m	D
5m8g_B	b	m	D
5bmV_D	b	m	D
5bmV_B	b	m	D
5osk_B	b	m	D
5osk_D	b	m	D
4o2a_D	b	m	D
4o2a_B	b	m	D
5jvd_B	b	m	D
5jvd_D	b	m	D
5nfz_B	b	m	D
5nfz_D	b	m	D
6ff_D	b	m	D
6ff_B	b	m	D
5m7e_D	b	m	D
5m7e_B	b	m	D
4yj2_D	b	m	D
4yj2_B	b	m	D
4yj3_D	b	m	D
4yj3_B	b	m	D
6fii_D	b	m	D
6fii_B	b	m	D
5m8d_D	b	m	D
5m8d_B	b	m	D
5la6_B	b	m	D
5la6_D	b	m	D
5xag_D	b	m	D
5xag_B	b	m	D
5j2u_B	b	m	D
5j2u_D	b	m	D
4wbn_D	b	m	D
4wbn_B	b	m	D
5mio_B	b	m	D
6fkj_D	b	m	D
6fkj_B	b	m	D
5ng1_B	b	m	D
5ng1_D	b	m	D
6bbn_B	b	m	D
6bbn_D	b	m	D
4tuy_B	b	m	D
4tuy_D	b	m	D
1jff_B	b	f	D
5nqu_B	b	m	D
5lyj_B	b	m	D
5lyj_D	b	m	D
5ov7_D	b	m	D
5ov7_B	b	m	D
4o4j_B	b	m	D
4o4j_D	b	m	D
5xaf_B	b	m	D
5xaf_D	b	m	D
5nd4_B	b	f	D
5mf4_D	b	m	D
5mf4_B	b	m	D
3j8x_B	b	f	D
3jas_B	b	f	D
5yls_D	b	m	T
5yls_B	b	m	D
6evy_B	b	f	T
6dpv_B	b	f	D
6evz_B	b	f	D
3jak_B	b	f	T
6dpw_B	b	f	T
5cao_B	b	m	D

TABLES

5cao_D	b	m	D
6ewo_B	b	f	D
5xkg_B	b	m	D
5xkg_D	b	m	T
6boc_B	b	m	D
6boc_D	b	f	D
3jar_B	b	f	D
6boi_B	b	f	D
6cvn_A	b	f	D
6cvn_C	b	f	D
5ylj_B	b	m	D
5ylj_D	b	m	T
6evx_B	b	f	D
5xkf_D	b	m	T
5xkf_B	b	m	D
5yl2_B	b	m	D
5yl2_D	b	m	T
4zhq_D	b	m	D
4zhq_B	b	m	D
4zi7_B	b	m	D
4zi7_D	b	m	D
3j8y_B	b	NA	D
5xiw_B	b	m	D
5xiw_D	b	m	T
5jcb_B	b	m	D
5jcb_D	b	m	D
5xkh_B	b	m	D
5xkh_D	b	m	T
5xp3_D	b	m	T
5xp3_B	b	m	D
5jqg_B	b	m	D
5jqg_D	b	m	T
3jaw_B	b	f	T
6cvj_C	b	f	D
6cvj_B	b	f	D
5xke_B	b	m	D
5xke_D	b	m	T
4zol_B	b	m	D
4zol_D	b	m	D
6bol_B	b	f	D
3ryc_D	b	m	T
3ryc_B	b	m	D
3ryf_B	b	m	T
3ryf_D	b	m	T
4f61_B	b	m	D
3ryi_B	b	m	D
4eb6_B	b	m	D
4eb6_D	b	m	D
3ut5_B	b	m	D
3ut5_D	b	m	D
4hna_B	b	m	D
4f6r_B	b	m	D
4lnu_B	b	m	D
5eyp_B	b	m	D
1sao_B	b	m	D
3du7_D	b	m	T
1tvk_B	b	f	D
1sa1_B	b	m	D
3e22_B	b	m	D
1z2b_B	b	m	D
1tub_B	b	f	D
3j6f_B	b	f	D
5mm4_B	b	f	D
1ffx_B	b	m	D
3hkb_B	b	m	D
3n2k_B	b	m	D
4x1y_D	b	m	D
4x1y_B	b	m	D
4x20_B	b	m	D
4x20_D	b	m	D

3hkd_B	b	m	D
3hkc_B	b	m	D
4xti_D	b	m	D
4xti_B	b	m	D
3hke_B	b	m	D
3n2g_B	b	m	D
4x1k_B	b	m	D
4x1k_D	b	m	D
5kx5_D	b	m	D
5kx5_B	b	m	D
5ucy_B	b	f	D
4u3j_B	b	m	T
4ffb_B	b	m	T
5w3h_B	b	f	D
5w3j_B	b	f	D
5w3f_B	b	f	D
5mjs_A	b	f	D
5mlv_C	b	f	D
2vap_A	z	m	D
1w5e_A	z	m	T
1fsz_A	z	m	D
1w5b_A	z	m	T
1w5b_B	z	m	T
1w5a_A	z	m	T
1w5a_B	z	m	T
4m8i_A	z	f	D
5h5g_A	z	f	D
5h5g_B	z	m	D
5xdu_A	z	f	D
5xdt_A	z	f	D
3voa_A	z	f	D
3vob_A	z	f	D
5xdv_A	z	f	D
5xdw_A	z	f	D
3vo8_A	z	f	D
3wgn_A	z	f	T
5h5h_A	z	f	D
5h5i_A	z	NA	D
4dxd_A	z	f	D
5mn4_A	z	f	D
5mn6_B	z	m	D
5mn6_A	z	m	D
5mn8_A	z	m	T
5mn5_A	z	m	T
5mn5_B	z	m	T
3wgl_A	z	m	D
3wgm_A	z	f	T
3wgk_A	z	m	D
1rlu_A	z	m	T
4kwe_A	z	m	D
5zue_A	z	m	T
2qiy_A	z	m	T
1rq7_A	z	m	D
5v68_E	z	m	D
5v68_B	z	m	D
2rho_B	z	m	D
2rho_A	z	m	T
2rhl_A	z	m	D
2rhl_B	z	m	D
1ofu_A	z	m	D
1ofu_B	z	m	D
2vaw_A	z	m	D
2r6r_I	z	m	D
2r75_I	z	m	T

TABLES

Table 5 – Deposited structures used for actin superfamily analysis

<i>PDB ID</i>	<i>Family</i>	<i>Polymerisation state</i>	<i>Nucleotide state</i>
4bql_B	crenactin	m	D
4bql_A	crenactin	m	D
5ly3_A	crenactin	m	D
5mwl_A	crenactin	f	D
4cj7_A	crenactin	m	D
4bql_D	crenactin	m	D
5ljv_A	mamk	f	D
5ljw_B	mamk	m	T
5ljw_A	mamk	m	T
5aey_A	parm	f	T
4a61_A	parm	m	T
4a62_A	parm	f	T
2zgy_A	parm	m	D
2zgz_A	parm	m	T
1mwm_A	parm	m	D
1jcg_A	mreb	f	T
4czk_A	mreb	f	T
4czf_A	mreb	f	D
4czh_A	mreb	f	D
4czg_A	mreb	f	D
4czj_A	mreb	f	T
4czl_A	mreb	m	D
4czm_B	mreb	m	T
4czm_A	mreb	m	T
4a2b_A	ftsa	f	T
4a2a_A	ftsa	f	T
1e4g_T	ftsa	m	T
3wqt_B	ftsa	f	T
3wqt_C	ftsa	f	T
3wto_A	ftsa	m	T
3wqt_A	ftsa	f	T
3wqu_C	ftsa	f	T
3wqu_A	ftsa	f	T
5jlf_A	actin	f	D
4cbw_A	actin	m	T
4cbu_A	actin	m	T
5mvv_A	actin	m	T
5ogw_A	actin	f	D
5ce3_A	actin	m	T
4ci6_A	actin	m	T
4m63_D	actin	m	T
4m63_E	actin	m	T
4m63_C	actin	m	T
5wfn_A	actin	m	T
4rwt_A	actin	m	T
3mn9_A	actin	m	T
2hf4_A	actin	m	T
3mn7_A	actin	m	T
3mn6_A	actin	m	T
3mmv_A	actin	m	T
2hf3_A	actin	m	D
3el2_A	actin	m	T
3eku_A	actin	m	T
3eks_A	actin	m	T
4jhd_A	actin	m	T
1nmi_A	actin	m	T
1nmd_A	actin	m	T
1nlv_A	actin	m	T
3ci5_A	actin	m	T
3cip_A	actin	m	T
1cof_A	actin	m	T
3chw_A	actin	m	T
3a5n_C	actin	m	T
3a5l_C	actin	m	D
3a5o_C	actin	m	T
3a5m_C	actin	m	T
5jllh_A	actin	f	D
1d4x_A	actin	m	T

4efh_A	actin	m	D
1cog_A	actin	m	T
1dej_A	actin	m	T
1hlu_A	actin	m	T
2btf_A	actin	m	T
6fit_H	actin	f	T
3ub5_A	actin	m	T
3u4l_A	actin	m	T
2oan_A	actin	m	T
3ffk_E	actin	m	T
2asp_A	actin	m	T
4gy2_B	actin	m	T
3buz_B	actin	m	T
2ff6_A	actin	m	T
3cjb_A	actin	m	T
4b1w_B	actin	m	T
3tpq_D	actin	m	T
3u9z_A	actin	m	D
2qor_A	actin	m	T
2fxu_A	actin	m	T
4pkh_F	actin	m	D
3mn5_A	actin	m	T
3ffk_B	actin	m	T
3sjh_A	actin	m	T
3u8x_A	actin	m	T
3u9d_C	actin	m	T
3u9d_A	actin	m	T
1ijj_A	actin	m	T
1sqk_A	actin	m	D
3ue5_A	actin	m	T
2gwk_B	actin	m	T
50oe_A	actin	f	T
4k43_A	actin	m	D
4k42_A	actin	m	D
1eqy_A	actin	m	T
2hmp_A	actin	m	T
2aso_A	actin	m	T
2pav_A	actin	m	T
1s22_A	actin	m	T
1wua_A	actin	m	T
1esv_A	actin	m	T
1lot_B	actin	m	T
3hbt_A	actin	m	T
1yxq_A	actin	m	T
2hmp_B	actin	m	T
1qz6_A	actin	m	T
2gwj_A	actin	m	T
1ma9_B	actin	m	T
1yxq_B	actin	m	T
4z94_A	actin	m	T
4pki_A	actin	m	T
4pkg_A	actin	m	T
6fm2_A	actin	m	D
2vcp_A	actin	m	T
5onv_A	actin	f	D
50oc_A	actin	f	D
6fhl_A	actin	f	DPi
5ood_A	actin	f	DPi
50of_A	actin	f	D
2a42_A	actin	m	T
2dik_A	actin	m	T
2a3z_A	actin	m	T
2a4l_A	actin	m	T
3j8a_A	actin	f	D
2a4o_A	actin	m	T
2zwh_A	actin	f	D
1j6z_A	actin	m	D
1atn_A	actin	m	T
4b1z_B	actin	m	T
3m6g_A	actin	m	T
1nwk_A	actin	m	T
2q97_A	actin	m	T

TABLES

1y64_A	actin	m	T
2vyp_A	actin	m	T
2ff3_B	actin	m	T
4pkh_A	actin	m	D
1t44_A	actin	m	T
2q31_A	actin	m	T
3m1f_A	actin	m	T
4b1y_B	actin	m	T
3tpq_B	actin	m	T
2v52_B	actin	m	T
2q1n_A	actin	m	T
4hot_B	actin	m	T
4hoy_B	actin	m	T
4hox_B	actin	m	T
1mdu_B	actin	m	T
2pbd_A	actin	m	T
2vyp_B	actin	m	T
1rgi_A	actin	m	T
6avb_A	actin	f	D
6av9_A	actin	f	D
2v51_B	actin	m	T
2yjf_A	actin	m	T
2yjf_E	actin	m	T
2yje_A	actin	m	T
4b1v_A	actin	m	T
4b1z_A	actin	m	T
4b1u_B	actin	m	T
4ho3_B	actin	m	T
2a5x_A	actin	m	T
4hov_B	actin	m	T
1kxp_A	actin	m	T
2qou_A	actin	m	T
2asm_A	actin	m	T
1qz5_A	actin	m	T
4pl8_B	actin	m	T
4pl8_A	actin	m	T
3tpq_E	actin	m	T
3tpq_A	actin	m	T
5yu8_A	actin	m	D
2gwk_A	actin	m	T
4b1x_B	actin	m	T
4eah_D	actin	m	T
1h1v_A	actin	m	T
4k41_A	actin	m	T
2q36_A	actin	m	T
5ubo_A	actin	m	T
3cjc_A	actin	m	T
6cth_A	actin	f	D
6cig_A	actin	f	D
6cid_A	actin	f	D
6bnp_F	actin	f	D
6bnp_A	actin	f	D
6bnp_B	actin	f	D
6bnp_D	actin	f	D
3tu5_A	actin	m	T
3j8i_D	actin	f	D
3daw_A	actin	m	T
1rfq_A	actin	m	T
1rfq_B	actin	m	T
1rdw_X	actin	m	T
4wyb_A	actin	m	T
1lcu_A	actin	m	T
4pkh_I	actin	m	D
1p8z_A	actin	m	T
3w3d_A	actin	m	T
1yag_A	actin	m	T
5nbm_C	actin	m	T
5nbn_C	actin	m	T
1yvn_A	actin	m	T

6 REFERENCES

- Abreu, N., Mannoubi, S., Ozyamak, E., Pignol, D., Ginet, N., and Komeili, A. (2014). Interplay between Two Bacterial Actin Homologs, MamK and MamK-Like, Is Required for the Alignment of Magnetosome Organelles in *Magnetospirillum magneticum* AMB-1. *J. Bacteriol.* 196, 3111–3121.
- Addinall, S.G., and Lutkenhaus, J. (1996). FtsZ-spirals and -arcs determine the shape of the invaginating septa in some mutants of *Escherichia coli*. *Mol. Microbiol.* 22, 231–237.
- Afonine, P.V., Poon, B.K., Read, R.J., Sobolev, O.V., Terwilliger, T.C., Urzhumtsev, A., and Adams, P.D. (2018). Real-space refinement in PHENIX for cryo-EM and crystallography. *Acta Crystallogr. Sect. Struct. Biol.* 74, 531–544.
- Alushin, G.M., Lander, G.C., Kellogg, E.H., Zhang, R., Baker, D., and Nogales, E. (2014). High-Resolution Microtubule Structures Reveal the Structural Transitions in $\alpha\beta$ -Tubulin upon GTP Hydrolysis. *Cell* 157, 1117–1129.
- Amos, L.A., and Löwe, J. (2017). Overview of the Diverse Roles of Bacterial and Archaeal Cytoskeletons. In *Prokaryotic Cytoskeletons*, J. Löwe, and L.A. Amos, eds. (Springer International Publishing), pp. 1–26.
- Andreu, J.M., Schaffner-Barbero, C., Huecas, S., Alonso, D., Lopez-Rodriguez, M.L., Ruiz-Avila, L.B., Núñez-Ramírez, R., Llorca, O., and Martín-Galiano, A.J. (2010). The Antibacterial Cell Division Inhibitor PC190723 Is an FtsZ Polymer-stabilizing Agent That Induces Filament Assembly and Condensation. *J. Biol. Chem.* 285, 14239–14246.
- Araújo-Bazán, L., Ruiz-Avila, L.B., Andreu, D., Huecas, S., and Andreu, J.M. (2016). Cytological Profile of Antibacterial FtsZ Inhibitors and Synthetic Peptide MciZ. *Front. Microbiol.* 7.
- Artola, M., Ruiz-Avila, L.B., Vergoñós, A., Huecas, S., Araujo-Bazán, L., Martín-Fontecha, M., Vázquez-Villa, H., Turrado, C., Ramírez-Aportela, E., Hoegl, A., et al. (2015). Effective GTP-Replacing FtsZ Inhibitors and Antibacterial Mechanism of Action. *ACS Chem. Biol.* 10, 834–843.
- Artola, M., Ruíz-Avila, L.B., Ramírez-Aportela, E., Martínez, R.F., Araujo-Bazán, L., Vázquez-Villa, H., Martín-Fontecha, M., Oliva, M.A., Martín-Galiano, A.J., Chacón, P., et al. (2016). The structural assembly switch of cell division protein FtsZ probed with fluorescent allosteric inhibitors. *Chem. Sci.*
- Ausmees, N., Kuhn, J.R., and Jacobs-Wagner, C. (2003). The Bacterial Cytoskeleton: An Intermediate Filament-Like Function in Cell Shape. *Cell* 115, 705–713.
- Aylett, C.H.S., and Duggin, I.G. (2017). The Tubulin Superfamily in Archaea. In *Prokaryotic Cytoskeletons*, J. Löwe, and L.A. Amos, eds. (Springer International Publishing), pp. 393–417.
- Aylett, C.H.S., Löwe, J., and Amos, L.A. (2011). New Insights into the Mechanisms of Cyto motive Actin and Tubulin Filaments. *Int. Rev. Cell Mol. Biol.* 292, 1–71.
- Bagchi, S., Tomenius, H., Belova, L.M., and Ausmees, N. (2008). Intermediate filament-like proteins in bacteria and a cytoskeletal function in *Streptomyces*. *Mol. Microbiol.* 70, 1037–1050.

REFERENCES

- Baranova, N., Radler, P., Hernandez-Rocamora, V.M., Alfonso, C., Lopez-Pelegrin, M., Rivas, G., Vollmer, W., and Loose, M. (2018). FtsZ assembles the bacterial cell division machinery by a diffusion-and-capture mechanism. *BioRxiv* 485656.
- Barry, R.M., and Gitai, Z. (2011). Self-assembling enzymes and the origins of the cytoskeleton. *Curr. Opin. Microbiol.* 14, 704–711.
- Bartlett, T.M., Bratton, B.P., Duvshani, A., Miguel, A., Sheng, Y., Martin, N.R., Nguyen, J.P., Persat, A., Desmarais, S.M., VanNieuwenhze, M.S., et al. (2017). A Periplasmic Polymer Curves *Vibrio cholerae* and Promotes Pathogenesis. *Cell* 168, 172–185.e15.
- Becker, E., Herrera, N.C., Gunderson, F.Q., Derman, A.I., Dance, A.L., Sims, J., Larsen, R.A., and Pogliano, J. (2006). DNA segregation by the bacterial actin AlfA during *Bacillus subtilis* growth and development. *EMBO J.* 25, 5919–5931.
- Bendezú, F.O., Hale, C.A., Bernhardt, T.G., and Boer, P.A.J. de (2009). RodZ (YfgA) is required for proper assembly of the MreB actin cytoskeleton and cell shape in *E. coli*. *EMBO J.* 28, 193–204.
- Berleman, J.E., Vicente, J.J., Davis, A.E., Jiang, S.Y., Seo, Y.-E., and Zusman, D.R. (2011). FrzS Regulates Social Motility in *Myxococcus xanthus* by Controlling Exopolysaccharide Production. *PLOS ONE* 6, e23920.
- Bharat, T.A.M., Murshudov, G.N., Sachse, C., and Löwe, J. (2015). Structures of actin-like ParM filaments show architecture of plasmid-segregating spindles. *Nature* 523, 106–110.
- Bi, E., and Lutkenhaus, J. (1991). FtsZ ring structure associated with division in *Escherichia coli*. *Nature* 354, 161–164.
- Billaudeau, C., Chastanet, A., Yao, Z., Cornilleau, C., Mirouze, N., Fromion, V., and Carballido-López, R. (2017). Contrasting mechanisms of growth in two model rod-shaped bacteria. *Nat. Commun.* 8, ncomms15370.
- Bisson-Filho, A.W., Discola, K.F., Castellen, P., Blasios, V., Martins, A., Sforça, M.L., Garcia, W., Zeri, A.C.M., Erickson, H.P., Dessen, A., et al. (2015). FtsZ filament capping by MciZ, a developmental regulator of bacterial division. *Proc. Natl. Acad. Sci.* 112, E2130–E2138.
- Bisson-Filho, A.W., Hsu, Y.-P., Squyres, G.R., Kuru, E., Wu, F., Jukes, C., Sun, Y., Dekker, C., Holden, S., VanNieuwenhze, M.S., et al. (2017). Treadmilling by FtsZ filaments drives peptidoglycan synthesis and bacterial cell division. *Science* 355, 739–743.
- de Boer, P., Crossley, R., and Rothfield, L. (1992). The essential bacterial cell-division protein FtsZ is a GTPase. *Nature* 359, 254–256.
- Bork, P., Sander, C., and Valencia, A. (1992). An ATPase domain common to prokaryotic cell cycle proteins, sugar kinases, actin, and hsp70 heat shock proteins. *Proc. Natl. Acad. Sci. U. S. A.* 89, 7290–7294.
- Bowman, G.R., Comolli, L.R., Zhu, J., Eckart, M., Koenig, M., Downing, K.H., Moerner, W.E., Earnest, T., and Shapiro, L. (2008). A polymeric protein anchors the chromosomal origin/ParB complex at a bacterial cell pole. *Cell* 134, 945–955.
- Bramhill, D., and Thompson, C.M. (1994). GTP-dependent polymerization of *Escherichia coli* FtsZ protein to form tubules. *Proc. Natl. Acad. Sci.* 91, 5813–5817.

- Bramkamp, M., Emmins, R., Weston, L., Donovan, C., Daniel, R.A., and Errington, J. (2008). A novel component of the division-site selection system of *Bacillus subtilis* and a new mode of action for the division inhibitor MinCD. *Mol. Microbiol.* 70, 1556–1569.
- Bringmann, M., Landrein, B., Schudoma, C., Hamant, O., Hauser, M.-T., and Persson, S. (2012). Cracking the elusive alignment hypothesis: the microtubule–cellulose synthase nexus unraveled. *Trends Plant Sci.* 17, 666–674.
- Brouhard, G.J., and Rice, L.M. (2018). Microtubule dynamics: an interplay of biochemistry and mechanics. *Nat. Rev. Mol. Cell Biol.* 19, 451–463.
- Buey, R.M., Díaz, J.F., and Andreu, J.M. (2006). The Nucleotide Switch of Tubulin and Microtubule Assembly: A Polymerization-Driven Structural Change. *Biochemistry* 45, 5933–5938.
- Buss, J., Coltharp, C., Huang, T., Pohlmeier, C., Wang, S.-C., Hatem, C., and Xiao, J. (2013). In vivo organization of the FtsZ-ring by ZapA and ZapB revealed by quantitative super-resolution microscopy. *Mol. Microbiol.* 89, 1099–1120.
- Buss, J.A., Peters, N.T., Xiao, J., and Bernhardt, T.G. (2017). ZapA and ZapB form an FtsZ-independent structure at midcell. *Mol. Microbiol.* n/a-n/a.
- Cabeen, M.T., Charbon, G., Vollmer, W., Born, P., Ausmees, N., Weibel, D.B., and Jacobs-Wagner, C. (2009). Bacterial cell curvature through mechanical control of cell growth. *EMBO J.* 28, 1208–1219.
- Cabeen, M.T., Herrmann, H., and Jacobs-Wagner, C. (2011). The domain organization of the bacterial intermediate filament-like protein crescentin is important for assembly and function. *Cytoskeleton* 68, 205–219.
- Caldas, P., López-Pelegrín, M., Pearce, D.J.G., Budanur, N.B., Brugués, J., and Loose, M. (2019). ZapA stabilizes FtsZ filament bundles without slowing down treadmilling dynamics. *BioRxiv* 580944.
- Carlton, J.G., and Martin-Serrano, J. (2007). Parallels Between Cytokinesis and Retroviral Budding: A Role for the ESCRT Machinery. *Science* 316, 1908–1912.
- Cassini, A., Högberg, L.D., Plachouras, D., Quattrocchi, A., Hoxha, A., Simonsen, G.S., Colomb-Cotinat, M., Kretzschmar, M.E., Devleeschauwer, B., Cecchini, M., et al. (2019). Attributable deaths and disability-adjusted life-years caused by infections with antibiotic-resistant bacteria in the EU and the European Economic Area in 2015: a population-level modelling analysis. *Lancet Infect. Dis.* 19, 56–66.
- Centres for Disease Control and Prevention (2013). Antibiotic Resistance Threats in the United States.
- Cha, J.H., and Stewart, G.C. (1997). The divIVA minicell locus of *Bacillus subtilis*. *J. Bacteriol.* 179, 1671–1683.
- Chaikeeratisak, V., Nguyen, K., Khanna, K., Brilot, A.F., Erb, M.L., Coker, J.K.C., Vavilina, A., Newton, G.L., Buschauer, R., Pogliano, K., et al. (2017). Assembly of a nucleus-like structure during viral replication in bacteria. *Science* 355, 194–197.
- Charon, N.W., Cockburn, A., Li, C., Liu, J., Miller, K.A., Miller, M.R., Motaleb, Md.A., and Wolgemuth, C.W. (2012). The Unique Paradigm of Spirochete Motility and Chemotaxis. *Annu. Rev. Microbiol.* 66, 349–370.

REFERENCES

- Chernyatina, A.A., Guzenko, D., and Strelkov, S.V. (2015). Intermediate filament structure: the bottom-up approach. *Curr. Opin. Cell Biol.* 32, 65–72.
- Chong, S., Mersha, F.B., Comb, D.G., Scott, M.E., Landry, D., Vence, L.M., Perler, F.B., Benner, J., Kucera, R.B., Hirvonen, C.A., et al. (1997). Single-column purification of free recombinant proteins using a self-cleavable affinity tag derived from a protein splicing element. *Gene* 192, 271–281.
- Chou, S.Z., and Pollard, T.D. (2019). Mechanism of actin polymerization revealed by cryo-EM structures of actin filaments with three different bound nucleotides. *Proc. Natl. Acad. Sci.* 116, 4265–4274.
- Coltharp, C., Buss, J., Plumer, T.M., and Xiao, J. (2016). Defining the rate-limiting processes of bacterial cytokinesis. *Proc. Natl. Acad. Sci.* 201514296.
- Crick, F.H.C. (1952). Is α -Keratin a Coiled Coil? *Nature* 170, 882–883.
- Dandliker, W.B., Hsu, M.L., Levin, J., and Rao, B.R. (1981). Equilibrium and kinetic inhibition assays based upon fluorescence polarization. *Methods Enzymol.* 74 Pt C, 3–28.
- Deng, X., Fink, G., Bharat, T.A.M., He, S., Kureisaite-Ciziene, D., and Löwe, J. (2017). Four-stranded mini microtubules formed by *Prostheco bacter* BtubAB show dynamic instability. *Proc. Natl. Acad. Sci.* 201705062.
- Deng, X., Llamazares, A.G., Wagstaff, J., Hale, V.L., Cannone, G., McLaughlin, S.H., Kureisaite-Ciziene, D., and Löwe, J. (2019). Bactofilins form non-polar filaments that bind to membranes directly. *BioRxiv* 617639.
- Derman, A.I., Becker, E.C., Truong, B.D., Fujioka, A., Tucey, T.M., Erb, M.L., Patterson, P.C., and Pogliano, J. (2009). Phylogenetic analysis identifies many uncharacterized actin-like proteins (Alps) in bacteria: regulated polymerization, dynamic instability and treadmilling in Alp7A. *Mol. Microbiol.* 73, 534–552.
- Derman, A.I., Nonejuie, P., Michel, B.C., Truong, B.D., Fujioka, A., Erb, M.L., and Pogliano, J. (2012). Alp7R Regulates Expression of the Actin-Like Protein Alp7A in *Bacillus subtilis*. *J. Bacteriol.* 194, 2715–2724.
- Diaz, J.F., Kralicek, A., Mingorance, J., Palacios, J.M., Vicente, M., and Andreu, J.M. (2001). Activation of Cell Division Protein FtsZ CONTROL OF SWITCH LOOP T₃ CONFORMATION BY THE NUCLEOTIDE γ -PHOSPHATE. *J. Biol. Chem.* 276, 17307–17315.
- Dobro, M.J., Samson, R.Y., Yu, Z., McCullough, J., Ding, H.J., Chong, P.L.-G., Bell, S.D., and Jensen, G.J. (2013). Electron cryotomography of ESCRT assemblies and dividing *Sulfolobus* cells suggests that spiraling filaments are involved in membrane scission. *Mol. Biol. Cell* 24, 2319–2327.
- Dobro, M.J., Oikonomou, C.M., Piper, A., Cohen, J., Guo, K., Jensen, T., Tadayon, J., Donermeyer, J., Park, Y., Solis, B.A., et al. (2017). Uncharacterized bacterial structures revealed by electron cryotomography. *J. Bacteriol.* JB.00100-17.
- Dominguez, R., and Holmes, K.C. (2011). Actin Structure and Function. *Annu. Rev. Biophys.* 40, 169–186.

- Domínguez-Escobar, J., Chastanet, A., Crevenna, A.H., Fromion, V., Wedlich-Söldner, R., and Carballido-López, R. (2011). Processive Movement of MreB-Associated Cell Wall Biosynthetic Complexes in Bacteria. *Science* 333, 225–228.
- Donovan, C., Heyer, A., Pfeifer, E., Polen, T., Wittmann, A., Krämer, R., Frunzke, J., and Bramkamp, M. (2015). A prophage-encoded actin-like protein required for efficient viral DNA replication in bacteria. *Nucleic Acids Res.* 43, 5002–5016.
- Du, S., Pichoff, S., Kruse, K., and Lutkenhaus, J. (2018). FtsZ filaments have the opposite kinetic polarity of microtubules. *Proc. Natl. Acad. Sci.* 115, 10768–10773.
- Duggin, I.G., Aylett, C.H.S., Walsh, J.C., Michie, K.A., Wang, Q., Turnbull, L., Dawson, E.M., Harry, E.J., Whitchurch, C.B., Amos, L.A., et al. (2015). CetZ tubulin-like proteins control archaeal cell shape. *Nature* 519, 362–365.
- Duman, R., Ishikawa, S., Celik, I., Strahl, H., Ogasawara, N., Troc, P., Löwe, J., and Hamoen, L.W. (2013). Structural and genetic analyses reveal the protein SepF as a new membrane anchor for the Z ring. *Proc. Natl. Acad. Sci.* 110, E4601–E4610.
- Durand-Heredia, J., Rivkin, E., Fan, G., Morales, J., and Janakiraman, A. (2012). Identification of ZapD as a Cell Division Factor That Promotes the Assembly of FtsZ in *Escherichia coli*. *J. Bacteriol.* 194, 3189–3198.
- Ebersbach, G., Briegel, A., Jensen, G.J., and Jacobs-Wagner, C. (2008). A self-associating protein critical for chromosome attachment, division, and polar organization in *caulobacter*. *Cell* 134, 956–968.
- Eddy, S.R. (2011). Accelerated Profile HMM Searches. *PLOS Comput. Biol.* 7, e1002195.
- Edgar, R.C. (2004). MUSCLE: multiple sequence alignment with high accuracy and high throughput. *Nucleic Acids Res.* 32, 1792–1797.
- El-Gebali, S., Mistry, J., Bateman, A., Eddy, S.R., Luciani, A., Potter, S.C., Qureshi, M., Richardson, L.J., Salazar, G.A., Smart, A., et al. (2019). The Pfam protein families database in 2019. *Nucleic Acids Res.* 47, D427–D432.
- Elsen, N.L., Lu, J., Parthasarathy, G., Reid, J.C., Sharma, S., Soisson, S.M., and Lumb, K.J. (2012). Mechanism of Action of the Cell-Division Inhibitor PC190723: Modulation of FtsZ Assembly Cooperativity. *J. Am. Chem. Soc.* 134, 12342–12345.
- Em, M., F, M., B, N., A, D., D, D., Dr, Z., and T, M. (2010). Bacterial motility complexes require the actin-like protein, MreB and the Ras homologue, MglA. *EMBO J.* 29, 315–326.
- Ent, F. van den, and Löwe, J. (2000). Crystal structure of the cell division protein FtsA from *Thermotoga maritima*. *EMBO J.* 19, 5300–5307.
- van den Ent, F., Amos, L.A., and Löwe, J. (2001). Prokaryotic origin of the actin cytoskeleton. *Nature* 413, 39–44.
- van den Ent, F., Izoré, T., Bharat, T.A., Johnson, C.M., and Löwe, J. (2014). Bacterial actin MreB forms antiparallel double filaments. *ELife* 3, e02634.

REFERENCES

- Erb, M.L., Kraemer, J.A., Coker, J.K.C., Chaikerasitsak, V., Nonejuie, P., Agard, D.A., and Pogliano, J. (2014). A bacteriophage tubulin harnesses dynamic instability to center DNA in infected cells. *ELife* 3, e03197.
- Erickson, H.P. (2019). Microtubule assembly from single flared protofilaments - forget the cozy corner? *Biophys. J.* S0006349519303844.
- Erickson, H.P., Anderson, D.E., and Osawa, M. (2010). FtsZ in bacterial cytokinesis: cytoskeleton and force generator all in one. *Microbiol. Mol. Biol. Rev.* MMBR 74, 504–528.
- Errington, J. (2015). Bacterial morphogenesis and the enigmatic MreB helix. *Nat. Rev. Microbiol.* 13, 241–248.
- Ettema, T.J.G., Lindås, A.-C., and Bernander, R. (2011). An actin-based cytoskeleton in archaea. *Mol. Microbiol.* 80, 1052–1061.
- Eun, Y.-J., Kapoor, M., Hussain, S., and Garner, E.C. (2015). Bacterial filament systems: towards understanding their emergent behavior and cellular functions. *J. Biol. Chem.* jbc.R115.637876.
- Evans, P. (2006). Scaling and assessment of data quality. *Acta Crystallogr. D Biol. Crystallogr.* 62, 72–82.
- Fair, R.J., and Tor, Y. (2014). Antibiotics and Bacterial Resistance in the 21st Century. *Perspect. Med. Chem.* 6, 25–64.
- Fenton, A.K., Lambert, C., Wagstaff, P.C., and Sockett, R.E. (2010a). Manipulating Each MreB of *Bdellovibrio bacteriovorus* Gives Diverse Morphological and Predatory Phenotypes. *J. Bacteriol.* 192, 1299–1311.
- Fenton, A.K., Hopley, L., Butan, C., Subramaniam, S., and Sockett, R.E. (2010b). A coiled-coil-repeat protein ‘Ccrp’ in *Bdellovibrio bacteriovorus* prevents cellular indentation, but is not essential for vibroid cell morphology. *FEMS Microbiol. Lett.* 313, 89–95.
- Fink, G., and Aylett, C.H.S. (2017). Tubulin-Like Proteins in Prokaryotic DNA Positioning. In *Prokaryotic Cytoskeletons*, J. Löwe, and L.A. Amos, eds. (Springer International Publishing), pp. 323–356.
- Fink, G., and Löwe, J. (2015). Reconstitution of a prokaryotic minus end-tracking system using TubRC centromeric complexes and tubulin-like protein TubZ filaments. *Proc. Natl. Acad. Sci.* 112, E1845–E1850.
- Fiuza, M., Letek, M., Leiba, J., Villadangos, A.F., Vaquera, J., Zanella-Cléon, I., Mateos, L.M., Molle, V., and Gil, J.A. (2010). Phosphorylation of a Novel Cytoskeletal Protein (RsmP) Regulates Rod-shaped Morphology in *Corynebacterium glutamicum*. *J. Biol. Chem.* 285, 29387–29397.
- Foster, T.J. (2017). Antibiotic resistance in *Staphylococcus aureus*. Current status and future prospects. *FEMS Microbiol. Rev.* 41, 430–449.
- Fu, G., Huang, T., Buss, J., Coltharp, C., Hensel, Z., and Xiao, J. (2010). In Vivo Structure of the *E. coli* FtsZ-ring Revealed by Photoactivated Localization Microscopy (PALM). *PLOS ONE* 5, e12680.

- Fujita, J., Maeda, Y., Nagao, C., Tsuchiya, Y., Miyazaki, Y., Hirose, M., Mizohata, E., Matsumoto, Y., Inoue, T., Mizuguchi, K., et al. (2014). Crystal structure of FtsA from *Staphylococcus aureus*. *FEBS Lett.* 588, 1879–1885.
- Galli, E., and Gerdes, K. (2010). Spatial resolution of two bacterial cell division proteins: ZapA recruits ZapB to the inner face of the Z-ring. *Mol. Microbiol.* 76, 1514–1526.
- Galli, E., and Gerdes, K. (2012). FtsZ-ZapA-ZapB Interactome of *Escherichia coli*. *J. Bacteriol.* 194, 292–302.
- Garcia-Seisdedos, H., Empereur-Mot, C., Elad, N., and Levy, E.D. (2017). Proteins evolve on the edge of supramolecular self-assembly. *Nature* 548, 244–247.
- Garner, E.C., Bernard, R., Wang, W., Zhuang, X., Rudner, D.Z., and Mitchison, T. (2011). Coupled, Circumferential Motions of the Cell Wall Synthesis Machinery and MreB Filaments in *B. subtilis*. *Science* 333, 222–225.
- Gayathri, P., and Harne, S. (2017). Structure and Dynamics of Actin-Like Cytomotive Filaments in Plasmid Segregation. In *Prokaryotic Cytoskeletons*, J. Löwe, and L.A. Amos, eds. (Springer International Publishing), pp. 299–321.
- Gayathri, P., Fujii, T., Møller-Jensen, J., Ent, F. van den, Namba, K., and Löwe, J. (2012). A Bipolar Spindle of Antiparallel ParM Filaments Drives Bacterial Plasmid Segregation. *Science* 338, 1334–1337.
- Gebremichael, Y., Chu, J.-W., and Voth, G.A. (2008). Intrinsic Bending and Structural Rearrangement of Tubulin Dimer: Molecular Dynamics Simulations and Coarse-Grained Analysis. *Biophys. J.* 95, 2487–2499.
- Gerdes, K., Larsen, J.E., and Molin, S. (1985). Stable inheritance of plasmid R1 requires two different loci. *J. Bacteriol.* 161, 292–298.
- Gerstein, M., and Altman, R.B. (1995). Average Core Structures and Variability Measures for Protein Families: Application to the Immunoglobulins. *J. Mol. Biol.* 251, 161–175.
- Gerstein, M., and Chothia, C. (1991). Analysis of protein loop closure: Two types of hinges produce one motion in lactate dehydrogenase. *J. Mol. Biol.* 220, 133–149.
- Geyer, E.A., Burns, A., Lalonde, B.A., Ye, X., Piedra, F.-A., Huffaker, T.C., and Rice, L.M. (2015). A mutation uncouples the tubulin conformational and GTPase cycles, revealing allosteric control of microtubule dynamics.
- Gibson, D.G., Young, L., Chuang, R.-Y., Venter, J.C., Hutchison, C.A., and Smith, H.O. (2009). Enzymatic assembly of DNA molecules up to several hundred kilobases. *Nat. Methods* 6, 343–345.
- Gitai, Z., Dye, N.A., Reisenauer, A., Wachi, M., and Shapiro, L. (2005). MreB Actin-Mediated Segregation of a Specific Region of a Bacterial Chromosome. *Cell* 120, 329–341.
- Gola, S., Munder, T., Casonato, S., Manganelli, R., and Vicente, M. (2015). The essential role of SepF in mycobacterial division. *Mol. Microbiol.* 97, 560–576.
- Gorrec, F., and Löwe, J. (2018). Automated Protocols for Macromolecular Crystallization at the MRC Laboratory of Molecular Biology. *JoVE J. Vis. Exp.* e55790.

REFERENCES

- Grant, B.J., Rodrigues, A.P.C., ElSawy, K.M., McCammon, J.A., and Caves, L.S.D. (2006). Bio3d: an R package for the comparative analysis of protein structures. *Bioinformatics* 22, 2695–2696.
- Grego, S., Cantillana, V., and Salmon, E.D. (2001). Microtubule Treadmilling in Vitro Investigated by Fluorescence Speckle and Confocal Microscopy. *Biophys. J.* 81, 66–78.
- Gueiros-Filho, F.J., and Losick, R. (2002). A widely conserved bacterial cell division protein that promotes assembly of the tubulin-like protein FtsZ. *Genes Dev.* 16, 2544–2556.
- Gupta, S., Banerjee, S.K., Chatterjee, A., Sharma, A.K., Kundu, M., and Basu, J. (2015). Essential protein SepF of mycobacteria interacts with FtsZ and MurG to regulate cell growth and division. *Microbiology* 161, 1627–1638.
- Haeusser, D.P., and Margolin, W. (2016). Splitsville: structural and functional insights into the dynamic bacterial Z ring. *Nat. Rev. Microbiol.* 14, 305–319.
- Hale, C.A., and de Boer, P.A.J. (1997). Direct Binding of FtsZ to ZipA, an Essential Component of the Septal Ring Structure That Mediates Cell Division in *E. coli*. *Cell* 88, 175–185.
- Hall, M.D., Yasgar, A., Peryea, T., Braisted, J.C., Jadhav, A., Simeonov, A., and Coussens, N.P. (2016). Fluorescence polarization assays in high-throughput screening and drug discovery: a review. *Methods Appl. Fluoresc.* 4, 022001.
- Hamoen, L.W., Meile, J.-C., De Jong, W., Noirot, P., and Errington, J. (2006). SepF, a novel FtsZ-interacting protein required for a late step in cell division. *Mol. Microbiol.* 59, 989–999.
- Hara, F., Yamashiro, K., Nemoto, N., Ohta, Y., Yokobori, S., Yasunaga, T., Hisanaga, S., and Yamagishi, A. (2007). An Actin Homolog of the Archaeon *Thermoplasma acidophilum* That Retains the Ancient Characteristics of Eukaryotic Actin. *J. Bacteriol.* 189, 2039–2045.
- Hay, N.A., Tipper, D.J., Gygi, D., and Hughes, C. (1999). A Novel Membrane Protein Influencing Cell Shape and Multicellular Swarming of *Proteus mirabilis*. *J. Bacteriol.* 181, 2008–2016.
- Hayward, S., and Berendsen, H.J. (1998). Systematic analysis of domain motions in proteins from conformational change: new results on citrate synthase and T4 lysozyme. *Proteins* 30, 144–154.
- He, S., and Scheres, S.H.W. (2017). Helical reconstruction in RELION. *J. Struct. Biol.* 198, 163–176.
- Hempel, A.M., Cantlay, S., Molle, V., Wang, S.-B., Naldrett, M.J., Parker, J.L., Richards, D.M., Jung, Y.-G., Buttner, M.J., and Flärdh, K. (2012). The Ser/Thr protein kinase AfsK regulates polar growth and hyphal branching in the filamentous bacteria *Streptomyces*. *Proc. Natl. Acad. Sci. U. S. A.* 109, E2371–E2379.
- Herrmann, H., and Aebi, U. (2016). Intermediate Filaments: Structure and Assembly. *Cold Spring Harb. Perspect. Biol.* 8, a018242.
- Heyda, J., Mason, P.E., and Jungwirth, P. (2010). Attractive Interactions between Side Chains of Histidine-Histidine and Histidine-Arginine-Based Cationic Dipeptides in Water. *J. Phys. Chem. B* 114, 8744–8749.
- Hill, T.L., and Kirschner, M.W. (1982). Bioenergetics and kinetics of microtubule and actin filament assembly-disassembly. *Int. Rev. Cytol.* 78, 1–125.

- Holmes, J.A., Follett, S.E., Wang, H., Meadows, C.P., Varga, K., and Bowman, G.R. (2016). Caulobacter PopZ forms an intrinsically disordered hub in organizing bacterial cell poles. *Proc. Natl. Acad. Sci.* *113*, 12490–12495.
- Holmes, N.A., Walshaw, J., Leggett, R.M., Thibessard, A., Dalton, K.A., Gillespie, M.D., Hemmings, A.M., Gust, B., and Kelemen, G.H. (2013). Coiled-coil protein Scy is a key component of a multiprotein assembly controlling polarized growth in *Streptomyces*. *Proc. Natl. Acad. Sci. U. S. A.* *110*, E397–406.
- Huecas, S., Llorca, O., Boskovic, J., Martín-Benito, J., Valpuesta, J.M., and Andreu, J.M. (2008). Energetics and Geometry of FtsZ Polymers: Nucleated Self-Assembly of Single Protofilaments. *Biophys. J.* *94*, 1796–1806.
- Huecas, S., Ramírez-Aportela, E., Vergoñós, A., Núñez-Ramírez, R., Llorca, O., Díaz, J.F., Juan-Rodríguez, D., Oliva, M.A., Castellen, P., and Andreu, J.M. (2017). Self-Organization of FtsZ Polymers in Solution Reveals Spacer Role of the Disordered C-Terminal Tail. *Biophys. J.* *113*, 1831–1844.
- Hug, L.A., Baker, B.J., Anantharaman, K., Brown, C.T., Probst, A.J., Castelle, C.J., Butterfield, C.N., Hernsdorf, A.W., Amano, Y., Ise, K., et al. (2016). A new view of the tree of life. *Nat. Microbiol.* *1*6048.
- Hurley, K.A., Santos, T.M.A., Nepomuceno, G.M., Huynh, V., Shaw, J.T., and Weibel, D.B. (2016). Targeting the Bacterial Division Protein FtsZ. *J. Med. Chem.* *59*, 6975–6998.
- Hussain, S., Wivagg, C.N., Szwedziak, P., Wong, F., Schaefer, K., Izoré, T., Renner, L.D., Holmes, M.J., Sun, Y., Bisson-Filho, A.W., et al. (2018). MreB filaments align along greatest principal membrane curvature to orient cell wall synthesis. *ELife* *7*, e32471.
- Igaev, M., and Grubmüller, H. (2018). Microtubule assembly governed by tubulin allosteric gain in flexibility and lattice induced fit. *ELife* *7*.
- Ingerson-Mahar, M., Briegel, A., Werner, J.N., Jensen, G.J., and Gitai, Z. (2010). The metabolic enzyme CTP synthase forms cytoskeletal filaments. *Nat. Cell Biol.* *12*, 739–746.
- Invitrogen (4th edition). Technical Resource Guide: Fluorescence Polarization.
- Ishikawa, S., Kawai, Y., Hiramatsu, K., Kuwano, M., and Ogasawara, N. (2006). A new FtsZ-interacting protein, YlmF, complements the activity of FtsA during progression of cell division in *Bacillus subtilis*. *Mol. Microbiol.* *60*, 1364–1380.
- Izard, J., McEwen, B.F., Barnard, R.M., Portuese, T., Samsonoff, W.A., and Limberger, R.J. (2003). Tomographic reconstruction of treponemal cytoplasmic filaments reveals novel bridging and anchoring components: Filament bridging and anchoring. *Mol. Microbiol.* *51*, 609–618.
- Izoré, T., Kureisaite-Ciziene, D., McLaughlin, S.H., and Löwe, J. (2016). Crenactin forms actin-like double helical filaments regulated by arcadin-2. *ELife* *5*, e21600.
- Jacquier, N., Frandi, A., Pillionel, T., Viollier, P.H., and Greub, G. (2014). Cell wall precursors are required to organize the chlamydial division septum. *Nat. Commun.* *5*, 3578.
- Jameson, D.M. (2001). The Seminal Contributions of Gregorio Weber to Modern Fluorescence Spectroscopy. In *New Trends in Fluorescence Spectroscopy: Applications to Chemical and Life*

REFERENCES

- Sciences, B. Valeur, and J.-C. Brochon, eds. (Berlin, Heidelberg: Springer Berlin Heidelberg), pp. 35–58.
- Jenkins, C., Samudrala, R., Anderson, I., Hedlund, B.P., Petroni, G., Michailova, N., Pinel, N., Overbeek, R., Rosati, G., and Staley, J.T. (2002). Genes for the cytoskeletal protein tubulin in the bacterial genus *Prostheco bacter*. *Proc. Natl. Acad. Sci.* 99, 17049–17054.
- Jones, L.J.F., Carballido-López, R., and Errington, J. (2001). Control of Cell Shape in Bacteria. *Cell* 104, 913–922.
- Kabsch, W. (2010). XDS. *Acta Crystallogr. D Biol. Crystallogr.* 66, 125–132.
- Kang, C.-M., Abbott, D.W., Park, S.T., Dascher, C.C., Cantley, L.C., and Husson, R.N. (2005). The *Mycobacterium tuberculosis* serine/threonine kinases PknA and PknB: substrate identification and regulation of cell shape. *Genes Dev.* 19, 1692–1704.
- Katzmann, E., Müller, F.D., Lang, C., Messerer, M., Winklhofer, M., Plitzko, J.M., and Schüler, D. (2011). Magnetosome chains are recruited to cellular division sites and split by asymmetric septation. *Mol. Microbiol.* 82, 1316–1329.
- Kaul, M., Zhang, Y., Parhi, A.K., LaVoie, E.J., Tuske, S., Arnold, E., Kerrigan, J.E., and Pilch, D.S. (2013). Enterococcal and streptococcal resistance to PC190723 and related compounds: Molecular insights from a FtsZ mutational analysis. *Biochimie* 95, 1880–1887.
- Kaul, M., Mark, L., Zhang, Y., Parhi, A.K., Lyu, Y.L., Pawlak, J., Saravolatz, S., Saravolatz, L.D., Weinstein, M.P., LaVoie, E.J., et al. (2015). TXA709, an FtsZ-Targeting Benzamide Prodrug with Improved Pharmacokinetics and Enhanced In Vivo Efficacy against Methicillin-Resistant *Staphylococcus aureus*. *Antimicrob. Agents Chemother.* 59, 4845–4855.
- Kaval, K.G., and Halbedel, S. (2012). Architecturally the same, but playing a different game. *Virulence* 3, 406–407.
- Kawai, Y., Asai, K., and Errington, J. (2009). Partial functional redundancy of MreB isoforms, MreB, Mbl and MreBH, in cell morphogenesis of *Bacillus subtilis*. *Mol. Microbiol.* 73, 719–731.
- Keffer, J.L., Huecas, S., Hammill, J.T., Wipf, P., Andreu, J.M., and Bewley, C.A. (2013). Chrysopaentins are competitive inhibitors of FtsZ and inhibit Z-ring formation in live bacteria. *Bioorg. Med. Chem.* 21, 5673–5678.
- Kelemen, G.H. (2017). Intermediate Filaments Supporting Cell Shape and Growth in Bacteria. In *Prokaryotic Cytoskeletons*, J. Löwe, and L.A. Amos, eds. (Springer International Publishing), pp. 161–211.
- Kiefel, B.R., Gilson, P.R., and Beech, P.L. (2004). Diverse Eukaryotes have Retained Mitochondrial Homologues of the Bacterial Division Protein FtsZ. *Protist* 155, 105–115.
- Knowles, J., and Gromo, G. (2003). A guide to drug discovery: Target selection in drug discovery. *Nat. Rev. Drug Discov.* 2, 63–69.
- Komeili, A., Li, Z., Newman, D.K., and Jensen, G.J. (2006). Magnetosomes Are Cell Membrane Invaginations Organized by the Actin-Like Protein MamK. *Science* 311, 242–245.

- Kraemer, J.A., Erb, M.L., Waddling, C.A., Montabana, E.A., Zehr, E.A., Wang, H., Nguyen, K., Pham, D.S.L., Agard, D.A., and Pogliano, J. (2012). A Phage Tubulin Assembles Dynamic Filaments by an Atypical Mechanism to Center Viral DNA within the Host Cell. *Cell* **149**, 1488–1499.
- Krissinel, E., and Henrick, K. (2007). Inference of Macromolecular Assemblies from Crystalline State. *J. Mol. Biol.* **372**, 774–797.
- Krupka, M., Rowlett, V.W., Morado, D., Vitrac, H., Schoenemann, K., Liu, J., and Margolin, W. (2017). *Escherichia coli* FtsA forms lipid-bound minirings that antagonize lateral interactions between FtsZ protofilaments. *Nat. Commun.* **8**, ncomms15957.
- Kühn, J., Briegel, A., Mörschel, E., Kahnt, J., Leser, K., Wick, S., Jensen, G.J., and Thanbichler, M. (2010). Bactofilins, a ubiquitous class of cytoskeletal proteins mediating polar localization of a cell wall synthase in *Caulobacter crescentus*. *EMBO J.* **29**, 327–339.
- Larsen, R.A., Cusumano, C., Fujioka, A., Lim-Fong, G., Patterson, P., and Pogliano, J. (2007). Treadmilling of a prokaryotic tubulin-like protein, TubZ, required for plasmid stability in *Bacillus thuringiensis*. *Genes Dev.* **21**, 1340–1352.
- Laskowski, R.A., and Swindells, M.B. (2011). LigPlot+: multiple ligand-protein interaction diagrams for drug discovery. *J. Chem. Inf. Model.* **51**, 2778–2786.
- Lenarcic, R., Halbedel, S., Visser, L., Shaw, M., Wu, L.J., Errington, J., Marenduzzo, D., and Hamoen, L.W. (2009). Localisation of DivIVA by targeting to negatively curved membranes. *EMBO J.* **28**, 2272–2282.
- Levy, E.D., Erba, E.B., Robinson, C.V., and Teichmann, S.A. (2008). Assembly reflects evolution of protein complexes. *Nature* **453**, 1262–1265.
- Li, Y., Hsin, J., Zhao, L., Cheng, Y., Shang, W., Huang, K.C., Wang, H.-W., and Ye, S. (2013). FtsZ Protofilaments Use a Hinge-Opening Mechanism for Constrictive Force Generation. *Science* **341**, 392–395.
- Li, Z., Trimble, M.J., Brun, Y.V., and Jensen, G.J. (2007). The structure of FtsZ filaments in vivo suggests a force-generating role in cell division. *EMBO J.* **26**, 4694–4708.
- Lin, L., and Thanbichler, M. (2013). Nucleotide-independent cytoskeletal scaffolds in bacteria. *Cytoskeleton* **70**, 409–423.
- Lindås, A.-C., and Bernander, R. (2013). The cell cycle of archaea. *Nat. Rev. Microbiol.* **11**, 627–638.
- Lindås, A.-C., Karlsson, E.A., Lindgren, M.T., Ettema, T.J.G., and Bernander, R. (2008). A unique cell division machinery in the Archaea. *Proc. Natl. Acad. Sci.* **105**, 18942–18946.
- Lindås, A.-C., Valegård, K., and Ettema, T.J.G. (2017). Archaeal Actin-Family Filament Systems. In *Prokaryotic Cytoskeletons*, J. Löwe, and L.A. Amos, eds. (Springer International Publishing), pp. 379–392.
- Loose, M., and Mitchison, T.J. (2014). The bacterial cell division proteins FtsA and FtsZ self-organize into dynamic cytoskeletal patterns. *Nat. Cell Biol.* **16**, 38–46.
- Low, H.H., Moncrieffe, M.C., and Löwe, J. (2004). The crystal structure of ZapA and its modulation of FtsZ polymerisation. *J. Mol. Biol.* **341**, 839–852.

REFERENCES

- Löwe, J., and Amos, L.A. (1998). Crystal structure of the bacterial cell-division protein FtsZ. *Nature* 391, 203–206.
- Löwe, J., and Amos, L.A. (2009). Evolution of cytomotive filaments: The cytoskeleton from prokaryotes to eukaryotes. *Int. J. Biochem. Cell Biol.* 41, 323–329.
- Löwe, J., Ent, F. van den, and Amos, L.A. (2004). Molecules of the Bacterial Cytoskeleton. *Annu. Rev. Biophys. Biomol. Struct.* 33, 177–198.
- Löwe, J., He, S., Scheres, S.H.W., and Savva, C.G. (2016). X-ray and cryo-EM structures of monomeric and filamentous actin-like protein MamK reveal changes associated with polymerization. *Proc. Natl. Acad. Sci. U. S. A.* 113, 13396–13401.
- Luciano, J., Agrebi, R., Gall, A.V.L., Wartel, M., Fiegna, F., Ducret, A., Brochier-Armanet, C., and Mignot, T. (2011). Emergence and Modular Evolution of a Novel Motility Machinery in Bacteria. *PLOS Genet.* 7, e1002268.
- Lutkenhaus, J. (2007). Assembly Dynamics of the Bacterial MinCDE System and Spatial Regulation of the Z Ring. *Annu. Rev. Biochem.* 76, 539–562.
- Lynch, E.M., Hicks, D.R., Shepherd, M., Endrizzi, J.A., Maker, A., Hansen, J.M., Barry, R.M., Gitai, Z., Baldwin, E.P., and Kollman, J.M. (2017). Human CTP synthase filament structure reveals the active enzyme conformation. *Nat. Struct. Mol. Biol.* 24, 507–514.
- Maddox, P., Straight, A., Coughlin, P., Mitchison, T.J., and Salmon, E.D. (2003). Direct observation of microtubule dynamics at kinetochores in *Xenopus* extract spindles: implications for spindle mechanics. *J. Cell Biol.* 162, 377–382.
- Makarova, K.S., and Koonin, E.V. (2010). Two new families of the FtsZ-tubulin protein superfamily implicated in membrane remodeling in diverse bacteria and archaea. *Biol. Direct* 5, 33.
- Makarova, K.S., Yutin, N., Bell, S.D., and Koonin, E.V. (2010). Evolution of diverse cell division and vesicle formation systems in Archaea. *Nat. Rev. Microbiol.* 8, 731–741.
- Marbouty, M., Saguez, C., Cassier-Chauvat, C., and Chauvat, F. (2009). Characterization of the FtsZ-Interacting Septal Proteins SepF and Ftn6 in the Spherical-Celled Cyanobacterium *Synechocystis* Strain PCC 6803. *J. Bacteriol.* 191, 6178–6185.
- Margalit, D.N., Romberg, L., Mets, R.B., Hebert, A.M., Mitchison, T.J., Kirschner, M.W., and RayChaudhuri, D. (2004). Targeting cell division: small-molecule inhibitors of FtsZ GTPase perturb cytokinetic ring assembly and induce bacterial lethality. *Proc. Natl. Acad. Sci. U. S. A.* 101, 11821–11826.
- Marston, A.L., Thomaides, H.B., Edwards, D.H., Sharpe, M.E., and Errington, J. (1998). Polar localization of the MinD protein of *Bacillus subtilis* and its role in selection of the mid-cell division site. *Genes Dev.* 12, 3419–3430.
- Martín-Galiano, A.J., Buey, R.M., Cabezas, M., and Andreu, J.M. (2010). Mapping Flexibility and the Assembly Switch of Cell Division Protein FtsZ by Computational and Mutational Approaches. *J. Biol. Chem.* 285, 22554–22565.

- Matsui, T., Yamane, J., Mogi, N., Yamaguchi, H., Takemoto, H., Yao, M., and Tanaka, I. (2012). Structural reorganization of the bacterial cell-division protein FtsZ from *Staphylococcus aureus*. *Acta Crystallogr. D Biol. Crystallogr.* 68, 1175–1188.
- Matsui, T., Han, X., Yu, J., Yao, M., and Tanaka, I. (2014). Structural change in FtsZ Induced by intermolecular interactions between bound GTP and the T7 loop. *J. Biol. Chem.* 289, 3501–3509.
- Mazouni, K., Pehau-Arnaudet, G., England, P., Bourhy, P., Girons, I.S., and Picardeau, M. (2006). The Scc Spirochetal Coiled-Coil Protein Forms Helix-Like Filaments and Binds to Nucleic Acids Generating Nucleoprotein Structures. *J. Bacteriol.* 188, 469–476.
- McCoy, A.J., Grosse-Kunstleve, R.W., Adams, P.D., Winn, M.D., Storoni, L.C., and Read, R.J. (2007). Phaser crystallographic software. *J. Appl. Crystallogr.* 40, 658–674.
- McCullough, J., Clippinger, A.K., Talledge, N., Skowrya, M.L., Saunders, M.G., Naismith, T.V., Colf, L.A., Afonine, P., Arthur, C., Sundquist, W.I., et al. (2015). Structure and membrane remodeling activity of ESCRT-III helical polymers. *Science* 350, 1548–1551.
- McIntosh, J.R., O'Toole, E., Morgan, G., Austin, J., Ulyanov, E., Ataullakhanov, F., and Gudimchuk, N. (2018). Microtubules grow by the addition of bent guanosine triphosphate tubulin to the tips of curved protofilaments. *J Cell Biol* 217, 2691–2708.
- Mendler, K., Chen, H., Parks, D.H., Hug, L.A., and Doxey, A.C. (2018). AnnoTree: visualization and exploration of a functionally annotated microbial tree of life. *BioRxiv* 463455.
- Merino, F., Pospich, S., Funk, J., Wagner, T., Küllmer, F., Arndt, H.-D., Bieling, P., and Raunser, S. (2018). Structural transitions of F-actin upon ATP hydrolysis at near-atomic resolution revealed by cryo-EM. *Nat. Struct. Mol. Biol.* 25, 528–537.
- Michie, K.A., and Löwe, J. (2006). Dynamic filaments of the bacterial cytoskeleton. *Annu. Rev. Biochem.* 75, 467–492.
- Miraldi, E.R., Thomas, P.J., and Romberg, L. (2008). Allosteric models for cooperative polymerization of linear polymers. *Biophys. J.* 95, 2470–2486.
- Miroux, B., and Walker, J.E. (1996). Over-production of proteins in *Escherichia coli*: mutant hosts that allow synthesis of some membrane proteins and globular proteins at high levels. *J. Mol. Biol.* 260, 289–298.
- Mk, K., Ca, M., and E, H. (2011). BacM, an N-terminally processed bactofilin of *Myxococcus xanthus*, is crucial for proper cell shape. *Mol. Microbiol.* 80, 1031–1051.
- Mogilner, A., and Oster, G. (2003). Polymer Motors: Pushing out the Front and Pulling up the Back. *Curr. Biol.* 13, R721–R733.
- Mohr, K.I. (2016). History of Antibiotics Research. *Curr. Top. Microbiol. Immunol.* 398, 237–272.
- Møller-Jensen, J., Borch, J., Dam, M., Jensen, R.B., Roepstorff, P., and Gerdes, K. (2003). Bacterial Mitosis. *Mol. Cell* 12, 1477–1487.
- Monahan, L.G., Robinson, A., and Harry, E.J. (2009). Lateral FtsZ association and the assembly of the cytokinetic Z ring in bacteria. *Mol. Microbiol.* 74, 1004–1017.

REFERENCES

- Montabana, E.A., and Agard, D.A. (2014). Bacterial tubulin TubZ-Bt transitions between a two-stranded intermediate and a four-stranded filament upon GTP hydrolysis. *Proc. Natl. Acad. Sci. U. S. A.* *111*, 3407–3412.
- Mukherjee, A., and Lutkenhaus, J. (1994). Guanine nucleotide-dependent assembly of FtsZ into filaments. *J. Bacteriol.* *176*, 2754–2758.
- Mukherjee, A., Dai, K., and Lutkenhaus, J. (1993). Escherichia coli cell division protein FtsZ is a guanine nucleotide binding protein. *Proc. Natl. Acad. Sci.* *90*, 1053–1057.
- Müller, F.D., Raschdorf, O., Nudelman, H., Messerer, M., Katzmann, E., Plitzko, J.M., Zarivach, R., and Schüler, D. (2014). The FtsZ-Like Protein FtsZm of Magnetospirillum gryphiswaldense Likely Interacts with Its Generic Homolog and Is Required for Biomineralization under Nitrate Deprivation. *J. Bacteriol.* *196*, 650–659.
- Murshudov, G.N., Vagin, A.A., and Dodson, E.J. (1997). Refinement of Macromolecular Structures by the Maximum-Likelihood Method. *Acta Crystallogr. D Biol. Crystallogr.* *53*, 240–255.
- Murzin, A.G., Brenner, S.E., Hubbard, T., and Chothia, C. (1995). SCOP: A structural classification of proteins database for the investigation of sequences and structures. *J. Mol. Biol.* *247*, 536–540.
- Narita, A. (2011). Minimum requirements for the actin-like treadmilling motor system. *BioArchitecture* *1*, 205–208.
- Narita, A., Oda, T., and Maéda, Y. (2011). Structural basis for the slow dynamics of the actin filament pointed end. *EMBO J.* *30*, 1230–1237.
- Nikolovska-Coleska, Z., Wang, R., Fang, X., Pan, H., Tomita, Y., Li, P., Roller, P.P., Krajewski, K., Saito, N.G., Stuckey, J.A., et al. (2004). Development and optimization of a binding assay for the XIAP BIR3 domain using fluorescence polarization. *Anal. Biochem.* *332*, 261–273.
- Nogales, E., and Scheres, S.H.W. (2015). Cryo-EM: A Unique Tool for the Visualization of Macromolecular Complexity. *Mol. Cell* *58*, 677–689.
- Nogales, E., Downing, K.H., Amos, L.A., and Löwe, J. (1998). Tubulin and FtsZ form a distinct family of GTPases. *Nat. Struct. Mol. Biol.* *5*, 451–458.
- Nogueira, M.L.C., Sforça, M.L., Chin, Y.K.-Y., Mobli, M., Handler, A., Gorbatyuk, V.Y., Robson, S.A., King, G.F., Gueiros-Filho, F.J., and Zeri, A.C. de M. (2015). Backbone and side chain NMR assignments of Geobacillus stearothermophilus ZapA allow identification of residues that mediate the interaction of ZapA with FtsZ. *Biomol. NMR Assign.* *9*, 387–391.
- Notredame, C., Higgins, D.G., and Heringa, J. (2000). T-coffee: a novel method for fast and accurate multiple sequence alignment. Edited by J. Thornton. *J. Mol. Biol.* *302*, 205–217.
- Obita, T., Saksena, S., Ghazi-Tabatabai, S., Gill, D.J., Perisic, O., Emr, S.D., and Williams, R.L. (2007). Structural basis for selective recognition of ESCRT-III by the AAA ATPase Vps4. *Nature* *449*, 735–739.
- Oda, T., Iwasa, M., Aihara, T., Maéda, Y., and Narita, A. (2009). The nature of the globular- to fibrous-actin transition. *Nature* *457*, 441–445.
- Oda, T., Takeda, S., Narita, A., and Maéda, Y. (2019). Structural Polymorphism of Actin. *J. Mol. Biol.*

- OECD (2018). Stemming the Superbug Tide: Just A Few Dollars More (OECD).
- Oliva, M.A., Cordell, S.C., and Löwe, J. (2004). Structural insights into FtsZ protofilament formation. *Nat. Struct. Mol. Biol.* *11*, 1243–1250.
- Oliva, M.A., Trambaiolo, D., and Löwe, J. (2007). Structural Insights into the Conformational Variability of FtsZ. *J. Mol. Biol.* *373*, 1229–1242.
- Oliva, M.A., Halbedel, S., Freund, S.M., Dutow, P., Leonard, T.A., Veprintsev, D.B., Hamoen, L.W., and Löwe, J. (2010). Features critical for membrane binding revealed by DivIVA crystal structure. *EMBO J.* *29*, 1988–2001.
- Ortiz, C., Kureisaite-Ciziene, D., Schmitz, F., McLaughlin, S.H., Vicente, M., and Löwe, J. (2015). Crystal structure of the Z-ring associated cell division protein ZapC from *Escherichia coli*. *FEBS Lett.* *589*, 3822–3828.
- Ortiz, C., Natale, P., Cueto, L., and Vicente, M. (2016). The keepers of the ring: regulators of FtsZ assembly. *FEMS Microbiol. Rev.* *40*, 57–67.
- Osawa, M., and Erickson, H.P. (2013). Liposome division by a simple bacterial division machinery. *Proc. Natl. Acad. Sci.* *110*, 11000–11004.
- Osteryoung, K.W., and Pyke, K.A. (2014). Division and Dynamic Morphology of Plastids. *Annu. Rev. Plant Biol.* *65*, 443–472.
- Ouellette, S.P., Karimova, G., Subtil, A., and Ladant, D. (2012). Chlamydia co-opts the rod shape-determining proteins MreB and Pbp2 for cell division. *Mol. Microbiol.* *85*, 164–178.
- Pacheco-Gómez, R., Cheng, X., Hicks, M.R., Smith, C.J.I., Roper, D.I., Addinall, S., Rodger, A., and Dafforn, T.R. (2013). Tetramerization of ZapA is required for FtsZ bundling. *Biochem. J.* *449*, 795–802.
- Park, K.-T., Du, S., and Lutkenhaus, J. (2015). MinC/MinD copolymers are not required for Min function. *Mol. Microbiol.* *98*, 895–909.
- Parks, D.H., Chuvochina, M., Waite, D.W., Rinke, C., Skarszewski, A., Chaumeil, P.-A., and Hugenholtz, P. (2018). A standardized bacterial taxonomy based on genome phylogeny substantially revises the tree of life. *Nat. Biotechnol.* *36*, 996–1004.
- Patrick, J.E., and Kearns, D.B. (2008). MinJ (YvjD) is a topological determinant of cell division in *Bacillus subtilis*. *Mol. Microbiol.* *70*, 1166–1179.
- Pei, J., Kim, B.-H., and Grishin, N.V. (2008). PROMALS3D: a tool for multiple protein sequence and structure alignments. *Nucleic Acids Res.* *36*, 2295–2300.
- Perrin, F. (1926). Polarisation de la lumière de fluorescence. Vie moyenne des molécules dans l'état excité. *J Phys Radium* *7*, 390–401.
- Pettersen, E.F., Goddard, T.D., Huang, C.C., Couch, G.S., Greenblatt, D.M., Meng, E.C., and Ferrin, T.E. (2004). UCSF Chimera—A visualization system for exploratory research and analysis. *J. Comput. Chem.* *25*, 1605–1612.

REFERENCES

- Pilhofer, M., and Jensen, G.J. (2013). The bacterial cytoskeleton: more than twisted filaments. *Curr. Opin. Cell Biol.* 25, 125–133.
- Pilhofer, M., Ladinsky, M.S., McDowall, A.W., Petroni, G., and Jensen, G.J. (2011). Microtubules in Bacteria: Ancient Tubulins Build a Five-Protofilament Homolog of the Eukaryotic Cytoskeleton. *PLOS Biol.* 9, e1001213.
- Polka, J.K., Kollman, J.M., Agard, D.A., and Mullins, R.D. (2009). The Structure and Assembly Dynamics of Plasmid Actin AlfA Imply a Novel Mechanism of DNA Segregation. *J. Bacteriol.* 191, 6219–6230.
- Polka, J.K., Kollman, J.M., and Mullins, R.D. (2014). Accessory factors promote AlfA-dependent plasmid segregation by regulating filament nucleation, disassembly, and bundling. *Proc. Natl. Acad. Sci.* 111, 2176–2181.
- Popp, D., Xu, W., Narita, A., Brzoska, A.J., Skurray, R.A., Firth, N., Goshdastider, U., Maéda, Y., Robinson, R.C., and Schumacher, M.A. (2010). Structure and Filament Dynamics of the pSK41 Actin-like ParM Protein IMPLICATIONS FOR PLASMID DNA SEGREGATION. *J. Biol. Chem.* 285, 10130–10140.
- Popp, D., Narita, A., Lee, L.J., Ghoshdastider, U., Xue, B., Srinivasan, R., Balasubramanian, M.K., Tanaka, T., and Robinson, R.C. (2012). Novel Actin-like Filament Structure from *Clostridium tetani*. *J. Biol. Chem.* 287, 21121–21129.
- Raddi, G., Morado, D.R., Yan, J., Haake, D.A., Yang, X.F., and Liu, J. (2012). Three-Dimensional Structures of Pathogenic and Saprophytic *Leptospira* Species Revealed by Cryo-Electron Tomography. *J. Bacteriol.* 194, 1299–1306.
- Ramamurthi, K.S., and Losick, R. (2008). ATP-Driven Self-Assembly of a Morphogenetic Protein in *Bacillus subtilis*. *Mol. Cell* 31, 406–414.
- Ramamurthi, K.S., and Losick, R. (2009). Negative membrane curvature as a cue for subcellular localization of a bacterial protein. *Proc. Natl. Acad. Sci.* 106, 13541–13545.
- Ramirez, D., Garcia-Soriano, D.A., Raso, A., Feingold, M., Rivas, G., and Schwille, P. (2016). Chiral vortex dynamics on membranes is an intrinsic property of FtsZ, driven by GTP hydrolysis. *BioRxiv* 079533.
- Ramírez-Aportela, E., López-Blanco, J.R., Andreu, J.M., and Chacón, P. (2014). Understanding Nucleotide-Regulated FtsZ Filament Dynamics and the Monomer Assembly Switch with Large-Scale Atomistic Simulations. *Biophys. J.* 107, 2164–2176.
- Rasmussen, C.G., Wright, A.J., and Müller, S. (2013). The role of the cytoskeleton and associated proteins in determination of the plant cell division plane. *Plant J.* 75, 258–269.
- RayChaudhuri, D., and Park, J.T. (1992). *Escherichia coli* cell-division gene *ftsZ* encodes a novel GTP-binding protein. *Nature* 359, 251–254.
- Richter, M., Kube, M., Bazylnski, D.A., Lombardot, T., Glöckner, F.O., Reinhardt, R., and Schüler, D. (2007). Comparative Genome Analysis of Four Magnetotactic Bacteria Reveals a Complex Set of Group-Specific Genes Implicated in Magnetosome Biomineralization and Function. *J. Bacteriol.* 189, 4899–4910.

- Rioux, J.-B., Philippe, N., Pereira, S., Pignol, D., Wu, L.-F., and Ginet, N. (2010). A Second Actin-Like MamK Protein in *Magnetospirillum magneticum* AMB-1 Encoded Outside the Genomic Magnetosome Island. *PLOS ONE* 5, e9151.
- Rivas, G., López, A., Mingorance, J., Ferrándiz, M.J., Zorrilla, S., Minton, A.P., Vicente, M., and Andreu, J.M. (2000). Magnesium-induced Linear Self-association of the FtsZ Bacterial Cell Division Protein Monomer THE PRIMARY STEPS FOR FtsZ ASSEMBLY. *J. Biol. Chem.* 275, 11740–11749.
- Rivera, C.R., Kollman, J.M., Polka, J.K., Agard, D.A., and Mullins, R.D. (2011). Architecture and Assembly of a Divergent Member of the ParM Family of Bacterial Actin-like Proteins. *J. Biol. Chem.* 286, 14282–14290.
- Roach, E.J., Kimber, M.S., and Khursigara, C.M. (2014). Crystal structure and site-directed mutational analysis reveals key residues involved in *Escherichia coli* ZapA function. *J. Biol. Chem.* 289, 23276–23286.
- Rohou, A., and Grigorieff, N. (2015). CTFFIND4: Fast and accurate defocus estimation from electron micrographs. *J. Struct. Biol.* 192, 216–221.
- Roseboom, W., Nazir, M.G., Meiresonne, N.Y., Mohammadi, T., Verheul, J., Buncherd, H., Bonvin, A.M.J.J., De Koning, L.J., De Koster, C.G., De Jong, L., et al. (2018). Mapping the Contact Sites of the *Escherichia coli* Division-Initiating Proteins FtsZ and ZapA by BAMG Cross-Linking and Site-Directed Mutagenesis. *Int. J. Mol. Sci.* 19, 2928.
- Ruiz-Avila, L.B., Huecas, S., Artola, M., Vergoñós, A., Ramírez-Aportela, E., Cercenado, E., Barasoain, I., Vázquez-Villa, H., Martín-Fontecha, M., Chacón, P., et al. (2013). Synthetic Inhibitors of Bacterial Cell Division Targeting the GTP-Binding Site of FtsZ. *ACS Chem. Biol.* 8, 2072–2083.
- Russo, C.J., Scotcher, S., and Kyte, M. (2016). A precision cryostat design for manual and semi-automated cryo-plunge instruments. *Rev. Sci. Instrum.* 87, 114302.
- Saalbach, G., Hempel, A.M., Vigouroux, M., Flärdh, K., Buttner, M.J., and Naldrett, M.J. (2013). Determination of Phosphorylation Sites in the DivIVA Cytoskeletal Protein of *Streptomyces coelicolor* by Targeted LC–MS/MS. *J. Proteome Res.* 12, 4187–4192.
- Salje, J., Gayathri, P., and Löwe, J. (2010). The ParMRC system: molecular mechanisms of plasmid segregation by actin-like filaments. *Nat. Rev. Microbiol.* 8, 683–692.
- Salje, J., van den Ent, F., de Boer, P., and Löwe, J. (2011). Direct membrane binding by bacterial actin MreB. *Mol. Cell* 43, 478–487.
- Samson, R.Y., Obita, T., Hodgson, B., Shaw, M.K., Chong, P.L.-G., Williams, R.L., and Bell, S.D. (2011). Molecular and Structural Basis of ESCRT-III Recruitment to Membranes during Archaeal Cell Division. *Mol. Cell* 41, 186–196.
- Samson, R.Y., Dobro, M.J., Jensen, G.J., and Bell, S.D. (2017). The Structure, Function and Roles of the Archaeal ESCRT Apparatus. In *Prokaryotic Cytoskeletons*, J. Löwe, and L.A. Amos, eds. (Springer International Publishing), pp. 357–377.
- Schaffner-Barbero, C., Gil-Redondo, R., Ruiz-Avila, L.B., Huecas, S., Läppchen, T., den Blaauwen, T., Diaz, J.F., Morreale, A., and Andreu, J.M. (2010). Insights into Nucleotide Recognition by Cell Division Protein FtsZ from a mant-GTP Competition Assay and Molecular Dynamics. *Biochemistry* 49, 10458–10472.

REFERENCES

- Scheffel, A., Gruska, M., Faivre, D., Linaroudis, A., Plitzko, J.M., and Schüler, D. (2006). An acidic protein aligns magnetosomes along a filamentous structure in magnetotactic bacteria. *Nature* **440**, 110–114.
- Scheres, S.H.W. (2012). RELION: Implementation of a Bayesian approach to cryo-EM structure determination. *J. Struct. Biol.* **180**, 519–530.
- Schlieper, D., Oliva, M.A., Andreu, J.M., and Löwe, J. (2005). Structure of bacterial tubulin BtubA/B: Evidence for horizontal gene transfer. *Proc. Natl. Acad. Sci. U. S. A.* **102**, 9170–9175.
- Schöneberg, J., Lee, I.-H., Iwasa, J.H., and Hurley, J.H. (2017). Reverse-topology membrane scission by the ESCRT proteins. *Nat. Rev. Mol. Cell Biol.* **18**, 5–17.
- Schumacher, D., and Søgaard-Andersen, L. (2017). Regulation of Cell Polarity in Motility and Cell Division in *Myxococcus xanthus*. *Annu. Rev. Microbiol.* **71**, null.
- Schumacher, M.A., Glover, T.C., Brzoska, A.J., Jensen, S.O., Dunham, T.D., Skurray, R.A., and Firth, N. (2007). Segrosome structure revealed by a complex of ParR with centromere DNA. *Nature* **450**, 1268–1271.
- Shen, H., Fallas, J.A., Lynch, E., Sheffler, W., Parry, B., Jannetty, N., Decarreau, J., Wagenbach, M., Vicente, J.J., Chen, J., et al. (2018). De novo design of self-assembling helical protein filaments. *Science* **362**, 705–709.
- Shi, C., Fricke, P., Lin, L., Chevelkov, V., Wegstroth, M., Giller, K., Becker, S., Thanbichler, M., and Lange, A. (2015). Atomic-resolution structure of cytoskeletal bactofilin by solid-state NMR. *Sci. Adv.* **1**, e1501087.
- Shiomi, D., and Margolin, W. (2007). Dimerization or oligomerization of the actin-like FtsA protein enhances the integrity of the cytokinetic Z ring. *Mol. Microbiol.* **66**, 1396–1415.
- Snider, N.T., and Omary, M.B. (2014). Post-translational modifications of intermediate filament proteins: mechanisms and functions. *Nat. Rev. Mol. Cell Biol.* **15**, 163–177.
- Spang, A., Saw, J.H., Jørgensen, S.L., Zaremba-Niedzwiedzka, K., Martijn, J., Lind, A.E., van Eijk, R., Schleper, C., Guy, L., and Ettema, T.J.G. (2015). Complex archaea that bridge the gap between prokaryotes and eukaryotes. *Nature* **521**, 173–179.
- Specht, M., Schätzle, S., Graumann, P.L., and Waidner, B. (2011). *Helicobacter pylori* Possesses Four Coiled-Coil-Rich Proteins That Form Extended Filamentous Structures and Control Cell Shape and Motility. *J. Bacteriol.* **193**, 4523–4530.
- Stahlberg, H., Kutejová, E., Muchová, K., Gregorini, M., Lustig, A., Müller, S.A., Olivieri, V., Engel, A., Wilkinson, A.J., and Barák, I. (2004). Oligomeric structure of the *Bacillus subtilis* cell division protein DivIVA determined by transmission electron microscopy. *Mol. Microbiol.* **52**, 1281–1290.
- Stokes, N.R., Sievers, J., Barker, S., Bennett, J.M., Brown, D.R., Collins, I., Errington, V.M., Foulger, D., Hall, M., Halsey, R., et al. (2005). Novel Inhibitors of Bacterial Cytokinesis Identified by a Cell-based Antibiotic Screening Assay. *J. Biol. Chem.* **280**, 39709–39715.
- Strauss, M.P., Liew, A.T.F., Turnbull, L., Whitchurch, C.B., Monahan, L.G., and Harry, E.J. (2012). 3D-SIM Super Resolution Microscopy Reveals a Bead-Like Arrangement for FtsZ and the Division Machinery: Implications for Triggering Cytokinesis. *PLoS Biol* **10**, e1001389.

- Su, M. (2019). goCTF: Geometrically optimized CTF determination for single-particle cryo-EM. *J. Struct. Biol.* 205, 22–29.
- Sun, Q., and Margolin, W. (1998). FtsZ Dynamics during the Division Cycle of Live *Escherichia coli* Cells. *J. Bacteriol.* 180, 2050–2056.
- Swillens, S. (1995). Interpretation of binding curves obtained with high receptor concentrations: practical aid for computer analysis. *Mol. Pharmacol.* 47, 1197–1203.
- Sycuro, L.K., Pincus, Z., Gutierrez, K.D., Biboy, J., Stern, C.A., Vollmer, W., and Salama, N.R. (2010). Peptidoglycan crosslinking relaxation promotes *Helicobacter pylori*'s helical shape and stomach colonization. *Cell* 141, 822–833.
- Szewczak-Harris, A., and Löwe, J. (2018). Cryo-EM reconstruction of AlfA from *Bacillus subtilis* reveals the structure of a simplified actin-like filament at 3.4-Å resolution. *Proc. Natl. Acad. Sci.* 115, 3458–3463.
- Szewczak-Harris, A., Wagstaff, J., and Löwe, J. (2019). Cryo-EM structure of the MinCD copolymeric filament from *Pseudomonas aeruginosa* at 3.1 Å resolution. *BioRxiv* 638619.
- Szwedziak, P., and Ghosal, D. (2017). FtsZ-ring Architecture and Its Control by MinCD. In *Prokaryotic Cytoskeletons*, J. Löwe, and L.A. Amos, eds. (Springer International Publishing), pp. 213–244.
- Szwedziak, P., and Löwe, J. (2013). Do the divisome and elongasome share a common evolutionary past? *Curr. Opin. Microbiol.* 16, 745–751.
- Szwedziak, P., Wang, Q., Freund, S.M., and Löwe, J. (2012). FtsA forms actin-like protofilaments. *EMBO J.* 31, 2249–2260.
- Szwedziak, P., Wang, Q., Bharat, T.A.M., Tsim, M., and Löwe, J. (2015). Architecture of the ring formed by the tubulin homologue FtsZ in bacterial cell division. *ELife* 3, e04601.
- Tacconelli, E., Carrara, E., Savoldi, A., Harbarth, S., Mendelson, M., Monnet, D.L., Pulcini, C., Kahlmeter, G., Kluytmans, J., Carmeli, Y., et al. (2018). Discovery, research, and development of new antibiotics: the WHO priority list of antibiotic-resistant bacteria and tuberculosis. *Lancet Infect. Dis.* 18, 318–327.
- Tan, C.M., Therien, A.G., Lu, J., Lee, S.H., Caron, A., Gill, C.J., Lebeau-Jacob, C., Benton-Perdomo, L., Monteiro, J.M., Pereira, P.M., et al. (2012). Restoring Methicillin-Resistant *Staphylococcus aureus* Susceptibility to β -Lactam Antibiotics. *Sci. Transl. Med.* 4, 126ra35–126ra35.
- Tanaka, T. (2010). Functional Analysis of the Stability Determinant AlfB of pBET131, a Miniplasmid Derivative of *Bacillus subtilis* (natto) Plasmid pLS32. *J. Bacteriol.* 192, 1221–1230.
- Tanaka, K., Takeda, S., Mitsuoka, K., Oda, T., Kimura-Sakiyama, C., Maéda, Y., and Narita, A. (2018). Structural basis for cofilin binding and actin filament disassembly. *Nat. Commun.* 9, 1860.
- Teeffelen, S. van, Wang, S., Furchtgott, L., Huang, K.C., Wingreen, N.S., Shaevitz, J.W., and Gitai, Z. (2011). The bacterial actin MreB rotates, and rotation depends on cell-wall assembly. *Proc. Natl. Acad. Sci.* 108, 15822–15827.

REFERENCES

- The Review on Antimicrobial Resistance (2015). Securing New Drugs for Future Generations: The Pipeline of Antibiotics (The Review on Antimicrobial Resistance).
- Theriot, J.A. (2000). The Polymerization Motor. *Traffic* 1, 19–28.
- Tinsley, E., and Khan, S.A. (2006). A novel FtsZ-like protein is involved in replication of the anthrax toxin-encoding pXOI plasmid in *Bacillus anthracis*. *J. Bacteriol.* 188, 2829–2835.
- Tocheva, E.I., Matson, E.G., Morris, D.M., Moussavi, F., Leadbetter, J.R., and Jensen, G.J. (2011). Peptidoglycan Remodeling and Conversion of an Inner Membrane into an Outer Membrane during Sporulation. *Cell* 146, 799–812.
- Toro-Nahuelpan, M., Müller, F.D., Klumpp, S., Plitzko, J.M., Bramkamp, M., and Schüler, D. (2016). Segregation of prokaryotic magnetosomes organelles is driven by treadmilling of a dynamic actin-like MamK filament. *BMC Biol.* 14, 88.
- Trachtenberg, S., Dorward, L.M., Speransky, V.V., Jaffe, H., Andrews, S.B., and Leapman, R.D. (2008). Structure of the Cytoskeleton of *Spiroplasma melliferum* BC3 and Its Interactions with the Cell Membrane. *J. Mol. Biol.* 378, 778–789.
- Turk, D. (2013). MAIN software for density averaging, model building, structure refinement and validation. *Acta Crystallogr. D Biol. Crystallogr.* 69, 1342–1357.
- Uebe, R., and Schüler, D. (2016). Magnetosome biogenesis in magnetotactic bacteria. *Nat. Rev. Microbiol.* 14, 621–637.
- Usluer, G.D., DiMaio, F., Yang, S.K., Hansen, J.M., Polka, J.K., Mullins, R.D., and Kollman, J.M. (2018). Cryo-EM structure of the bacterial actin AlfA reveals unique assembly and ATP-binding interactions and the absence of a conserved subdomain. *Proc. Natl. Acad. Sci. U.S.A.* 115, 3356–3361.
- Vaughan, S., Wickstead, B., Gull, K., and Addinall, S.G. (2004). Molecular Evolution of FtsZ Protein Sequences Encoded Within the Genomes of Archaea, Bacteria, and Eukaryota. *J. Mol. Evol.* 58, 19–29.
- Wagstaff, J., and Löwe, J. (2018). Prokaryotic cytoskeletons: protein filaments organizing small cells. *Nat. Rev. Microbiol.* 16, 187–201.
- Wagstaff, J.M., Tsim, M., Oliva, M.A., García-Sánchez, A., Kureisaite-Ciziene, D., Andreu, J.M., and Löwe, J. (2017). A Polymerization-Associated Structural Switch in FtsZ That Enables Treadmilling of Model Filaments. *MBio* 8, e00254-17.
- Waidner, B., Specht, M., Dempwolff, F., Haeberer, K., Schaetzle, S., Speth, V., Kist, M., and Graumann, P.L. (2009). A Novel System of Cytoskeletal Elements in the Human Pathogen *Helicobacter pylori*. *PLOS Pathog.* 5, e1000669.
- Walshaw, J., Gillespie, M.D., and Kelemen, G.H. (2010). A novel coiled-coil repeat variant in a class of bacterial cytoskeletal proteins. *J. Struct. Biol.* 170, 202–215.
- Wang, X., and Lutkenhaus, J. (1996). FtsZ ring: the eubacterial division apparatus conserved in archaeobacteria. *Mol. Microbiol.* 21, 313–319.
- Ward, M.J., Lew, H., and Zusman, D.R. (2000). Social motility in *Myxococcus xanthus* requires FrzS, a protein with an extensive coiled-coil domain. *Mol. Microbiol.* 37, 1357–1371.

- Wegner, A. (1976). Head to tail polymerization of actin. *J. Mol. Biol.* 108, 139–150.
- Whitelegge, J.P., Coutre, J. le, Lee, J.C., Engel, C.K., Privé, G.G., Faull, K.F., and Kaback, H.R. (1999). Toward the bilayer proteome, electrospray ionization-mass spectrometry of large, intact transmembrane proteins. *Proc. Natl. Acad. Sci.* 96, 10695–10698.
- Wickham, H. (2017). tidyverse: Easily Install and Load the “Tidyverse.”
- Williams, C.J., Headd, J.J., Moriarty, N.W., Prisant, M.G., Videau, L.L., Deis, L.N., Verma, V., Keedy, D.A., Hintze, B.J., Chen, V.B., et al. (2018). MolProbity: More and better reference data for improved all-atom structure validation. *Protein Sci.* 27, 293–315.
- Wohlleben, W., Mast, Y., Stegmann, E., and Ziemert, N. (2016). Antibiotic drug discovery. *Microb. Biotechnol.* 9, 541–548.
- Woldemeskel, S.A., McQuillen, R., Hessel, A.M., Xiao, J., and Goley, E.D. (2017). A conserved coiled-coil protein pair focuses the cytokinetic Z-ring in *Caulobacter crescentus*. *Mol. Microbiol.* 105, 721–740.
- Xinyi Huang (2003). Fluorescence Polarization Competition Assay: The Range of Resolvable Inhibitor Potency Is Limited by the Affinity of the Fluorescent Ligand. *J. Biomol. Screen.* 8, 34–38.
- Yang, R., Bartle, S., Otto, R., Stassinopoulos, A., Rogers, M., Plamann, L., and Hartzell, P. (2004). AglZ is a filament-forming coiled-coil protein required for adventurous gliding motility of *Myxococcus xanthus*. *J. Bacteriol.* 186, 6168–6178.
- Yang, X., Lyu, Z., Miguel, A., McQuillen, R., Huang, K.C., and Xiao, J. (2017). GTPase activity-coupled treadmilling of the bacterial tubulin FtsZ organizes septal cell wall synthesis. *Science* 355, 744–747.
- Yao, Q., Jewett, A.I., Chang, Y.-W., Oikonomou, C.M., Beeby, M., Iancu, C.V., Briegel, A., Ghosal, D., and Jensen, G.J. (2017). Short FtsZ filaments can drive asymmetric cell envelope constriction at the onset of bacterial cytokinesis. *EMBO J.* 36, 1577–1589.
- Yoshida, Y., Kuroiwa, H., Hirooka, S., Fujiwara, T., Ohnuma, M., Yoshida, M., Misumi, O., Kawano, S., and Kuroiwa, T. (2009). The Bacterial ZapA-like Protein ZED Is Required for Mitochondrial Division. *Curr. Biol.* 19, 1491–1497.
- You, Y., Elmore, S., Colton, L.L., Mackenzie, C., Stoops, J.K., Weinstock, G.M., and Norris, S.J. (1996). Characterization of the cytoplasmic filament protein gene (cfpA) of *Treponema pallidum* subsp. *pallidum*. *J. Bacteriol.* 178, 3177–3187.
- Yuan, Y., Peng, Q., Wu, D., Kou, Z., Wu, Y., Liu, P., and Gao, M. (2015). Effects of Actin-Like Proteins Encoded by Two *Bacillus pumilus* Phages on Unstable Lysogeny, Revealed by Genomic Analysis. *Appl. Environ. Microbiol.* 81, 339–350.
- Yutin, N., and Koonin, E.V. (2012). Archaeal origin of tubulin. *Biol. Direct* 7, 10.
- Zaremba-Niedzwiedzka, K., Caceres, E.F., Saw, J.H., Bäckström, D., Juzokaite, L., Vancaester, E., Seitz, K.W., Anantharaman, K., Starnawski, P., Kjeldsen, K.U., et al. (2017). Asgard archaea illuminate the origin of eukaryotic cellular complexity. *Nature* 541, 353–358.

REFERENCES

- Zehr, E.A., Kraemer, J.A., Erb, M.L., Coker, J.K.C., Montabana, E.A., Pogliano, J., and Agard, D.A. (2014). The structure and assembly mechanism of a novel three-stranded tubulin filament that centers phage DNA. *Struct. Lond. Engl.* 1993 22, 539–548.
- Zheng, S., Palovcak, E., Armache, J.-P., Cheng, Y., and Agard, D. (2016). Anisotropic Correction of Beam-induced Motion for Improved Single-particle Electron Cryo-microscopy. *BioRxiv* 061960.
- Zheng, S.Q., Palovcak, E., Armache, J.-P., Verba, K.A., Cheng, Y., and Agard, D.A. (2017). MotionCor2: anisotropic correction of beam-induced motion for improved cryo-electron microscopy. *Nat. Methods* 14, 331–332.
- Zivanov, J., Nakane, T., Forsberg, B.O., Kimanius, D., Hagen, W.J., Lindahl, E., and Scheres, S.H. (2018). New tools for automated high-resolution cryo-EM structure determination in RELION-3. *ELife* 7, e42166.